CHARGED PARTICLE PSEUDO-RAPIDITY DISTRIBUTIONS IN MINIMUM BIAS AND INTERMEDIATE VECTOR BOSON EVENTS AT $\sqrt{s}$ = 1800 GEV

BY

FREDERICK D. SNIDER

MARCH, 1990

THE UNIVERSITY OF CHICAGO

CHARGED PARTICLE PSEUDO-RAPIDITY DISTRIBUTIONS IN MINIMUM BIAS AND INTERMEDIATE VECTOR BOSON EVENTS AT $\sqrt{s} = 1800$ GEV

A DISSERTATION SUBMITTED TO
THE FACULTY OF THE DIVISION OF THE PHYSICAL SCIENCES
IN CANDIDACY FOR THE DEGREE OF
DOCTOR OF PHILOSOPHY

DEPARTMENT OF PHYSICS

BY
FREDERICK D. SNIDER

CHICAGO, ILLINOIS
MARCH, 1990

Acknowledgements

This experiment is the culmination of many years of dedicated effort by the members of the CDF Collaboration, the staff of the Fermilab Tevatron Collider, and the CDF technical and support staff. I am indebted to them for providing the opportunity to work on this project.

I would like to thank my advisor, Henry Frisch, for his guidance throughout this work. His many suggestions and critical comments have contributed greatly to the analysis and the thesis. His ability to extract a few essential, physically relevant features of a seemingly difficult problem I hope some day to possess.

For their assistance in the analysis of the W and Z data, I am greatly indebted to Claudio Campagnari, Paul Derwent and Marshall Miller. As I recall the steady stream of information and data they provided, despite my constant pestering and inane questions, it is difficult to imagine a group more easy and pleasurable with whom to work.

For several years, from the design and construction of the VTPC through the analysis of the first data from the chamber, I had the great pleasure of working with Morris Binkley, John Huth, Bob Kephart and Adam Para at Fermilab. To Morris, I owe many hours of engaging discussions as we explored how to understand and use the device we had built. John provided a great deal of help in the same task, along with numerous, interesting discussions on topics both in and out of physics. From Bob and Adam, I received many useful suggestions and a great deal of support throughout the of construction of the detector, development of software and early stages of data analysis.

The efficiency measurements were made possible through the dedicated and meticulous work of Candies Kastner and Joanne Lindo in the Fermilab Film Analysis Lab. I thank them for their patient work in this difficult task.

I owe special thanks to Jonathan Rosner for his very careful reading of the thesis. Robert Sachs also provided useful comments.

I am particularly grateful for the opportunity to work with Maki Sekiguchi, a fellow graduate student working at Fermilab on the VTPC. I shall always admire his drive and value the time we worked together.

I thank my office mates George Redlinger, Sunil Somalwar and Yeong-Dong Tsai for the many discussions and activities that so greatly enhanced my enjoyment of life at the University. Learning physics with them was fun.

For providing an intellectually stimulating and pleasurable environment in which to work, I thank the many people — graduate students, postdocs, professors, undergrads and secretaries — who make up the High Energy Physics Department. I will remember fondly the time I spent here.

In the middle of my graduate student career, I had the great fortune to meet and marry Debbie Lucas. Her knowledge, insight, love and companionship continue to provide a great and essential source of strength in my life.

I dedicate this thesis to the memory of W.L. Childers.

Table of Contents

List of Tables

List of Illustrations

Abstract

We present measurements of the pseudo-rapidity ($\eta = \ln(\tan(\theta/2))$, where θ is the polar angle in the lab frame) distribution of charged particles ($dN_{ch}/d\eta$) produced within $|\eta| \leq 3.5$ in proton-antiproton collisions at $\sqrt{s}$ of 630 and 1800 GeV. We measure $dN_{ch}/d\eta$ at $\eta = 0$ to be 3.18±0.06(stat)±0.10(sys) at 630 GeV, and 3.95±0.03(stat)±0.13(sys) at 1800 GeV. Some systematic errors in the ratio of $dN_{ch}/d\eta$ at the two energies cancel, and we measure 1.26±0.01±0.04 for the ratio of $dN_{ch}/d\eta$ at 1800 GeV to that at 630 GeV within $|\eta| \leq 3$. Comparing to lower energy data, we observe an increase in $dN_{ch}/d\eta$ at $\eta = 0$ that is faster than $\ln(s)$.

We also measure the ratio of $dN_{ch}/d\eta$ for charged particles produced in events in which an intermediate vector boson is observed in the decay channel $W^{\pm} \rightarrow e^{\pm}\nu$ or $Z^0 \rightarrow e^+e^-$ to that in minimum bias events as a function of the boson p_t. The absence of strongly interacting particles in the boson final state allows an unambiguous separation of the particles produced by the spectator system from those of the hard parton-parton collision. We find that at $p_t = 0$, the ratio averaged within $|\eta| < 3$ is 1.22±0.08±0.12 in W events, and 1.31±0.21±0.11 in Z events, indicating that particle production by the spectator system in hard collisions is very similar to that in minimum bias events, with only a slight enhancement. These results do not support predictions for these quantities based upon two models of minimum bias particle production, including the Dual Parton Model and a simple impact parameter model. We observe an increase of about 20% over similar results reported by the UA1 collaboration at 630 GeV.

Chapter 1

Introduction

For over a decade, particle physicists have possessed a remarkably successful theory describing the short range behavior of hadron constituent interactions, Quantum Chromodynamics (QCD) [1]. Such striking phenomena as high transverse momentum (p_t) "jets" in proton-anti-proton ($\bar{p}p$) collisions [2,3,4], energy scaling violations in jet cross sections [2], and the p_t spectrum of W and Z bosons [5,6], each characteristic of hard scattering of quarks and gluons (hadron constituents), all are well described by QCD. Compared to the total cross section, however, hard scattering events such as W boson production occur only rarely. The vast majority of interactions at high energy involve relatively "soft" collisions with low p_t transfers and many-body final states. Although in principle, QCD describes quark and gluon interactions on all distance scales, limitations inherent in currently available solution techniques prevent direct calculation of the long distance behavior. It is indeed one of the ironies of modern particle physics that those interactions most easily observed and studied remain among the least understood.

Lacking a basic theoretical description of multiparticle production, researchers studying multiparticle production have measured an array of properties of soft (or so-called "minimum bias") hadron-hadron collisions in an attempt to characterize the essential features of the interactions. Such measures as the multiplicity distribution, two-particle correlation functions, and the angular distribution of secondaries provide particularly interesting insights into multiparticle production mechanisms. The angular distribution has long played an important role in this effort.

In this document, we present a measurement of the angular distribution of charged secondaries produced in $\bar{p}p$ collisions at a center-of-mass (CM) energy ($\sqrt{s}$) of 1800 GeV, an increase by a factor of two over the highest energy previously studied [7]. In order to compare lower energy data and to observe the energy dependence directly, we perform the same measurement at $\sqrt{s} = 630$ GeV. We recorded data using the Collider Detector at Fermilab (CDF) at the Fermilab Tevatron Collider during the winter and spring of 1987. The detector was constructed and operated by the CDF Collaboration (Appendix A). Before introducing more details of this measurement, we will trace some of the history of the study of multiparticle production placing particular emphasis on the role played by angular distributions in the investigation.

1.1 Historical overview

The study of angular distributions in hadron interactions began soon after the 1947 discovery of charged pions produced in emulsions exposed to cosmic rays. The early experiments relied on cosmic rays to provide high energy particles and recorded interactions in photographic emulsions [8] or cloud chambers [9]. Although plagued by ambiguities in particle identification, technological limitations in reconstructing the complex interactions involving high atomic weight nuclei, and poor statistics [10], measurements of angular distributions by some of these early experiments provided the first evidence that multiple production of pions was a fundamental process in nuclear interactions [11,12], and not merely a cascade similar to those in found high energy electromagnetic interactions.

The development of high energy particle accelerators allowed detailed, systematic study of particle production processes. Particle accelerators at the University of Chicago, Columbia University, Carnegie Institute of Technology,[1] the University of Rochester and University of California at Berkeley generated beams of sufficient energy to produce pions and other secondary beams, and began producing results in many high statistics, high quality experiments. Anderson *et al.*, using liquid hydrogen targets at the University of Chicago synchrocyclotron [13], and Roberts and Tinlot, using water targets at the University of Rochester [14], extracted the total cross section for $\pi^{\pm}p$ scattering by integrating angular distributions measured with scintillation counters. At Brookhaven, Fowler *et al.* [10] convincingly demonstrated the existence of multiple particle production using neutrons incident on a hydrogen-filled cloud chamber. The same experiment found large forward-backward asymmetries in the angular and longitudinal momentum distributions of the final state baryons: the incident nucleons (and pions in other experiments), after accounting for charge exchanges, exhibited a strong preference toward forward scattering peaked at high momentum. The remaining particles in the events were distributed at much lower momentum and over wide angles in the CM frame. This apparent "transparency" [15] of hadrons, evident in the correlation of incident and final state momenta, represents some of the earliest evidence for the composite nature of hadrons.

Multiparticle production in strong interactions was the focus of intense investigation throughout the latter part of the 1950's and 1960's. Several features of particle production soon became evident. First, the angular distribution of secondaries in the center of mass frame was highly peaked in the forward and backward directions [16,17,18,19]. The form of the distribution was consistent with a mechanism in which particles are produced by the decay of objects (such as excited states of the incident particles) in motion in the CM frame [18,19]. Second, the mean p_t of secondaries tended to be quite small, on the order of 0.4 GeV/c, independent of the CM energy [20]. The evidence for this observation extended up to cosmic ray

[1] Now Carnegie Mellon University.

energies (about 3000 GeV/c in the lab frame). Third, the p_t spectrum of secondaries appeared consistent with an exponential [20] or a Gaussian [21]. Fourth, the mean multiplicity varied slowly with energy (consistent with ($\langle n \rangle = A + B \ln(s)$) [21]). And finally, the total inelastic pp cross section was approximately constant across the range of energies available at the Brookhaven Alternating Gradient Synchrotron [22] (protons with momentum up to 28 GeV/c in the lab frame, incident on nuclear targets).

As the energy of available accelerators increased, so too did the number and type of secondary particles produced. The resulting complexity of the final states, along with the increasing number of open channels in the final state, made analysis of results and presentation of data increasingly cumbersome. Some experimenters found simplicity by virtue of the limited phase space acceptance of their spectrometers, and measured distributions with respect to a particular final state particle independent of the remainder of the final state [16,22,23]. Others, with the misfortune to possess equipment with superior acceptance (such as liquid hydrogen bubble chambers), measured distributions for every distinct channel that could be identified [17,18,24]. All experimenters generally evaluated angular distributions in the CM frame (see, for instance, refs. [17,18]). Momentum distributions, however, were presented as ($d^2\sigma/d\Omega dp$), evaluated either in the lab frame [25] or the CM frame [19].

Despite this complexity, angular distribution measurements continued to yield new information, as long as the final state consisted of just a few particles. In these cases, phase shifts extracted from the data provided evidence for the existence and angular momentum state of hadron resonances [22].

A solution to the problem of how to study complex final states came in two suggestions inspired by two important hypotheses, all four advanced by Feynman [26] and Benecke and collaborators [27]. In the first suggestion, the authors advocated the measurement of distributions with respect to a particular subset of final state particles, independent of all others. Feynman termed these "inclusive" distributions. (Distributions in which the state of *each* final state particle is defined he called "exclusive" distributions.) This approach, Feynman argued, represented the only sensible response given the rapidly falling exclusive cross sections with increasing CM energy. At asymptotic energies, he continued, exclusive cross sections may approach zero, whereas inclusive cross sections, by summing over the ever increasing number of open channels, would remain finite.

The second suggestion proposes the use of rapidity and transverse momentum to characterize the momentum state, and pseudo-rapidity for the angular distribution. This choice of variables simplifies comparisons of data presented in the laboratory and CM frames in the following way. The rapidity, y, defined by

$$y = \frac{1}{2}\ln\left(\frac{E+p_{\|}}{E-p_{\|}}\right), \tag{1.1}$$

where E is the particle energy and $p_{\|}$ is the component of momentum along some axis (generally chosen parallel to the incident momentum) measures the boost between the longitudinal rest frame of a particle with $p_{\|}$ and the frame in which E and $p_{\|}$ are measured. The rapidity of a particle in one frame is therefore related to its rapidity in another frame by a simple linear transformation. Coupled with the Lorentz invariant transverse momentum, the rapidity provides a convenient alternative to direct angular and momentum measurements. The pseudo-rapidity, η, defined by

$$\eta = -\ln\left\{\tan\left(\frac{\theta}{2}\right)\right\}, \tag{1.2}$$

where θ is the angle of the particle with respect to some axis in the laboratory frame, is closely related to the rapidity at high energies defined relative to the same axis. For certain experiments, the pseudo-rapidity has the advantage that it does not require measurement of the momentum. In the relativistic limit, η is identical to y and should therefore transform like rapidity for high energy particles.

Feynman and Benecke *et al.* then each proposed a hypothesis concerning the behavior of inclusive distributions at high energy given an appropriate choice of variables [26,27]. Benecke *et al.* hypothesized that when viewed from the rest frame of either the target or the projectile, the longitudinal momentum distribution (and therefore, the angular distribution) should approach a limiting distribution as $\sqrt{s} \rightarrow \infty$ — the so-called "limiting fragmentation" hypothesis. Feynman suggested a stronger form: assuming the transverse momentum distribution to be limited in a way independent of the longitudinal momentum, the inclusive distributions should be energy independent when taken as a function of x, where $x = 2p_{||}/\sqrt{s}$. This is the "scaling" hypothesis. The choice of x as the scaling variable effectively extended the limiting fragmentation hypothesis from the fragmentation region (i.e., x near 0 and 1) into the central region as well. Thus the term "Feynman scaling" came to mean the independence of of the inclusive rapidity (or pseudo-rapidity) distribution in the central region on energy.

Both hypotheses, scaling and limiting fragmentation, were expected to be especially robust since they were derived independent of any dynamical considerations and rested only reasonable and very generally held assumptions. In 1972, Koba, Neilsen and Olesen proved that Feynman scaling implied a particular form of scaling in the multiplicity distribution: the distribution nP_n taken as a function of $n/\langle n \rangle$ must be energy independent [28], where P_n is the probability for the occurrence of multiplicity n. This result is known as the KNO scaling hypothesis. Once again, derivation of the result required making no dynamical assumptions.

Much of the experimental work on multiparticle production during the next 15 years was devoted to tests of scaling. An essential element of this effort was the advance of the hadron-hadron collider, a development which resulted in dramatic increases in the CM energy at which collisions could be observed. The CERN Intersecting Storage Ring (ISR) provided the highest energy collisions yet observed. By 1972, there were not only theoretical, but also experimental reasons to believe that the onset of scaling had already been observed at ISR energies [29]. The early results of Ratner *et al.* [30] up to $\sqrt{s} = 63$ GeV, using a single arm spectrometer to measure the *invariant* cross section ($Ed^3\sigma/dp^3$), *appeared* to confirm scaling of the inclusive p_t spectrum, at least over a limited range of p_t. Later results tended to confirm these conclusions [31,32]: the low p_t regime exhibited scaling in both the fragmentation and central regions. The approach to scaling, however, depended upon the value of x and the particular particle species under consideration.

These ISR experiments, plus one at Fermilab, then reported an effect which changed the emphasis of subsequent research: high p_t particles occurred several orders of magnitude more frequently than expected on the basis of exponential or Gaussian extrapolations to data at low p_t [31,32,33]. The high p_t regime promised hope that the parton structure of hadrons, along with the scale invariance observed in deep-inelastic scattering, might be confirmed in hadron-hadron interactions.

During the following years, rather than studying the basic mechanisms of multiparticle production, most researchers concentrated on studying the short distance behavior of hadron constituent interactions [34]. Nonetheless, there were several significant experiments. The first, at the ISR, consisted of a streamer chamber with wide angle coverage at an interaction region. Although intrinsically lacking the full acceptance of bubble chamber experiments, the higher energies offered by the collider, along with the significantly larger acceptance than that provided by previous spectrometers at the ISR, combined to make an experiment well suited to the study of particle production. Using this detector, Thomé *et al.* [35] showed conclusive evidence for the violation of Feynman scaling in pseudo-rapidity distributions (see fig. 1) across the entire range of ISR energies (from $\sqrt{s}$ = 23.6 GeV to $\sqrt{s}$ = 62.8 GeV).

The second experiment, designated the UA5 collaboration at the CERN S$\bar{p}$pS collider, followed a design almost identical to the ISR experiment, but with improved acceptance to accommodate the broadening pseudo-rapidity distribution. The UA5 group eventually extended measurements of particle production ratios, multiplicities and pseudo-rapidity distributions (fig. 2) up to $\sqrt{s}$ = 900 GeV [7,36]. Their results demonstrated three striking features. First, the central pseudo-rapidity density

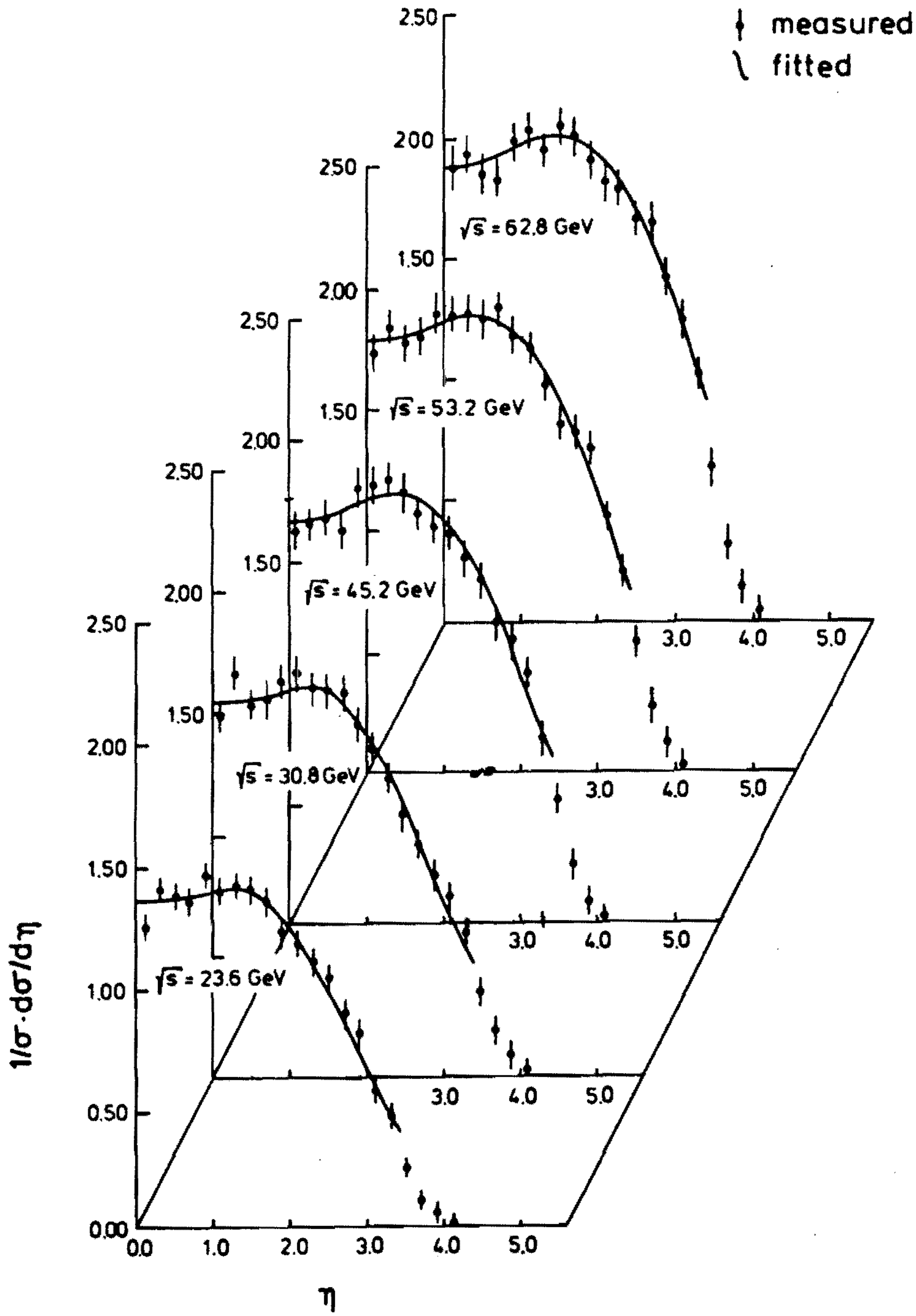

Figure 1. Pseudo-rapidity density for $\sqrt{s}$ = 23.6 to 62.8 GeV (from ref. [35]).

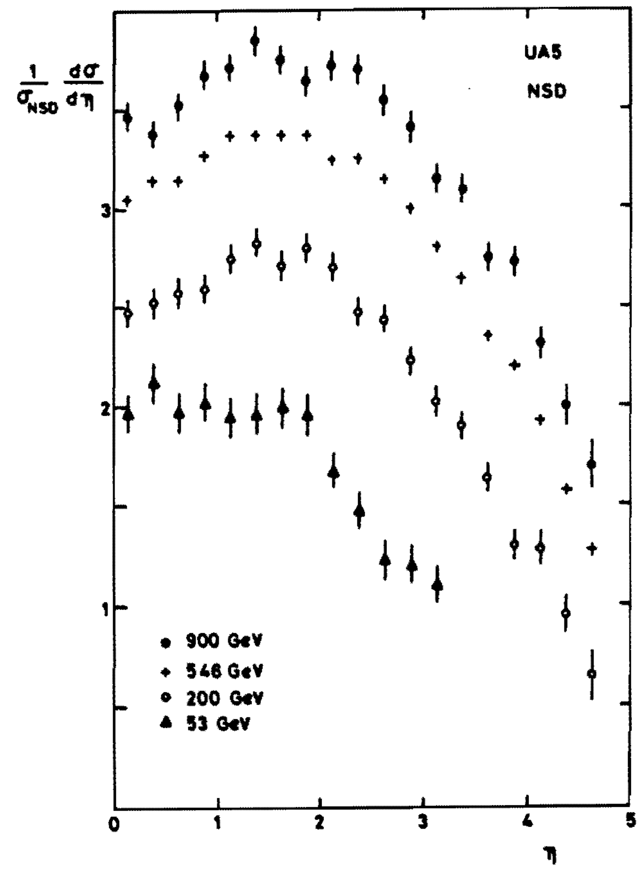

Figure 2. Pseudo-rapidity density observed at the S$\bar{p}$pS (from ref. [7]).

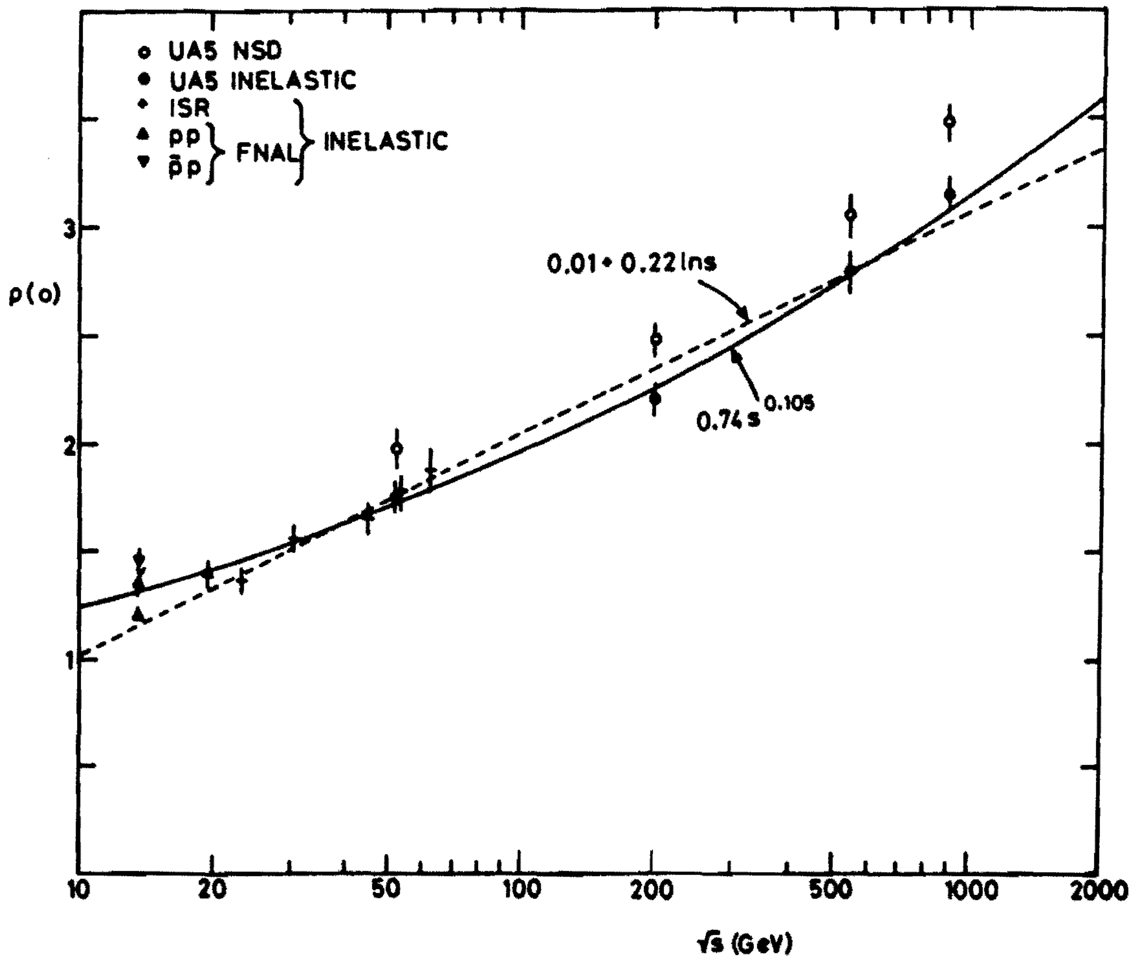

Figure 3. $dN_{ch}/d\eta$ at $\eta = 0$ vs. $\sqrt{s}$ (from refs. [7,35,37]).

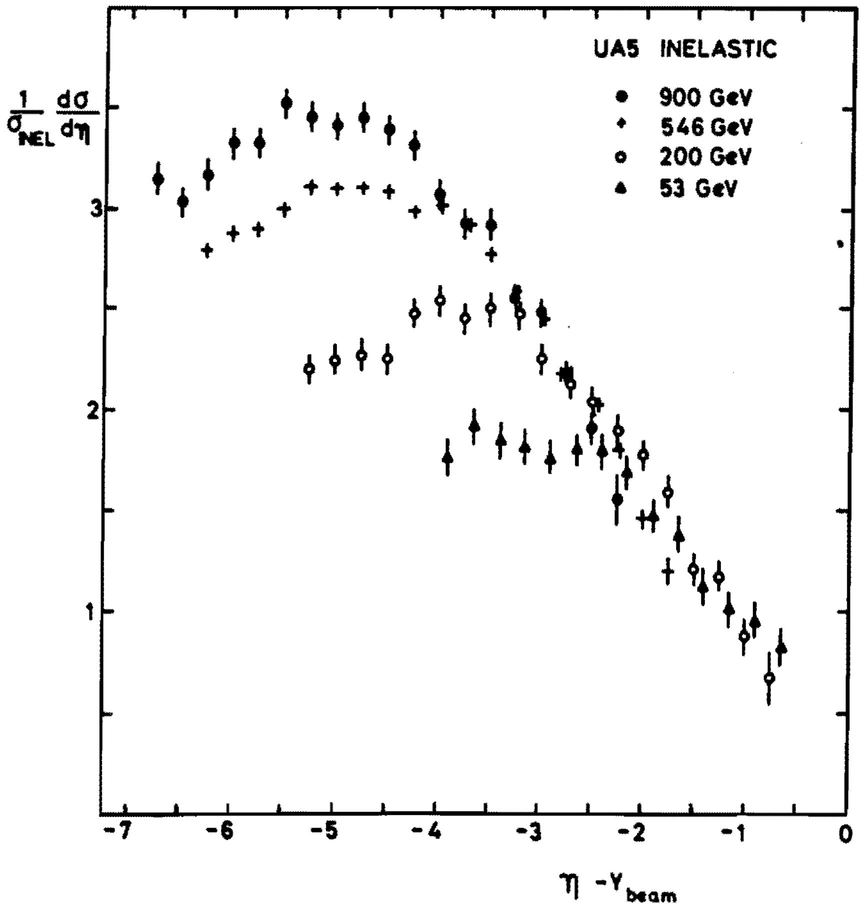

Figure 4. Pseudo-rapidity density vs. $\eta - y_{beam}$ (from refs. [7,35]).

($\rho(\eta = 0) = (dN_{ch}/d\eta)_{\eta=0}$) grows at a rate consistent with $\ln(s)$ [7], as shown in fig. 3. Also shown in fig. 3 are the results from the ISR [35] and lower energy data from Fermilab [37]. Second, scaling in the fragmentation region is observed to about the 10–20% level [7]. The comparison of data at different energies, shown in fig. 4, is accomplished by plotting $dN_{ch}/d\eta$ as a function of $y_{lab} = \eta - y_{beam}$, corresponding to the approximate rapidity distribution as observed in the rest frame of one of the target particles. Third, the multiplicity distribution at energies up to $\sqrt{s} = 546$ GeV exhibits a clear violation in the KNO scaling parameters.

The Fermilab $\bar{p}p$ collider represents the most recent development in this story. Capable of accelerating beams to 900 GeV, the collider allows the study of interactions up to $\sqrt{s} = 1800$ GeV in the CM frame of the interactions.

1.2 Theoretical development

A number of phenomenological models have been proposed to describe multiparticle production. Many have fallen into disuse from their lack of predictive power. All have some arbitrary parameters which must be fit from experiment. From that point, however, they differ greatly in the extent to which they predict the energy dependence of those parameters (and therefore, say, inclusive distributions) without further experimental input [38]. Some, such as the multiperipheral approach [39], described early data with remarkable success, but, unable to account for violations in Feynman scaling and the faster than $\ln(s)$ growth of the multiplicity (see Horn in ref. [29]), came to describe an increasingly smaller fraction of the observed phase space (see, for instance, [40]). Although these deserve some note in the historical record, they will not be discussed here.

In this section, we will focus instead on the development of two of the most common approaches used today which lead to models both consistent with existing data, and which predict the energy dependence of inclusive distributions. Broadly speaking, these models can be described either as statistical hydrodynamical models, or as string fragmentation models that incorporate ideas of parton-parton interactions.[2]

1.2.1 Statistical hydrodynamical models

The suggestion that multiparticle production might occur in high energy interactions emerged slowly during the 1930's in work related to Quantum Electrodynamics. Wataghin [44] and Heisenberg [45] showed that field theory is valid only up to some universal high energy limit.[3] Later, Heisenberg extended this work and conjectured that the breakdown at this limit might include multiparticle production [47].

Four years before multiparticle production was observed directly, Fermi constructed a statistical model for multiple pion production [48], making only two assumptions: first, that the collision time was long compared to the fundamental time scale of the interaction; second, that the number of internal degrees of freedom in the interacting matter after collision was large. From these assumptions, Fermi deduced the multiplicity, transverse momentum and angular distributions independent of the underlying dynamics of the interaction. In 1953, Landau added the principles of relativistic hydrodynamics in order to describe the time evolution of the hadronic matter after the collision in a more rigorous manner [49].

Although the model as first proposed by Fermi and Landau failed to describe the early data [50], their statistical approach, exactly because it was insensitive to the underlying interaction, laid the foundation for a model still in use today. Remarkably, the essential features of the modern form, now called the Statistical

[2]The recently developed class of parton-branching models, the authors [41] claim, is "inspired" by QCD, particularly by such features as gluon bremsstrahlung and gluon splitting [42]. Although these models produce several quite interesting predictions [43] (dealing mostly with multiplicity distributions), they appear not to have addressed the question of pseudo-rapidity distributions *per se*.

[3]The original texts are in German, and I rely on Marshak [11] and Lattes, Fujimoto and Hasegawa [46] for their paraphrases of the originals.

Hydrodynamical Model, are the same as the version Landau proposed in 1953. The primary improvements in the current version, due to Pokorski and Van Hove, are the inclusion of valence parton constituents in order to account for leading particles (e.g., protons at large x) and the expectation that gluons dominate interactions at small p_t [51] (see fig. 5).

The general predictions of the model include a power law dependence of the mean multiplicity on s ($\langle n \rangle \propto s^{0.25}$), an exponential p_t spectrum (although this is not an essential feature of the model at high p_t), and a faster than $\ln(s)$ dependence of the rapidity distribution in the central region. Figure 6 shows predictions of the pseudo-rapidity distribution given by Wehrberger and Weiner [52].

1.2.2 Parton structured string fragmentation models

The quark-parton model [53,54] and QCD enjoyed much success in describing hard scattering phenomena in hadron interactions. Unfortunately, the growth of the coupling constant at low q^2 and the resultant failure of perturbative calculational techniques — the basis for all previous successes — denied a similar success to phenomena on the confinement scale such as multiparticle production. One hope for producing reasonable models of multiparticle production lay in superimposing certain features of the quark-parton model onto a model that characterized the non-perturbative aspects of particle production. In this way, one might obtain a description of low p_t physics that leads naturally and smoothly from the domain of soft interactions into that of hard scattering processes.

1.2.2.1 The Dual Parton Model

One such attempt is the Dual Parton Model (DPM) [55], proposed as an extention of earlier models constructed from Regge-Mueller theory and the $(1/N_f)$ expansion of QCD [56]. In the limit of a large number of flavors (N_f), QCD can be expressed in terms of a topological expansion. One then associates each topolog-

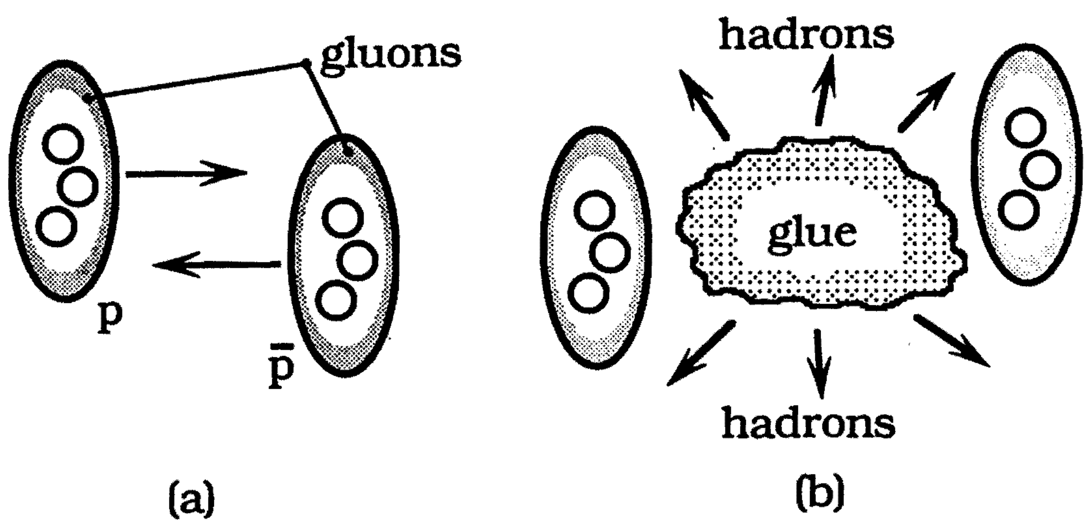

Figure 5. $\bar{p}p$ collision as viewed in Statistical Hydrodynamical Model. (a) Before the collision. (b) After the collision. The valence quarks fly away producing leading particles. The gluons interact and remain behind, producing the particles observed in the central region.

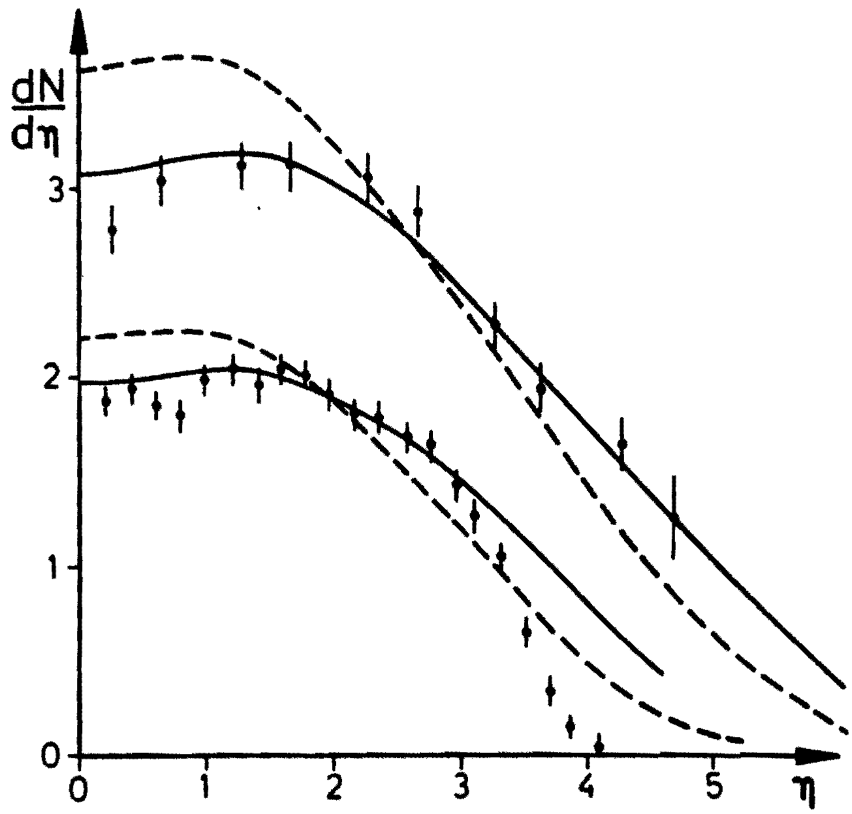

Figure 6. Fits of Statistical Hydrodynamical Model to $dN_{ch}/d\eta$. The dashed curve is an SHM prediction assuming a velocity of sound of $c/2$, and the solid curve assuming $c/\sqrt{3}$ (characteristic of an ideal relativistic fluid). The curves are from ref. [52], and the data from UA5.

ical configuration in the forward elastic amplitude (for $N_f = 3$) with a particular inelastic production diagram (the "cut-Pomeron"). Unitarity relates each forward elastic amplitude, which can be described by a particular Regge trajectory, to the corresponding inelastic amplitude.

An interaction can be envisioned as an initial exchange and separation of color, as illustrated in fig. 7. "Chains", corresponding to the cut Pomerons, form between the colored elements of each particle. Each chain then fragments into particles according to universal fragmentation functions (e.g. as measured in deep-inelastic scattering and e^+e^- scattering). Inserting the parton distribution functions, and fitting elastic and diffractive cross sections to obtain the Regge couplings and trajectories, one obtains a quantitative model for multiparticle production with no remaining free parameters.

For energies up to at least $\sqrt{s} = 20$ TeV, the DPM predicts an energy dependence in $\rho(0)$ consistent with $\ln(s)$ [57], and is in reasonable agreement with the data up to $\sqrt{s}$ 900 GeV [55,57].

By the assumption of chain fragmentation universality, the ratio of the number of chains in two given events should equal the ratio of average multiplicities for those events. This simple relationship between the multiplicities and the number of chains permits one to calculate the ratio of mean multiplicities produced by the "spectator system"[4] in different types of hard scattering events [58]. Consider, for example, a $\bar{p}p$ collision that produces an intermediate vector boson (e.g., the W), which then decays leptonically (fig. 8). The leptonic decay ensures that no final state interactions occur between the decay products and the spectator system. Since the annihilating partons leave the spectator system with net color, chains must form between corresponding pieces in each of the incident particles, just as in a soft collision. By counting the number of chains in the W event, and comparing to the

[4]The spectator system refers to the valence and sea quarks, and their attendant gluons, that do not directly participate in the hard scatter.

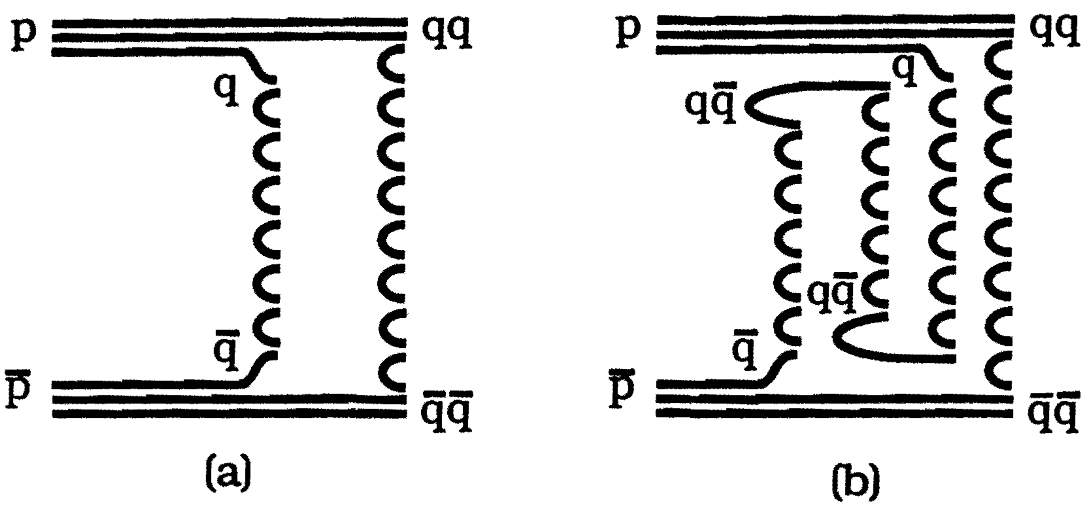

Figure 7. Minimum bias $\bar{p}p$ interaction in the Dual Parton Model. (a) The leading-order two-chain diagram. (b) A second-order diagram with additional chains from a single rescattering.

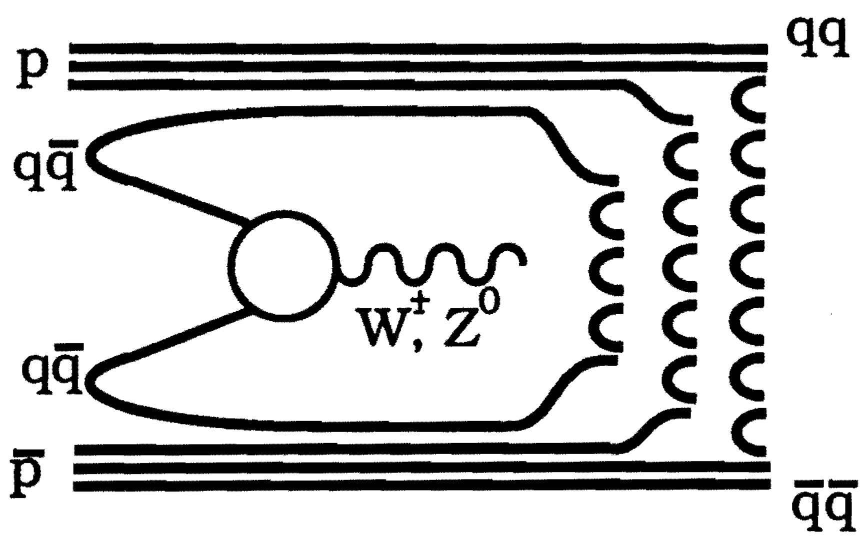

Figure 8. Production of W or Z boson in the Dual Parton Model. Sea-sea (pictured) and valence-sea production (same number of chains) contribute about 80% to the total production cross section [59].

number in the minimum bias event (fig. 7), one obtains a prediction for the ratio of multiplicities:

$$\frac{\langle n^W \rangle}{\langle n^{\bar{p}p} \rangle} = \frac{N^W_{chain}}{N^{\bar{p}p}_{chain}} = \frac{3}{2}. \qquad (1.3)$$

Since the density of particles in rapidity is also a universal parameter of chain fragmentation, this result should hold for $dN_{ch}/d\eta$ as well.

1.2.2.2 Perturbative method

A more recent approach taken by Sjöstrand and van Zijl [60] uses explicit perturbative calculations to determine the probability of single (or multiple) constituent interactions at low p_t. The parton-parton cross section is assumed to be

$$\frac{d\sigma}{dp_t{}^2} = \sum_{i,j,k} \iiint dx_1 dx_2 d\hat{t}\, \hat{\sigma}^k_{ij}(\hat{s},\hat{t},\hat{u}) f^1_i(x_1, Q^2) f^2_j(x_2, Q^2) \delta\left(p_t{}^2 - \frac{\hat{t}\hat{u}}{\hat{s}}\right). \qquad (1.4)$$

We have defined $\hat{\sigma}^k_{ij}$ as the hard-scattering cross section for the kth subprocess possible between partons i and j in the incident particles; and f^m_i as the structure function for parton i in the incident particle m, evaluated at a scale Q^2. The quantity x_i is the longitudinal momentum fraction of parton i, while $\hat{s}$, $\hat{t}$ and $\hat{u}$ are the Mandelstam variables evaluated for the parton-parton system (i.e., $\hat{s} = x_1 x_2 s$).

Integrating the differential cross section down to $p_t = p_{t_{min}}$ (in order to maintain convergence of the integral), we get the hard scattering cross section

$$\sigma_{hard}(p_{t_{min}}) = \int_{p_{t_{min}}^2}^{s/4} \frac{d\sigma}{dp_t{}^2} dp_t{}^2. \qquad (1.5)$$

The ratio $\sigma_{hard}/\sigma_{tot}$ (ignoring elastic and diffractive scattering) is then interpreted as the average number of parton-parton collisions per event.

The authors then introduce an impact parameter and assume that the mean number of constituent interactions is proportional to the overlap of the incoming hadrons. The requirement that the mean number of constituent interactions, averaged over impact parameters, equal the ratio $\sigma_{hard}/\sigma_{tot}$ constrains the constant of proportionality. The number in a given event at a particular impact parameter is distributed according to a Poisson distribution. The distribution of impact parameters corresponds to a dense (Gaussian) core superimposed onto a broad, soft (Gaussian) tail. Strings are then drawn between scattered constituents in a manner similar to the DPM, except that more complicated color configurations are allowed. Strings fragment according to universal fragmentation functions.

The resulting model contains two parameters: the total cross section, σ_{tot} (obtained from experiment), and an energy independent regularization scale to enforce smooth behavior of the cross section as $p_t \to 0$. Many assumptions in the model are open to debate, such as the validity of the leading order perturbation calculations used to obtain σ_{hard}. Somewhat remarkably, however, the model reproduces many features of the existing data quite well, such as the pseudo-rapidity distributions for $\sqrt{s}$ in the range 200-900 GeV (fig. 9). The authors also claim the model can predict the ratio of multiplicities in W events to that in minimum bias events (as they do for high p_t jet events). They offer no predictions for either the ratio or the absolute magnitude of the pseudo-rapidity density at $\sqrt{s} = 1800$ GeV.

1.2.3 Impact parameter model

One other model, which predicts the multiplicity in W events and other high p_t processes, deserves note. Callen and Frankel [61] construct a geometrical model of hadron-hadron interactions with no dynamical assumptions with the exception that the mean multiplicity is proportional to the geometrical overlap of the incoming hadrons:

$$\langle n(b)\rangle = A + BV(b), \tag{1.6}$$

where n is the multiplicity, b is the impact parameter and V(b) is the geometrical overlap as a function of the impact parameter. The multiplicity in a given event is assumed to be Poisson distributed. The mean multiplicity for a minimum bias event is given by:

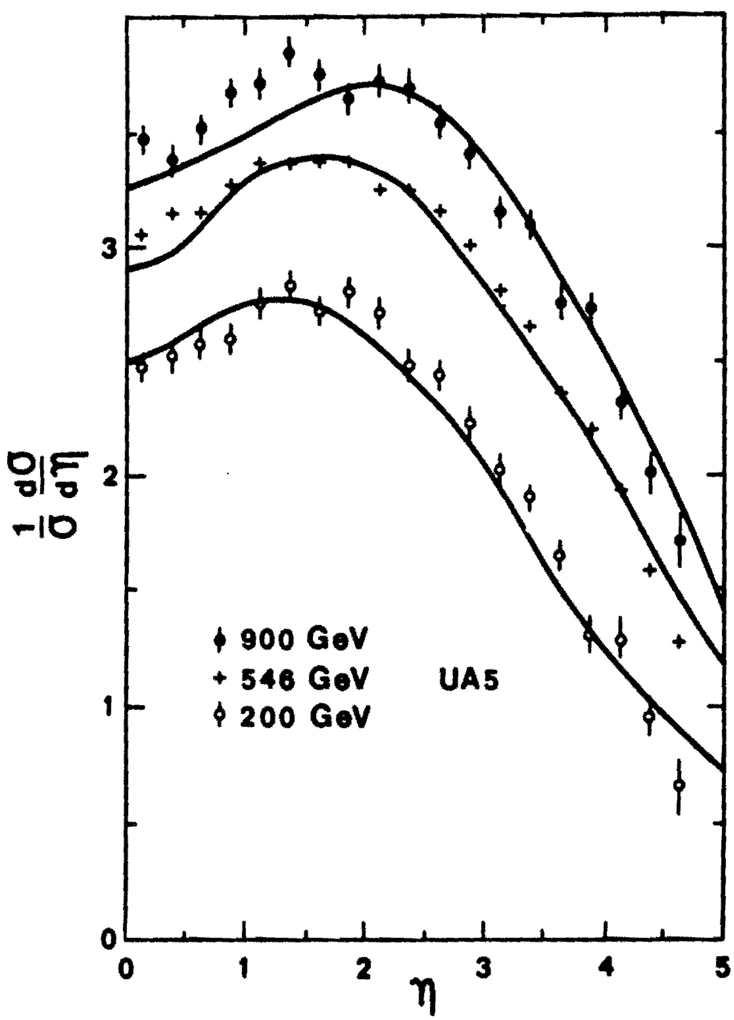

Figure 9. Fits to $dN_{ch}/d\eta$ in a hard scattering model (from ref. [60, Phys. Rev. D]).

$$\langle n \rangle = \frac{\int db\, b(A + BV(b))}{\int db\, b}. \tag{1.7}$$

Fits to minimum bias data constrain the parameters for a given form of $V(b)$.

The cross section for hard parton-parton interactions is assumed to be proportional to the product of the number of partons in the overlapping region. This implies that the mean multiplicity in hard scattering events is

$$\langle n_{hard} \rangle = \frac{\int db\, bV^2(b)(A + BV(b))}{\int db\, bV^2(b)}. \tag{1.8}$$

This model predicts no difference between multiplicity enhancements in such processes as W boson production or high p_t jet production.

1.3 The measurement

This thesis describes a measurement of the pseudo-rapidity distribution of charged particles at $\sqrt{s}$ equal to 630 and 1800 GeV. We measure the distribution within $|\eta| < 3.5$. Since the detector is unchanged, and the same analysis is applied to the data at both energies, systematic errors tend to cancel in the ratio of the η distributions at the two energies.

Measurements of the type presented here are often described in the literature under the heading of "minimum bias" physics, especially with regard to collider data. This term, however, is somewhat mis-leading as it suggests that events are selected from a stream of inelastic events so as to minimize selection bias. Driven by the simultaneous requirements of admitting as many events as possible while rejecting as many background events as possible within constraints posed by a beam pipe passing through the entire detector etc., we place strong requirements on the set of events that can trigger the detector and pass other selection criteria. The trigger and selection will be addressed in later sections.

We also describe a measurement of the ratio of $dN_{ch}/d\eta$ in events in which a W boson is produced (observed via the W$\rightarrow e\nu$ decay mode) to that of minimum bias events, as a function of the p_t of the W boson. This data was recorded during a nine month run in the fall of 1988 through the spring of 1989. The detector used for this later run is essentially the same as that used for the earlier, although many details and numerous operating parameters changed between the two. By taking the ratio of $dN_{ch}/d\eta$, however, we expect systematic errors to cancel and thereby avoid the necessity of understanding all these changes.

In this work, we present an inclusive measurement: a particle need only be observed to have charge to be included in the observed distribution, independent of all other observed (and unobserved) particles in the event. We define the "observed" $dN_{ch}/d\eta$ distribution, ρ_{obs}, as

$$\rho_{obs}(\eta_i) = \frac{N_t^i(\eta)}{N_{ev}\mathcal{A}_i^\eta\,\Delta\eta_i}, \tag{1.9}$$

where N_t^i is the number of charged tracks in some interval $\Delta\eta$ centered at η_i, N_{ev} is the total number of events in the sample, and $\mathcal{A}_i^\eta$ is the geometrical acceptance for η. The acceptance is defined as the fraction of all events in which the detector is sensitive to tracks within the η interval around η_i. Note that we will also refer to ρ_{obs} as the "uncorrected" $dN_{ch}/d\eta$ distribution.

Various systematic effects (e.g., tracking efficiency, charged particle decays, azimuthal acceptance, etc.) introduce bias into the observed value of N_t^i. To remove this bias, we estimate the magnitude of the various effects and apply a series of multiplicative corrections to ρ_{obs} to obtain an estimate of the true $dN_{ch}/d\eta$ distribution.

1.4 Outline

The remainder of this thesis is devoted to a detailed discussion of the measurements outlined above. Relevant features of the CDF detector are described in Chapter 2. Chapter 3 explains details of the reconstruction program used to interpret the detector output, and the corrections and systematic uncertainties introduced. In Chapter 4, we examine details of the $dN_{ch}/d\eta$ analysis for minimum bias data and estimate the remaining necessary correction factors and systematic uncertainties. We present the results for the $dN_{ch}/d\eta$ measurement in Chapter 5. The W analysis, results and discussion are presented in Chapter 6. Finally, Chapter 7 contains a summary of the conclusions from these measurements.

Chapter 2

Experimental Apparatus

The Collider Detector at Fermilab (CDF) is an azimuthally symmetric detector designed to study various properties of $\bar{p}p$ collisions in the center-of-mass frame. The detector (figure 10) consists of a large central detector made up of two independent tracking chambers (the Vertex Time Projection Chamber and the Central Tracking Chamber) inside a solenoid magnet, all surrounded by electromagnetic shower counters, hadronic calorimeters, and muon detectors; and two identical forward/backward detectors each consisting of time-of-flight scintillation counters (the Beam-Beam Counters) in front of electromagnetic shower counters and hadronic calorimeters, followed by a toroidal muon spectrometer. For technical details of the CDF detector, the reader should consult reference [62]. For coordinate and notational conventions, please refer to Appendix B.

In the following sections, we will describe briefly those subsystems of the CDF detector which generated data used in the present analysis. In Section 2.1, we present some features of the Fermilab Tevatron Collider. Section 2.2 provides details of the BBC system, which was used as part of the detector trigger. Charged particle tracking information comes from the inner-most tracking detector, the VTPC, described in Section 2.3. Finally, Section 2.4 outlines pertinent details of the calorimeters and calorimeter trigger systems used in the detection of W boson candidates.

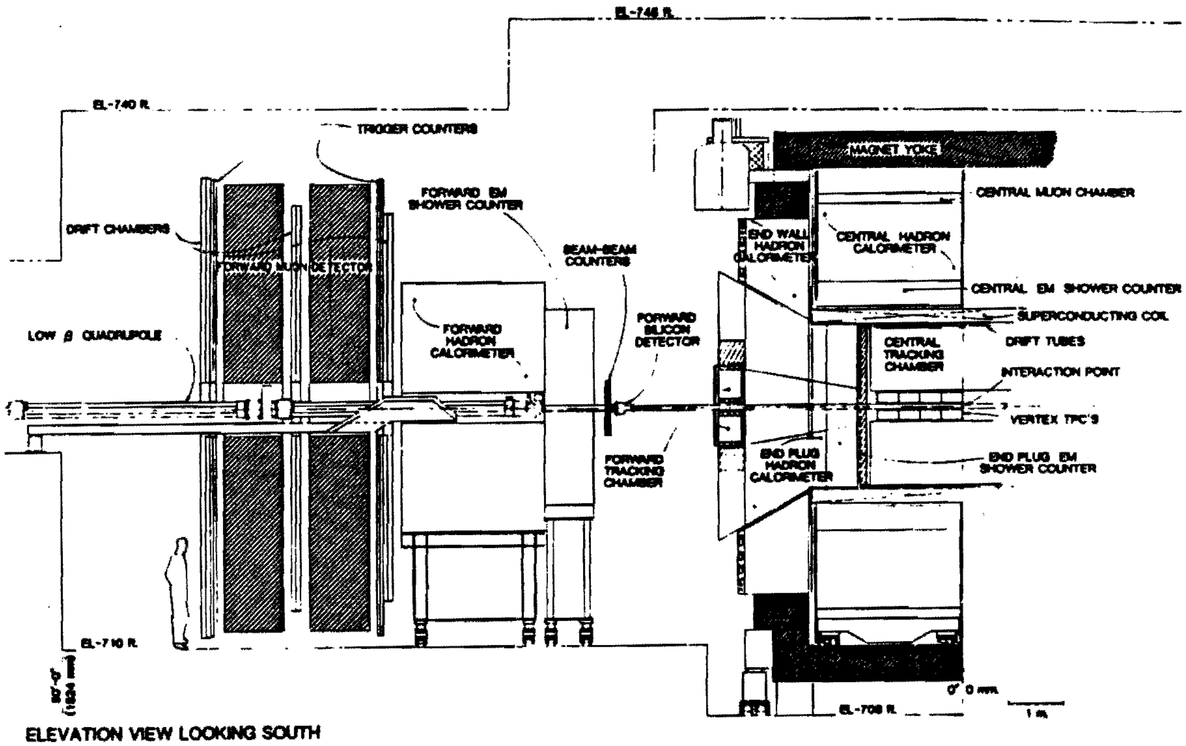

Figure 10. Cross-sectional view of one half of CDF detector.

2.1 The Fermilab Tevatron

The Fermilab Tevatron Collider is a superconducting proton synchrotron with a raduis of 1 km, capable of simultaneously accelerating counter-rotating beams of protons and anti-protons to energies of 900 GeV. During the 1987 run, protons (and anti-protons) were stored in the machine in three groups, or "bunches", equally spaced about the ring (six bunches for the 1988–1989 run). Each bunch (labelled as A–C or A–F for the 1987 and 1988–1989 runs respectively) contained between 10^9 to a few times 10^{10} particles. Proton and anti-proton bunches collide at three interaction points about the ring, including "B0", the point at the center of the CDF detector. Within a bunch, the density of particles along the beam direction is approximately Gaussian with a standard deviation of 40 cm. Collisions, therefore, occur along an extended region within the detector. The density of collisions in this region should be approximately Gaussian with a standard deviation of 35 cm.

Special quadrupole (low-β) magnets located on either side of B0 focus the beam to a diameter of about 200 μm, which allows operation at high luminosity.[1] All data presented here were obtained during low-β operation, although the majority of minimum bias data was recorded at relatively low luminosity (e.g., of order 10^{28} cm^{-2}sec^{-1}).

Once injected into the Tevatron, the particles remain within the accelerator for hours to allow data taking. The typical duration of such a "store" is between 12–24 hours. Many "runs", each characterized by a particular configuration of the detector and the trigger, can be recorded during a single store.

[1]Peak instantaneous luminosities attained during the 1987 run were of order 10^{29} cm^{-2}sec^{-1}, and of order 2×10^{30} cm^{-2}sec^{-1} during the 1988–1989 run.

2.2 The Beam-Beam Counters

The beam-beam counters [63] consists of two planes of scintillation counters that provide trigger and timing information. The planes are placed symmetrically forward and backward of the interaction point (see fig. 10). Excellent time resolution ($\sigma < 200$ ps) allows precise measurement of the interaction time, a crude measurement of the vertex position ($\sigma \lessapprox 6$ cm), and tagging of beam-halo particles (those striking the BBC coincident with the in-coming bunch crossing the plane of the BBC).

Each BBC plane (figure 11) consists of 16 counters arranged in a rectangular array around the beam pipe. The array is segmented into quadrants with four counters in each quadrant. Measuring within the vertical or horizontal planes, the BBC covers the range in polar angle from 0.32° to 4.47° (corresponding to the η range 3.24 to 5.90). Two phototubes, one at each end of every scintillator, detect light from charged particles traversing the counter. Time and pulse height information is recorded for each phototube using single hit TDC's and ADC's.

The detector trigger employs the fast, analog signals from BBC phototubes. Pulses first feed into fixed threshold discriminators. All discriminator outputs from a single BBC plane are then combined in a logical "or", and the result tested for a coincidence of east and west planes within a 15 ns gate around the time of the beam crossing. The coincidence signal feeds into one of 12 inputs into the first level detector trigger (Level 1). The detector can be triggered by any combination of the Level 1 inputs. During a typical minimum bias run (for both 1987 and 1988–1989 data presented here), the BBC alone is used to trigger the detector. The W boson analysis (1988–1989 data only) requires a more sophisticated trigger to reduce background and enhance the W boson signal-to-noise ratio. Essential details of the trigger are described in section 6.1.2.

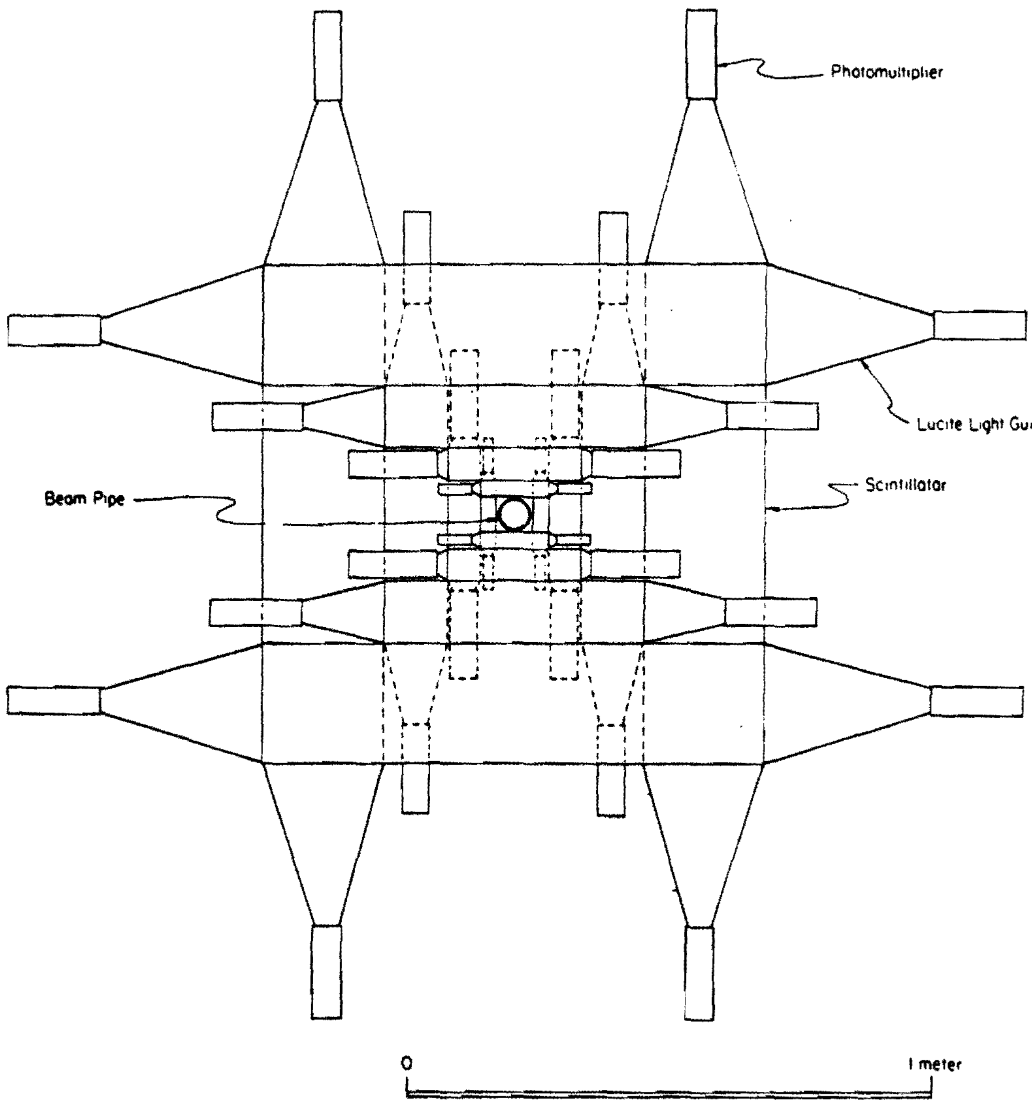

Figure 11. Beam-beam counter array as seen from the beam axis.

2.3 The Vertex Time Projection Chamber

The Vertex Time Projection Chamber[64] is a set of eight time projection chambers (see fig. 10 for the detector arrangment within the central CDF detector) that measure the trajectory of charged paricles between 7 and 21 cm from the beam axis. Each chamber (called a module) surrounds the beam pipe and consists of two planes of sense wires (proportional chambers) attached to opposite ends of back-to-back drift regions (fig. 12). Each drift region is 15.25 cm long, a length chosen such that the maximum drift time is less than the time between bunch crossings in the accelerator (3.5 μsec during 6-bunch operation). The sense wire planes, segmented azimuthally into octants, are aligned perpendicular to the beam axis. Each octant has 24 sense wires and 24 cathode pads. The sense wires are arranged perpendicular to a radial line through the center of the octant.

The chambers are mounted end-to-end, the drift direction parallel to the beam axis and the 1.5 T magnetic field from the solenoid. Alternate chambers are rotated by 11.5° in ϕ in order to prevent particles travelling along narrow, insensitive regions near octant boundaries from traversing several modules undetected. Two sets of modules result, the modules in each with the same relative ϕ orientation: even numbered modules are denoted as ϕ_- set, odd numbered modules as the ϕ_+ set. The rotation also allows limited small-angle stereo reconstruction of tracks which traverse more than one module. The assembly of eight modules is mounted within a gas-tight vessel; the chamber gas is argon-ethane 50/50.

An emphasis on low-density, long-radiation length materials in the mechanical structures, electronics and signal cables and the use of a beryllium beam pipe help minimize losses from multiple Coulomb scattering and contamination of the charged particle signal from conversion electrons and secondaries from hadronic interaction.

Ionization deposited in a chamber drifts away from the center of the module, crosses a screen dividing the drift region from the proportional chamber, and collects on the nearest sense wire after amplification by a factor between 2–4 $\times$ 10^4 in the

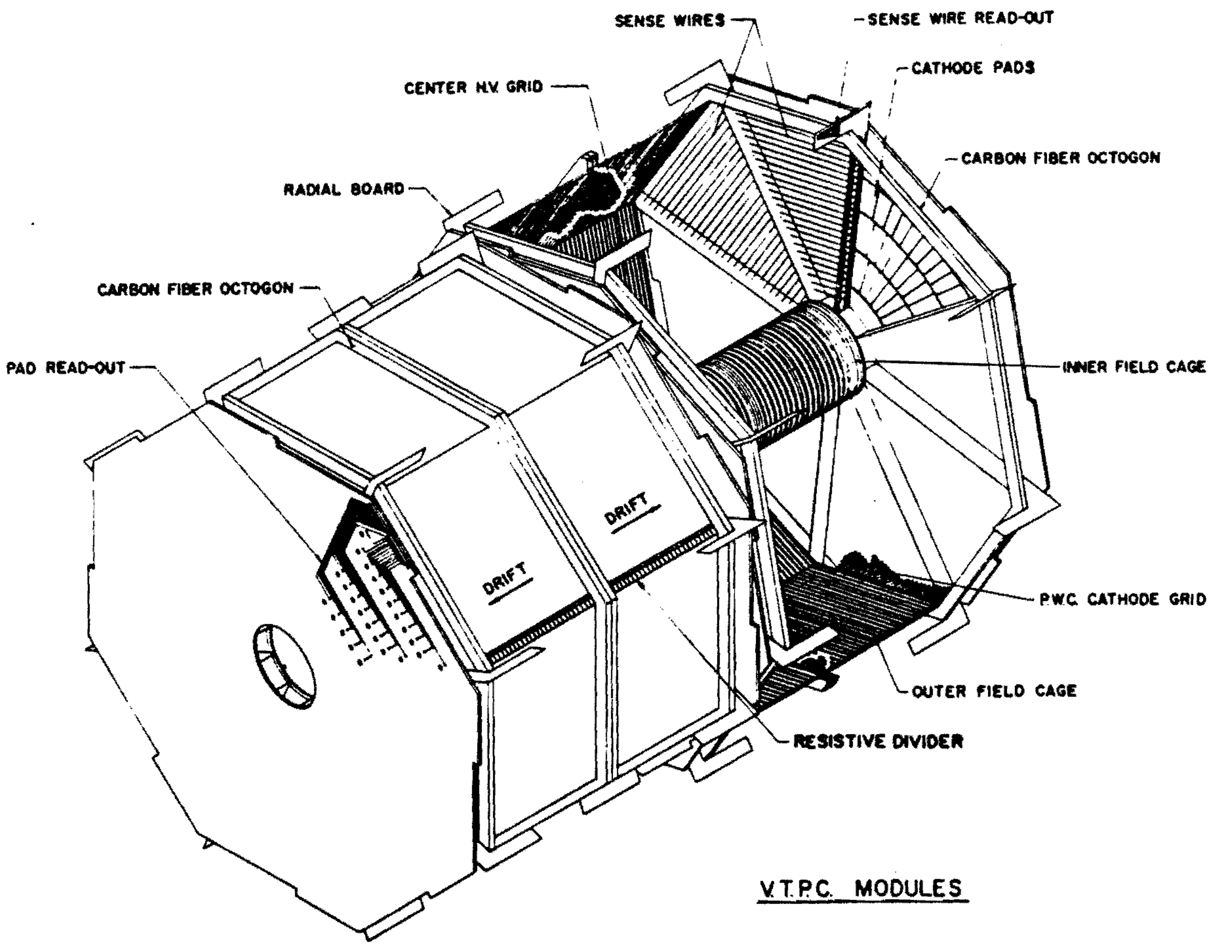

Figure 12. Cutaway view of two VTPC modules showing mounting configuration. Adjacent modules are rotated by 11.5° around the beam axis.

chamber gas. As the initial charge is amplified in the gas, a signal is induced on the cathode pads nearest the point along the wire at which the avalanche occurs. Preamplifiers mounted on the chamber amplify the charge from the wire and pass the signal into an Amplifier-Shaper-Discriminator (ASD) circuit outside the gas volume. The ASD produces a time-over-threshold output signal, the threshold fixed at a value equivalent to about six electrons entering the proportional chamber within the 30 nsec integration time of the ASD. The time-over-threshold signal is sent to a multi-hit Time-to-Digital Converter (TDC) that digitizes the leading and trailing edge times of all ASD transitions in buckets of 8 ns, the equivalent of about 380 μm in drift distance.

Although the cathode pads can, in principle, provide 3-dimensional space-points for each hit in the chamber, three quarters of the pads lack the necessary electronics. Those pads which are fully instrumented are located at relatively low angles where tracks are likely to cross more than one module and, therefore, have stereo information. Since the pad reconstruction depends strongly on the output of the wire reconstruction, these few operating pads were not found to be useful for this analysis. The author strongly recommends that any future attempt to repeat this measurement, or any subsequent chamber to replace the VTPC, have a robust, 3-dimensional capability.

2.3.1 Chamber performance

2.3.1.1 Resolution

We measure the resolution of the chamber by reconstructing tracks within individual octants, fitting them to straight lines and studying the resulting χ^2 distributions. Figure 13 shows the resolution squared for tracks parallel to the wire plane as a function of the drift distance to the wire. Within the statistics of the measurement, the resolution function for 90° tracks is linear, consistent with expectations for a diffusion-limited resolution.

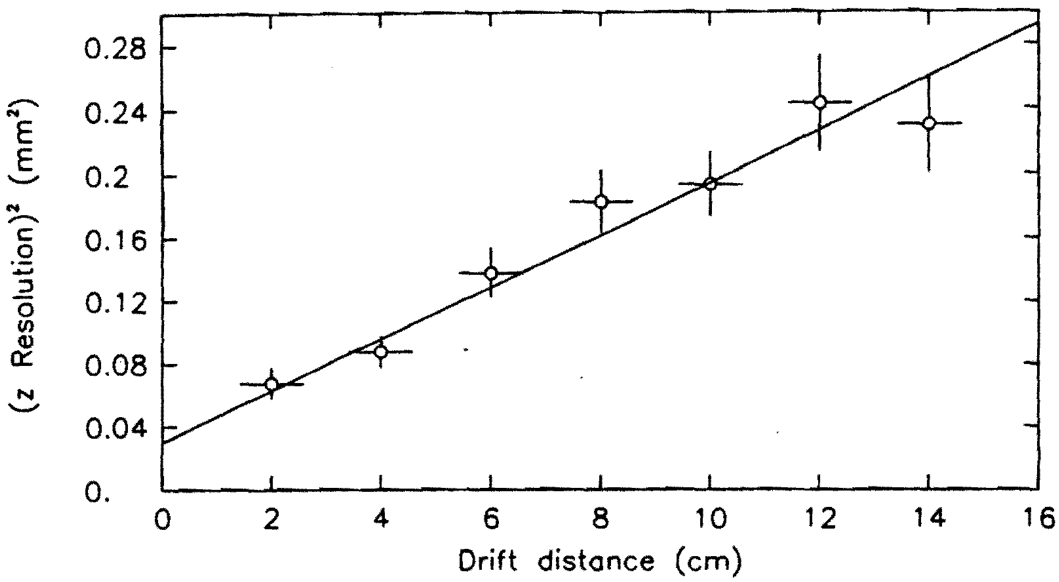

Figure 13. VTPC resolution squared vs. drift distance. The line is drawn to guide the eye.

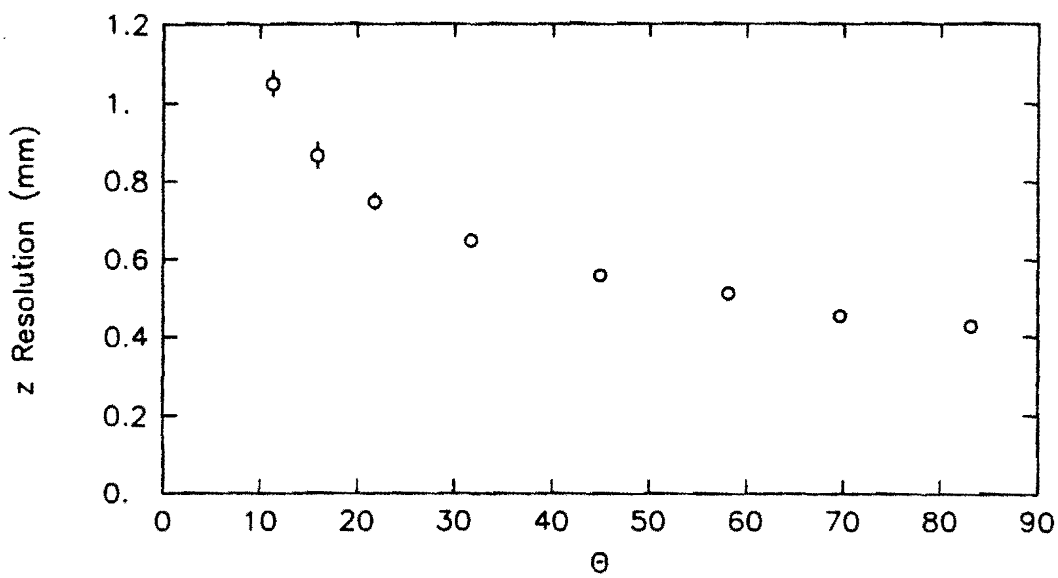

Figure 14. VTPC resolution vs. polar angle. This resolution curve applies to isolated tracks within a single octant.

A much stronger dependence is observed as a function of the polar angle. The plot of resolution versus polar angle (figure 14) exhibits a resolution of about 420 μm for 90° tracks (averaged over drift distance), and declines sharply with decreasing polar angle. Chamber simulations indicate that transverse diffusion dominates the low angle resolution. The curve in fig. 14 applies to isolated tracks traversing a single octant. Tracks which cross module boundaries (i.e., mainly those below 45°) suffer an appreciable degradation in resolution from such systematic effects as chamber alignment and slope-dependent non-linearities. We will turn full attention to these effects shortly.

2.3.1.2 Dead time and two track separation

The width of the time-over-threshold signal from the ASD, and therefore the implied width of pulses from the chamber itself, determines the two track resolution of the chamber. The equation:

$$(\text{width}) = (\text{wire spacing}) \cot\theta + 0.9 \text{ cm} \tag{2.1}$$

provides a reasonably good model for the average pulse width observed in cosmic ray data in a prototype production module. The constant term is determined by the decay constant for the analog electronics and represents the response of the system to the simultaneous arrival of many electrons, while the angular term is determined by the length of the volume along the drift direction in which ionization is deposited. Figure 15 shows the pulse width for cosmic ray data after subtracting the first term of equation 2.1. The plot is very nearly flat over a wide range of angles.

Data from the collider runs exhibit a significantly different pulse width characteristic (fig. 15). First, the constant term at large angles is smaller, reflecting a shorter decay constant in the analog amplifiers used during the collider run. Second, the constant term abruptly changes value near $\cot\theta = 2$, corresponding to the increased appearance of multiple pulses of short duration instead of the single, long pulses which dominate the behavior of the prototype data. The cause for the latter effect

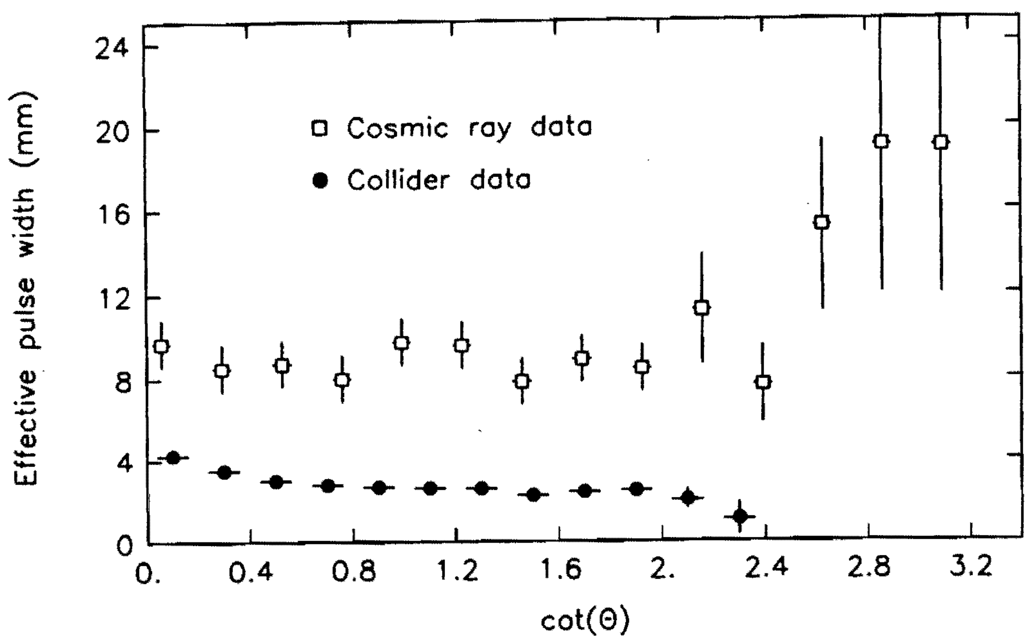

Figure 15. Effective analog pulse width vs. track angle. The effective pulse width is defined as the length of time the analog pulse is above the discriminator threshold, times the drift velocity, minus the first term in eq. 2.1.

lies in the interaction of the pulse shape as a function of angle with slight changes in the noise level and the effective discriminator threshold between the cosmic ray and collider runs. As tracks approach low angles, transverse diffusion and longitudinal fluctuations of ionization along the track trajectory become the primary effects that govern the pulse shape. At low angles, the highly irregular pulse shape that results may cross the discriminator threshold several times, producing multiple pulses associated with a single track.

Since the chamber was operated at a slightly lower gain and higher effective threshold during the collider runs than during the cosmic ray runs, the chamber became more susceptible to this effect during the collider runs. The basic relationship of equation 2.1 to the chamber dead time, however, is assumed to hold for the collider data, except that a constant term of 0.5 cm is assumed instead of 0.9 cm. From equation 2.1, we calculate that tracks separated by at least 0.06 units of η should be observed as independent tracks.

2.3.1.3 Insensitive regions along octant boundaries

Measurements made with a proportional chamber model and a radioactive source indicate that the region within about 3.0$\pm$1.5 mm of the boundary between octants has insufficient gain to detect particle tracks. The effect of this dead region on the geometrical acceptance is discussed in Section 3.6.2.

2.3.2 Chamber systematics

Extracting distances from TDC times requires several parameters that define the operating characteristics of the chamber. Given a TDC time, t, from a sense wire located a distance y_w from the beam axis, we calculate the position of the track relative to a line in the sense wire plane (parallel to the sense wires) located a distance y from the beam axis using the equations:

$$d = v_d(t - t_0^{cs}) + d^{cs} + f_z(\theta, y_w, d) \tag{2.2}$$

$$y = y_w + f_y(d) \tag{2.3}$$

where d the is distance (parallel to the drift direction) from the sense wire plane to the track; v_d is the drift velocity within the drift region; d^{cs} is the distance from cathode screen to the sense wire; t_0^{cs} is the offset in time scale (time of beam crossing relative to TDC start plus the minimum drift time across the proportional chamber); and $f_z(\theta, y_w, d)$ and $f_y(d)$ are functions which eliminate various systematic deviations from ideal behavior. Non-ideal behavior includes the effects of chamber mis-alignment, the "leading electron" effect and diffusion induced non-linearities.

We determine these parameters [65] by performing a simultaneous fit of the drift velocity, t_0, $f_z(\theta, y_w, d)$ and $f_y(d)$ on a large number of tracks within a single event, demanding tracks to have linear trajectories, and to originate from a common point. We find that t_0^{cs}, $f_z(\theta, y_w, d)$ and $f_y(d)$ are relatively stable over extended periods of time, whereas v_d can vary by a few percent on a run-by-run basis. The drift velocity is typically ~ 43 μm nsec^{-1}. Measurements of the drift velocity have a resolution of better than 0.5%.

The most significant deviation from ideal behaviour results as a consequence of the leading-edge timing of the electronics, the so-called leading electron effect. Figure 16 illustrates the paths which electrons follow as they drift toward sense wires. The TDC measures the arrival time of the leading electrons, those which follow the shortest time path from the track to the sense wire. For a track inclined with respect to the sense wire plane, the minimum time path leads from a point away from the center of the wire cell to the sense wire along a curved trajectory. The correction for this effect is zero for tracks at 90°, and approximately 2.5 cm for tracks near $\eta = 3.5$.

There are several other much smaller effects (~ 1 mm at most) which we will not discuss here. These effects include non-linearities caused by longitudinal and

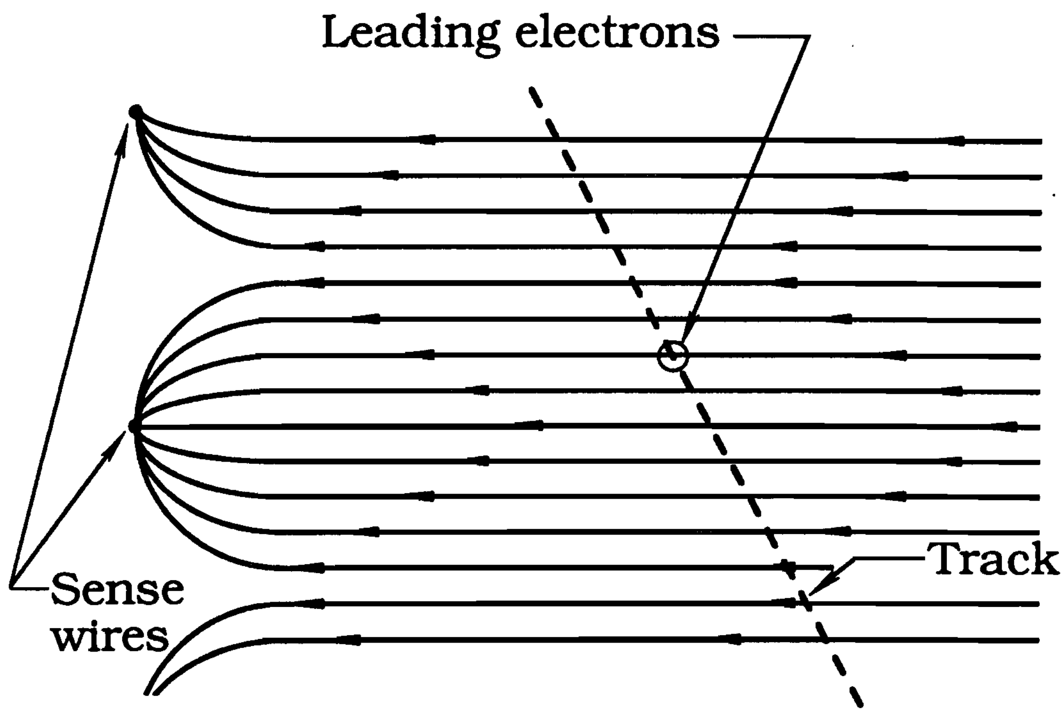

Figure 16. Leading electron effect. The minimum-time trajectory from a track to the sense wire is displaced farther from the center of the wire cell as the inclination of the track with respect to the sense wire plane increases.

Table 1. Typical values for the non-linearity correction functions $f_z(\eta, y_w, d)$ and $f_y(d)$ (in cm).

d (cm)	$f_y(d)$ (cm)	$f_z(\eta, y_w, d)$ (cm) ($y_w = 7.48$ cm) $\eta = 0.0$	1.5	3.0	($y_w = 11.28$ cm) $\eta = 0.0$	1.5	3.0	($y_w = 19.52$ cm) $\eta = 0.0$	1.5	3.0
1.0	0.063	0.024	0.417	2.238	0.027	0.419	2.240	0.033	0.425	2.246
7.0	0.065	0.056	0.459	2.500	0.058	0.461	2.503	0.064	0.467	2.509
12.0	0.066	0.071	0.479	2.631	0.074	0.482	2.633	0.079	0.488	2.639

The leading electron effect and diffusion induced non-linearities are assumed the same for all modules. Alignment corrections are applied octant-by-octant.

transverse diffusion, space charge (largely negligible for the 1987 data), and distortions caused by chamber mis-alignments and $E \times B$ effects. Although measured and parameterized as part of $f_z(\theta, y_w, d)$, the effects are uniformly small and have little effect on the results. Some typical values for $f_z(\theta, y_w, d)$ and $f_y(d)$ are tabulated in table 1.

Several independent techniques allow cross checks on the results of the fits described above. Examination of the TDC time distribution allows determination of t_0^{cs} and v_d. Using the discontinuity of tracks across the center of modules and the spread of tracks around the vertex point allows determination of the previous parameters plus $f_z(\theta, y_w, d)$ and $f_y(d)$ as a function of the module and octant. This technique also permits isolation of such effects as rotations, translations, leading electron effect and diffusion related non-linearities.

Chapter 3

VTPC Reconstruction Program

This chapter describes the program used to interpret data from the VTPC. The process includes finding and fitting particle tracks, and reconstructing the primary event vertex. We also discuss the systematic uncertainty introduced into the $dN_{ch}/d\eta$ measurement by the reconstruction program.

3.1 Track reconstruction program

Data from the wires in an individual octant, the smallest functional unit within the VTPC, represent the projection of charged particle trajectories onto a plane passing perpendicular to the wires through the azimuthal center of the octant. Figure 17 shows the wire data for a typical minimum bias event. The primary task of the reconstruction program is to group this 2-dimensional data into sets representing complete particle trajectories. In some cases (as when a particle traverses modules belonging to both module sets), the set may include projections onto more than one plane (r-z view), in which case the azimuthal position of the track can be estimated more precisely (assuming a linear trajectory). In the discussion to follow, we shall

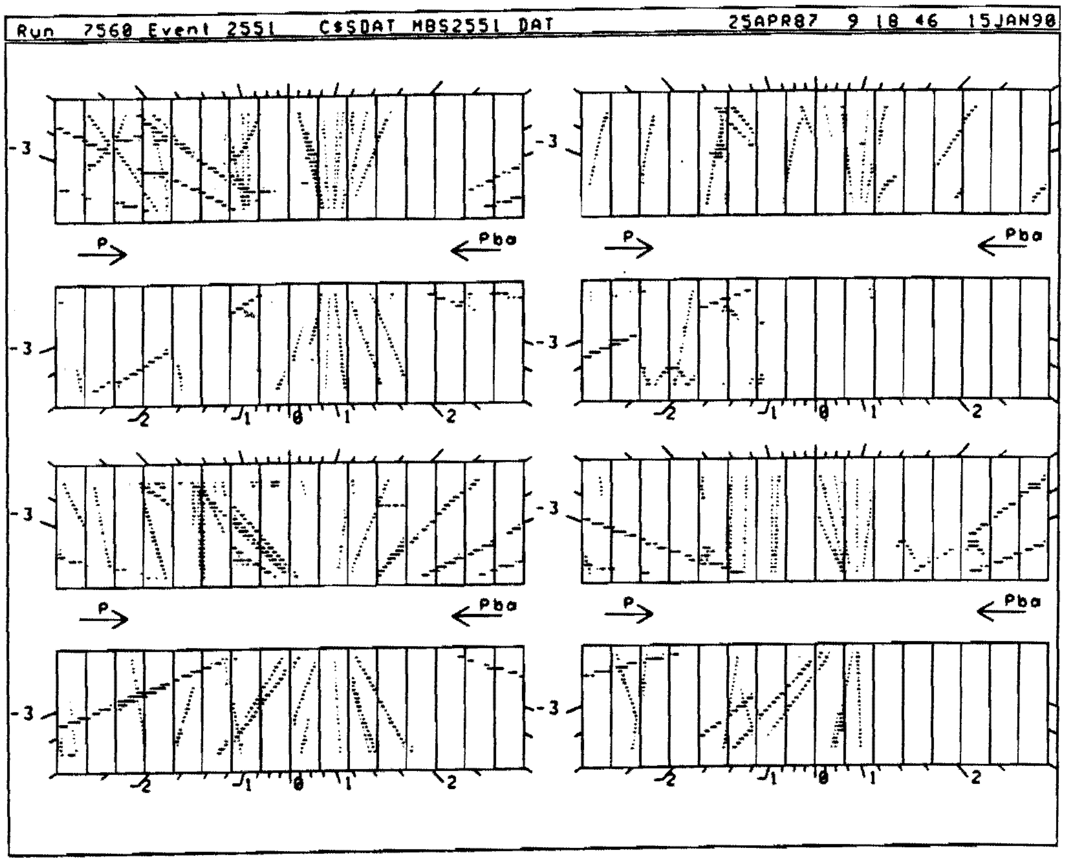

Figure 17. VTPC wire data display for a typical event. The display shows four longitudinal cross sections through the chamber and along the beam pipe. Each cross section, displayed in one quadrant of the picture, shows the wire data for *two* ϕ-slices on opposite sides of the beam pipe. Modules consist of three consecutive vertical lines (starting from either end): the ones on each end represent the cathode planes, and the one in the middle the center high voltage screen. Cathode planes of adjacent modules are represented by a single line. For simplicity, the display ignores the relative rotation between adjacent modules and displays all raw data within a ϕ-slice as though it were projected onto a single plane. The ϕ-slice numbering starts at 0 for the upper, and 3 for the lower ϕ-slice in the upper-left quadrant of the picture, and increases to the lower-left, then the upper-right and lower-right quadrants. The markings on the outside of the modules show the η scale.

refer to tracks with data from a single r-z view only as "2-dimensional" tracks, although the azimuthal position is known to lie within a single octant; tracks with data from more than one r-z view (with fit parameters from a stereo reconstruction) will be referred to as "3-dimensional."

The VTPC reconstruction program employs a multiple-pass algorithm that combines features of road following and angular histogramming techniques, the details of which we will describe shortly. Each pass searches for tracks that satisfy some set of criteria, then removes those tracks (and the associated TDC hits) from further consideration by subsequent passes. The criteria become progressively less demanding in terms of the allowed track curvature and quality of information. The passes, in order of execution, perform the functions of vertex finding, histogramming and vertex constrained road following, "filling," and unconstrained road following. Each step is discussed in the ensuing sections.

Figure 18 shows the η distribution of tracks found during each stage of the reconstruction. No further track selection is performed. A linear fit performed without reference to the vertex position provides the angle of a track with respect to the beam axis, and therefore the value of η at which it contributes to fig. 18.

3.1.1 Vertex finding

The program first reconstructs tracks independently within individual octants. This approach has several advantages over a first step that attempts to find tracks globally: almost all tracks appear as relatively straight lines in a single octant, simplifying the task of reconstruction; the number of hits within a single octant is small, thereby reducing combinatoric factors in the number of roads to be examined. The algorithm defines roads based upon sets of three collinear hits, then searches for associated hits within some fixed width window of the road.

Tracks found in this manner are fit to straight lines in the r-z plane corresponding to the octant center, and are then projected back to the beam axis (the z-axis). The

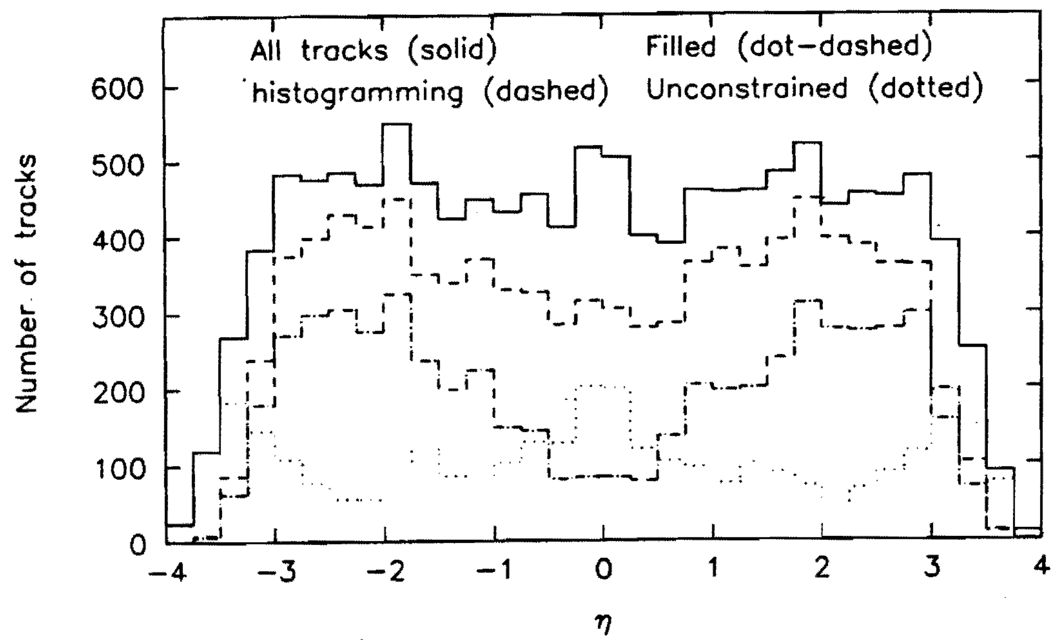

Figure 18. Angular distribution of tracks found during each stage of the reconstruction. The top curve shows the distribution of tracks found by the full reconstruction. The other curves show the contributions to this total by tracks reconstructed during the histogramming and vertex constrained road following, by those found during histogramming *and* subjected to filling, and by those found during unconstrained road following. The sample contains 349 events.

z intercepts for all tracks are grouped into clusters, defined as a sets of intercepts with no more than 2 cm separating nearest neighbors. Each cluster defines a vertex candidate. For each cluster, iterative fits over the region with highest local density of intercepts (within a 1.5 cm window) determine the vertex position. The primary vertex is chosen as the cluster with the largest number of tracks used in the fit.

3.1.2 Histogramming and road following

Once the event vertex is known, the program calculates the angle of each hit with respect to the vertex and enters the value in an angular histogram. Linear (or approximately linear) tracks appear in the histogram as peaks (figure 19). The program uses these peaks to define the position of roads, then follows these roads evaluating all TDC information within a certain window in an attempt to associate as many hits as possible with the track. This procedure is performed independently on the ϕ_+ and ϕ_- sets of modules, and on ϕ-slices within those sets.

The reconstruction accepts only very high quality tracks at this stage. Any candidate with fewer than 80% of the number of leading hits expected on the basis of chamber geometry and track trajectory is rejected. Leading hits, those suitable for use in fits, are defined as either the first hit on a wire, or those hits separated from a previously found leading hit by at least a distance consistent with the expected pulse width plus a few millimeters, and separated from the previous hit by a minimum of a few millimeters.

The program next attempts to join pairs of 2-D track segments found in the two module sets. Any pair of tracks with a reconstructed trajectory consistent with chamber geometry is considered a module-crossing candidate. Tracks belonging to more than one candidate pair resolve to the pair with the smallest angular difference between its constituent segments. Accepted track pairs are re-defined as single, 3-D tracks. Figure 20 shows the tracks in a typical event found by this step of the reconstruction.

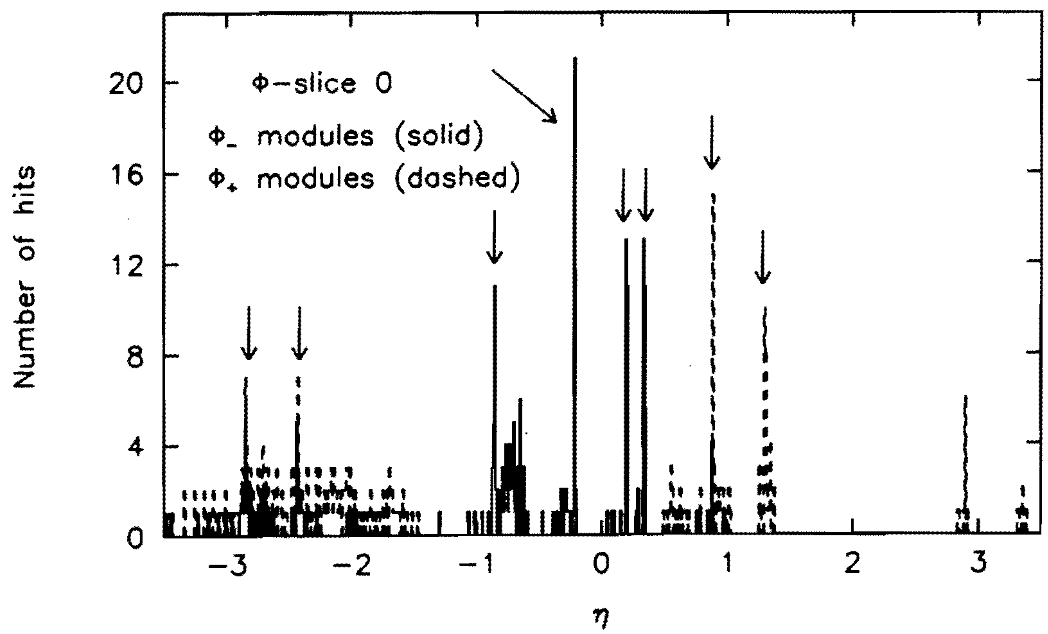

Figure 19. Angular histogram for a typical event. The histogram shown here is from ϕ-slice 0 for the event pictured in fig. 17. The arrows indicate the locations of tracks found by the histogram algorithm. These tracks can be seen in ϕ-slice 0 (upper-most picture in upper-left quadrant) of fig. 20.

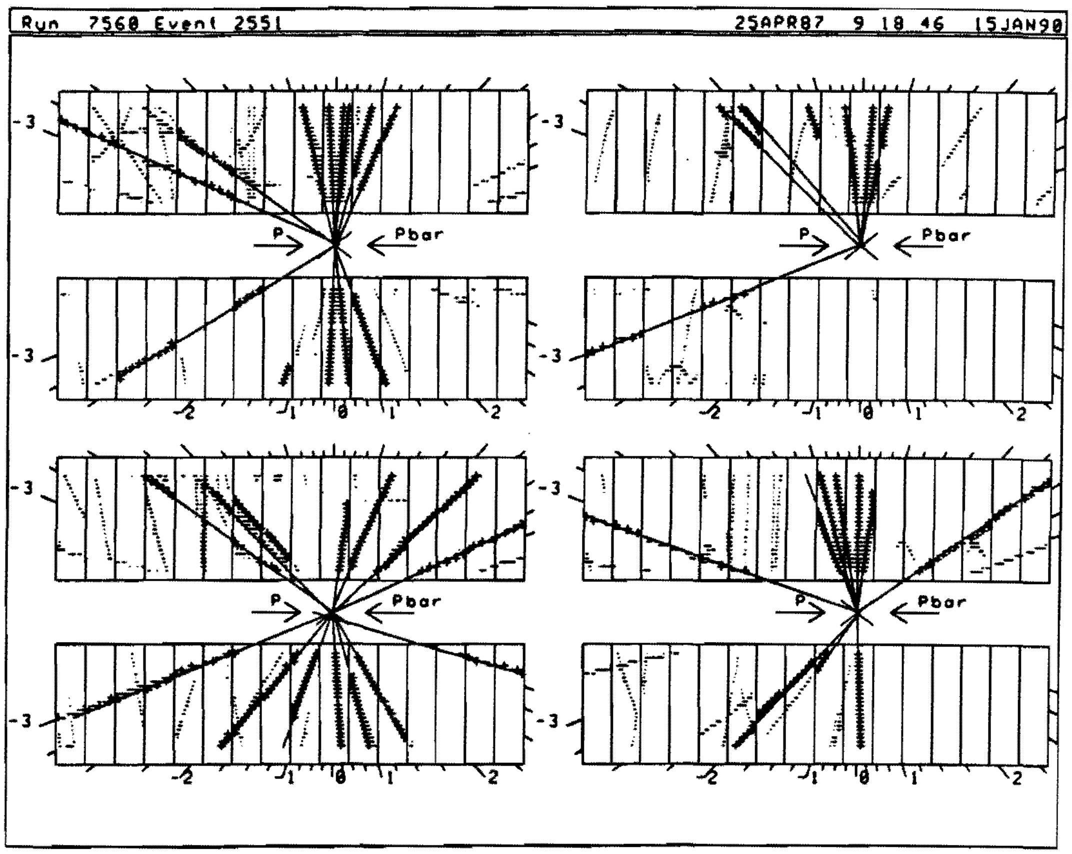

Figure 20. Typical event after histogramming reconstruction step. The event is the same as that pictured in fig. 17.

3.1.3 Filling

The set of remaining 2-D tracks contains some tracks which are in fact 3-D, but for which only one of the constituent 2-D segments is found. In order to complete these tracks, and also to improve the quality of other 2-D tracks, the program searches along the trajectory of all 2-D tracks for hits which may have been missed. The search pattern crosses module and octant boundaries and considers hits that lie within a window and have not been removed by a previous pass. The width of the window is less restrictive than that used in the previous pass, and the window position is updated based upon a fit of the five outer-most (in radius) hits nearest the wire under consideration. This technique allows the program to follow the trajectory of low p_t tracks better than the fixed road of the previous pass, which demands an almost linear trajectory. Although the likelihood of making incorrect associations of hits to tracks is also increased, the number of hits under consideration has been greatly reduced by the previous pass.

After filling 2-D tracks, the program fills all remaining tracks which contain fewer than 90% of the number of leading hits expected on the basis of geometry. All hits associated with tracks during these two filling steps are removed from consideration by the next pass. Figure 21 shows a typical event through this stage of reconstruction.

3.1.4 Unconstrained road following

The final pass generates road candidates among sets of four collinear hits taken from the outer five wire layers (or all wire layers in the end modules). The road need not point at the event vertex. As hits are associated with the track candidate, the position of the road is updated based upon a fit of the outer-most five hits nearest the wire under consideration. Figure 22 shows a typical event after passing through the entire reconstruction process.

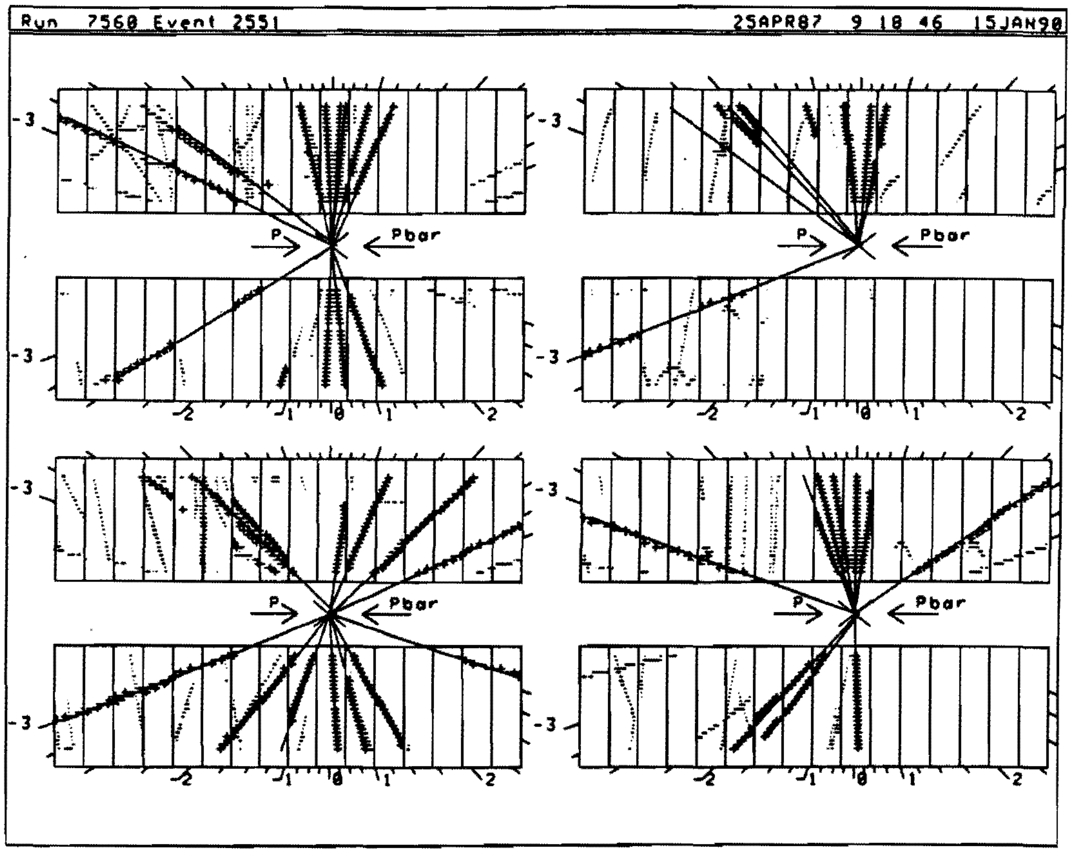

Figure 21. Typical event after the filling step in the reconstruction. The event is the same as that pictured in fig. 17. Note the now completely reconstructed track in ϕ-slice 7 at $\eta \approx -1.75$, seen only partly reconstructed in fig. 20.

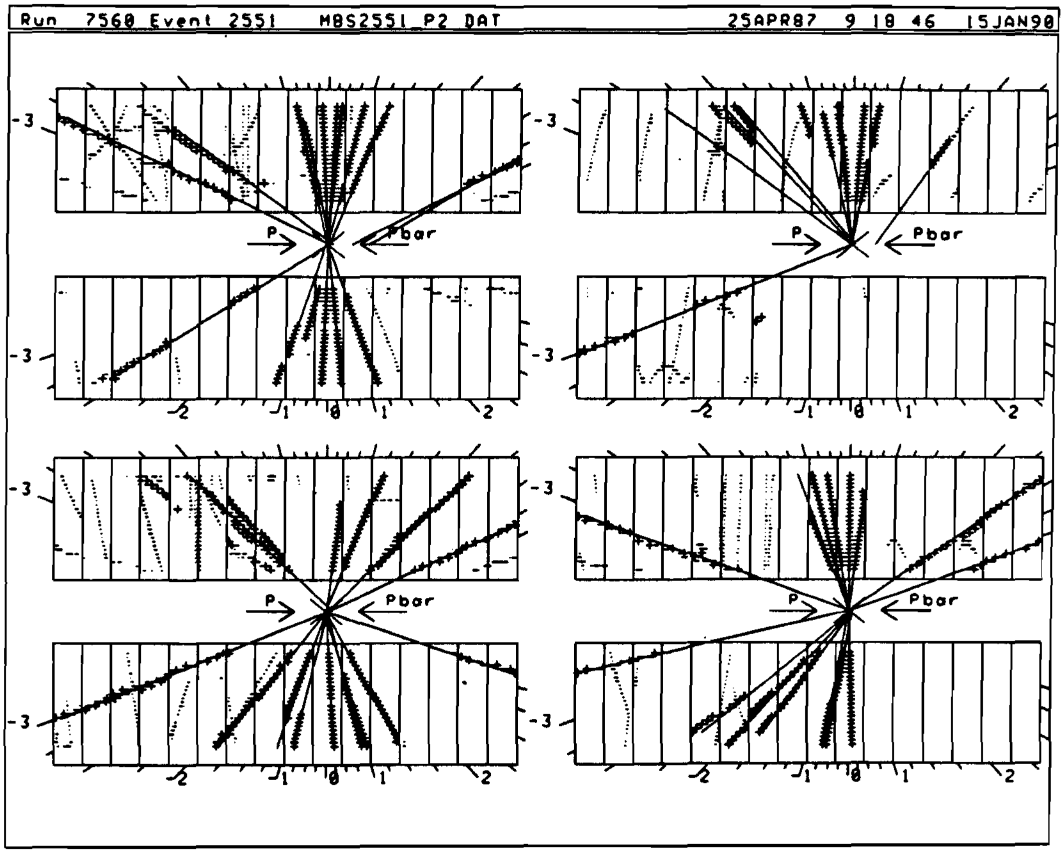

Figure 22. A typical, fully reconstructed event. The event is the same as that pictured in fig. 17. Note the additional low angle tracks (see, for example, ϕ-slice 0, $\eta \approx 2.9$ and ϕ-slice 3, $\eta \approx 3.0$), and the ϕ-boundary-crossing track (ϕ-slices 4 and 5, $\eta \approx -0.8$) found during the final step in the reconstruction procedure.

3.1.5 Track fitting and re-calculation of vertex position

After completing all stages of reconstruction, we perform "de-weighted" fits (see Appendix C) to the resulting tracks. No vertex constraint is imposed. Using the same vertex algorithm described above, we re-calculate the vertex position from the unconstrained fits. Use of full tracks in the calculation improves the quality of the vertex over that determined from octant segments, the latter lacking some of the corrections used in the global fits. Figure 23 shows a comparison of the vertex position calculated from octant segments to that determined from full tracks as a function of the number of tracks. We find that the two positions agree within 0.5 cm in at least 79% of all events with 10 or more tracks used in the vertex calculation, but in only 53% of events with fewer than 10 tracks used in the calculation. Overall, the vertex calculations agree within 0.5 cm in about 75% of all events.

A vertex constrained fit (not using the de-weighting scheme) is also applied to all tracks. Since the vertex can significantly increase the lever arm for many tracks, these fits generally improve the accuracy of η measurements for primary tracks.

3.2 Tracking efficiency corrections

Multiplicity measurements using the VTPC rely on the correct interpretation of raw data by the reconstruction program in a large sample of events. In order to understand the resulting observed multiplicity distribution, the effects of systematic mis-interpretation by the reconstruction algorithm must be measured and eliminated. The standard statistic used for this purpose is the reconstruction efficiency, the mean ratio of the number of tracks which should be found (within some region of

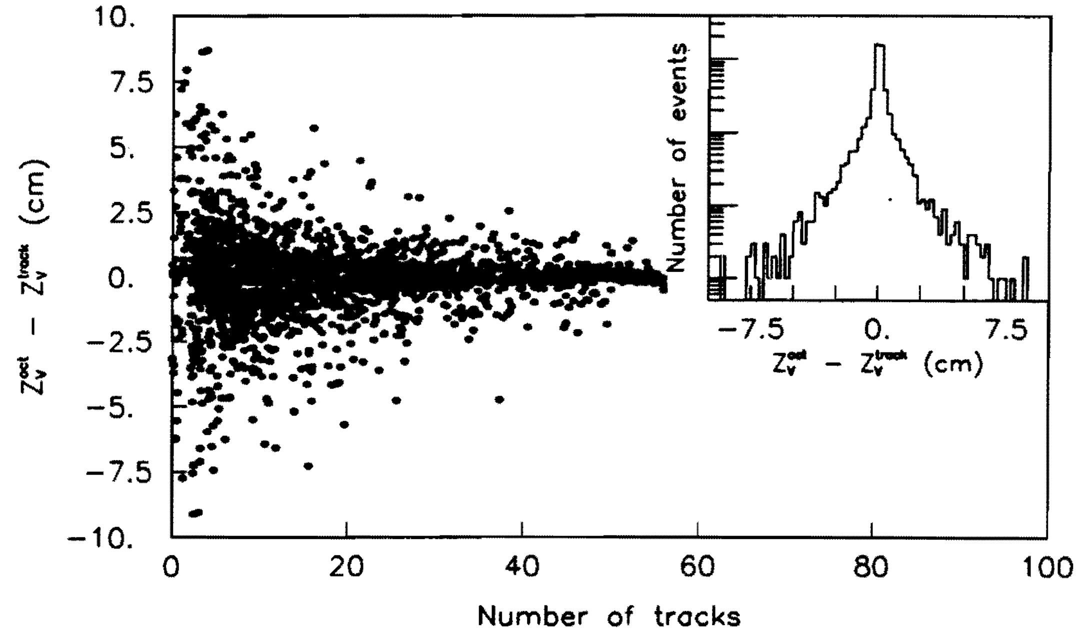

Figure 23. Comparison of first and second pass vertex calculations. The first pass uses "octant segments" to deduce the vertex position (z_v^{oct}), while the second pass uses fully reconstructed tracks (z_v^{tracks}). The "number of tracks" refers to the number of fully reconstructed tracks used in the second pass calculation. The inset shows the projection of the scatterplot onto the y-axis.

an appropriate parameter space) to the number actually reconstructed. One method to estimate the efficiency is to compare the results of the reconstruction program with that of an "ideal" algorithm. In the present analysis, we test the performance of the reconstruction program against a standard provided by human scanners assumed to possess "nearly" ideal pattern recognition capabilities. The extremely pictorial nature of the VTPC event display makes such a visual scan "easy."

3.2.1 Method of efficiency measurement

The visual scan proceeds by supplying scanners with pictures of events already reconstructed by the reconstruction program (RP) used to obtain the observed $dN_{ch}/d\eta$ distributions. The pictures show all tracks found by the RP, and all hits associated with those tracks. Events are also viewed on a color graphics terminal using a program that allows "mistakes" made by the RP to be corrected. The efficiency correction is calculated by comparing on an event-by-event basis the tracks present before and after the scan. Details of the display program, scanning procedures and efficiency calculations follow in the next sections.

3.2.1.1 The display program

The event display program used for the scan combines features of the standard reconstruction program with those of an event display. Once an event is displayed, the program operator can elect to delete or add hits associated with a given track; create a track which was missed by the RP; or delete a track found spuriously through random combinations of unrelated hits. The program retains all information about the history of every track manipulated during the scanning process. If a track found by the RP is modified by the scanners, the program creates a new version of the track, marks it as "modified" and logically connects it to the original, unmodified version. This fact allows the effects of the hand scan to be monitored on a track-by-track basis.

3.2.1.2 Scanning procedures

The actual scanning process employed two non-physicists trained specifically for the task of scanning events in the VTPC. Both scanners had several years prior experience scanning film from bubble chambers, and eight months experience scanning the Central Tracking Chamber for an analysis similar to that presented here. Except for a brief training period, the scanners worked independently on different sets of events. The training period consisted of several days of instruction and supervised work, followed by a week of unsupervised but closely monitored scanning. During this time, both scanners worked on identical data sets. After this breaking-in period, each scanner received a distinct data set. "Real" data scanning began after another short period had elapsed. Neither scanner was informed about the time at which real data scanning began.

A set of scanning rules (Appendix D) defined when various actions by the scanners were allowed or mandated, although almost total discretion was provided concerning matters of pattern recognition (ie., no maximum χ^2 cuts, etc.). In a convention similar to that used in the RP, ambiguities were resolved in a manner which minimized the number of particles in the solution. An event was considered complete when to the best of their ability, the scanners determined that all tracks in the event possessed all available information produced by the chamber.

To provide a check on the consistency of the results, the data sets for the scanners were periodically exchanged so as to obtain a small set of control events scanned by both. A complete discussion of systematic checks of the results is presented in a later section.

The ultimate goal of the hand scan was to obtain a final correction which introduced a systematic error of $< 5\%$ in the final, corrected $dN_{ch}/d\eta$ distribution. As we will demonstrate later, we failed to meet this objective at most angles. A total of 574 events passed through the hand scan. Of these, 171 belonged to the control sample and were scanned by both, leaving 403 unique events used to determine the final corrections. The multiplicity distribution of the event sample was selected so as to obtain uniform statistical significance over the broadest possible range of multiplicities.

3.2.1.3 Efficiency calculation

Calculation of the track-finding efficiency from scan data relies on the assumption that failures in the pattern recognition depend systematically upon some set of observables. Consider the case where the failure to find a track is entirely random, ie., there is a fixed probability, P_m, that the reconstruction misses a real track. Assume also that given a track found by the RP, there is a fixed probability, P_s, that it is a spurious association of unrelated hits in the chamber, ie., a "spurious track." If we denote by N_f the mean number of tracks per event originally found, N_m the number missed by the reconstruction, N_s the number of spurious tracks and N_t the true number of tracks per event, then in the limit of a large number of events, we can write:

$$\begin{aligned} N_t &= N_f + N_m - N_s \\ &= N_f + P_m N_t - P_s N_f \end{aligned} \tag{3.1}$$

where P_m and P_s are given by

$$P_m = \frac{N_m}{N_t}, \text{ and } P_s = \frac{N_s}{N_f}. \tag{3.2}$$

If we now define the track-finding efficiency, ϵ, as the constant of proportionality between N_t and N_f,

$$N_t \epsilon = N_f, \tag{3.3}$$

then we get

$$\epsilon = \frac{1 - P_m}{1 - P_s}. \tag{3.4}$$

Multiplying the observed track density by the factor

$$C_{\text{eff}} = \frac{1}{\epsilon} \tag{3.5}$$

yields the efficiency corrected track density.

In reality, the probabilities P_m and P_s are not fixed, but rather depend on several parameters. Provided that a given set of values for these parameters can be characterized by approximately fixed probabilities, the simple model described above generalizes immediately by introducing P_m and P_s as functions of the relevant parameters: one divides the data sample into several pieces, each with nearly fixed values of P_m and P_s, and uses eq. 3.4 to calculate the efficiency for each.

To obtain the probabilities P_m and P_s from the scan data, we first classify tracks into four categories which define the state of the track both before and after the scan. We designate a track belonging to each of these categories in the following manner:

BP:AP—a track found by the RP that passes the track selection in its original form; also passes the track selection in its final form (after the scan).

BP:AF—a track found by the RP that passes the track selection in its original form; either absent after the scan (ie., marked as a spurious track and therefore ignored), or present but fails the track selection in its final form (i.e., N_s).

BF:AP—either not found by the RP, or found but fails the track selection in its original form; passes the track selection in its final form (i.e., N_m).

BF:AF—either fails track selection in both its original and final forms, or absent is in one form and fails in the other.

The value for N_t = the total number of BP:AP plus BF:AP tracks, while N_f = the total number of BP:AP plus BP:AF tracks.

3.2.2 Results of scan

In order to make a useful measurement of the tracking efficiency, we must first identify those parameters to which P_m and P_s are sensitive. Sensible candidates include the polar angle η, the event z vertex position, and the local density of activity in the chamber (local track density plus background activity). Evidence for each of these is discussed below.

Consider the chamber response as a function of η. Near $\eta = 0$, the chamber resolution is relatively high and the pulse quality produced by each wire good (single pulses corresponding to about 0.5 cm of drift distance). At larger values of η, the resolution is significantly worse and the pulse quality very poor (multiple pulses of widely varying widths and spacings over a length $\approx$ (wire spacing) $\times \cot\theta$). Since the reconstruction efficiency is expected to depend upon the quality of information, we will assume that P_m and P_s depend upon η.

Figure 24 shows plots of $dN_{ch}/d\eta$ (uncorrected) for different regions of Δz, where Δz is the distance from the event vertex to the center high voltage screen of the nearest VTPC module ($\Delta z = \min(|z_v - z_{cs_i}|)$, for i =2–5, where z_v is the z vertex position, and z_{cs_i} is the z position of the center high voltage screen in VTPC module "i"). Differences between the distributions demonstrate clear z and η dependencies

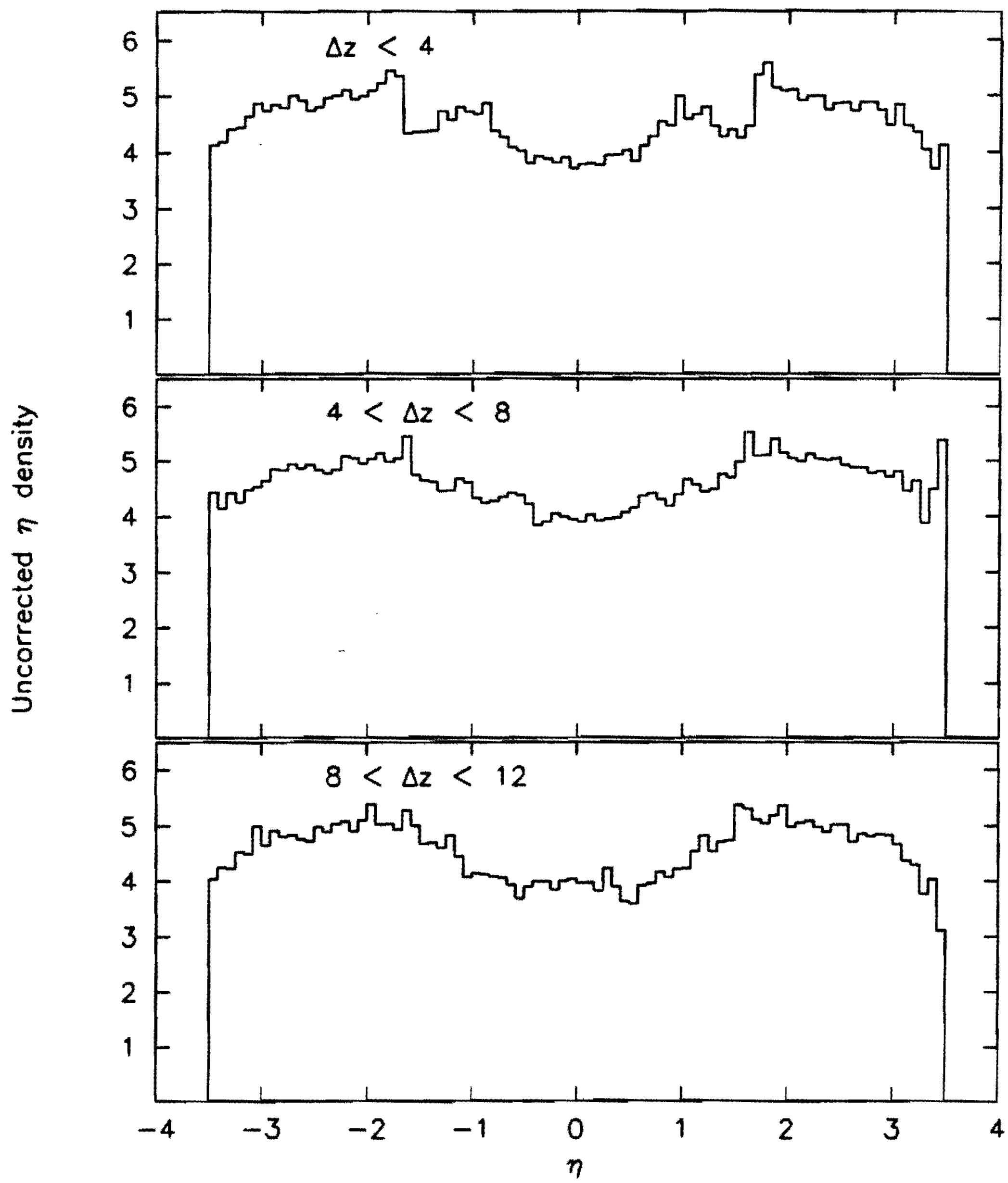

Figure 24. Uncorrected $dN_{ch}/d\eta$ as a function of the relative vertex position. We define the relative vertex position, Δz, as the distance to the center of the nearest VTPC module.

in the tracking efficiency. Later, we will use the z dependence as a systematic check of the efficiency measurement.

Local activity in the chamber could affect reconstruction performance by increasing the occurence of ambiguitites that confuse the algorithm. To test this dependence, define "local activity" as the number of hits within a window in η and ϕ of a specified width, $\Delta\eta$ and $\Delta\phi$ respectively. Figure 25 shows the corrections plotted as a function of the hit density for $\Delta\eta = 1.0$ and $\Delta\phi = \pi/8$. Although the plots generally suggest a decrease in the efficiency with increasing hit density, the dependence is neither strong, nor apparent in all η slices. Figure 26 compares the $dN_{ch}/d\eta$ distribution measured for $\Delta z < 4$ cm after correction using the hit-density-dependent efficiencies shown in fig. 25, with the same distribution after correction with efficiencies derived by averaging over all hit densities. Since the corrected distributions are nearly identical, we will calculate the final efficiency corrections *independent* of the local hit density.

Figure 27 and table 2 show final values for the probabilities P_m and P_s, and the tracking efficiency correction $C_{\text{eff}}(\eta)$ as a function of the z vertex position. The statistical uncertainties in the values of $C_{\text{eff}}(\eta)$ demonstrate that we fail to meet the desired goals of statistical significance for values of $|\eta| > 3.0$. This deficiency results from the loss of statistics to the vertex cuts used in the final analysis. The efficiency corrected $dN_{ch}/d\eta$ distribution as a function of the relative vertex position is shown in fig. 28. From this plot, we observe that in addition to the statistical error in C_{eff}, there is a systematic error on the order of 11–12% for $|\eta| > 0.75$. The source of this uncertainty is discussed in the next section.

3.2.2.1 Mis-reconstruction errors

Minor reconstruction errors which result only in mis-measurement of η represent an additional source of systematic error which, if sufficiently severe, could require a correction. Tracks of this type fall into the BP:AP category and have only been

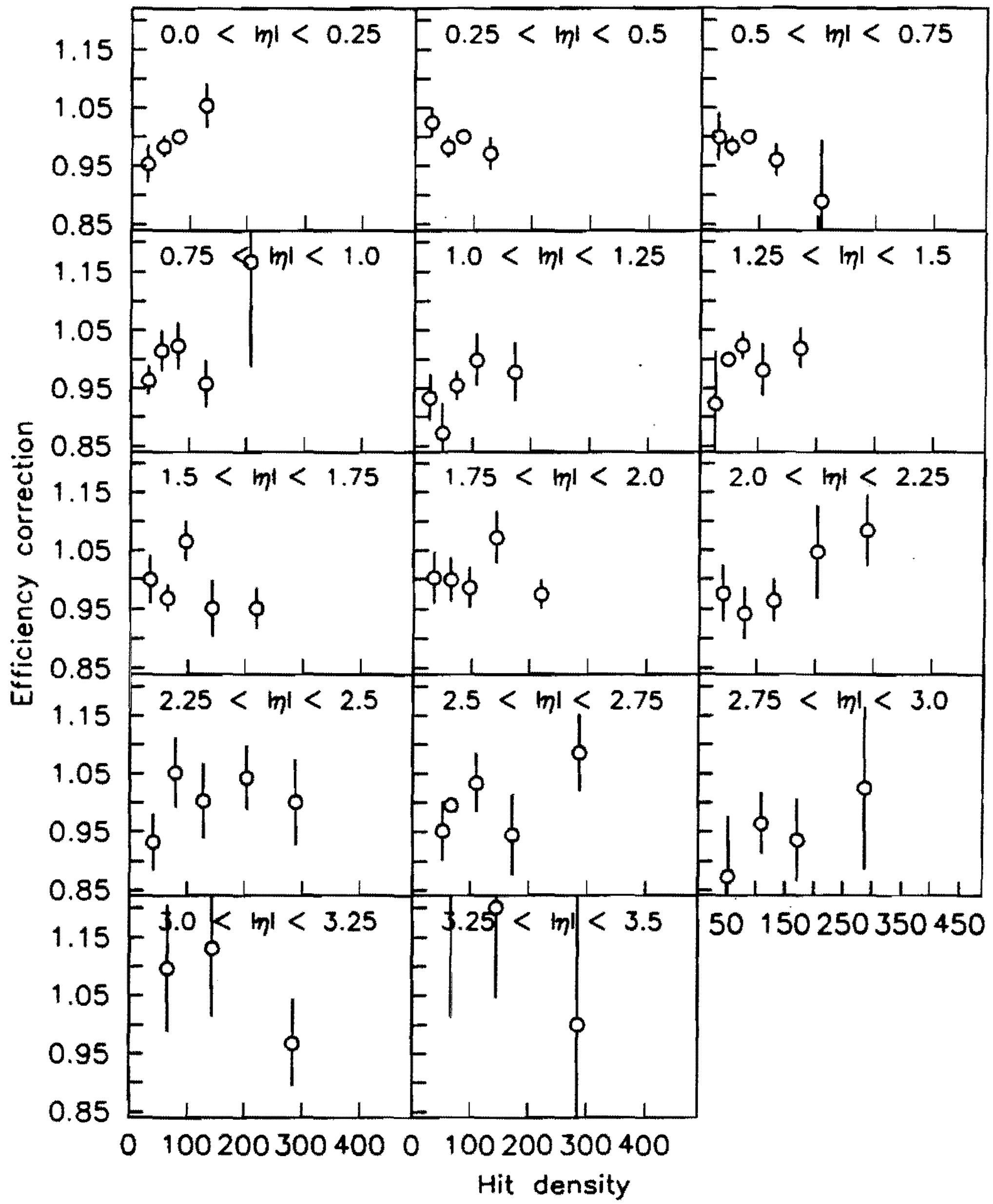

Figure 25. Efficiency correction vs. local hit density. Each plot represents the average for tracks within the specified η range. The hit density is defined in the text. The statistics are too poor to make a strong inference.

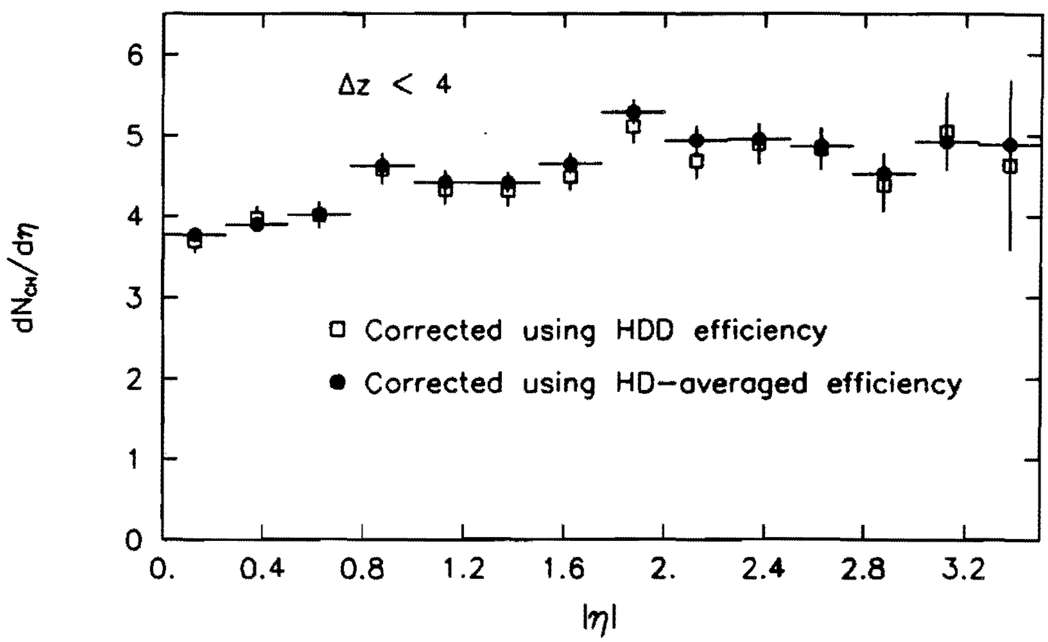

Figure 26. Effect of hit-density-dependent (HDD) corrections on $dN_{ch}/d\eta$. The dots correspond to the same distribution, but corrected using hit-density-averaged efficiencies (HD).

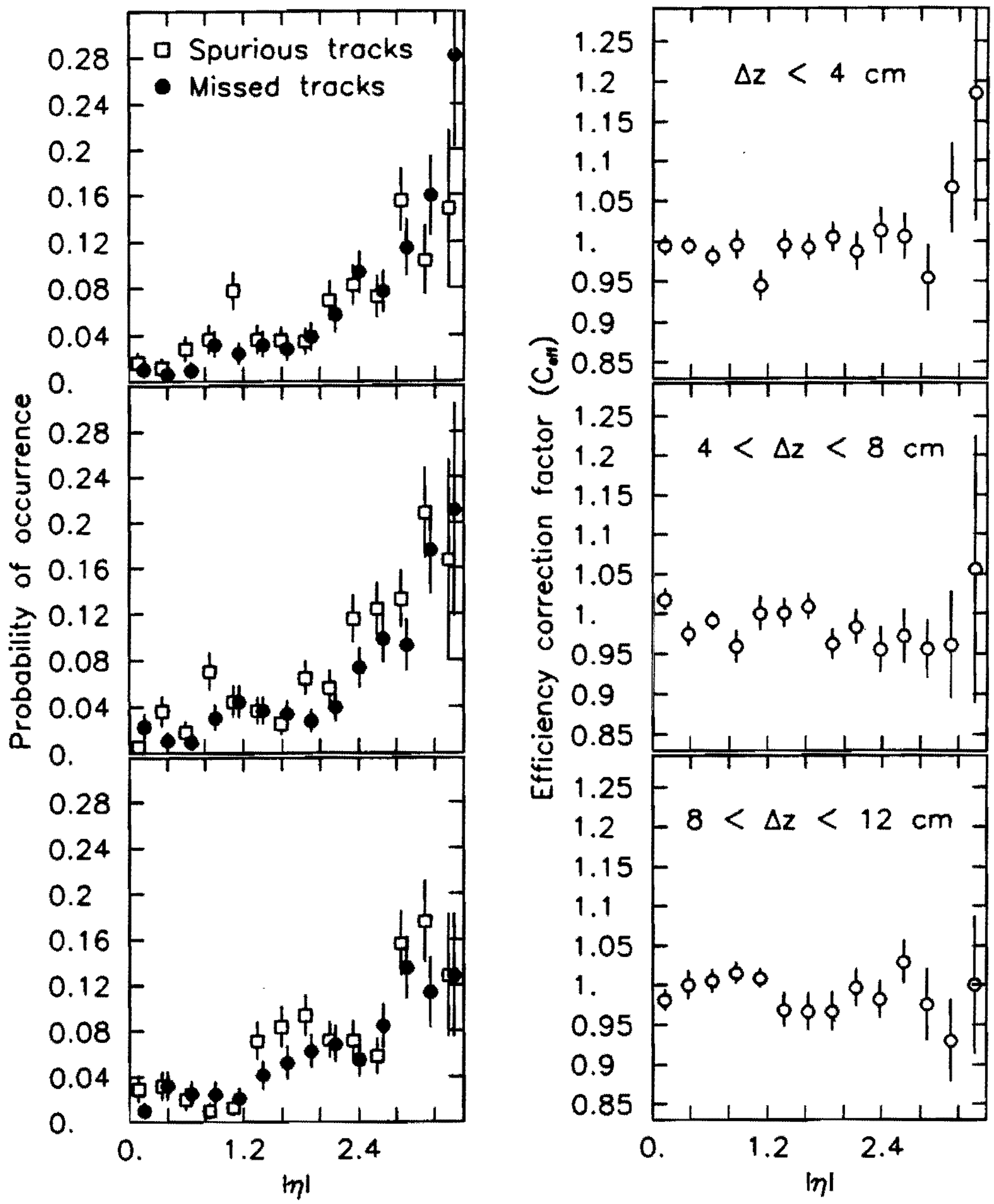

Figure 27. Efficiency correction vs. η as a function of Δz.

Table 2. Values of the efficiency correction, C_{eff}.

η range	$\Delta z < 4$ cm			4 cm $< \Delta z < 8$ cm			8 cm $< \Delta z < 12$ cm		
	$C_{\mathrm{eff}}(\eta)$	N_f	N_t	$C_{\mathrm{eff}}(\eta)$	N_f	N_t	$C_{\mathrm{eff}}(\eta)$	N_f	N_t
0.00-0.25	0.996±0.012	189	188	1.017±0.013	174	177	0.981±0.014	207	203
0.25-0.50	0.994±0.010	173	172	0.974±0.015	195	190	1.000±0.019	190	190
0.50-0.75	0.981±0.013	216	212	0.991±0.011	220	218	1.005±0.015	202	203
0.75-1.00	0.995±0.018	222	221	0.959±0.020	243	233	1.015±0.013	204	207
1.00-1.25	0.944±0.019	270	255	1.000±0.021	206	206	1.008±0.012	242	244
1.25-1.50	0.996±0.018	223	222	1.000±0.017	249	249	0.968±0.021	253	245
1.50-1.75	0.992±0.016	254	252	1.008±0.016	238	240	0.967±0.024	241	233
1.75-2.00	1.004±0.018	234	235	0.962±0.018	264	254	0.966±0.024	268	259
2.00-2.25	0.987±0.024	231	228	0.983±0.020	233	229	0.996±0.024	250	249
2.25-2.50	1.012±0.028	243	246	0.955±0.028	243	232	0.982±0.024	224	220
2.50-2.75	1.005±0.028	207	208	0.971±0.032	210	204	1.029±0.028	208	214
2.75-3.00	0.954±0.041	174	166	0.956±0.036	181	173	0.975±0.045	160	156
3.00-3.25	1.066±0.056	106	113	0.960±0.066	101	97	0.930±0.052	114	106
3.25-3.50	1.185±0.162	27	32	1.056±0.167	18	19	1.000±0.087	39	39
3.50-3.75	—	0	0	—	0	0	—	0	0

The value of Δz is the distance from the event vertex to the center of the nearest VTPC module; N_f is the number of tracks found by the ARP; and N_t is the number of tracks remaining after the scan.

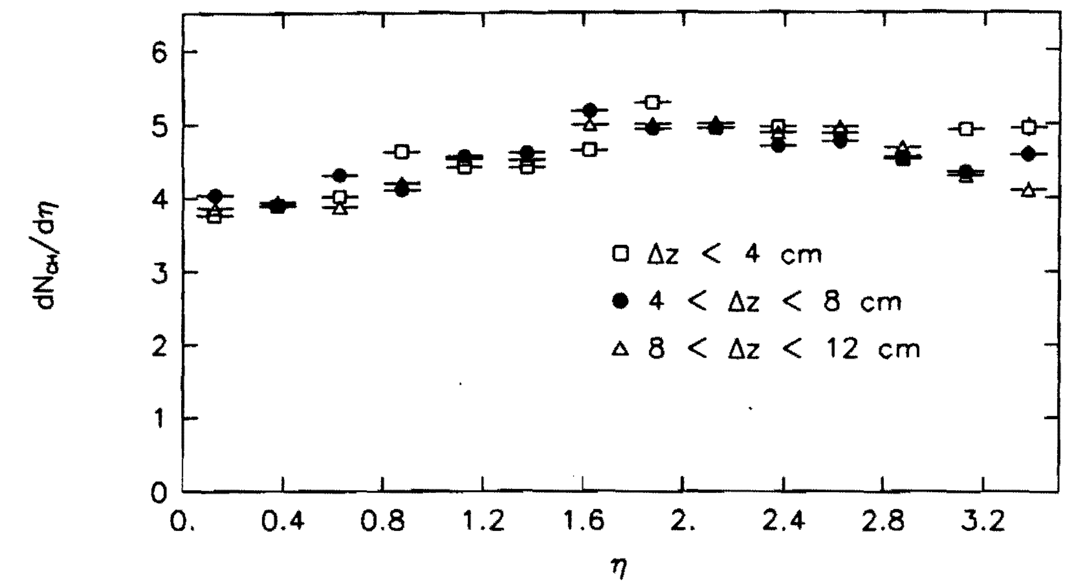

Figure 28. $dN_{ch}/d\eta$ as a function of vertex position after application of efficiency corrections.

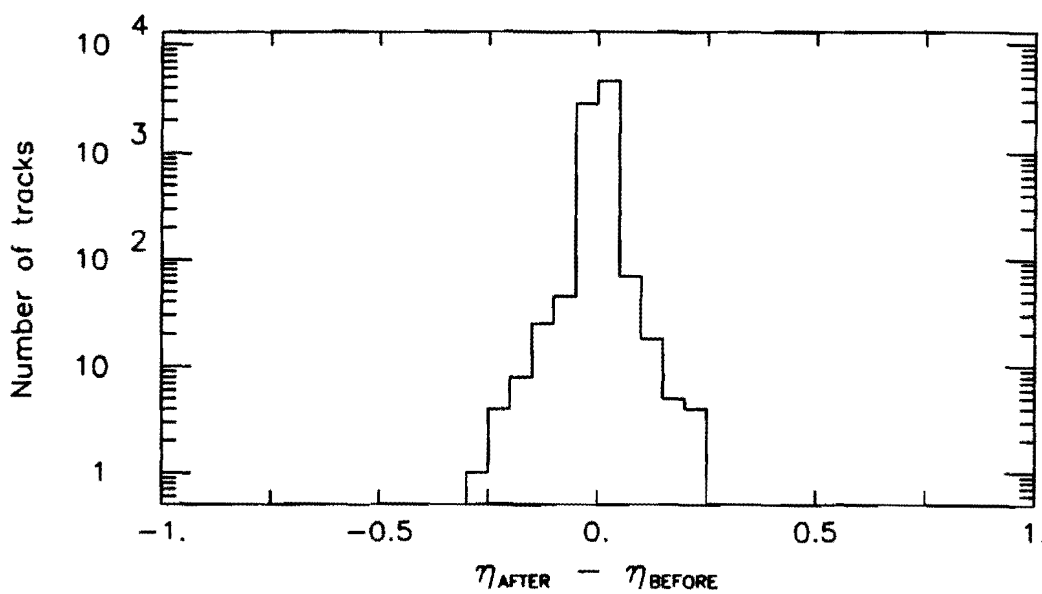

Figure 29. Effect of reconstruction errors on η. $\Delta\eta$ for a given track is the difference in the value of η calculated before and after modification in the scan. The plot includes all relative vertex positions.

modified during the scan (addition or deletion of hits). Figure 29 shows the difference between the original and final values of η for BP:AP tracks. The width of the peak suggests that mis-measurement errors caused by the reconstruction are not a serious problem.

3.2.3 Systematic uncertainties in the tracking efficiency

Figure 28 shows the $dN_{ch}/d\eta$ distribution, measured as a function of Δz, after correction for tracking efficiency. We observe that the tracking efficiency as measured by the scan does not entirely compensate for changes in the efficiency as a function of η and Δz. The various features within each distribution are highly correlated with sharp changes in the fraction of tracks which traverse more than one VTPC module, and significant differences between distributions are observed at these features. The discrepancies are consistent with the occasional splitting of tracks (i.e., failing to join pairs) which cross several modules into two distinct tracks, a problem observed and partially corrected during the scan. The systematic uncertainties in the efficiency must be of the same order as the differences in these distributions.

Consider a track that has been split into two tracks. In general, we expect the hits for a given member of the pair to lie predominantly, if not entirely, within either the ϕ_+ or ϕ_- set of modules. This characteristic provides a method to distinguish such tracks from others. Define the "module occupancy" as the number of hits on the track divided by the number of hits expected considering only the module sets in which hits are actually found, and the "exit occupancy" as the number of hits found divided by the total number which should be on the track irrespective of which modules actually have hits. Split tracks should have an exit occupancy much lower than the module occupancy.

Figure 30 shows a plot of the exit occupancy versus the module occupancy. Table 3 lists the values of $dN_{ch}/d\eta$ as a function of restrictions on these occupancies. Results are listed using tracking efficiencies calculated both with and without oc-

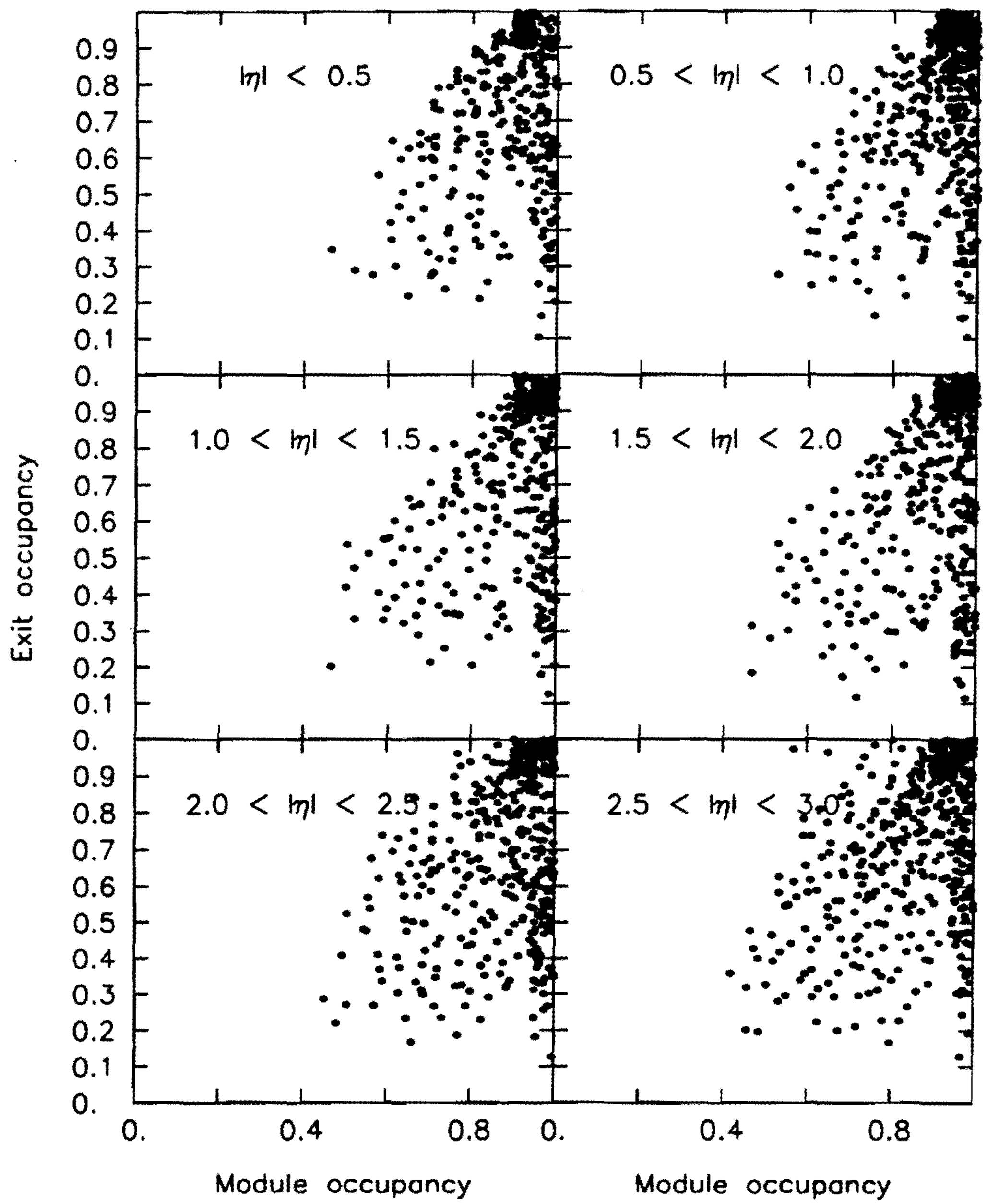

Figure 30. Exit occupancy vs. module occupancy. Note the increasing frequency of low exit occupancy and high module occupancy as η increases.

Table 3. The effect of track occupancy on $dN_{ch}/d\eta$.

1800 GeV							
		$m < 0.9$, $x > 0.4$		$m < 0.9$, $x > 0.5$		$m < 0.8$, $x > 0.5$	
η range	No cuts	with	w/o	with	w/o	with	w/o
0.00-0.25	3.952±0.020	3.940	3.932	3.938	3.930	3.939	3.931
0.25-0.50	3.968±0.020	3.965	3.942	3.962	3.927	3.965	3.930
0.50-0.75	4.096±0.021	4.097	4.050	4.087	4.003	4.097	4.012
0.75-1.00	4.305±0.021	4.353	4.222	4.421	4.142	4.394	4.160
1.00-1.25	4.556±0.022	4.580	4.409	4.601	4.292	4.597	4.323
1.25-1.50	4.508±0.021	4.379	4.343	4.418	4.184	4.432	4.219
1.50-1.75	4.939±0.022	4.848	4.711	4.825	4.621	4.844	4.660
1.75-2.00	5.012±0.022	4.952	4.730	4.963	4.563	4.994	4.615
2.00-2.25	4.887±0.022	4.822	4.761	4.846	4.526	4.849	4.573
2.25-2.50	4.713±0.022	4.670	4.667	4.623	4.499	4.606	4.525
2.50-2.75	4.704±0.023	4.650	4.664	4.629	4.546	4.631	4.571
2.75-3.00	4.377±0.024	4.287	4.322	4.315	4.258	4.318	4.278
3.00-3.25	4.280±0.031	4.256	4.216	4.288	4.178	4.298	4.187
3.25-3.50	4.245±0.068	4.067	4.155	4.041	4.129	4.042	4.130
630 GeV							
		$m > 0.9$, $x < 0.4$		$m > 0.9$, $x < 0.5$		$m > 0.8$, $x < 0.5$	
η range	No cuts	with	w/o	with	w/o	with	w/o
0.00-0.25	3.18±0.05	3.19	3.18	3.19	3.18	3.19	3.18
0.25-0.50	3.10±0.05	3.10	3.10	3.11	3.08	3.11	3.09
0.50-0.75	3.32±0.05	3.33	3.30	3.32	3.25	3.32	3.26
0.75-1.00	3.55±0.05	3.51	3.48	3.64	3.41	3.62	3.43
1.00-1.25	3.59±0.05	3.47	3.47	3.62	3.38	3.61	3.40
1.25-1.50	3.69±0.05	3.47	3.53	3.61	3.41	3.62	3.44
1.50-1.75	3.98±0.05	3.75	3.77	3.87	3.71	3.89	3.74
1.75-2.00	4.15±0.06	3.88	3.89	4.09	3.76	4.11	3.80
2.00-2.25	3.88±0.05	3.73	3.77	3.85	3.59	3.85	3.63
2.25-2.50	3.72±0.05	3.65	3.69	3.65	3.56	3.64	3.57
2.50-2.75	3.69±0.06	3.66	3.67	3.62	3.56	3.63	3.58
2.75-3.00	3.39±0.06	3.34	3.37	3.37	3.32	3.37	3.34
3.00-3.25	3.35±0.07	3.35	3.34	3.41	3.32	3.41	3.32
3.25-3.50	3.47±0.16	3.39	3.46	3.38	3.45	3.38	3.45

Tracks with module occupancy greater than m, and exit occupancy less than x are excluded. The column under "with" refers to efficiency corrections which include module/exit occupancy cuts, while the column under "without" refers to efficiency corrections made without cuts. Since the statistics of all measurements are comparable, only the statistical uncertainties of the measurements without cuts are shown.

cupancy cuts. Note the change in shape between the distributions corrected using efficiencies with and without occupancy cuts. The change is about the same magnitude as the differences between η distributions measured at different Δz values, and is large in those η regions where discrepancies between measurements at different Δz values are the largest. We take this as an indication that the occupancy cuts preferentially eliminate partially reconstructed 3-D tracks, i.e., those consistent with split tracks.

For $|\eta| > 0.5$, we have chosen to use as the final result the distribution for exit occupancy less than 0.4, module occupancy greater than 0.9, corrected without occupancy cuts. The difference between this distribution and that measured without occupancy cuts is approximately equal to half of the apparent over-efficiency observed in the Δz dependence of $dN_{ch}/d\eta$. The systematic uncertainty in the efficiency measurement is taken as the maximum difference between $dN_{ch}/d\eta$ measured at different vertex positions: ± 0.50 at 1800 GeV, and ± 0.4 at 630 GeV (about 11%). Although large differences occur only for values of $|\eta|$ near 1.0, the uncertainty is assumed to apply to all regions with a significant number of module-crossing tracks. See Appendix E for further discussion of this problem.

3.2.4 Systematic checks of the efficiency measurement

Several systematic checks exist to probe the quality of the scan result. The first of these, the requirement that the $dN_{ch}/d\eta$ distribution be independent of the z vertex postion, is discussed in the previous section. Deviations from this expectation allow us to estimate systematic uncertainties.

A second check is provided by the samples of events scanned by both scanners. Figure 31 shows the probabilities and corrections derived from these identical samples of events. The two sets of corrections agree within statistics, indicating that the scanners on average arrived at the same decisions. (The differences in the probabilities reflect differences only in the method employed by the two scanners to reach

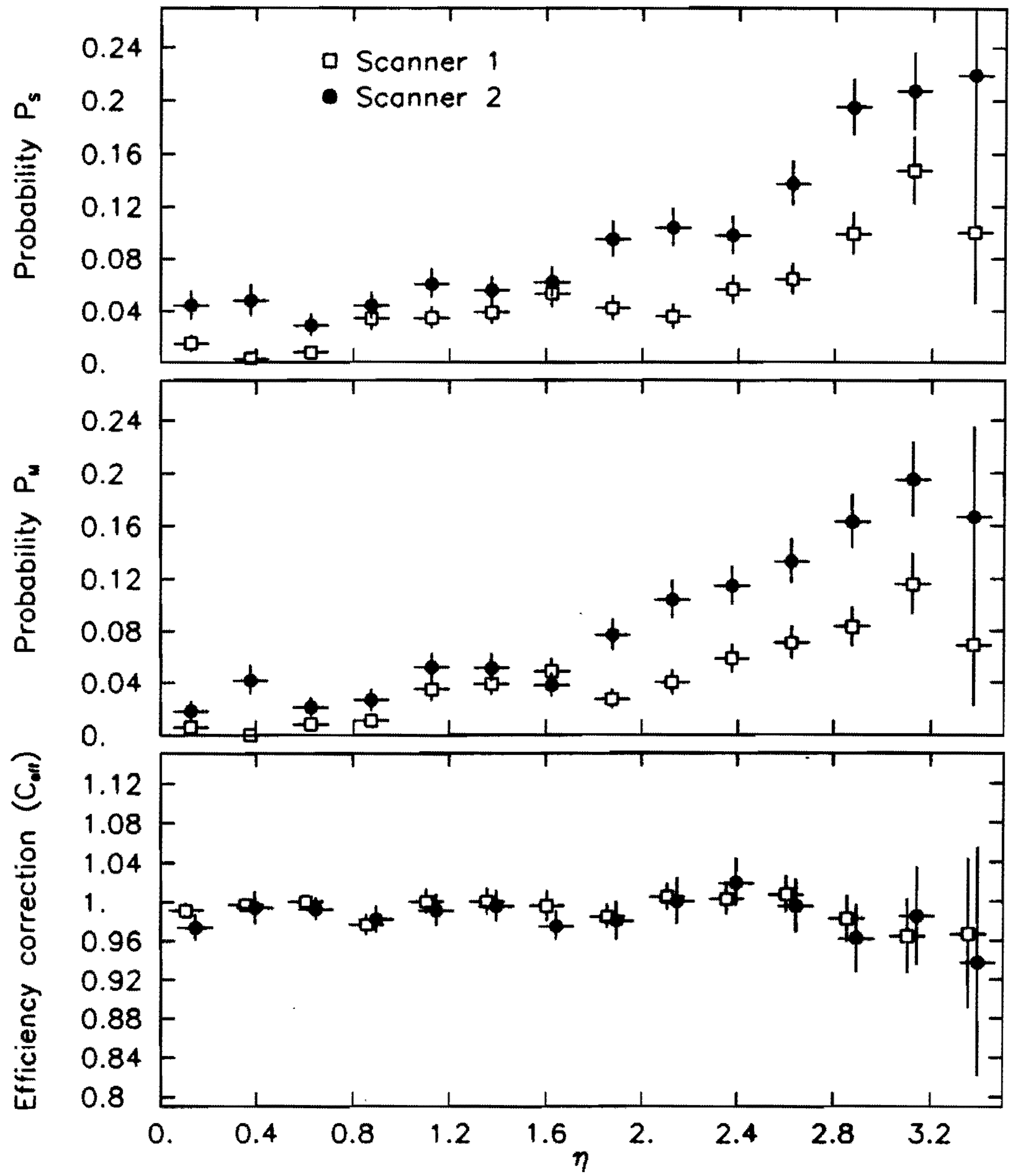

Figure 31. Dependence of efficiency correction on scanner. The plots show P_s, P_m, and C_{eff} obtained individually by the two scanners for identical data sets.

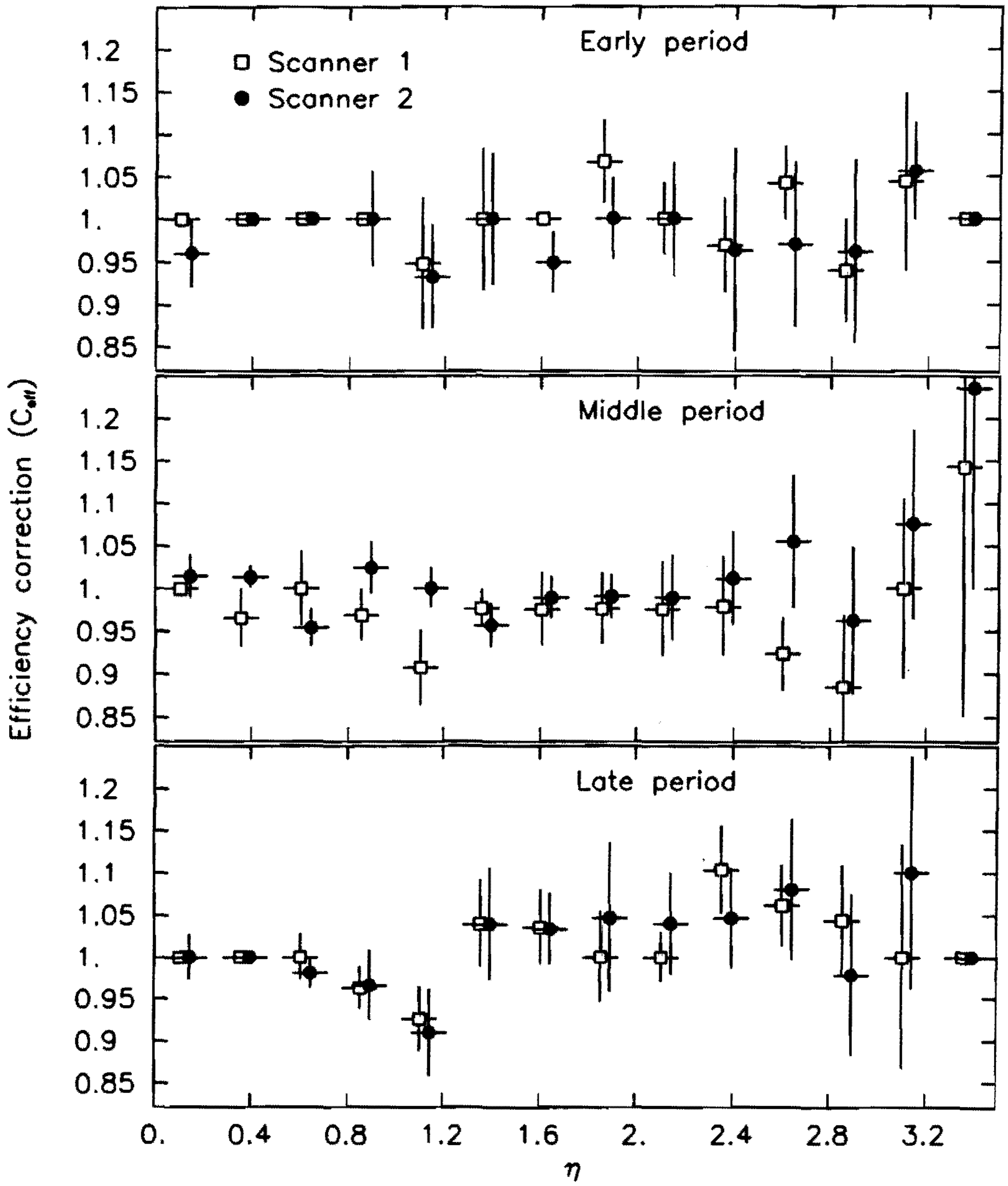

Figure 32. Efficiency correction vs. time for each scanner. The plots show the corrections obtained by each scanner (using independent data sets) in three distinct time periods during the scan.

decisions, not in the true probabilities.) Finally, figure 32 shows the corrections as a function of time for each scanner. It is interesting to note that the corrections within any single time period agree better than the entire time series for either scanner. This suggests that the differences within the time series are dominated by the particular event selection used during each time period (it changed throughout the measurement) rather than by any time dependence in the discretion of the scanners.

As a third check, a very small number of events (nine) scanned first by the scanners was re-scanned by physicists familiar with the details of the VTPC. After track selection, the physicist scanned sample is identical to that produced by the scanners for $|\eta| < 1.25$ (see fig. 33). For larger $|\eta|$, the physicists tended to obtain slightly lower values for C_{eff}, although the two sets of results are consistent.

Finally, we note that of the 23 events consistent with $W^{\pm} \rightarrow e^{\pm}\nu$ decays found in the 1987 data, tracks belonging to 22 of the $e^{\pm}$ candidates were found in the VTPC. Tracking information from the Central Tracking Chamber (CTC) [66] indicates that the one which was not found passed almost directly along the boundary between two octants. All of the $e^{\pm}$ candidates were found within $|\eta| < 1$.

3.2.5 Low p_t cutoff

The VTPC operates in a 1.5 Tesla magnetic field coaxial with the beam axis, and the resulting curvature of tracks causes a loss of tracking efficiency for particles with p_t less than about 50 MeV/c. These tracks spiral entirely within the outer radius of the VTPC. Results from chamber simulation [67] suggest that the efficiency for tracks above 100 MeV/c is nearly uniform and near unity, while that for $p_t = 50$ MeV/c tracks approaches only 0.5, falling rapidly to zero below 50 MeV/c.

Since the VTPC does not (generally) measure the p_t of tracks, the p_t dependence of the tracking efficiency presents a potentially serious problem if we are to avoid reliance upon the simulation for efficiency estimates. Scanning, however, introduces a sharp low p_t cutoff through the efficiency correction: scanners delete tracks found

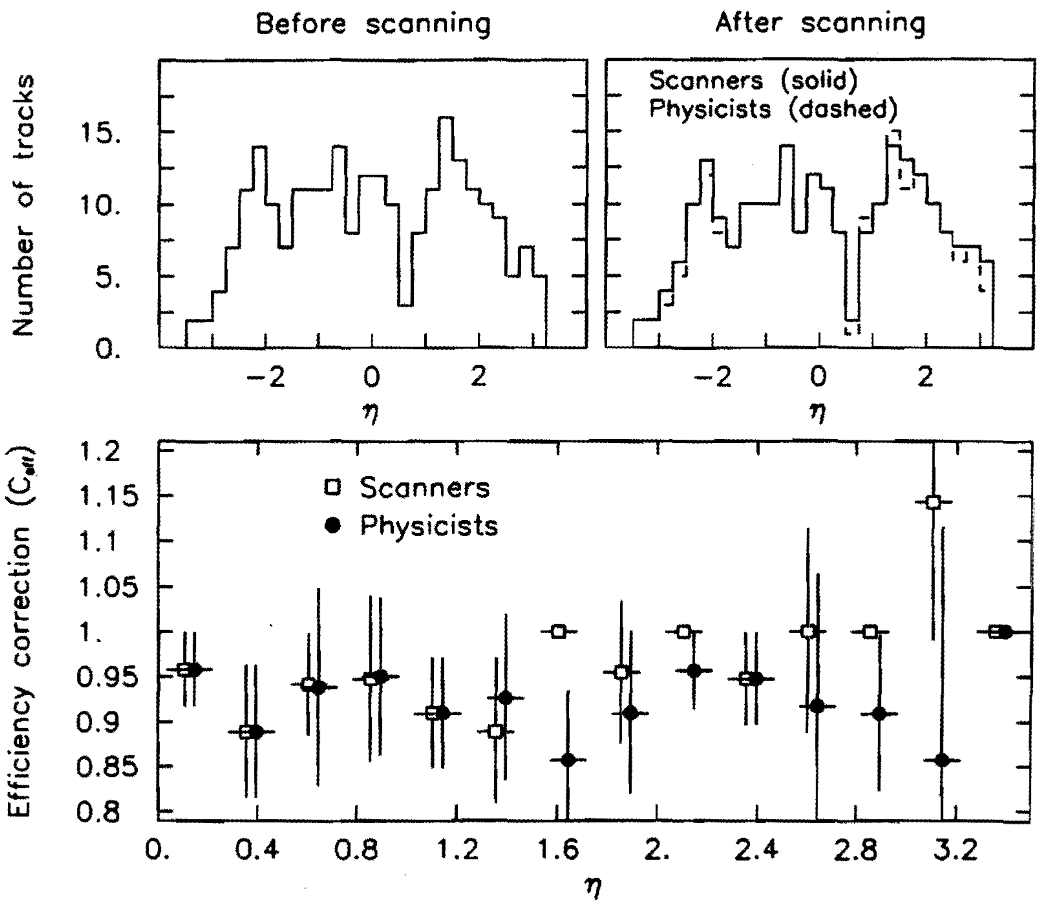

Figure 33. Comparison of scanner vs. physicist scans. For a common sample of nine events, we show the initial distribution of tracks, the distribution of tracks after the respective scans, and the corrections derived from each.

Table 4. Fraction of charged particles with $p_t < {p_t}^{min}$ assuming three different functional forms of the p_t spectrum below $p_t = 0.4$ GeV/c, for $\sqrt{s}$ of 630 and 1800 GeV.

p_t^{min}	Fraction of tracks					
	Be^{-Cp_t}		$B + Cp_t + D{p_t}^2$		$Ap_0^n/(p_t + p_0)^n$	
(GeV/c)	630	1800	630	1800	630	1800
0.25	0.007	0.006	0.005	0.005	0.008	0.008
0.50	0.025	0.022	0.019	0.021	0.029	0.028
0.75	0.051	0.047	0.041	0.044	0.059	0.056
1.00	0.084	0.078	0.069	0.074	0.095	0.091

by the reconstruction that spiral within the outer radius of the chamber, and ignore those missed. A sharp p_t limit allows correction of the η distribution by extrapolating the inclusive p_t spectrum to $p_t = 0$, and adjusting the η distribution to compensate for the fraction of tracks lost below the p_t cutoff. Although this technique should work well in the central region, at lower angles, tracks that exit the end modules before reaching the outer radius of the chamber, introduce considerable uncertainty in the value and the sharpness of the p_t cutoff.

Three different functional forms (listed in table 4) are used to model the shape of the invariant cross section ($E\frac{d^3\sigma}{dp^3}$) below $p_t = 0.4$ GeV/c [69]. The shape above $p_t =$ 0.4 GeV/c is fit to the form $A(\frac{p_0}{p_t+p_0})^n$ [68] using data from CDF in reference [69]. The parameters for the shape below 0.4 GeV/c are fixed by demanding continuity of the cross section and the first derivative (and second for the quadratic form) at $p_t = 0.4$ GeV/c.

The fraction of tracks below some value of p_t is determined by integrating dN_{ch}/dp_t. Values for this fraction are tabulated in table 4 for several values of the p_t cutoff for each of the functional forms. The value assumed for the low p_t correction is 0.03±0.02 for both 630 and 1800 GeV.

3.2.6 Summary of efficiency corrections

1. We have found that the reconstruction efficiency depends critically upon η and the position of the event vertex (fig. 24), but not significantly upon the local density of chamber activity (fig. 26).

2. Using data from a visual scan we measure the correction for the tracking efficiency to be $< 5\%$ for values of $|\eta| < 3.0$, and $< 10\%$ out to $|\eta| < 3.5$ (fig. 27 and table 2).

3. The estimated contribution to the systematic error in $dN_{ch}/d\eta$ from the statistics of the efficiency measurement is less than 2% for $|\eta| < 1.0$, less than 3.6% for $|\eta| < 3.0$, rising to about 17% for $|\eta| \sim 3.5$ (table 2).

4. The corrections fail to compensate fully for over-efficiences in the region of $|\eta| > 0.75$ (fig. 28), an effect which contributes an additional 11–12% to the systematic error. These regions correspond to angles at which the majority of tracks cross several wires in more than a single VTPC module.

5. A 50 MeV/c p_t cutoff imposed through the efficiency correction requires a uniform adjustment of the η distribution to compensate for the 3%±2% fraction of tracks with $p_t < 50$ MeV/c (table 4).

6. Mis-measurement of η due to reconstruction errors requires no correction (fig. 29).

Chapter 4

Data and Analysis

The data used for this analysis comes from a number of dedicated minimum bias run spread throughout the 1987 collider run. The large inelastic cross section allowed effective data taking under a broad range of instantaneous luminosities, but the majority of running occurred during relatively low luminosity periods at the end of low beta stores, the highest luminosities being reserved for the study of relatively rare hard scattering events. A list of runs and other relevant information is compiled in Appendix F.

The remainder of this chapter describes in detail the analysis of this data leading to the final measured values of $dN_{ch}/d\eta$. The detector trigger configuration is discussed in Section 4.1. Section 4.2 outlines the software event selection used to separate beam-gas background from $\bar{p}p$ collisions. Included in this section is a discussion of beam-gas background remaining after event selection, and some remarks on the fraction of signal lost to the selection process. A description of the track selection criteria follows in Section 4.3, with Section 4.4 devoted to the determination of geometrical acceptance corrections. Section 4.5 describes possible sources of charged particle background along with the appropriate corrections. Finally, a number of systematic checks are presented in Section 4.6.

4.1 Detector trigger

The "minimum bias" trigger requires at least a single hit in both the east and west BBCs in coincidence with the beam crossing. A total of 37,421 triggers were recorded during 10 runs at 1800 GeV, while 9387 triggers were recorded during a single run at 630 GeV. Pertinent statistics for each run are listed in Appendix F.

A detailed study of the trigger acceptance is very difficult to obtain for several reasons. First, the statistical properties of low p_t physics are not very well understood from either an empirical or theoretical point of view. Calculating efficiencies often depends upon the tails of poorly measured distributions, or assumptions about certain types of particle correlations. The picture becomes further clouded in the process of separating $\bar{p}p$ collisions from random background events described in the next section. Secondly, simulating the accelerator beam environment to obtain background estimates is prohibitively complicated. For these reasons, we make no attempt to use simulations to correct observed distributions for events which are *not* observed, either as a result of trigger inefficiencies, or losses during event selection.

There exist, however, several empirical techniques which shed light on both the question of trigger efficiency and that of background and losses incurred during event selection. The latter issue is discussed in detail in Section 4.2. Here we describe only the trigger efficiency under the assumption that the event selection is understood.

4.1.1 Runs with zero trigger bias

We study some features of the hardware trigger using data from runs in which the detector is triggered on random beam crossings. A total of 5266 events recorded from random beam crossings has been analyzed. Of these events, 186 pass the $\bar{p}p$ event classification criteria described in the next section. Examination of BBC data for these events reveals that nine, or 4.8±1.6%, would not satisfy the minimum bias trigger, and therefore, would not have been recorded during normal minimum bias running.

4.2 Event selection

Secondary particles produced in incidental collsions of beam particles with gas atoms, or directly with the material in or around the beam pipe, cause random coincidences in the BBC which satisfy the hardware trigger conditions. Events from such "beam-gas" (BG) triggers must be separated from "beam-beam" (BB) events during offline analysis. Additional sources of background include cosmic rays which traverse the detector in coincidence with beam crossings, and losses from the main ring accelerator (located directly above the CDF detector) which shower the detector with charged particles. The identification of out-of-time energy deposition in the calorimeters allow removal of both types of events. Also, in order to maintain consistency with the data sample used in the inclusive p_t measurement [69], we eliminate events with excessive noise in the CTC. Both of these cuts are applied before classifying events as either BB or BG, and are uncorrelated with the physics processes under study.

4.2.1 Event classification

After reconstruction of BBC and VTPC information, events from bunch crossings which contain both protons and anti-protons are classified as beam-beam if they satisfy at least one of the following two criteria: (1) at least four tracks in the VTPC with a minimum of one in each the forward and backward hemispheres; (2) a vertex position derived from the VTPC (requires a minimum of two tracks) within 16 cm of that obtained from the BBC (requires a minimum of three in-time hits in each set of BBCs). All other events are classified as beam-gas. Figure 34 shows the vertex distribution of events belonging to each classification for the 630 and

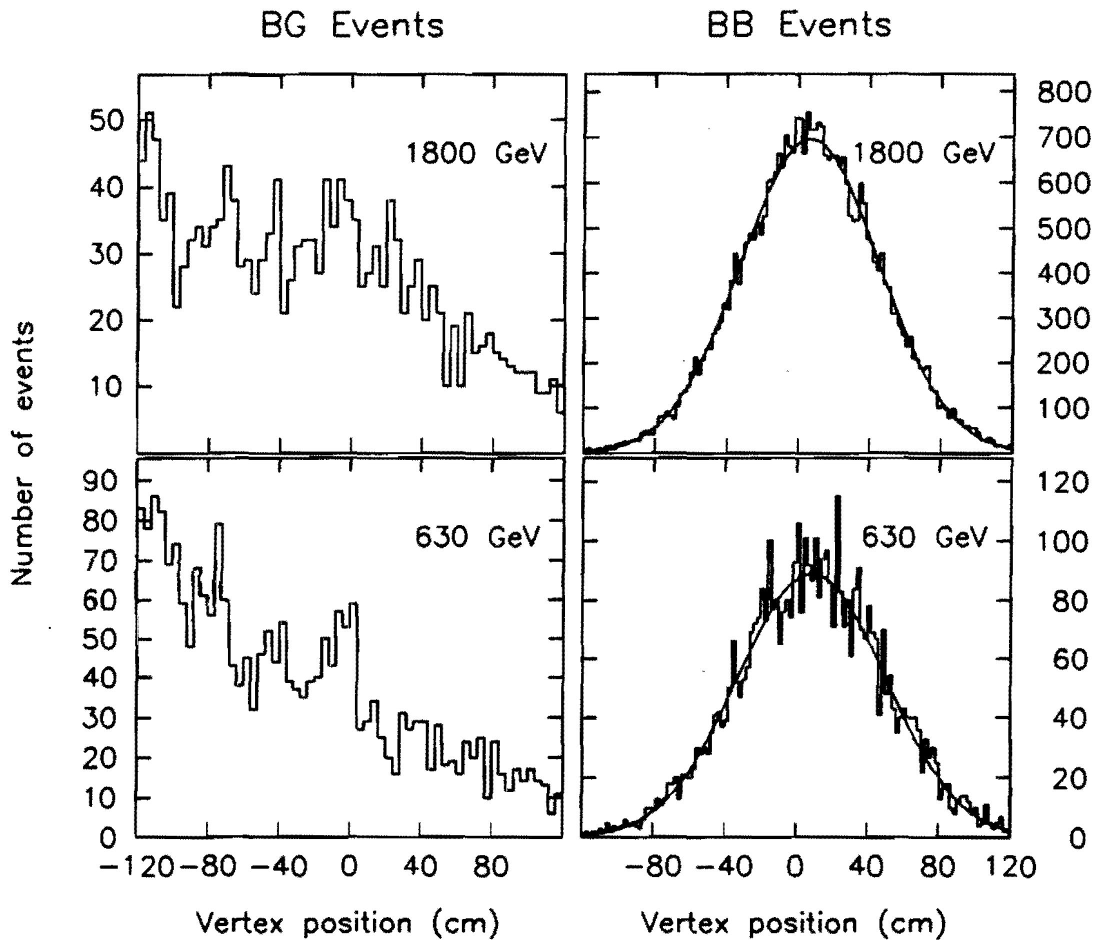

Figure 34. Vertex distributions for events classified as "beam-gas" and "beam-beam." The curves through the "BB" distributions are the results of fits to a Gaussian. The χ^2 of the fits are 183/117 degrees of freedom for the 1800 GeV data, and 120/117 degrees of freedom for the 630 GeV data.

Table 5. Run statistics for 630 and 1800 GeV data samples.

$\sqrt{s}$ (GeV)	Triggers	Bn/CTC CR/MR	BB events	BG events	All cuts
630	9387	1300	4736	3351	2837
1800	37421	791	34054	2576	20970

The table lists the total number of detector triggers used for this analysis; the number rejected as belonging to a missing bunch, coincident with excessive noise in the CTC, a cosmic-ray event, or a shower from the main ring (Bn/CTC/CR/MR); the number classified as BB and BG; and the number passing all cuts used to determine the value of $dN_{ch}/d\eta$.

1800 GeV data sets. Note that the BG distribution slopes downward to the right, suggesting, as expected, that the higher intensity proton beam is the source for the majority of BG events. The BB vertex distribution is Gaussian with a standard deviation of 38.7±0.2 cm for 1800 GeV data, and 41.2±0.5 cm for 630 GeV data, both consistent with expectations from accelerator parameters.

After classification, the BB event sample is further reduced by requiring that the event vertex lie within ±12 cm of the center grid of any of the middle four modules. This cut avoids non-uniformitites in the η acceptance caused by gaps between modules (see discussion in Section 3.2.2). Table 5 presents summary statistics for the data samples.

4.2.2 Beam-gas background

The rejection power of these selection criteria is analyzed using data from runs with missing $\bar{p}$ bunches. All triggers from such missing bunches should be classified as BG, and can be used as a BG control sample. The following calculation serves to estimate the level of BG background in the final event sample. Define $f_{bg \to bb}$ as the fraction of BG events mis-classified as BB, and f_{bg}^{fid} as the fraction of mis-classified events that lie within the vertex fiducial region. If we assume that the vertex distribution of BG events mis-classified as BB events is the same as the vertex distribution of BG events, then the fraction of BG events which pass all event selection criteria, f_{bg}^{pass}, is given by:

$$\begin{aligned} f_{bg}^{pass} &= f_{bg \to bb} \cdot f_{bg}^{fid} \\ &= \left(\frac{N_{bg \to bb}}{N_{bg}} \right) \left(\frac{N_{bg}^{fid}}{N_{bg}} \right), \end{aligned} \tag{4.1}$$

where N_{bg} is the total number of BG events in the control sample; $N_{bg \to bb}$ is the number mis-classified as BB; and N_{bg}^{fid} is the total number which lie within the vertex fiducial region.

Table 6 lists the number of triggers classified as BG and BB for each run with missing bunches, along with calculations of $f_{bg \to bb}$. The difference between the 630 and 1800 GeV values of $f_{bg \to bb}$ is well beyond statistics and is not understood. Figure 35 shows the vertex distributions for BG events classified as BG, and those mis-classified as BB. The low statistics in the latter plot prevent a confirmation of our assumption about the shape of the vertex distribution for mis-classified BG events, although we will consider the shape consistent with that of pure BG events. Table 7 contains estimates for f_{bg}^{fid}, the fraction of BG triggers which lie within the vertex fiducial volume. The estimates are based upon the vertex distribution for all events classified as BG from the minimum bias data set. This choice over-estimates the value of f_{bg}^{fid} since the set of events classified as BG must certainly contain BB events mis-classified as BG. The incidence of BB events mis-classified as BG is discussed in a later section.

Table 8 contains the result of calculations of f_{bg}^{pass}, the fraction of BG triggers that pass all event selection cuts, under various scenarios for the value of $f_{bg \to bb}$ and f_{bg}^{fid}. The most conservative limit on BG background is 2.4% at 630 GeV, and 0.25%

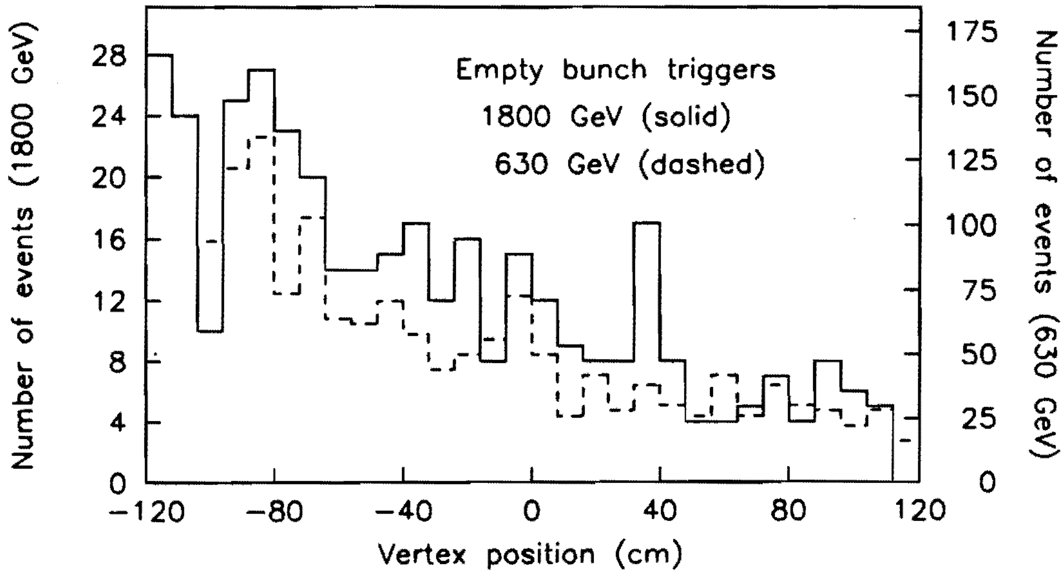

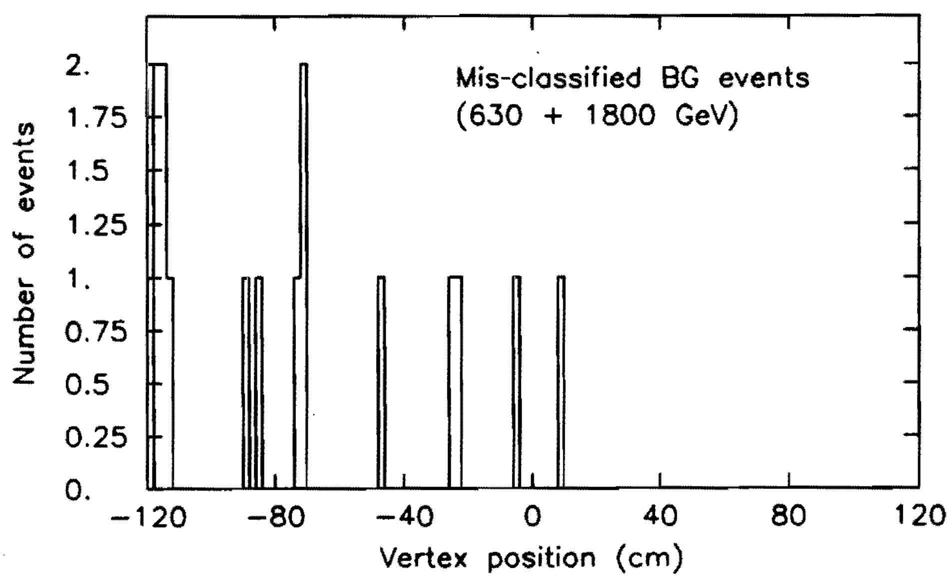

Figure 35. Vertex distribution for empty bunch data. The top plot shows the distribution for all events in the empty bunch data set. The lower plot show the distribution for all events mis-classified as beam-beam.

at 1800 GeV; assuming that the vertex distribution for mis-classified BG events is the same as that for all BG events, we obtain the much lower values of 0.13% at 630 GeV, and 0.08% at 1800 GeV.

4.2.3 Effect of beam-gas background on results

Figure 36 shows a plot of the normalized $dN_{ch}/d\eta$ distribution for BG events from

Table 6. The number of events classified as BB and BG in each missing bunch run, and the fraction of BG events mis-classified as BB ($f_{bg\to bb}$).

$\sqrt{s}$ (GeV)	Run	Bunch	BB	BG
1800	6985	A	0	37
		C	4	31
	6986	A	3	52
		C	1	49
	7242	A	0	51
		C	0	58
	7559	A	2	127
	7560	A	1	128
All 1800 runs:			11	533
	$f_{bg\to bb} = \frac{11}{544} = 0.020 \pm 0.006$			
630	7536	A	5	1274
	$f_{bg\to bb} = \frac{5}{1279} = 0.0039 \pm 0.0017$			
All runs:			16	1807
	$f_{bg\to bb} = \frac{16}{1823} = 0.0088 \pm 0.0022$			

Table 7. Fraction of beam-gas events within the vertex fiducial region (f_{bg}^{fid}, including the statistical uncertainty).

$\sqrt{s}$ (GeV)	N_{bg}	N_{bg}^{fid}	f_{bg}^{fid}
1800	2347	738	0.314±0.010
630	3869	1027	0.265±0.007
Sum:	6216	1765	0.284±0.006

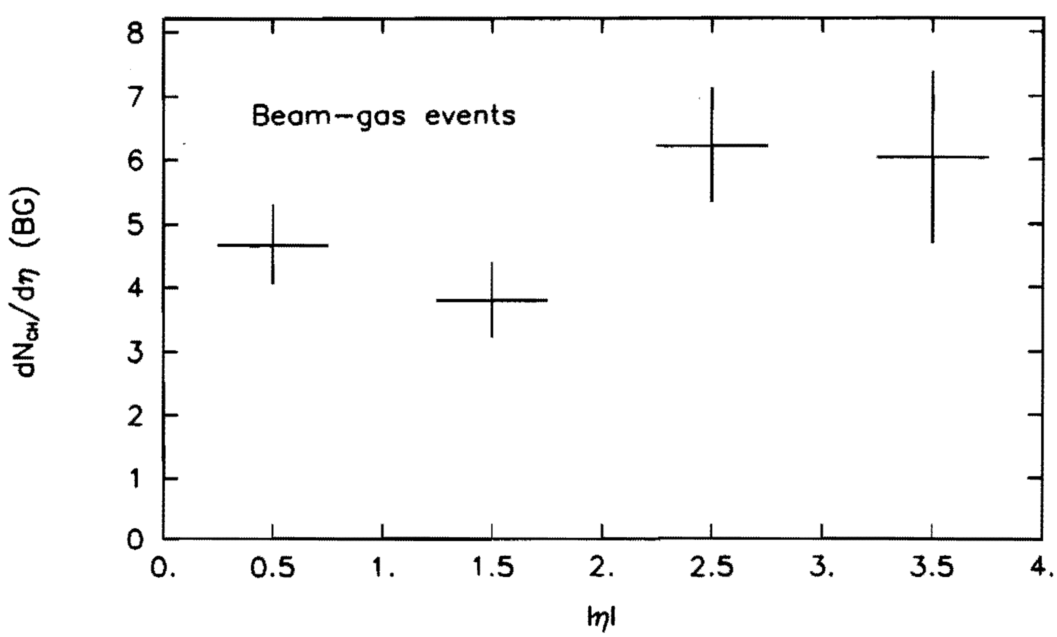

Figure 36. The η distribution for mis-classified beam-gas events.

Table 8. Estimated beam-gas background in data sample after event selection.

$f_{bg\to bb}$	f_{bg}^{fid}	f_{bg}^{pass} $(= f_{bg\to bb}\cdot f_{bg}^{fid})$	N_{bg}	N_{bg}^{pass}	Fraction passed
1800 GeV					
0.020	0.314	0.0063±0.0019	2576	16.3	0.0008±0.0002
	1.000	0.020±0.006	2576	52.6	0.0025±0.0008
0.009	0.314	0.0031±0.0007	2576	8.0	0.0004±0.0001
	1.000	0.009±0.006	2576	22.4	0.0011±0.0007
630 GeV					
0.004	0.265	0.0011±0.0005	3351	3.7	0.0013±0.0006
	1.000	0.004±0.002	3351	13.5	0.0048±0.0024
0.009	0.265	0.0024±0.0005	3351	8.1	0.0029±0.0006
	1.000	0.009±0.006	3351	30.4	0.011±0.007
0.020	1.000	0.020±0.006	3351	67.0	0.024±0.007

The table shows the fraction of BG events that pass all event selection cuts (f_{bg}^{pass}), and the fraction of events in the final BB sample that are mis-classified BG events (last column). Values in the first two columns come from tables 6 and 7. N_{bg} is the total number of events classified as BG, and N_{bg}^{pass} is the estimated number of BG events in the final BB event sample. Under each energy, the first line corresponds to the value of $f_{bg\to bb}$ estimated using empty bunch data at that energy; the second line to the average of $f_{bg\to bb}$ for the two energies. The last line under 630 GeV considers worst case values for all parameters.

the control sample misclassified as BB. The observed value of $dN_{ch}/d\eta$, ρ_{obs}, is given by:

$$\rho_{obs} = (1 - \epsilon_{bg})\rho + \epsilon_{bg}\rho_{bg} \tag{4.2}$$

where $\rho(\eta)$ is the true $dN_{ch}/d\eta$ distribution, ρ_{bg} the average η distribution in beam gas events, and ϵ_{bg} is the fraction of all events classified as BB which are actually BG. Inverting the equation, we obtain

$$\begin{aligned} \rho &= \rho_{obs}\left(\frac{1}{1-\epsilon_{bg}}\right)\left(1 - \epsilon_{bg}\frac{\rho_{bg}}{\rho_{obs}}\right) \\ &= \rho_{obs}C_{bg}, \end{aligned} \tag{4.3}$$

where the correction factor, C_{bg}, is defined as

$$C_{bg} = \left(\frac{1}{1-\epsilon_{bg}}\right)\left(1 - \epsilon_{bg}\frac{\rho_{bg}}{\rho_{obs}}\right). \tag{4.4}$$

Values for C_{bg} are compiled in table 9 under the various assumptions for the value of f_{bg}^{pass}, and therefore ϵ_{bg}. The correction is negligible in all scenarios.

We can also estimate the effect of BG background on the ratio of $dN_{ch}/d\eta$ at 1800 GeV to that at 630 GeV. Using equation 4.2, we obtain

$$\begin{aligned} \frac{\rho_{obs}^{1800}}{\rho_{obs}^{630}} &= \frac{(1-\epsilon_{bg}^{1800})\rho^{1800} + \epsilon_{bg}^{1800}\rho_{bg}}{(1-\epsilon_{bg}^{630})\rho^{630} + \epsilon_{bg}^{630}\rho_{bg}} \\ &\approx \frac{\rho^{1800}}{\rho^{630}}\left\{1 + \epsilon_{bg}^{630}\left(1 - \frac{\rho_{bg}}{\rho^{630}}\right) - \epsilon_{bg}^{1800}\left(1 - \frac{\rho_{bg}}{\rho^{1800}}\right)\right\} \\ &= \frac{\rho^{1800}}{\rho^{630}}(C_{bg}^{ratio})^{-1}, \end{aligned} \tag{4.5}$$

for small values of ϵ, where C_{bg}^{ratio} is the BG correction factor for the ratio. The values of the correction factor inverse tabulated in table 10 verify that the correction is negligible even under the worst case assumptions.

4.2.4 Loss of signal in event selection

A comparison of the vertex distribution for events classified as BG from the minimum bias sample to that expected on the basis of the BG control sample provides a useful

Table 9. Correction to $dN_{ch}/d\eta$ for the effect of beam-gas background.

f_{bg}^{pass}	ϵ_{bg}	C_{bg}
1800 GeV: $\frac{\rho_{bg}}{\rho_{obs}} \approx 0.5$		
0.0063±0.0019	0.0008±0.0002	1.00004
0.020±0.006	0.0025±0.0008	1.0013
630 GeV: $\frac{\rho_{bg}}{\rho_{obs}} \approx 0.67$		
0.0011±0.0005	0.0013±0.0006	1.0004
0.020±0.006	0.024±0.007	1.008

The first line under each energy uses the value of f_{bg}^{pass} estimated from empty bunch data at that energy; the second line uses the value obtained from the worst case assumptions (last line in table 8).

Table 10. Beam-gas correction factor for the ratio $\rho_{obs}^{1800}/\rho_{obs}^{630}$ (C_{bg}^{ratio}).

ϵ_{bg}^{630}	ϵ_{bg}^{1800}	$1 - (C_{bg}^{ratio})^{-1}$
0.0013±0.0006	0.0008±0.0002	3×10^{-5}
0.024±0.007	0.0025±0.0008	0.0067

The first line in the table shows the correction using values of ϵ_{bg} estimated from empty bunch data at each energy, while the second line shows the correction assuming worst case values.

check of the partial efficiency of the event selection procedure. To estimate the expected BG vertex distribution, we must add to the vertex distribution for bunches containing only protons (from the BG control sample) the vertex distribution for bunches containing only anti-protons. The latter distribution follows by assuming that the proton-only vertex distribution is the same as the anti-proton-only vertex distribution inverted about $z = 0$, and scaled by the ratio of anti-protons to protons in the machine.

Figure 37 shows a comparison of the vertex distribution for events classified as BG from the data, to that of the BG control sample plus the properly scaled anti-proton-only vertex distribution. A distinct difference in the shapes is observed near the center of the distributions. A difference distribution, obtained after renormalizing the expected $\bar{p}p$ BG vertex distribution to the value at the edges of the BG vertex distribution from the data, reveals a feature that is consistent with the shape of the vertex distribution for BB events (figure 38). These peaks are likely the result of mis-classification of BB events as BG. The curves in figure 38 correspond to the fits in figure 34 scaled by 0.105 for 1800 GeV, and 0.75 for 630 GeV.

In keeping with the philosophy of this analysis, we make no attempt to correct the absence of these unobserved events. We note only that the event selection algorithm fails to find 13±6% of the events which have measured vertices. Any further characterization of these events is not possible until they can be extracted from BG events.

4.3 Track selection

The VTPC reconstruction program finds many tracks which do not originate from the primary event vertex. We reduce the background from such tracks in the measured $dN_{ch}/d\eta$ distribution by requiring all tracks which contribute to the measurement to pass within a specified distance of the vertex. In order to eliminate

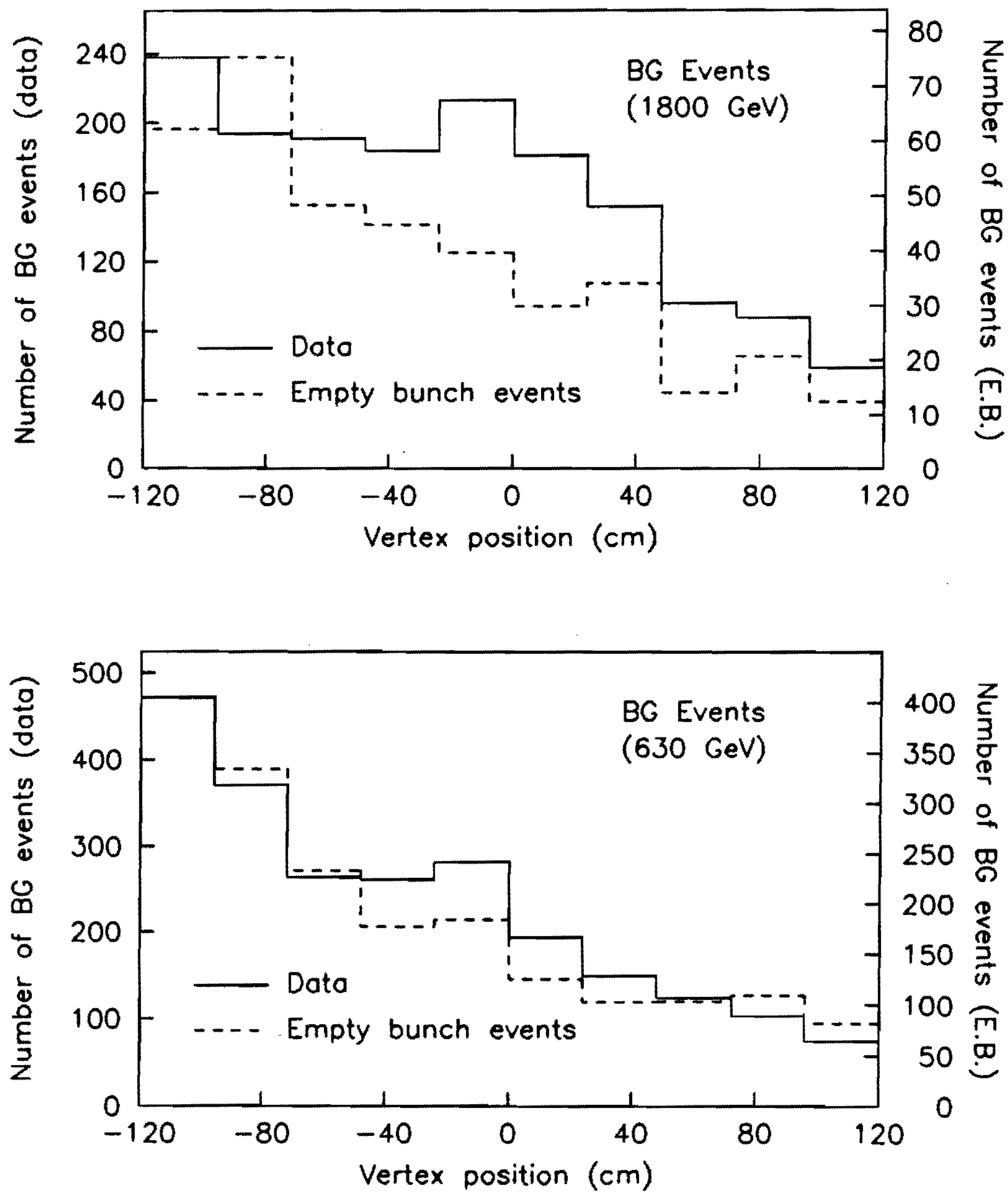

Figure 37. Comparison of vertex distributions for beam-gas events from data and empty bunch runs.

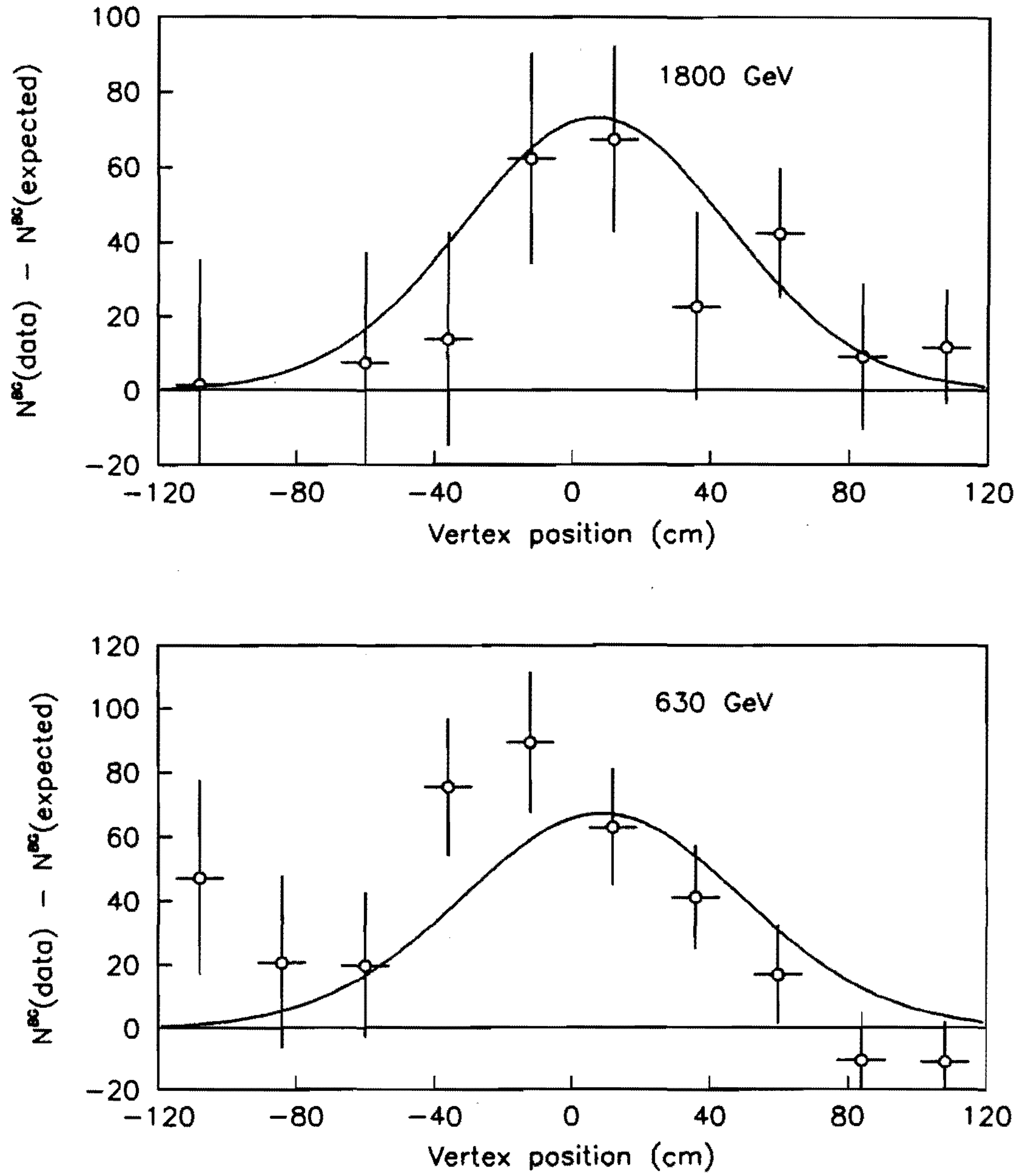

Figure 38. Deviation of beam-gas vertex distribution from expected distribution.

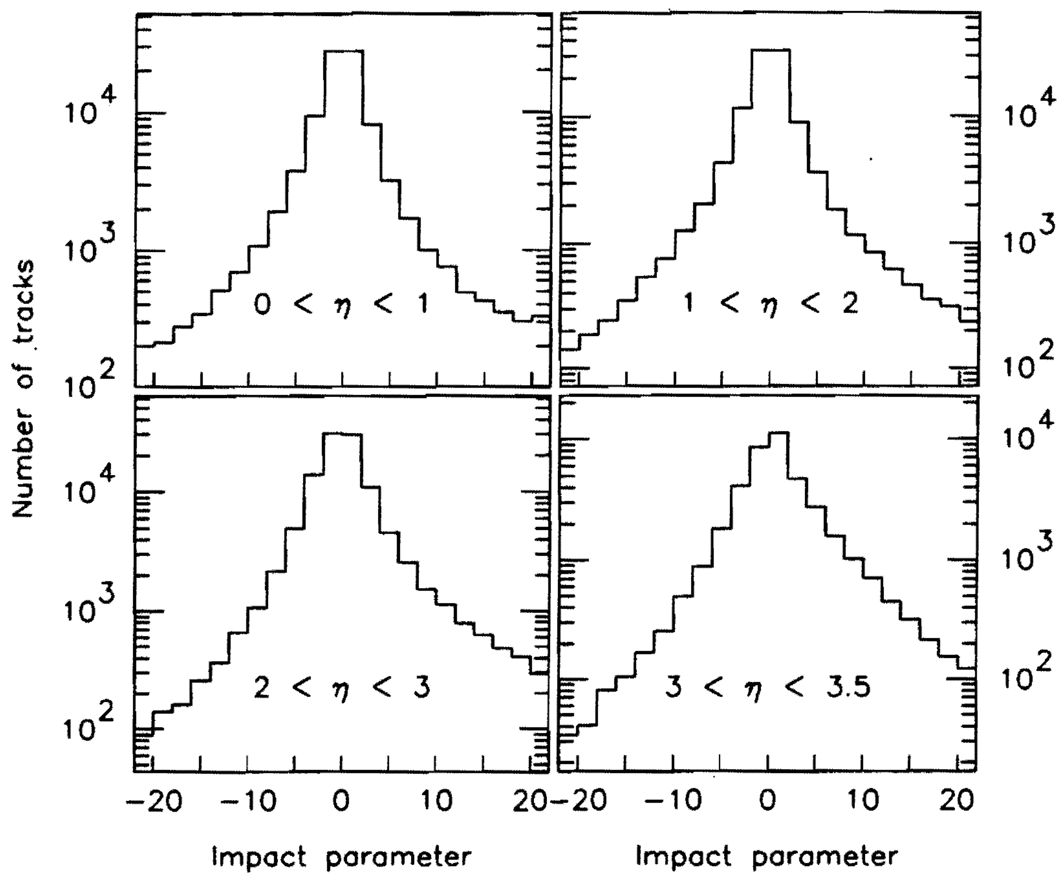

Figure 39. Impact parameter distribution within representative η slices. The plots show distribution for 1800 GeV data.

any angular dependence in this condition, we specify the cut in terms of the scaled impact parameter:

$$b = \frac{z_0 - z_v}{\sqrt{\sigma_{z_0}^2 + \sigma_{z_v}^2}}, \tag{4.6}$$

where z_0 is the intercept of the track with the beam axis calculated using de-weighted fits (see section 3.1.5), z_v is the vertex position from de-weighted fits, and σ_{z_0} and σ_{z_v} are the expected resolution of the track intercept and vertex position, respectively. The central peak of the impact parameter distribution (figure 39) is approximately independent of angle. The tails of the distribution, however, show significant angular dependence especially at small angles, although the relative number of tracks in the tails is less than 5%. In order to ensure that a very small fraction of primary tracks are lost to this cut, we demand that tracks have $|b| < 10$.

We also require that the trajectory of tracks traverse at least 11 of the 24 available wire layers in the chamber, thereby defining a fiducial volume in η for each event. Within the fiducial volume, the tracking efficiency is high and reasonably well measured. The η boundary of the fiducial volume must be carefully monitored on an event-by-event basis in order to establish the η acceptance of the chamber. Section 4.4 presents a detailed discussion of the acceptance measurement and related issues.

Figure 40 shows the raw angular distribution of tracks which satisfy the selection criteria, and the contribution of tracks found by each pass in the reconstruction. The value of η for tracks passing the selection criteria is obtained using the results of vertex-constrained fits (section 3.1.5).

Since the track selection inevitably admits some background, we must analyze all possible sources of background and subtract those tracks which pass the selection criteria. Section 4.5 contains a complete description of this calculation.

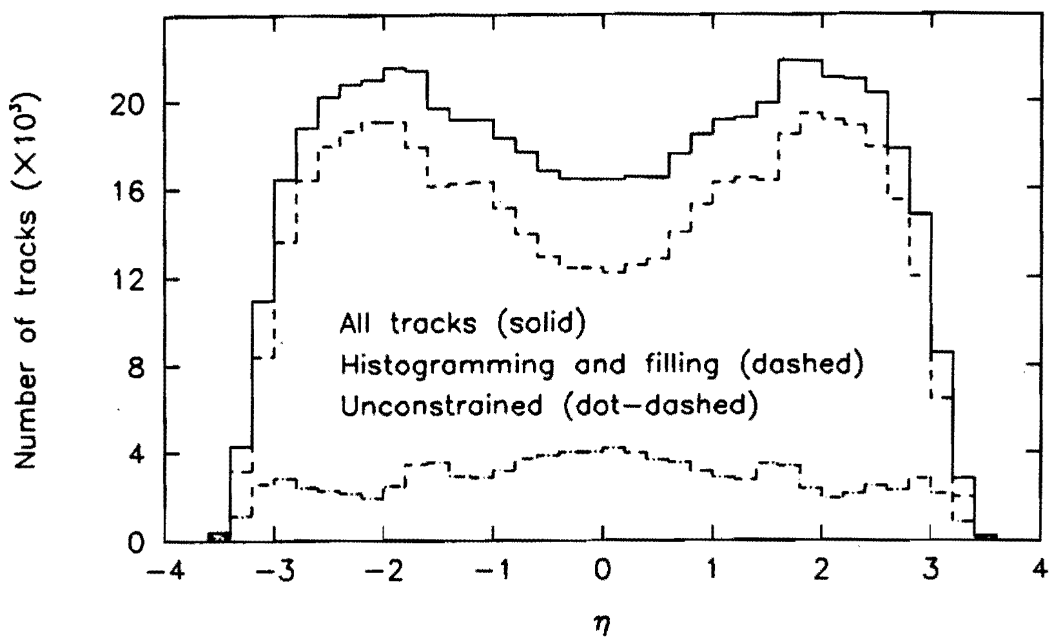

Figure 40. Raw angular distribution of tracks after track selection. Also plotted is the contribution to the total by tracks found by the first pass (histogramming followed by filling) and the second pass (unconstrained road following).

4.4 Corrections for geometrical acceptance

The acceptance of the VTPC for a given event is determined in part by fiducial cuts, and in part by chamber effects. In most cases, the acceptance is defined by lines approximately constant in polar angle (η) and azimuth (ϕ).

4.4.1 η acceptance

The region of the detector in which particle tracks will traverse 11 out of the 24 wire layers in the chamber defines the η fiducial volume. The η acceptance for a given event is unity within the fiducial volume, and zero outside. Figure 41 shows a plot of the average η acceptance for the 630 and 1800 GeV data samples.

After adjusting for the η acceptance, but before applying any other correction, we denote the η distribution as the "uncorrected" or "observed" η distribution (shown in fig. 42), $\rho_{obs}(\eta)$. We will now consider how mis-measurement of the η fiducial volume affects the acceptance correction.

4.4.1.1 Worst case estimate of uncertainty in η fiducial volume

Consider an event with a vertex located a distance z from the end of the chamber. Assume that σ_z is the precision to which this distance is known. If y denotes the distance from the beam axis to the 11th wire plane (i.e., to the boundary of the η fiducial volume), then we can write η in terms of measured quantities as:

$$\eta = -\frac{1}{2}\log\left(\frac{\sqrt{y^2+z^2}-z}{\sqrt{y^2+z^2}+z}\right).$$

Taking derivatives of this expression, we get:

$$\frac{d\eta}{dz} = \frac{1}{\sqrt{y_{fid}^2+z^2}}, \text{ and} \tag{4.7}$$

$$\frac{d\eta}{dy} = -\left(\frac{z}{y_{fid}}\right)\left(\frac{1}{\sqrt{y_{fid}^2+z^2}}\right). \tag{4.8}$$

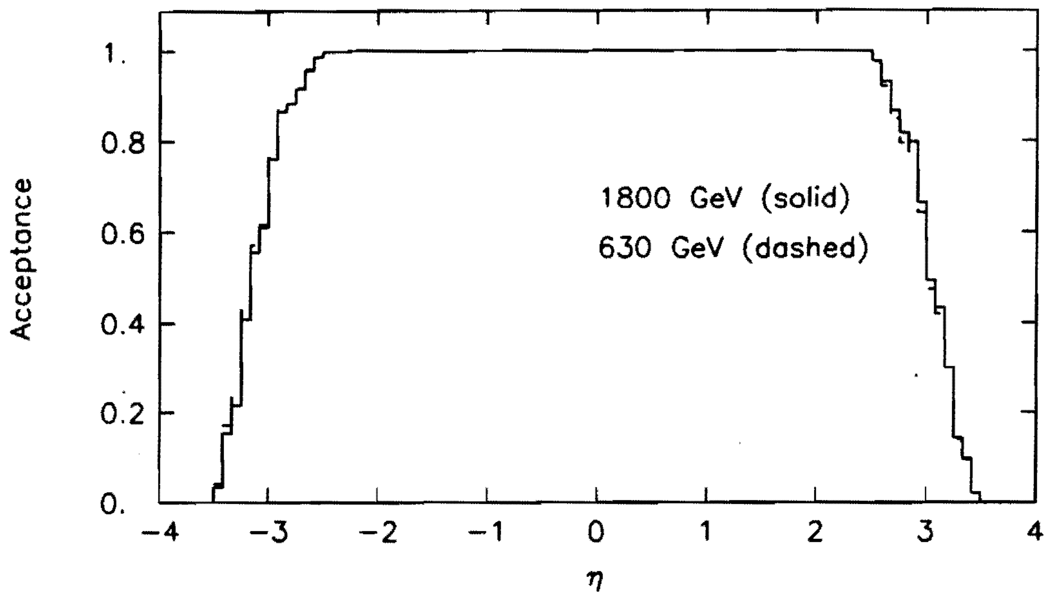

Figure 41. The average acceptance in η.

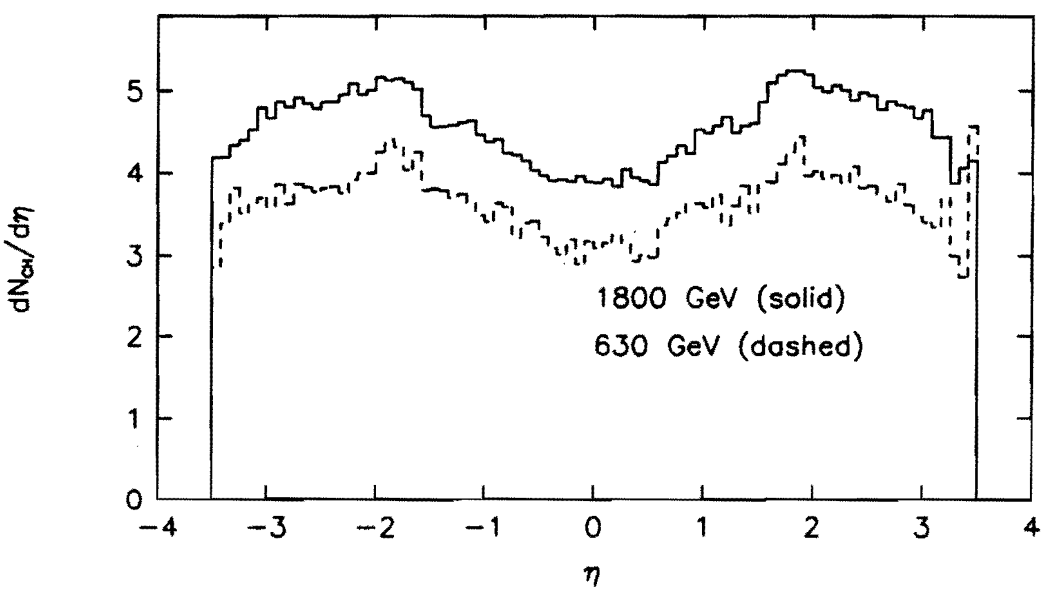

Figure 42. The observed $dN_{ch}/d\eta$ distribution (i.e., after application of η acceptance correction).

If we assume σ_y is the uncertainty in y, then we find that the assumed boundary of the fiducial volume is most sensitive to σ_z when z is small, and most sensitive to σ_y when z is large.

The 11th wire plane corresponds to a value for $y \approx 13$ cm, while cuts on the vertex position limit z within the range 88–200 cm. Using these values and assuming σ_z and $\sigma_y \approx 1$ cm to obtain worst case estimates of the uncertainty in the η fiducial volume, we find that $\sigma_\eta \approx 8 \times 10^{-2}$, dominated by the contribution from σ_y.

4.4.1.2 Effect of fiducial volume uncertainty on η acceptance correction

The effect of finite measurement resolution on a sample distribution is considered in Appendix G. In order to estimate the effect of smearing on the η acceptance, we must first identify the density function which the acceptance measurement is sampling ($\rho(\eta)$ in equation G.1 of Appendix G). To calculate the acceptance for a given event, we first measure the vertex position, then calculate the η boundary of the fiducial volume. Thus $\rho(\eta)$, the "acceptance density," must correspond to the distribution of η fiducial boundaries. We obtain the full acceptance curve (fig. 41) by integrating this acceptance density (fig. 43), provided we make an appropriate choice of sign for positive and negative η.

In table 11, we present the results of a comparison of the measured acceptance with that obtained by evaluating equation 3 using the measured acceptance density and several values of σ. If we take the difference between the measured acceptance before and after smearing as the magnitude of the systematic error in the η acceptance, then we obtain the errors quoted in the last column of table 11.

4.4.2 ϕ acceptance

Recall that the chamber gain is severely reduced within about 3 mm of octant boundaries causing a loss of efficiency for tracks which pass near these regions. We

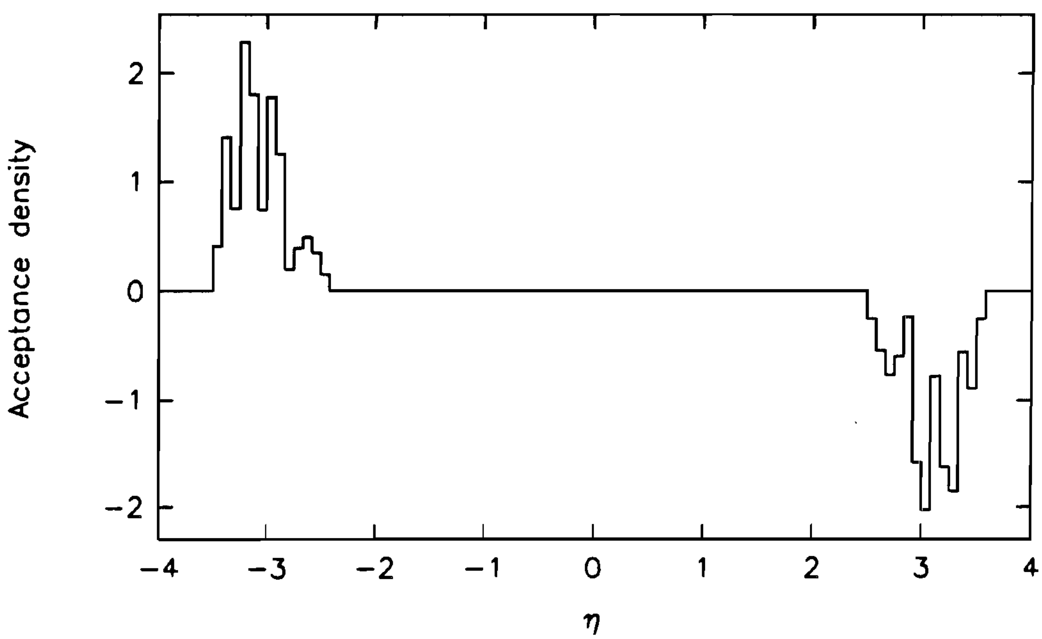

Figure 43. The acceptance density function in η. We obtain the function by differentiating the full acceptance curve. Within a factor of -1, the density is the distribution of η fiducial boundaries.

Table 11. Comparison of the measured acceptance with the smeared acceptance and the estimated systematic error resulting from smearing.

η range	Smeared acceptance			Measured accept.	Systematic error
	$\sigma = 0.1$	$\sigma = 0.075$	$\sigma = 0.05$		
0.00-0.25	1.000	1.000	1.000	1.000	0.00
0.25-0.50	1.000	1.000	1.000	1.000	0.00
0.50-0.75	1.000	1.000	1.000	1.000	0.00
0.75-1.00	1.000	1.000	1.000	1.000	0.00
1.00-1.25	1.000	1.000	1.000	1.000	0.00
1.25-1.50	1.000	1.000	1.000	1.000	0.00
1.50-1.75	1.000	1.000	1.000	1.000	0.00
1.75-2.00	1.000	1.000	1.000	1.000	0.00
2.00-2.25	0.999	0.999	1.000	1.000	0.00
2.25-2.50	0.996	0.998	0.999	0.999	0.00
2.50-2.75	0.936	0.939	0.940	0.941	0.01
2.75-3.00	0.780	0.787	0.793	0.801	0.02
3.00-3.25	0.464	0.465	0.466	0.467	0.00
3.25-3.50	0.135	0.126	0.119	0.109	0.02

Table 12. The azimuthal acceptance for high p_t tracks as a function of the number of hits required for a track to be observed (N_{min}), and the width of the dead region around radial boards (w).

	radius	Live fraction		
N_{min}	(cm)	$w = 2$ mm	$w = 3$ mm	$w = 4$ mm
24	6.74	0.924	0.887	0.849
14	12.94	0.961	0.941	0.921
8	16.66	0.969	0.954	0.939
6	17.90	0.972	0.957	0.943
4	19.14	0.973	0.960	0.947
2	20.38	0.975	0.963	0.950

can use this result to estimate the fraction of those tracks passing through a single module only which are lost within these insensitive regions.

The fraction of the azimuthal acceptance which is live is tabulated in table 12 assuming the dead region near octant boundaries is 2 mm, 3 mm, or 4 mm wide (on either side of the boundary). The left column indicates the minimum number of wires which must be traversed in order for a high p_t track to found.

Track curvature complicates this analysis since the minimum number of wires a track traverses for a given width of the dead region is a function of the p_t of the track. Assuming a width of 3 mm, a track with $p_t = 470$ MeV/c will cross about four wires when aligned such that it just grazes one boundary of the insensitive region. Approximately half of the p_t spectrum lies above this value. If we assume that the minimum number of wires is between four (corresponding to the minimum number of hits required for a track to be considered in the efficiency measurement) and 10, and assume that only half of the tracks are affected (corresponding to those with

p_t below about 470 GeV/c), then we obtain the value 0.97±0.02 for the azimuthal acceptance.

This result applies only to tracks which traverse a single VTPC module. Tracks which traverse more than one module must enter the sensitive volume of at least one of the modules. For each value of η, we average the azimuthal acceptance over the event vertex position, weighting the value quoted in the previous paragraph by the fraction of tracks which should traverse exactly one module. The results are tabulated in table 13.

Table 13. Azimuthal acceptance (averaged over event vertex position) as a function of η.

η range	Average acceptance	η range	Average acceptance
0.00-0.25	0.97±0.02	1.00-1.25	0.98±0.02
0.25-0.50	0.97±0.02	1.25-1.50	0.99±0.02
0.50-0.75	0.98±0.02	1.50-1.75	0.99±0.02
0.75-1.00	0.99±0.02	1.75-3.50	1.00

4.5 Charged particle background to $\frac{dN_{ch}}{d\eta}$

Charged particle multiplicity measurements are subject to several sources of background. Particles produced in the primary interaction may interact with the mechanical structures of the detector thereby generating charged secondaries which cannot be distinguished from primary particles. Particle decays which change the number of charged particles in the final state represent a second, distinct source of background. In this section, we outline the procedures used to estimate and subtract the dominant sources of background to the $dN_{ch}/d\eta$ measurement.

4.5.1 Subtracting background from $\frac{dN_{ch}}{d\eta}$

Before considering individual sources of background, we will discuss the general problem of subtracting a background distribution from the observed $dN_{ch}/d\eta$ distribution. (A more detailed solution of this problem is presented in Appendix H.1.) Define $\rho_i(\alpha, z)$ as the density of particle species 'i' with respect to the set of variables α, and the event vertex position, z. In the subsequent discussion, primed variables will refer to quantities relating to primary products of $\bar{p}p$ collisions. Thus $\rho_i(\eta', p_t')$ denotes the joint density of primary particle species 'i' in η and p_t, $\frac{d^2N_i}{d\eta' dp_t'}$.

Now consider a process by which particle species 'i', produced with joint density $\rho(\eta', p_t')$, gives rise to charged secondaries. We wish to calculate $\rho_B^i(\eta)$, the η density of these secondary particles which will contribute to $\rho_{obs}(\eta)$, the observed η distribution. The calculation in Appendix H.1 demonstrates that for each value of η, this problem reduces to an integral over η' of the density of primaries of type 'i' into η', the probability that secondary production occurs, and the density of secondaries into η which pass track selection, produced by primaries at η'. We write this as

$$\rho_B^i(\eta, z) = \int d\eta' \, \rho_i(\eta') P(\eta', z) \rho_s^i(\eta; \eta', z), \tag{4.9}$$

where $P(\eta', z)$ is defined as the average probability that the production mechanism occurs for a primary into η' originating from an event vertex at z; and $\rho_s^i(\eta; \eta', z)$ as the density of secondaries which pass track selection at η, produced by a primary originating at z into η'. The distributions ρ_B^i and ρ_i are defined as before, except that we have added a z dependence to ρ_B^i. This z dependence arises because P and ρ_s^i may depend upon the chamber geometry. If $\mathcal{A}(\eta, z)$ denotes the average chamber acceptance in η, then the average η distribution of secondaries which pass track selection, and therefore contribute to $\rho_{\mathrm{obs}}(\eta)$, is

$$\rho_B^i(\eta) = \int dz\, P_v(z) \mathcal{A}(\eta, z) \rho_B^i(\eta, z), \tag{4.10}$$

where $P_v(z)$ = the vertex distribution in the event sample. In order to subtract background, we must obtain estimates for the distributions in equation 4.9: $\rho_i(\eta')$, the distribution of the relevant primary particles species; $\rho_s^i(\eta; \eta', z)$, the distribution of secondaries passing track selection, produced by the particular mechanism; and $P(\eta', z)$, the probability that the production mechanism occurs for a primary into η' originating from z.

4.5.2 Background from photon conversions

4.5.2.1 Background distribution and correction factor

For the case of photon conversions, the probability that a photon conversion occurs depends upon the photon conversion cross section and the distribution of material along the photon trajectory. In particular, $P(\eta', z)$ is given by the average number of radiation lengths traversed at a given η'. Assume also that for all relevant energies,

$$\rho_s^\gamma(\eta; \eta', z) = N_e(\eta, z)\delta(\eta - \eta'),$$

where N_e = the effective number of electrons per conversion which can contribute to background (ie., pass track selection). From equation 4.9, this yields the background distribution

$$\begin{aligned} \rho_B^\gamma(\eta, z) &= \int d\eta'\, \rho_\gamma(\eta') P(\eta', z) N_e(\eta, z) \delta(\eta - \eta') \\ &= \rho_\gamma(\eta) P(\eta, z) N_e(\eta, z). \end{aligned} \tag{4.11}$$

Assuming that $\rho_\gamma(\eta)$, the photon η distribution, is proportional to $\rho_{ch}(\eta)$, the charged particle η distribution [36,70], we can rewrite equation 4.11 as:

$$\rho_B^\gamma(\eta, z) = \rho_{ch}(\eta) f_\gamma P(\eta, z) N_e(\eta, z),$$

where $f_\gamma = \langle N_\gamma \rangle / \langle N_{ch} \rangle$, the ratio of the mean photon multiplicity to the mean charged particle multiplicity. If we then assume that the tracking efficiency is nearly one, we get:

$$\rho_{obs}(\eta, z) = \rho_{ch}(\eta) + f_\gamma N_e(\eta, z) \rho_{ch}(\eta) P(\eta, z),$$

or, rearranging,

$$\begin{aligned} \rho_{ch}(\eta, z) &= \frac{\rho_{obs}(\eta, z)}{1 + f_\gamma P(\eta, z) N_e(\eta, z)} \\ &= \rho_{obs}(\eta, z) C_\gamma(\eta, z), \end{aligned} \tag{4.12}$$

where $C_\gamma(\eta, z)$, the correction for photon conversions, is defined as

$$C_\gamma(\eta, z) = \frac{1}{1 + f_\gamma P(\eta, z) N_e(\eta, z)}. \tag{4.13}$$

4.5.2.2 Estimatation of correction factor

A geometric argument allows calculation of N_e as a function of η and z. Consider the helical trajectory of an electron projected onto a plane rotated by an angle ϕ in azimuth with respect to the initial direction of the electron. For simplicity, the electron is assumed to originate from the beam axis. The plane, in this case, represents the mid-plane of an octant, while the projection approximates the track that would be reconstructed in that octant. The octant mid-plane is rotated by ϕ with respect to the original electron direction.

In general, if both electrons from a photon conversion traverse a single octant only, they will not be resolved as two particles because both are produced at the same η.[1] Therefore, the number of tracks which actually contribute to ρ_{ch} will

[1] If the momenta are greatly different, then the projections of the tracks onto the octant mid-plane *will* separate with increasing radius. As this occurs, however, one of the reconstructed tracks will point increasingly farther away from the vertex.

depend upon the information observed not only in the octant in which the conversion originally occurrs, but also in the two adjacent octants. Since the reconstruction program follows low p_t tracks across octant boundaries, only in certain cases will the combination of information from these three octants result in the identification of two independent tracks. The tracks must also satisfy the track selection criteria in order to contaminate the final η distribution.

To arrive at the effective number of electrons per conversion, we average over the relevant initial photon momenta the frequency at which zero, one or two tracks contribute to background. The shape of the photon p_t distribution (figure 44) is derived assuming all photons originate from π^0's[2] produced with a p_t spectrum proportional to the charged particle inclusive p_t spectrum. For simplicity, we approximate the charged particle p_t spectrum by exponential distributions.

To estimate $P(\eta, z)$, we simulate photons traversing material distributed in position and composition approximating the actual detector. The majority of mass in the chamber is concentrated in the field cages and cathode planes of the detector as well as in the beam pipe. The conversion probability is defined as the fraction of photons which convert within a specified fiducial volume[3] corresponding to the detector volume in which conversion pairs produce sufficient information to be reconstructed. Figure 45 presents the conversion probability, $P(\eta, z)$, for different slices in the simulated vertex position. The probability averaged over a Gaussian distributed vertex position centered at the middle of the detector with a standard deviation of 35 cm (figure 45) is also indicated. The plot reveals no significant z dependence of the conversion probability. For comparison, the assumed thickness

[2]Results from UA5 on inclusive photon production [36,70] suggest that other sources for photons are also present. Because the correction is relatively insensitive to the photon p_t spectrum (see Section 1), this is not a serious concern.

[3]For this and subsequent background calculations, the fiducial volume extends outward to the 20^{th} wire from the beam axis, and longitudinally to the center screen of the end modules.

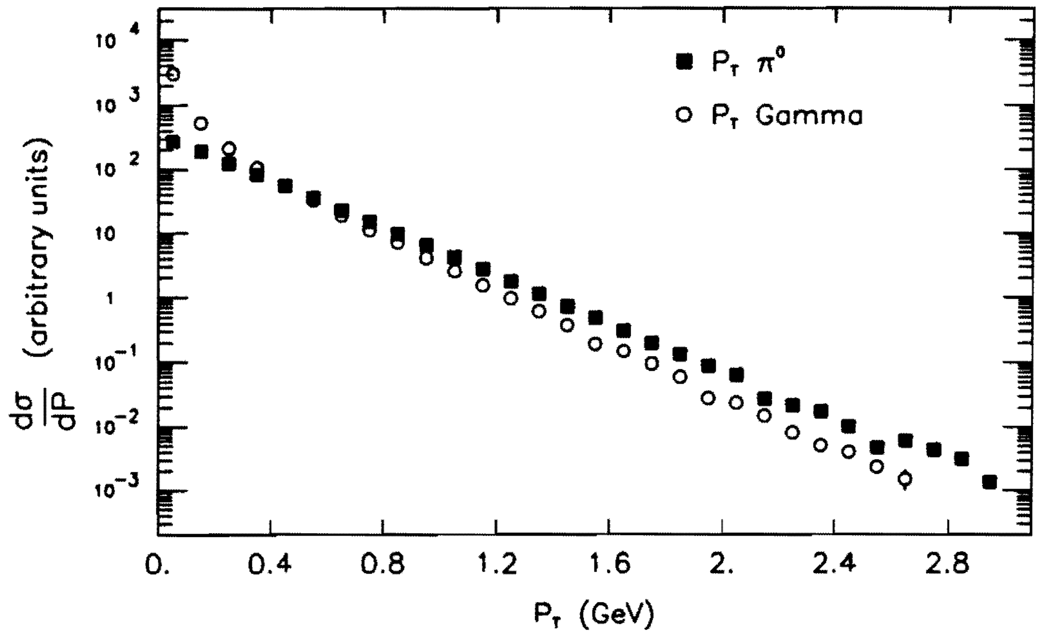

Figure 44. Assumed π^0 and photon p_t distribution used to study the photon conversion background at 1800 GeV. The π^0 spectrum is an exponential with exponential coefficient of -4.3 GeV^{-1}.

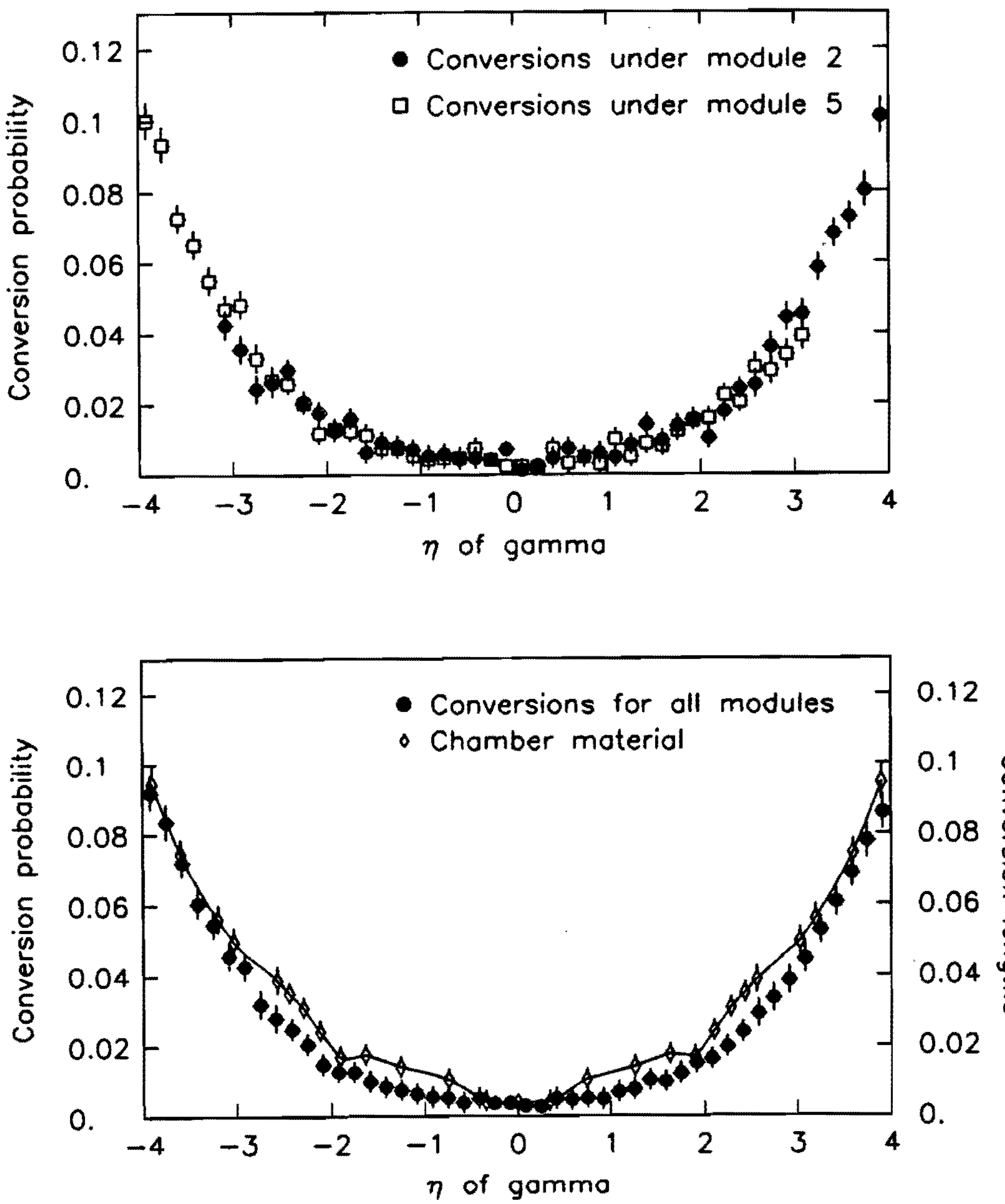

Figure 45. Photon conversion probability vs. η. The upper plot shows the conversion probability for vertices located within ± 12 cm of the center of the indicated modules. The lower plot shows the conversion probability averaged over vertex positions (within ± 12 cm of the center of the nearest module) calculated by the simulation, along with an independent calculation of the amount of material traversed by the average particle before leaving the fiducial volume of the detector.

of material (in conversion lengths) along a typical trajectory into the center of the active volume of the VTPC is also provided (figure 45).

To obtain an estimate for f_γ we appeal to an extrapolation from lower energy data on inclusive photon production. Figure 46 displays the average photon multiplicity obtained in inelastic pp and $\bar{p}$p collisions at lower CM energies. The UA5 collaboration measured the average photon multiplicity for non-single diffractive $\bar{p}$p collisions at $\sqrt{s} = 546$ GeV [36,70], and using Monte Carlo data, estimated a result for all inelastic collisions consistent with extrapolations from lower energies. We estimate the average photon yield for our data by extrapolating this lower energy result and using the same ratio between the inelastic and non-single diffractive yields as estimated by UA5. The result assumed for this analysis is $f_\gamma = 1.0 \pm 0.2$.

Collecting all these factors yields the correction factor, C_γ, for photon conversions depicted in figure 47. The correction for 630 GeV is slightly different owing to the small difference in the inclusive p_t spectrum of π^0's, and therefore, in the effective number of electrons per conversion.

4.5.2.3 Estimation of uncertainty in C_γ

Uncertainties in C_γ contribute to the systematic uncertainty in $dN_{ch}/d\eta$. Uncertainty in the values of C_γ, in turn, results from the uncertainty in the validity of the assumptions used to model the detector. The stability of C_γ relative to these assumptions defines the confidence interval of C_γ. The uncertainties plotted in figure 47 reflect the following considerations of the model:

1. Photon p_t spectrum — The photon p_t distribution affects the average number of electrons per conversion which contribute to background (N_e), although only mildly. Figure 48 shows N_e for two widely different values of the exponential coefficient used to approximate the p_t spectrum. A factor of 1.5 in the exponential results in an 8% change in N_e, and therefore, a less than 8% change in C_γ.

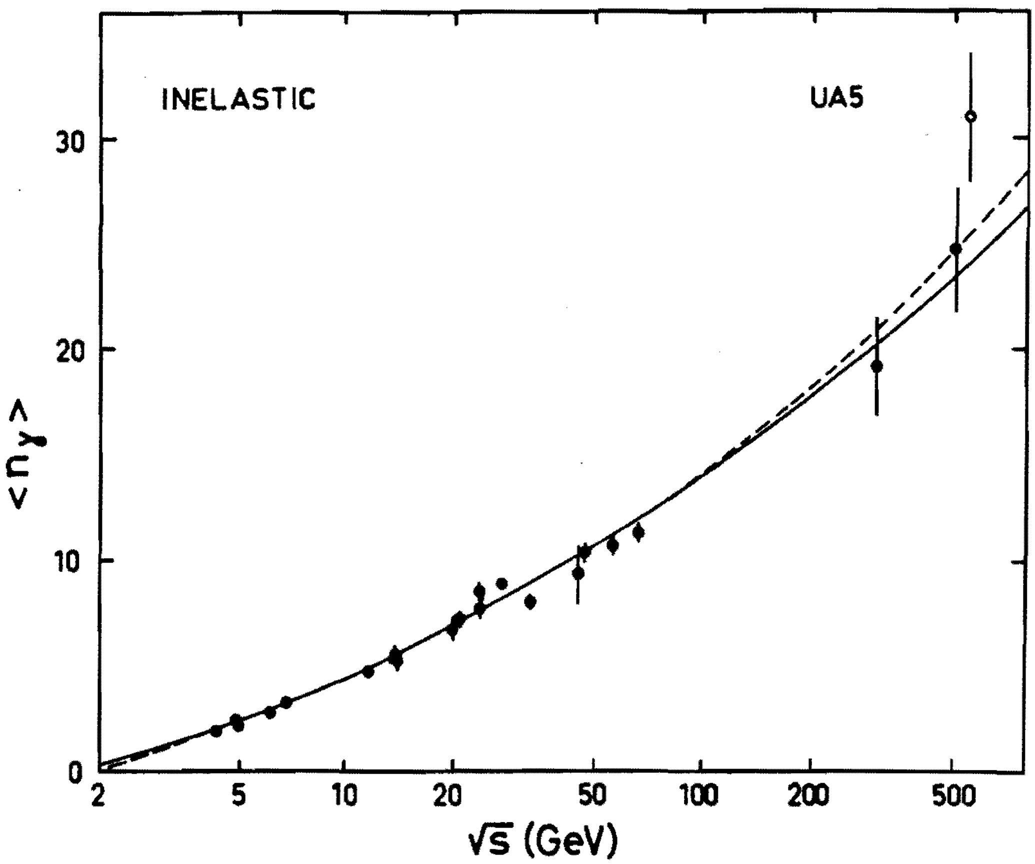

Figure 46. Inclusive photon multiplicities as a function of $\sqrt{s}$ for pp and $\bar{\mathrm{p}}$p collisions (from ref. [36]).

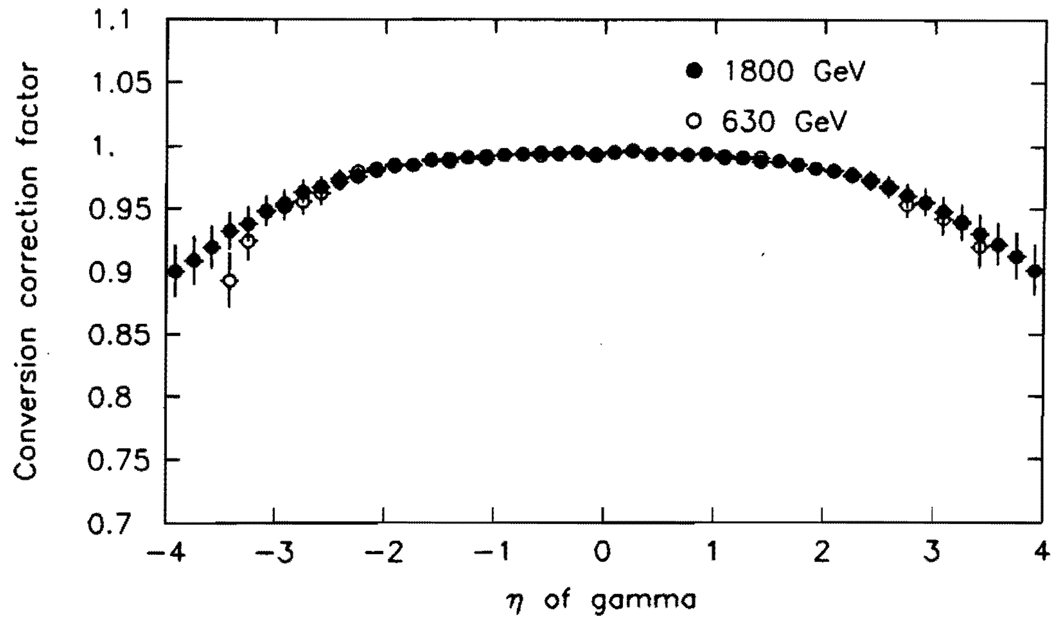

Figure 47. Photon conversion correction factor (C_γ) vs. η.

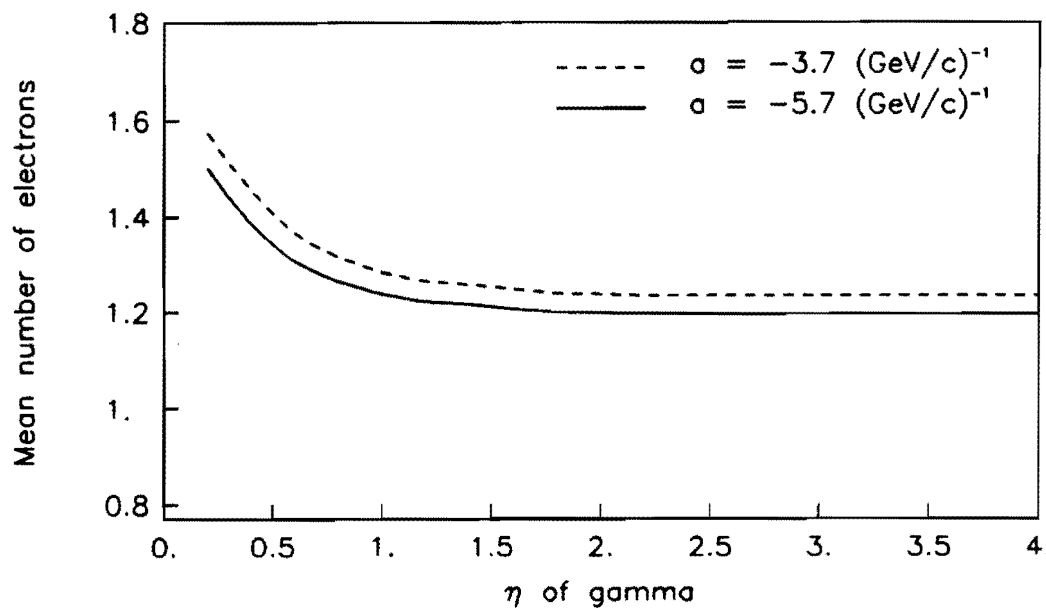

Figure 48. The effect of the photon p_t spectrum on the effective number of electrons per conversion. The curves represent the mean effective number of electrons vs. the η of the photon for two significantly different exponential slopes for the p_t spectrum.

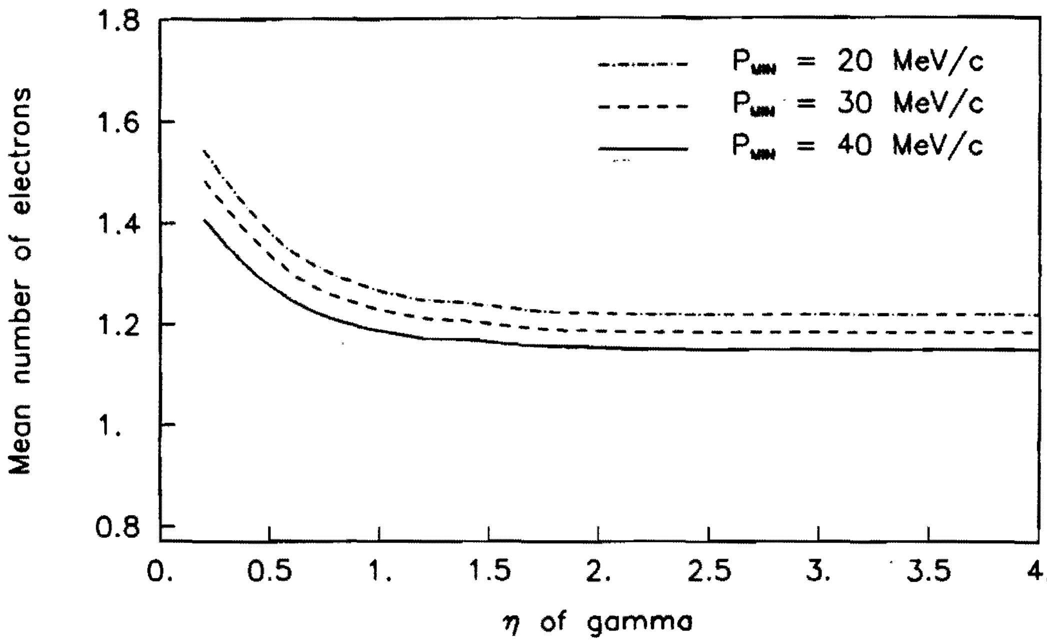

Figure 49. The effect of $p_{t_{\min}}$ on the effective number of electrons per conversion. The curves represent the mean effective number of electrons vs. the η of the photon for different values of $p_{t_{\min}}$.

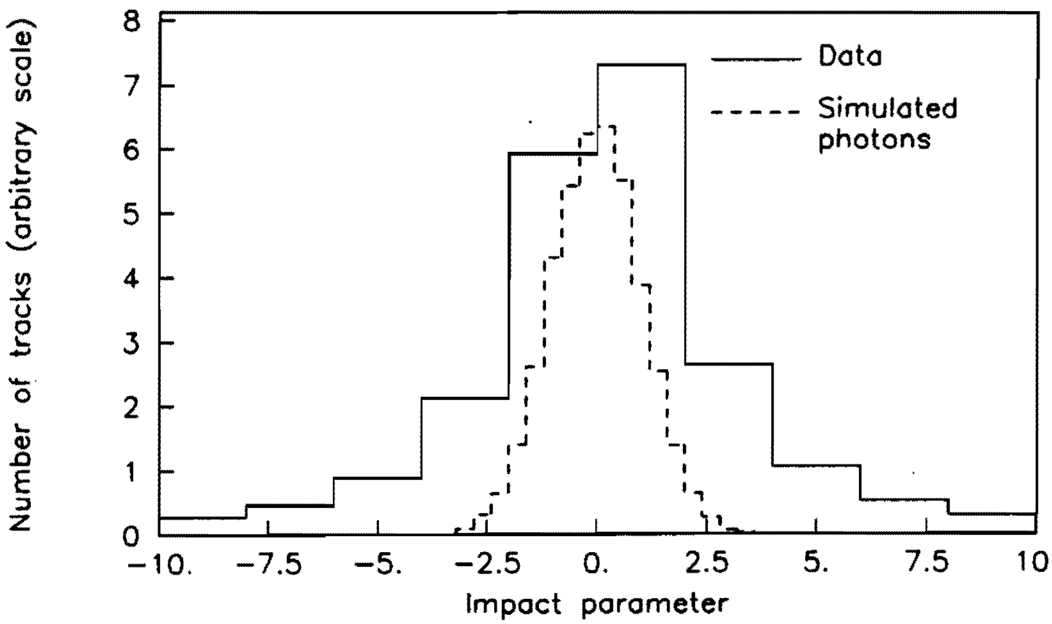

Figure 50. Simulated impact parameter distribution for tracks from conversion electrons. The plot also shows the same distribution for the 1800 GeV minimum bias data. (The small offset in the distribution for minimum bias data is an artifact of binning.)

2. p_t cutoff — As discussed in the previous section, the reconstruction efficiency for single tracks falls precipitously to zero between 50 MeV/c and 20 MeV/c. The calculations for C_γ assume a sharp cutoff in the reconstruction efficiency at a transverse momentum of $p_{t_{min}}$. The variation in N_e for values of $p_{t_{min}}$ within this range are plotted in figure 49. Allowing $p_{t_{min}}$ to vary between 20 MeV/c and 40 MeV/c results in less than 10% variation in the resulting value of C_γ.

3. Track selection — Figure 50 compares the impact parameter distributions for simulated conversion electrons to that of 1800 GeV minimum bias data. Although the simulated impact parameter distribution is not well modelled, the electron tracks clearly point almost directly back at the vertex. It is therefore reasonable to assume that the impact parameter distribution for conversion electrons is the same as that for normal tracks. Since the large majority of tracks are concentrated within the impact parameter cut used during track selection, we expect that the conversion correction will be stable against small changes in this cut.

4. Z vertex dependence — In the upper plot of fig. 45, we observe a small but systematic variation in the total material a photon traverses before escaping the detector fiducial volume as a function of the vertex position. As a result, there exists a small, systematic variation in the conversion correction as a function of the event vertex position. From the curves in fig. 45, we deduce that the variation in C_γ over the length of the chamber is only of order 1%, and therefore define the final correction as the value of C_γ averaged over z. The differences in the correction values as a function of the vertex position enter into the systematic uncertainty.

5. Fiducial volume — Since the great majority of photon conversions occur in the beam-pipe, inner field cage, or proportional chambers, the conversion probability is relatively insensitive to the choice of outer radius. A difference of up

to 3% at $\eta = 4$ is observed for 35 cm changes in the z boundary of the fiducial volume. The η regions most greatly affected, however, lie mostly beyond the range of the measurements presented here.

4.5.3 Background from K^0 decay

The analysis of background from decays of neutral kaons is complicated by the fact that, unlike the case for photon conversion, $\rho_s^{K^0}$ does not simplify to a δ-function. We estimate this distribution with a Monte Carlo simulation of K^0's traversing the chamber. The angle between each secondary and the K^0 is calculated for every decay within the fiducial volume. The point at which the secondary exits the fiducial volume is then calculated assuming a straight line trajectory for the secondary. The linear trajectory is projected onto the mid-plane of the octant in which the particle exits the detector. This projection provides values of η and z_0 for the reconstructed track. The resulting impact parameter (used for track selection) is smeared assuming the resolution of the detector. Although the linear trajectory assumption is not strictly true (especially for $p_t < 150$ MeV/c), its usage does not significantly change the result (since the correction is small). It does, however, simplify the necessary calculations.

We obtain the background distribution by integrating equation 4.9 over η' where the functions in the integrand are estimated from Monte Carlo distributions. The $\rho_{K^0}(\eta)$ distribution is normalized using measurements of the K_s rapidity distribution (dN/dy) at a rapidity of zero $(y = 0)$ performed by CDF at 1800 GeV [71], and by UA5 at various energies up to 546 GeV [72]. We use $\rho_{K^0}(\eta = 0) = 0.26 \pm 0.03$ at 1800 GeV. The UA5 measurements are extrapolated from 546 GeV to 630 GeV using a fit to the UA5 data quoted in reference [72], and the mean number of K_s particles produced within $|\eta| < 2.5$. We obtain $(dN_{K_s}/dy)_{y=0} = 0.146 \pm 0.012$ at 630 GeV.

The calculated background distributions, plotted in fig. 51 for 630 GeV and

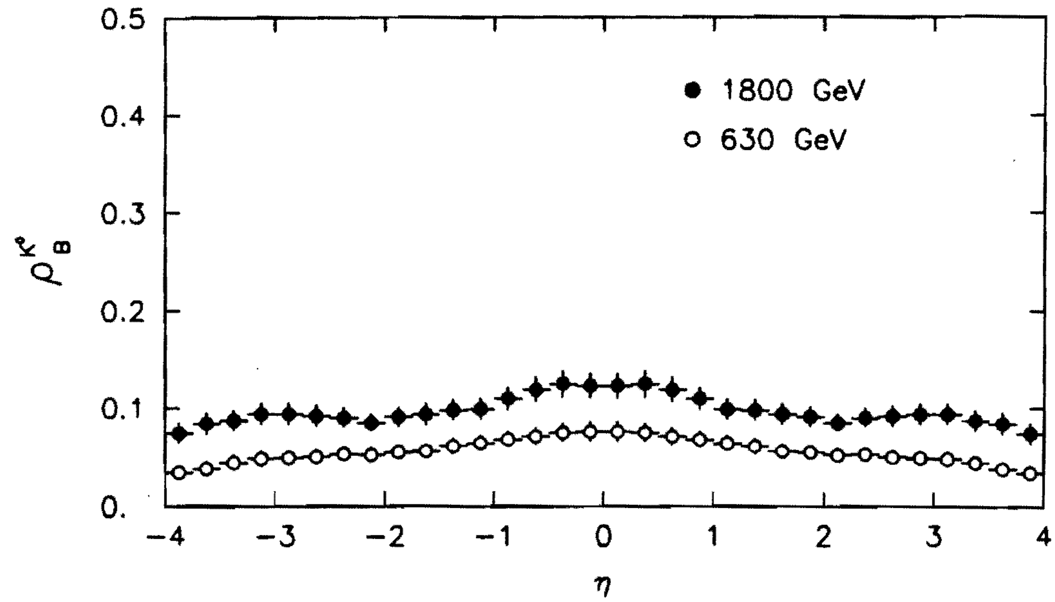

Figure 51. Contribution to $dN_{ch}/d\eta$ from K^0 decays ($\rho_B^{K^0}$).

1800 GeV, represent a correction of between 2–3% over the entire η range. This result is consistent with the upper bound found in Table 14 which assumes a worst case analysis. The uncertainties in fig. 51 represent the statistics in the simulation, as well as the sensitivity to model parameters, estimated using calculations similar to those described for C_γ.

4.5.4 Background from hadronic interactions

Like decays of K^0's, hadronic interactions produce charged secondaries at large angles compared to the incident particle direction. Thus, the background subtraction procedure is identical to that used for K^0 decays. The ρ_s^{had} distribution is estimated by simulating charged pions which traverse the material of the detector. We calculate the probability of interaction, $P(\eta, z)$, by summing the contributions to the nuclear interaction length of all materials traversed along various trajectories. Assuming a uniform vertex distribution under each individual module, the average interaction probability is obtained by weighting the module averages by the values of a Gaussian distribution (mean = 0, σ = 35 cm) sampled at the module centers (figure 52). Although the probability of interaction is not insignificant, very few of the resulting tracks pass track selection, leading to a (negligible) background distribution of less than 0.5% (figure 53). The correction to compensate for losses of primaries due to nuclear interactions is less than 1% for $|\eta| < 2$, and less than 3% for $|\eta < 3.5$.

4.5.5 Other decays

Several other potential decay sources of charged particle background exist, namely decays of Σ^0, Λ, Ξ^0, and π^0 Dalitz decays, in addition to charged mode decays of charged K's, Ξ, and Σ particles. Table 14 contains worst case calculations for all these sources assuming production ratios as measured by UA5 at 546 GeV [36]. Only Dalitz decays warrant inclusion as a correction.

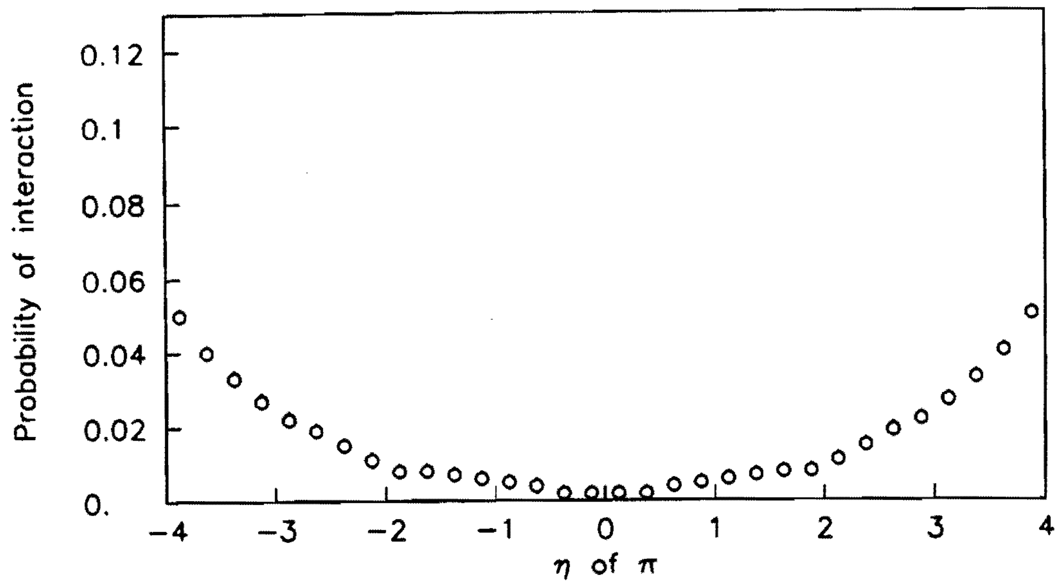

Figure 52. Probability of secondary hadronic interaction vs. η. The simulation averages over vertex position.

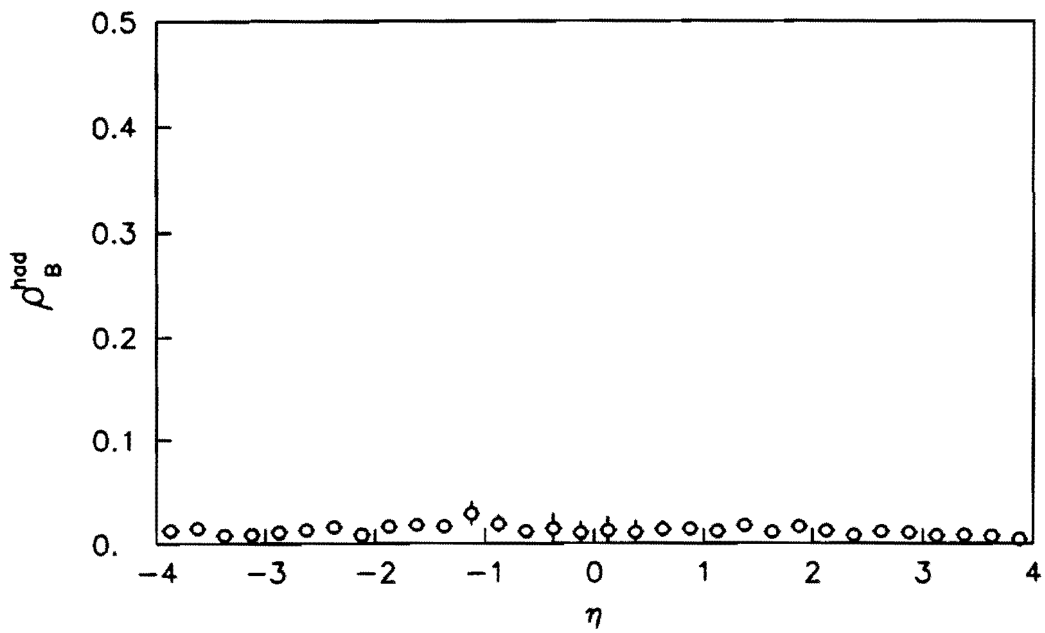

Figure 53. Contribution to $dN_{ch}/d\eta$ from secondary hadronic interactions (ρ_B^{had}). The same distribution is used for 630 GeV.

Table 14. Worst case analyses of background from particle decays.

Decay	B.R.	Prod. ratio	$c\tau$ (cm)	Active decays (%)	Backgnd limit (%)
$K_S \rightarrow \pi^+\pi^-$	0.686	0.04	2.7	100	4.8
$K_L \rightarrow \pi^+\pi^-\pi^0$	0.124				
$\pi^\pm\mu^\mp\nu$	0.271	0.04	1550	10	0.7
$\pi^\pm e^\mp\nu$	0.387				
$\Sigma^0 \rightarrow \Lambda\gamma$ and	1.00	0.19	7.9	100	2.6
$\Lambda \rightarrow p\pi^-$	0.64				
$\pi^0 \rightarrow e^+e^-\gamma$	0.012	0.39	—	100	1.0
$\Xi^0 \rightarrow \Lambda\pi^0$	1.00	0.004	8.7	100	0.4
$\hookrightarrow p\pi^-$	0.64				
$\Xi^- \rightarrow \Lambda\pi^-$	1.00	0.01	4.9	100	0.4
$\hookrightarrow p\pi^-$	0.64				
$K^\pm \rightarrow \pi^\pm\pi^\pm\pi^\mp$	0.056	0.079	371	10	0.16

We consider only those particles for which production yields are measured at SPS energies. For charged particles, only those decay modes which change the number of charged particles in the final state need be considered. In all cases, the analysis includes both particles and antiparticles. In the table, "B.R." refers to branching ratio; "production ratio" to the ratio of average multiplicity for the particular species to the average charged multiplicity; "active decays" denotes the fraction of decays estimated to occur within the fiducial volume of the detector; "background limit" is quoted as the ratio (in %) of background tracks to average charged multiplicity. We have assumed that the η distributions are proportional to the average charged particle η distributions.

Although the limit on background introduced by Λ and Σ^0 decays appears comparable to that estimated for K^0 decays, it should be noted that the difference between the upper limit and the estimates based upon simulation results is approximately a factor of two. Since the decay kinematics and lifetimes of K^0's and Λ's are on the same order of magnitude, it seems reasonable that a similar factor of two lies between the upper limit and estimated background for the latter. On this basis, we have decided to neglect this source of background in the simulation studies.

4.5.6 Summary of background to $\frac{dN_{ch}}{d\eta}$

Of potential sources for background to $dN_{ch}/d\eta$, only electrons from photon conversions, charged mode decays of neutral kaons, and small contributions from Dalitz decays contribute significantly to the observed $dN_{ch}/d\eta$ distribution.

1. We estimate photon conversions to contribute a background of 1% near $|\eta| = 0$, 6% at $|\eta| = 3$ and about 10% for $|\eta| > 3.5$ (fig. 47 and table 15).
2. Neutral kaon decays contribute between 2–3% over the entire η acceptance (fig. 51 and table 15).
3. Dalitz decays contribute about 1% (table 14) .
4. Secondary hadronic interactions contribute less than 0.5% in background from secondaries (fig. 53 and table 15); a correction of 1%–3%, however, is required to compensate for losses of primaries to secondary interactions (table 15).

Table 15. Distributions or correction factors for all significant sources of background, and losses due to secondary hadronic interactions.

η range	C_γ	$\rho_B^{K^0}$ 1800 GeV	$\rho_B^{K^0}$ 630 GeV	ρ_B^{had}	ρ_{loss}^{had}
0.00–0.25	0.996±0.003	0.123±0.013	0.076±0.010	0.012±0.013	0.002±0.002
0.25–0.50	0.996±0.004	0.125±0.014	0.075±0.009	0.012±0.011	0.002±0.002
0.50–0.75	0.996±0.004	0.119±0.013	0.071±0.009	0.013±0.007	0.004±0.002
0.75–1.00	0.994±0.004	0.110±0.012	0.068±0.008	0.017±0.006	0.005±0.002
1.00–1.25	0.993±0.004	0.099±0.011	0.064±0.008	0.021±0.005	0.006±0.002
1.25–1.50	0.991±0.004	0.098±0.011	0.061±0.008	0.017±0.006	0.007±0.002
1.50–1.75	0.989±0.004	0.094±0.011	0.056±0.007	0.015±0.003	0.008±0.002
1.75–2.00	0.986±0.005	0.091±0.010	0.055±0.007	0.017±0.005	0.008±0.002
2.00–2.25	0.981±0.005	0.085±0.009	0.052±0.007	0.010±0.003	0.011±0.002
2.25–2.50	0.972±0.007	0.090±0.010	0.053±0.007	0.012±0.002	0.015±0.002
2.50–2.75	0.967±0.009	0.092±0.011	0.050±0.007	0.012±0.002	0.019±0.002
2.57–3.00	0.956±0.010	0.094±0.011	0.049±0.007	0.011±0.002	0.022±0.002
3.00–3.25	0.947±0.013	0.094±0.011	0.048±0.008	0.008±0.001	0.027±0.002
3.25–3.50	0.934±0.014	0.087±0.011	0.044±0.007	0.008±0.001	0.033±0.002
3.50–3.75	0.917±0.017	0.084±0.011	0.038±0.007	0.011±0.001	0.040±0.002
3.75–4.00	0.904±0.021	0.074±0.011	0.034±0.007	0.008±0.001	0.050±0.002

4.6 Other systematic checks and uncertainties

Two additional effects which need to be explored are the sensitivity of the measurement to the normalized impact parameter cut, and the run dependence of the observed η distribution. Table 16 lists the measured values of $dN_{ch}/d\eta$ for three different settings of the impact parameter cut. No occupancy cuts are applied to these samples. The measured values change appreciably for $b_{max} = 5$, but only about 2% for $b_{max} = 15$. We conclude that the measured distribution is relatively insensitive to small changes in the impact parameter.

We expect that many systematic effects cancel in the ratio of the η distribution at 1800 GeV to that at 630 GeV. To explore the sensitivity of the ratio measurement to various cuts, we have measured the ratio for each set of cuts discussed in previous sections. The results of this comparison are tabulated in Table 17. In general, the value of the ratio at any given value of η is insensitive to the particular cuts used at the level of about 3%, while the average value within $|\eta| < 3$ is stable to within 1%. We assign a systematic uncertainty of 3% to the averages based upon several considerations. First, changes in the track fitting procedure can induce changes of this magnitude. Second, differences in the level of background at the two energies contribute between 1–2% in the systematic uncertainty. Finally, differences in the low p_t correction are at the level of about 0.5%, assuming that the same functional form suffices to parameterize the low p_t behaviour at both energies.

Figure 54 shows the uncorrected η distribution for each 1800 GeV run used for this measurement. Only the η acceptance correction has been applied. The error bars indicate statistical uncertainties only. All distributions are within statistical agreement.

Table 16. Dependence of $dN_{ch}/d\eta$ on the normalized impact parameter cut (b_{max}).

	1800 GeV			630 GeV		
η range	$b_{max}=10.0$	5.0	15.0	$b_{max}=10.0$	5.0	15.0
0.00-0.25	3.952±0.028	3.530	4.116	3.18±0.05	2.88	3.29
0.25-0.50	3.968±0.029	3.542	4.097	3.10±0.05	2.81	3.20
0.50-0.75	4.096±0.029	3.729	4.249	3.32±0.05	3.06	3.44
0.75-1.00	4.305±0.030	3.951	4.490	3.55±0.05	3.28	3.68
1.00-1.25	4.556±0.031	4.142	4.693	3.59±0.05	3.29	3.69
1.25-1.50	4.508±0.031	4.033	4.539	3.69±0.05	3.33	3.71
1.50-1.75	4.939±0.033	4.432	5.067	3.98±0.05	3.58	4.09
1.75-2.00	5.012±0.033	4.491	5.147	4.15±0.06	3.73	4.24
2.00-2.25	4.887±0.032	4.353	4.978	3.88±0.05	3.50	3.95
2.25-2.50	4.713±0.031	4.202	4.764	3.72±0.05	3.33	3.73
2.50-2.75	4.704±0.031	4.190	4.795	3.69±0.06	3.28	3.74
2.75-3.00	4.377±0.029	3.768	4.489	3.39±0.06	2.94	3.47
3.00-3.25	4.280±0.037	3.895	4.340	3.35±0.07	3.06	3.39
3.25-3.50	4.245±0.073	3.379	4.168	3.47±0.16	2.78	3.40

Table 17. Sensitivity of the ratio ρ^{1800}/ρ^{630} (as a function of $|\eta|$ and averaged within $|\eta| < 3$) to various cuts.

η range	No cuts	$m > 0.9$ $x < 0.4$	$m > 0.9$ $x < 0.5$	$m > 0.8$ $x < 0.5$	$b_{max} = 5.0$	$b_{max} = 15.0$
0.00-0.25	1.25±0.03	1.24	1.24	1.24	1.24	1.26
0.25-0.50	1.29±0.03	1.28	1.28	1.28	1.27	1.29
0.50-0.75	1.24±0.03	1.24	1.24	1.24	1.23	1.24
0.75-1.00	1.22±0.02	1.22	1.22	1.22	1.21	1.23
1.00-1.25	1.27±0.03	1.28	1.28	1.28	1.26	1.28
1.25-1.50	1.23±0.02	1.24	1.23	1.23	1.22	1.23
1.50-1.75	1.25±0.02	1.26	1.25	1.25	1.25	1.25
1.75-2.00	1.21±0.02	1.22	1.22	1.22	1.21	1.22
2.00-2.25	1.26±0.02	1.27	1.26	1.27	1.25	1.27
2.25-2.50	1.27±0.02	1.27	1.27	1.27	1.27	1.29
2.50-2.75	1.28±0.02	1.28	1.28	1.29	1.29	1.29
2.75-3.00	1.30±0.02	1.29	1.29	1.29	1.30	1.31
3.00-3.25	1.29±0.03	1.28	1.27	1.27	1.29	1.29
3.25-3.50	1.23±0.06	1.21	1.21	1.21	1.23	1.24
Ave.	1.258±0.008	1.258	1.255	1.257	1.250	1.263

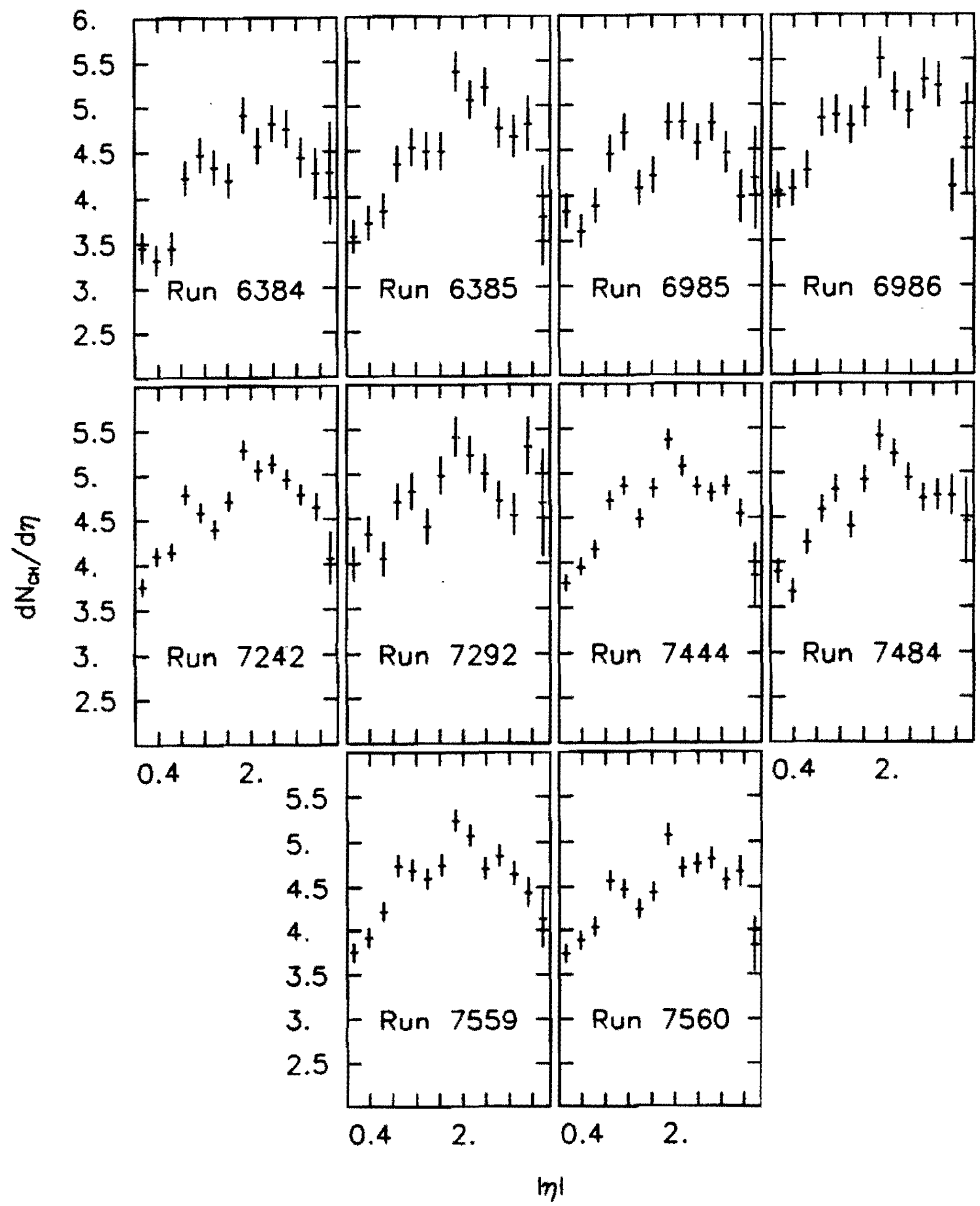

Figure 54. Uncorrected $dN_{ch}/d\eta$ distribution for different 1800 GeV runs. The uncertainties are purely statistical.

Chapter 5

The η Distribution in Minimum Bias Events

The final values for the $dN_{ch}/d\eta$ distribution are plotted in figure 55 and tabulated in table 18. Since systematic errors in the measurement affect neighboring η bins similarly, the size of the bins has been increased for $\eta > 1$ where the systematic errors are the largest. Also plotted are measurements made by UA5 at $\sqrt{s} = 546$ GeV (from reference [7]).

One notable characteristic of the central portion of the η distribution is the pronounced dip that occurs near $\eta = 0$. This feature is a consequence of the kinematic relationship between rapidity (eq. 1.1) and pseudo-rapidity (eq. 1.2).[1] In the limit that $p \approx E$, then η and y are identical, so that a uniform distribution in y implies a uniform distribution in η. For large values of η, the large longitudinal component of momentum ensures that this condition is always satisfied, even though typical

[1] Lyon, Risk and Tow [73], for example, perform an explicit derivation of the angular distribution starting from the invariant cross section $Ed^3\sigma/dp^3$. Although the form of the cross section they choose to work from is dated, the analysis serves to demonstrate the basic forms of the width and height of the η distribution in various kinematic limits. Another author, Tollestrup [74], performs an extensive analysis of the kinematic relationship between densities in rapidity and pseudo-rapidity, and the minimum observable transverse momentum.

values of p_t are on the order of 400 MeV/c. Near $\eta = 0$, however, many particles have neither transverse nor longitudinal components of relativisitic magnitudes. At exactly $\eta = 0$, the rapidity and pseudo-rapidity distributions satisfy the relation

$$\left(\frac{dN}{d\eta}\right)_{\eta=0} = \langle\beta\rangle \left(\frac{dN}{dy}\right)_{y=0}, \tag{5.1}$$

where $\beta = v/c$ and v is the particle velocity transverse to the beam axis [75]. Thus, we expect the central region to be depressed relative to the outlying regions, assuming a nearly uniform y distribution. The distribution measured at $\sqrt{s}$ of 546 GeV by UA5 shows an increase of about 15% from the minimum at $\eta = 0$ to the maximum value of $dN_{ch}/d\eta$ relative to the value at $\eta = 0$. Our measurements show an increase between 20-25% at both 630 and 1800 GeV. We will discuss the difference between our results and the UA5 result later in this section.

The ratio of $dN_{ch}/d\eta$ at 1800 GeV to that at 630 GeV is plotted in figure 56 and listed in table 19. Note that the large systematic uncertainties for $|\eta| > 1$ have largely cancelled. The scatter of points is approximately the same as the estimated statistical uncertainties; the ratio is consistent with being flat. The value of the ratio averaged within $|\eta| < 3.0$ is 1.26 ± 0.01(statistical)± 0.04(systematic).

In figure 57, we summarize the energy dependence of the particle density at $\eta = 0$. We also show values obtained by UA5 at $\sqrt{s} = 56$, 200, 546, and 900 GeV [7]. The curves show fits to a linear dependence on $\ln(s)$ (dashed line) and a quadratic dependence on $\ln(s)$ (solid curve). The result of the fits are in table 20. The fits clearly favor an energy dependence stronger than $\ln(s)$, confirming the trend observed by UA5.

Figure 58 shows $dN_{ch}/d\eta$ at $\eta = 0$ for all inelastic collisions over the range from $\sqrt{s} = 15$–900 GeV measured by other experiments [7,35,37]. Fits to these results are consistent with a linear dependence on $\ln(s)$. We should note, however, that the experimental details of the low energy and high energy results differ significantly. While the low energy results originate in fixed target experiments (primarily using bubble chamber targets), UA5 is a collider experiment. The bubble chamber ex-

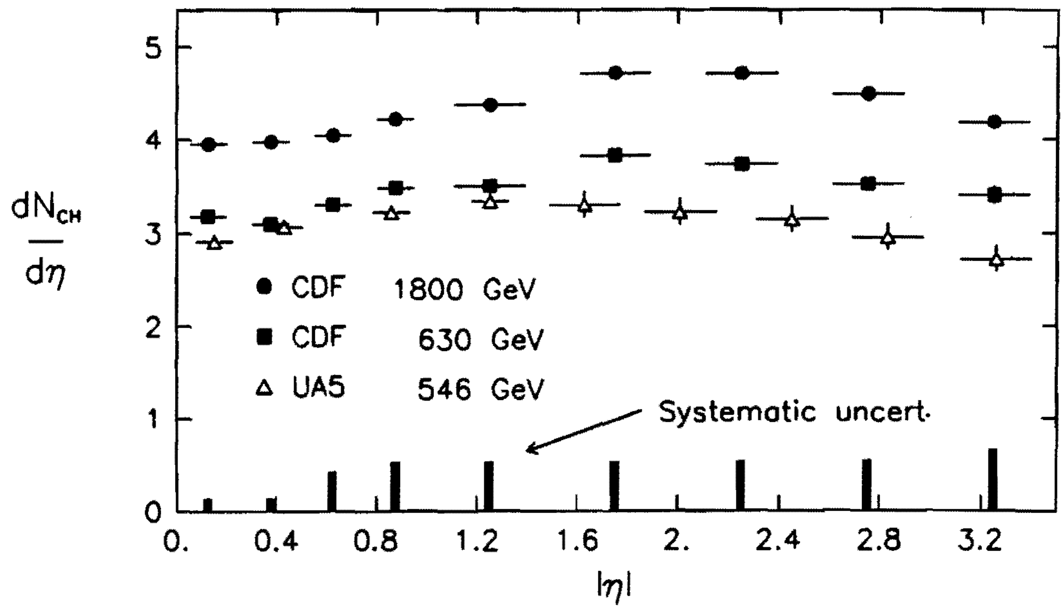

Figure 55. Fully corrected $dN_{ch}/d\eta$ vs. η. The statistical uncertainties are within the data points, while the systematic uncertainties (the values for 1800 GeV only) are indicated along the bottom of the plot. (The UA5 points are from [7].)

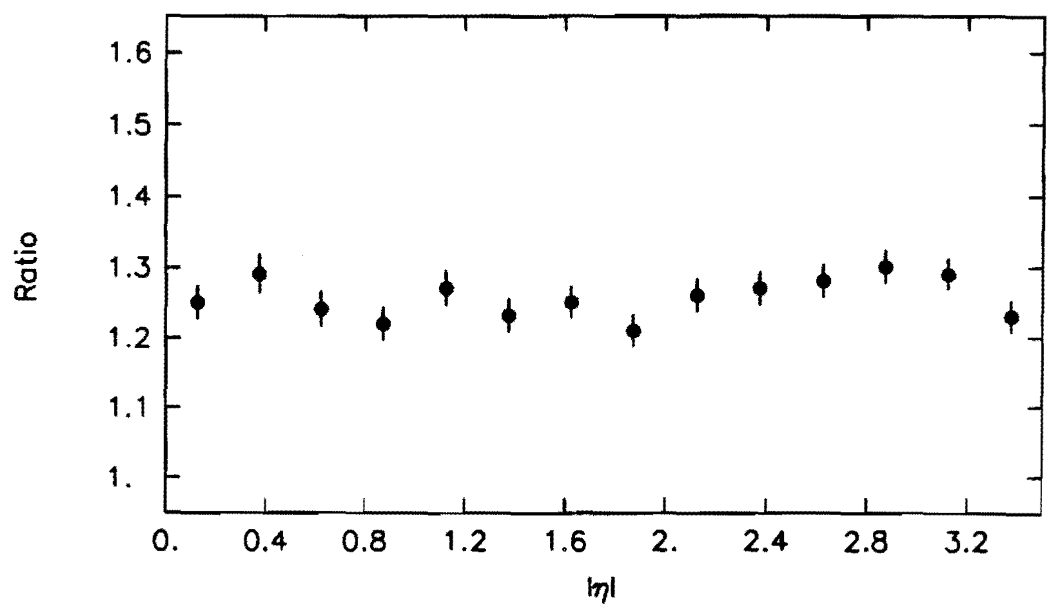

Figure 56. Ratio of $dN_{ch}/d\eta$ at 1800 GeV to that at 630 GeV.

Table 18. Fully corrected values of $dN_{ch}/d\eta$ vs. η at 1800 and 630 GeV.

	$dN_{ch}/d\eta \pm$ (stat) $\pm$ (sys)	
η range	1800 GeV	630 GeV
0.00-0.25	3.95±0.03±0.13	3.18±0.06±0.10
0.25-0.50	3.97±0.03±0.13	3.10±0.07±0.10
0.50-0.75	4.05±0.03±0.42	3.30±0.07±0.35
0.75-1.00	4.22±0.03±0.52	3.48±0.07±0.44
1.00-1.50	4.38±0.02±0.52	3.50±0.05±0.42
1.50-2.00	4.72±0.02±0.53	3.83±0.05±0.42
2.00-2.50	4.71±0.02±0.53	3.73±0.05±0.42
2.50-3.00	4.49±0.02±0.54	3.52±0.05±0.43
3.00-3.50	4.19±0.04±0.66	3.40±0.09±0.52

Table 19. Ratio of $dN_{ch}/d\eta$ at 1800 GeV to that at 630 GeV vs. η.

η range	Ratio±(stat)	η range	Ratio±(stat)
0.00-0.25	1.25±0.03	1.75-2.00	1.21±0.02
0.25-0.50	1.29±0.03	2.00-2.25	1.26±0.02
0.50-0.75	1.24±0.03	2.25-2.50	1.27±0.02
0.75-1.00	1.22±0.02	2.50-2.75	1.28±0.02
1.00-1.25	1.27±0.03	2.75-3.00	1.30±0.02
1.25-1.50	1.23±0.02	3.00-3.25	1.29±0.03
1.50-1.75	1.25±0.02	3.25-3.50	1.23±0.06
Ave. within $\|\eta\| < 3$: 1.26±0.01(stat)±0.04(sys)			

A systematic uncertainty of 0.04 applies to all values.

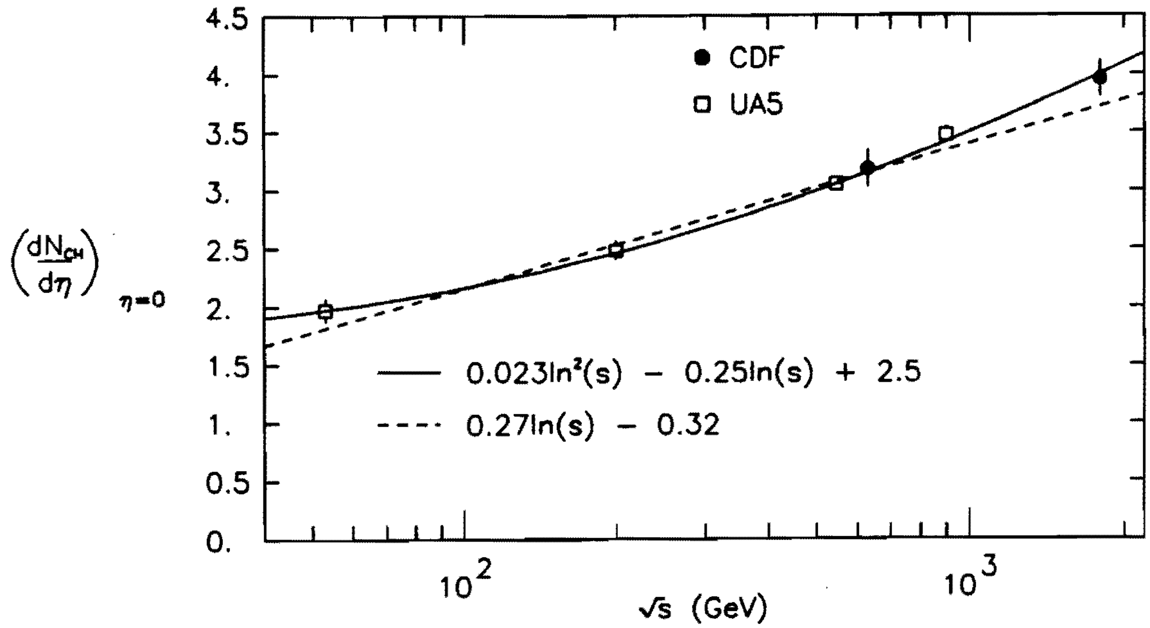

Figure 57. $dN_{ch}/d\eta$ at $\eta = 0$ vs. $\sqrt{s}$. The UA5 data points are taken from ref. [7].

Table 20. The results of fits to $dN_{ch}/d\eta$ at $\eta = 0$.

Results of fits to $\frac{dN_{ch}}{d\eta}$ at $\eta = 0$	
$(0.27 \pm 0.02)\ln(s) - (0.32 \pm 0.22)$	$\chi^2 = 8.95/4$ d.o.f.
$(0.023 \pm 0.008)\ln^2(s) - (0.25 \pm 0.19)\ln(s) + (2.5 \pm 1.0)$	$\chi^2 = 0.72/3$ d.o.f.

The curves are shown in fig. 57.

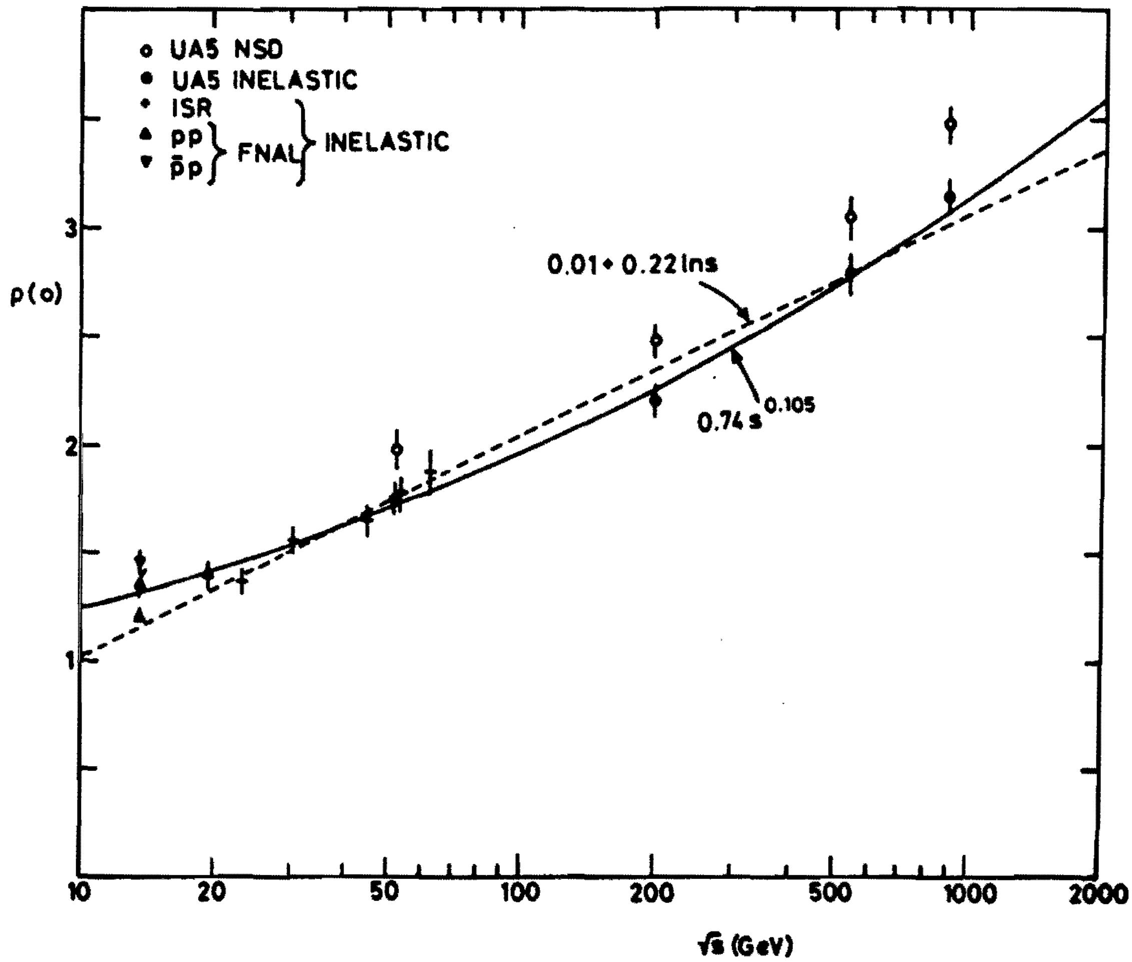

Figure 58. $dN_{ch}/d\eta$ at $\eta = 0$ for all inelastic events vs. $\sqrt{s}$ (from ref. [7]).

periments typically cover a broader kinematic range than do collider experiments, and more significantly, trigger on *all incident* protons (or antiproton), greatly reducing trigger bias relative to that of collider based experiments. As a result, the fixed target experiments observe directly a larger fraction of the total inelastic cross section, the colliders losing a significant fraction to the limited acceptance of the trigger system and the vacuum pipe in which the beam travels. To compare with the lower energy data, UA5 corrects their observed distribution (the so-called non-single diffractive result) for trigger efficiency to obtain the inelastic result. It is clear from the data, however, that the UA5 result alone is in sharp disagreement with an energy dependence linear in $\ln(s)$: two of their four data points lie a significant distance from the fit line. Their data alone is more consistent with a stronger than $\ln(s)$ energy dependence. This discrepancy in the shape of the energy dependence partially motivates our choice not to pursue Monte Carlo corrections for those portions of the cross section which cannot be directly observed. The data points of the fixed target experiments and the "inelastic" results of UA5 plotted in fig. 58 are likely not the same physical quantities.

For the same reason that the most significant result of this analysis is the ratio of the η distributions at two different energies, we view the most significant results at lower energy as the comparisons using the same detector — the UA5 data from 53–900 GeV. Our results confirm the trend observed by UA5 that the energy dependence of $dN_{ch}/d\eta$ is faster than $\ln(s)$.

Figure 59 shows the energy dependence of dN_{ch}/dy at $y = 0$ predicted by the Dual Parton Model [57], up to $\sqrt{s}$ around 20 TeV. The measurements of $dN_{ch}/d\eta$ at $\eta = 0$ by CDF and UA5 are also plotted. The predictions for dN_{ch}/dy must be scaled by $\langle\beta\rangle$ to obtain predictions for $dN_{ch}/d\eta$Åt CDF and UA5 energies, this requires a 15-25% decrease in dN_{ch}/dy to obtain $dN_{ch}/d\eta$ at $\eta = 0$. This implies a DPM prediction for $dN_{ch}/d\eta$ at $\eta = 0$ and $\sqrt{s} = 1800$ GeV in the neighborhood of

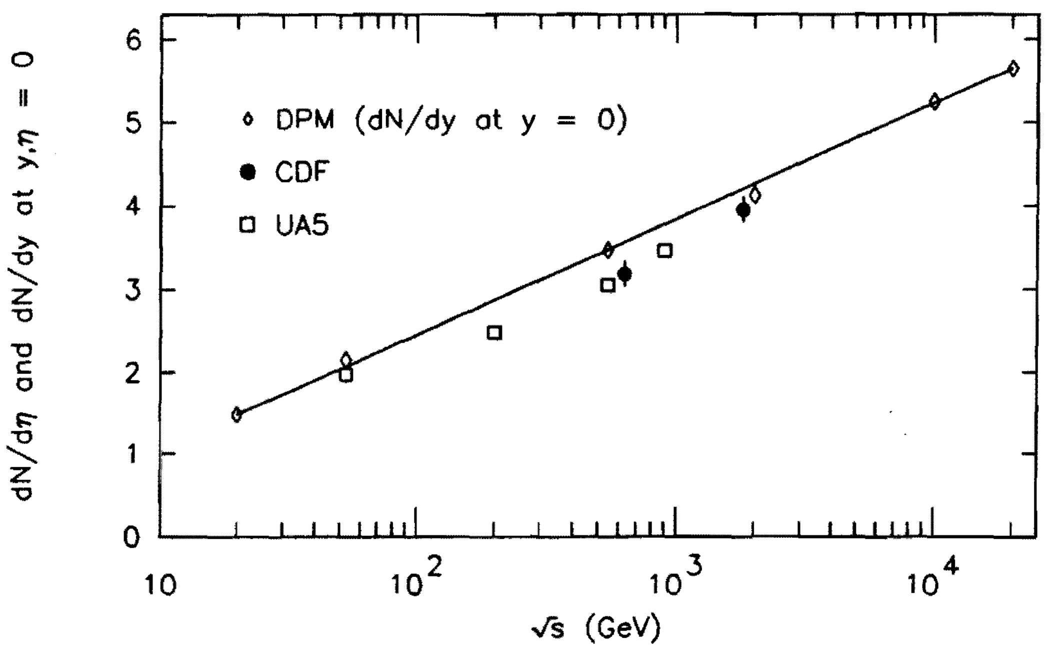

Figure 59. DPM prediction for dN_{ch}/dy at $y = 0$ vs. $\sqrt{s}$. The solid line is the DPM prediction [57]. The data points are from UA5 [7] and the present analysis.

3.5, below the CDF result. More generally, the DPM exhibits a linear dependence in $\ln(s)$, in conflict with the data.

We are aware of no published predictions of Statistical Hydrodynamical Models at $\sqrt{s} = 1800$ GeV. We note, however, that the predicted power-law s dependence of the mean multiplicity should also hold for the height of the η distribution, a fact in qualitative agreement with the data. A power law-fit yields an exponent of 0.103±0.008, smaller than the 0.25 predicted [76].

As noted earlier, the CDF measurements of $dN_{ch}/d\eta$ for $|\eta| > 1.5$ at 630 GeV differ systematically by about 1.3 σ (systematic) from those of UA5 at 546 GeV. We expect on the basis of the $\ln^2(s)$ fit to $dN_{ch}/d\eta$ at $\eta = 0$ an increase of about 3–4% between $\sqrt{s}$ of 546 and 630 GeV. Although one could argue that the difference is not statistically significant, the discrepancy bears some consideration.

The dominant systematic uncertainty in the CDF measurement enters from the tracking efficiency measurement. In Section 3.2.3, we discuss the fact that in certain regions of η, the efficiency correction based upon the visual scan does not fully compensate for changes in the efficiency as a function of the event vertex position. Using data at small values of η where the discrepancy is directly observable, we estimate the magnitude of the effect. Tracks within this η region have the majority of hits within a single module (or module set), with only a small fraction of hits in another module (or module set). Assuming the over-efficiency occurs at all values of η where a significant fraction of tracks cross more than one module, we decrease $dN_{ch}/d\eta$ (by as much as 10%) for all values of $\eta > 1.75$ where the problem cannot be observed directly. One could as easily argue, however, that in those regions where a significant portion of a trajectory is in each module set, the effect should be smaller than in those where most of the track is in only one module (i.e., where the effect turns out to be most observable). The scanning rules, furthermore, should tend to bias toward smaller multiplicities rather than larger.

UA5 assigns significant systematic uncertainty only to the trigger efficiency, for which they claim an uncertainty of ±2–3%. The magnitude of some corrections, however, is much larger than the corresponding correction at CDF. For instance, the average correction for photon conversions is 14%. Since the beam pipe through the UA5 detector is 0.05 radiation lengths at $\eta \sim 0$, and 2.6 for $\eta \sim 5$, significant corrections are required for photon conversions, secondary hadronic interactions, and losses of primaries to scattering. Corrections for geometrical acceptance are also significant. All these corrections are obtained from Monte Carlo. They estimate the flux of photons entering the detector by measuring the rate of electromagnetic *showers* identified as secondary vertices in the material of the beam pipe. None of these corrections or techniques should, in principle, present undue difficulty. The most recent UA5 data [7] (at $\sqrt{s}$ of 200, 546 and 900 GeV) were obtained using a beryllium beam pipe with greatly reduced material before the detector. These results are consistent with the earlier UA5 results at $\sqrt{s}$ of 546 GeV.

The largest corrections for each experiment are complementary. The design of the CDF detector minimizes the corrections necessary for secondary interactions; the streamer chamber used by UA5 has a tracking efficiency of nearly 100%. With the large systematic uncertainties present taken at face value, it is difficult to speculate about whether or not the observed differences should be considered as significant.

Chapter 6

The Event Underlying W and Z Production

In the context of the quark-parton model [53,54], the most striking features of hard hadron-hadron scattering events are described in terms of interactions between single partons in each of the colliding hadrons. The remaining partons, those which constitute the spectator system, contribute little to this description, since interactions between spectator constituents typically involve relatively small transfers of transverse momentum. In this picture, the overall event topology consists of the energetic final state from the hard parton-parton interaction superimposed upon the soft "underlying event" produced by spectator system interactions. Interestingly, the soft nature of spectator interactions makes hard scattering events a potentially incisive probe of the interaction mechanism in minimum bias events.

In this chapter, we present a measurement of the underlying event associated with $W^{\pm}$ and Z^0 boson production. More precisely, we will measure the ratio of the charged particle pseudo-rapidity distribution in $W^{\pm} \rightarrow e^{\pm}\nu$ events and $Z^0 \rightarrow e^+e^-$ events to that in minimum bias events. Bosons which decay into leptons are particularly well suited to this study for several reasons. First, the leptonic decay channels produce easily recognizable event signatures, and can be isolated into samples with relatively little background. Second, the leptonic decays themselves produce only one or two easily identified charged particles. And third, the final state leptons do not interact strongly, which minimizes possible final state perturbations to the spectator system. In effect, we can unambiguously isolate all final state particles that result from interactions within the spectator system.

The data studied in this part of the analysis were recorded during the 1988/1989 CDF run, a full year after the data presented in previous chapters. As might be expected, there are several differences in the experimental setup used for the two runs which are relevant to the analysis of VTPC data. First, the alignment of the chambers changed significantly between the two runs, which requires development of new alignment corrections. Second, the electric field in the drift region is higher during the later run than during the earlier. Thus, a new set of drift velocities and slope corrections are required. Third, the instantaneous luminosities delivered by the accelerator during the later run are between one and two orders of magnitude higher than those during the earlier. At these high luminosities, space-charge effects within the drift region are sufficiently large to produce significant non-linearities in the drift-time relationship. An additional set of luminosity dependent corrections is required to compensate for these space-charge distortions.

In order to perform the analysis, we will first assume that the tracking efficiency is approximately independent of the charged particle multiplicity. For the 1987 minimum bias data presented in the previous chapters, we showed this to be true within the statistical power of the efficiency measurement. We will not, however, measure the tracking efficiency for the data to be presented in this chapter.

The next step in the analysis will demonstrate that the value of $dN_{ch}/d\eta$ does not depend upon the instantaneous luminosity. We require such a test because the distributions of luminosity for the minimum bias data and the boson data we compared are somewhat different. Since the corrections for luminosity dependent non-linearities are large, one might imagine a luminosity dependence in the tracking efficiency which could in turn introduce a bias that does not fully cancel in the ratio.

We will then examine evidence showing that the systematic errors introduced by tracking inefficiencies, and contamination from conversion electrons and particle decays do in fact cancel in the ratio. To estimate the extent to which the former cancels, we will exploit the strong dependence of the tracking efficiency on the event vertex position. The variation in the ratio as a function of the vertex position indicates the degree to which the efficiency actually cancels. To demonstrate that background from extraneous sources of charged particles cancel as well, we will use the fact that the tails of the impact parameter distribution used for track selection consist primarily of background. Since the shape of the impact parameter distribution for background particles is significantly less peaked than that for signal tracks, the sensitivity of the ratio to the impact parameter cuts allows us to estimate the degree to which such background affects our result.

We will then show that the ratio is relatively insensitive to measurement errors in the boson p_t using two tests. The first shows that ratio for W events is stable against a cut in the leading jet E_t (excluding the electron). The second examines the effect on the ratio for Z events using a significantly less precise measure of the Z p_t than using the electron energies directly.

Before discussing the details of the analysis, we will outline the preparation of the data sets. In the final section, we will compare our results to existing data and discuss the physical significance.

6.1 Data samples

The following sections describe the triggers and cuts used to define samples of W and Z boson candidates, and the minimum bias sample from the 1988 data. We will discuss only the general features of the W and Z analyses and refer to published and internal CDF documentation for further details. The W and Z data sets are based upon the analysis of about 4.31 pb^{-1} of integrated luminosity.

6.1.1 Minimum bias data sample

To ensure proper calibration and monitoring of the calorimeters, a certain number of minimum bias events must be recorded concurrently with high E_t events. All standard combinations of high E_t calorimeters triggers—including those from which the boson samples are derived—also contain a minimum bias trigger, run simultaneously, but rate-limited to 50 mHz in Level 1. The minimum bias data sample we use consists of such minimum bias triggers extracted from a portion of the combined data stream. We select the portions used for this purpose in order to obtain a wide range of luminosities in the minimum bias sample. In other respects, the beam conditions represented in the minimum bias sample should be similar, although not identical to those represented in the boson sample.

6.1.2 W selection and data sample

The $W^{\pm} \rightarrow e^{\pm}\nu$ decay has two distinctive features: an isolated, high p_t electron accompanied by a large imbalance in the observed transverse components of momentum (so called "missing E_t", or $\not{E}_t$). These features provide a striking event signature, detected with high efficiency by triggering on energetic electromagnetic showers in the central region, then selecting events with a single well identified electron and large $\not{E}_t$ offline. Table 21 shows the parameters, by trigger level, which define the central electron trigger. For more detailed descriptions of the calorimeters and trigger, the reader should consult refs. [77,78,79,80].

The offline analysis refines the selection of electron candidates by first fully reconstructing energy clusters in the calorimeters and charged particle tracks in the CTC and VTPC. A set of electron identification cuts and global event cuts (summarized in table 22) reduces the set of triggered events to the W sample.

Table 21. Central electron trigger criteria.

Level 1:	CEM	E_t STT > 6 GeV; $\sum E_t > 6$ GeV.
Level 2:	CEM	cluster with $E_t^{EM} > 12$ GeV; towers in cluster satisfy: $\frac{\sum(E^{EM} + E^{Had})}{\sum e^{EM}} < 1.125.$
	CTC	CFT track with $p_t > 6$ GeV/c associated with the cluster.
Level 3:	CEM	same requirements as Level 2, but after running offline clustering and cleanup $L_{share} < 0.5$ (see Appendix I)
	CTC	same as Level 2 using better tracking

CEM refers to the central electromagnetic calorimeter; STT to the single tower threshold; CTC to the central tracking chamber; and CFT to the fast tracking hardware for the CTC. Only towers with energy above the STT contribute to the sum E_t calculation.

Table 22. W selection cuts.

Electron identification			
EM cluster position:	$\|\eta\|$	$<$	1.0
	$\phi > 2.1$ cm from edge of ϕ segments		
	$z > 9$ cm from crack at 90°		
Cluster E_t:	E_t	$>$	20 GeV
Leakage into hadronic compartment:	HAD/EM	$<$	0.05
Cluster E_t/track p_t (E/p):	$0.5 < E/p < 2.0$		
CTC track/strip chamber match:	$\Delta\phi$	$<$	2.5 cm
	Δz	$<$	3.0 cm
Strip chamber shower profile:	χ^2_{strip}	$<$	15
Energy sharing between lateral towers:	L_{share}	$<$	0.2
Global event measures			
Electron isolation (within $r = 0.4$):	$I(r = 0.4)$	$<$	0.1
Missing transverse energy:	$\not{E}_t$	$>$	20 GeV
Vertex position:	$\|z_v\|$	$<$	60 cm
Excluded EM pair mass:	$50 < m_{ee} < 150$ GeV		

Appendix I contains brief descriptions of the cuts, with more detailed descriptions in refs. [77,78,81].

A total of 2542 events pass the W selection cuts from an integrated luminosity of 4.31 pb^{-1}. The sample contains an estimated 5.5±0.7% background in the low transverse mass and W p_t region [78], primarily from W→ $\tau\nu$, where the τ decays to an electron and neutrinos. Figure 60 shows the transverse mass distribution for the sample superimposed upon a Monte Carlo calculation. The agreement between the data and Monte Carlo supports the low estimated background.

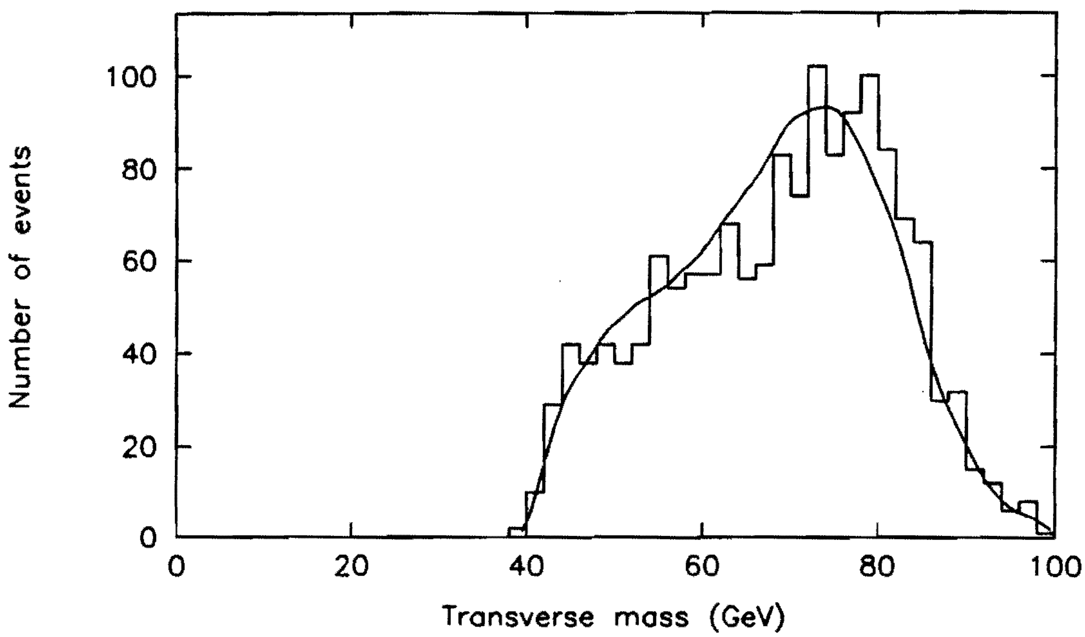

Figure 60. Transverse mass distribution. The curve is from a Monte Carlo calculation.

6.1.3 Z candidate selection and data sample

The selection of Z candidates follows the same electron identification for one of the two decay electrons as used in the W selection. The second decay electron must pass less stringent criteria, and may be found anywhere within the CEM calorimeter, as well as within restricted regions of the PEM calorimeter. Table 23 summarizes the selection cuts for Z candidates.

A total of 249 events pass these selection cuts from an integrated luminosity of 4.4 pb^{-1} recorded with the central electron trigger. The sample contains an estimated 3.1±1.5% background in the low p_t region, primarily from QCD sources which mimic two isolated electrons [78]. Figure 61 shows the electron pair invariant mass distribution, and exhibits a clear signal in the region of the Z mass. More detailed discussions of selection criteria and background can be found in refs. [78] and [79].

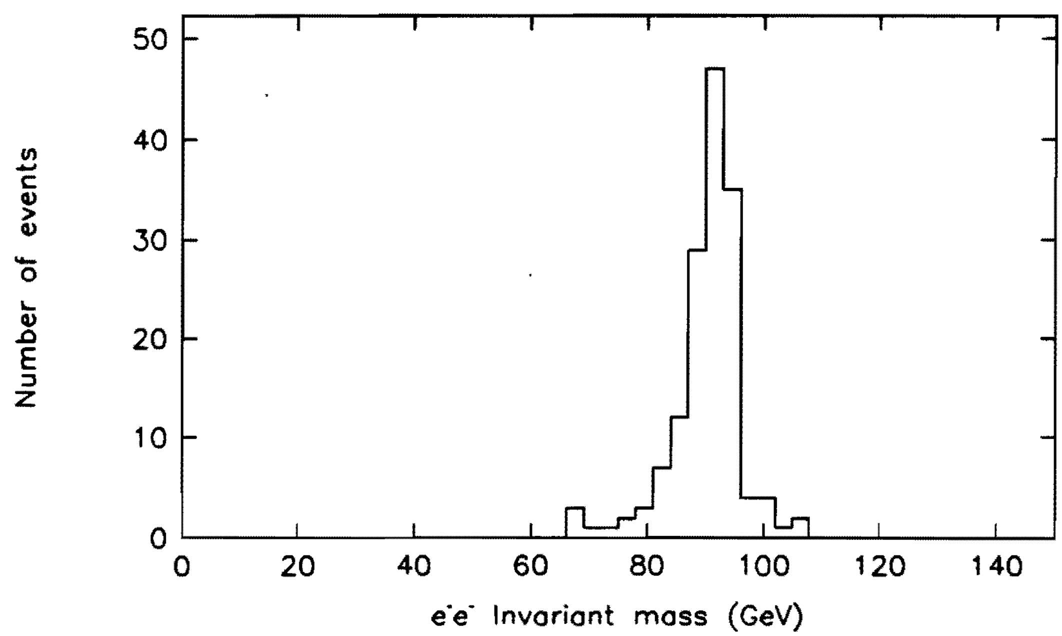

Figure 61. Electron-positron invariant mass distribution.

Table 23. Z selection cuts.

First electron identification			
EM cluster position:	$\lvert\eta\rvert$	<	1.0
	$\phi > 2.1$ cm from edge of ϕ segments		
	$z > 9$ cm from crack at 90°		
Cluster E_t:	E_t	>	20 GeV
Leakage into hadronic compartment:	HAD/EM	<	0.05
Cluster E_t/track $p_t(E/p)$:	$0.5 < E/p < 2.0$		
CTC track/strip chamber match:	$\Delta\phi$	<	2.5 cm
	Δz	<	3.0 cm
Strip chamber shower profile:	χ^2_{strip}	<	15
Energy sharing between lateral towers:	L_{share}	<	0.2
Second electron identification			
EM cluster position:	$\lvert\eta\rvert$	<	3.1
	CEM: same cuts as for first electron		
	PEM and FEM: $\phi > 5°$ from quadrant edge		
Cluster E_t:	E_t	>	10 GeV
Leakage into hadronic compartment:	HAD/EM	<	0.10
Cluster E_t/track $p_t(E/p)$ (CEM only):	$0.5 < E/p < 2.0$		
PEM shower profile (3×3 pads):	$\chi^2_{3\times3}$	<	20
Global event measures			
Electron isolation (first):	$I(r = 0.4)$	<	0.1
Electron isolation (second):	$I(r = 0.4)$	<	0.2
e^+e^- invariant mass ($m_{e^+e^-}$):	65 GeV $< M_{e^+e^-} <$ 115 GeV		
Vertex position:	$\lvert z_v\rvert$	<	60 cm

6.2 Analysis of the underlying event vs. boson p_t

6.2.1 The η distribution

Since the primary quantity of interest is the ratio of $dN_{ch}/d\eta$ within a fixed range in η, we need not correct for those systematic errors in the absolute value of $dN_{ch}/d\eta$ which will cancel in the ratio. Under the proper conditions, these include the geometrical acceptance, the tracking efficiency and background from photon conversions and particle decays. For the first two, it is sufficient that the shape of the vertex distributions be identical for the two data sets being compared. Cancellation of the third rests upon the validity of the assumption that the relative particle composition of the underlying event is approximately the same as for minumum bias events. We can set a limit on the differences in charged particle background by looking at the variation in the ratio as a function of the track selection.

The calculation of the observed $dN_{ch}/d\eta$ distribution for the data sets follows equation 1.9, which does not include any of the multiplicative correction factors. We select events and tracks as outlined in sections 4.2.1 and 4.3 for the minimum bias analysis:

1. **Event selection**: event vertex within 12 cm of the center of the nearest VTPC module. This cut eliminates large non-uniformities in the acceptance and tracking efficiency near $\eta = 0$.
2. **Track selection**: track trajectory must traverse at least 11 wires; absolute value of the impact parameter, b defined in equation 4.6, must be less than 10.

We define the ratio, R^i, by the equation:

$$R^i = \frac{\int_{\Delta\eta} \rho^i_{obs}(\eta)}{\int_{\Delta\eta} \rho^{MB}_{obs}(\eta)}, \tag{6.1}$$

where ρ^i_{obs} is the uncorrected η distribution observed in type "i" events ($i = W, Z$), and ρ^{MB}_{obs} is the uncorrected η distribution observed in minimum bias events.

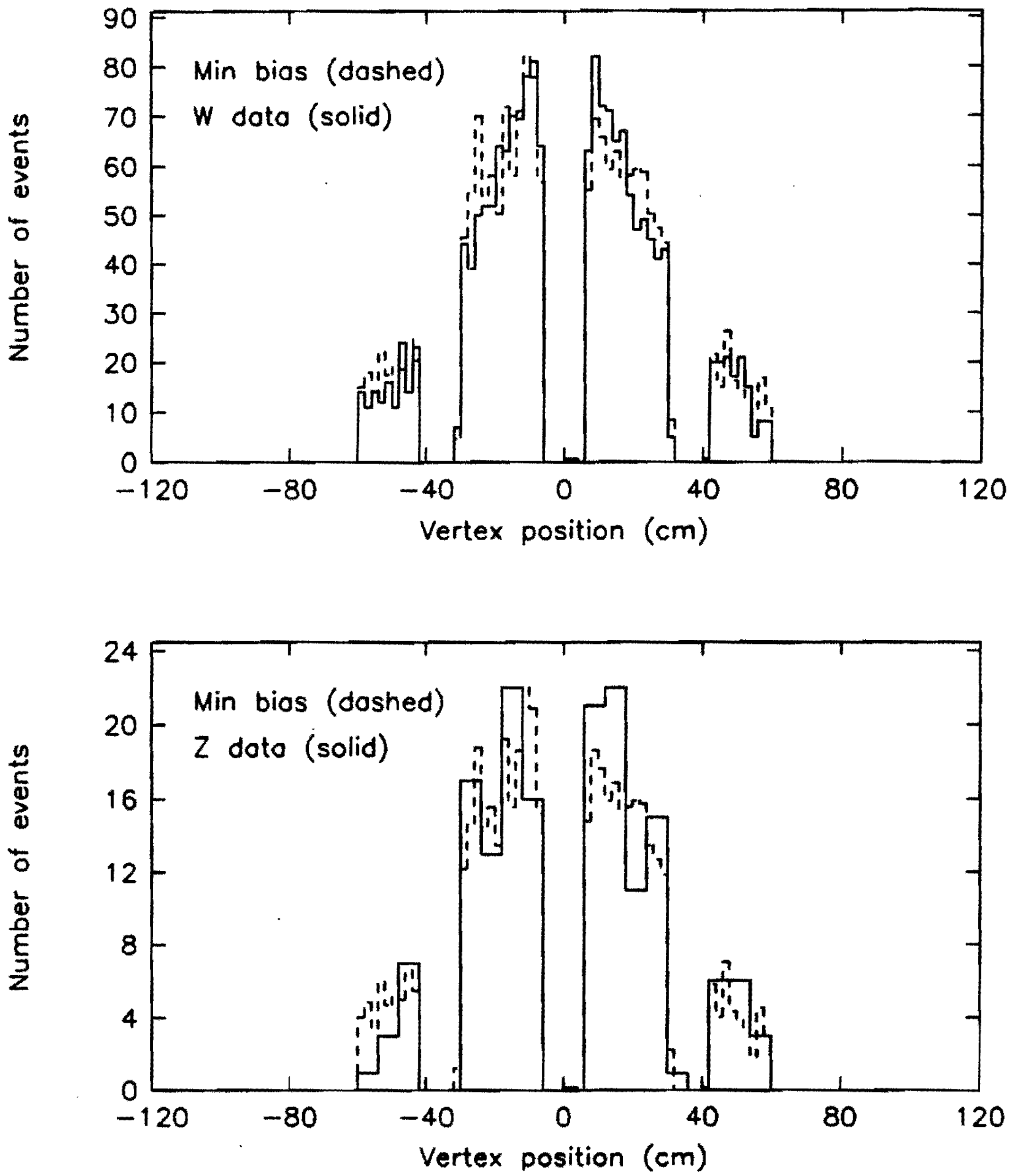

Figure 62. Vertex distributions for W and Z samples. The vertex distribution for the minimum bias reference sample is superimposed with an arbitrary vertical scale.

To check that the geometrical acceptance and tracking efficiency corrections actually cancel, we must compare vertex distributions for the three data sets. Figure 62 shows the vertex distributions for events from the W and Z samples superimposed upon that from the minimum bias sample used as reference for $dN_{ch}/d\eta$. Since the shape of the distributions are identical within statistics, we can safely average $dN_{ch}/d\eta$ over vertex positions before taking the ratio.

6.2.1.1 *Luminosity dependence of η distribution*

Positive ion currents in the drift region of the VPTC cause significant non-linearities in the drift-time relationship at high luminosity. The resulting distortions in particle tracks can lead to a luminosity dependence in the measured $dN_{ch}/d\eta$ distribution.

The distribution of luminosity for minimum bias events is similar to that for W events (fig. 63) for certain ranges in luminosity, although significant differences appear in other ranges. Figure 64 shows plots of $dN_{ch}/d\eta$ (corrected only for geometrical acceptance in η) for minimum bias events measured as a function of the instantaneous luminosity and vertex position. The plots are independent of luminosity within statistical errors. We will therefore average over luminosity.

6.2.1.2 *Removal of tracks from decay electrons*

Since no track within the VTPC are directly matched with the decay electron tracks in the CTC, we subtract the electron tracks from those of the underlying event using an η distribution for the decay electrons calculated indirectly using the electron cluster position within the calorimeters. This procedure requires assumptions about the azimuthal acceptance and tracking efficiency which will contribute to the overall systematic uncertainty in the final result. We will assume that for tracks within $|\eta| < 1$, the azimuthal acceptance is 0.95±0.02 (from table 12), and the effective tracking efficiency is 0.95±0.05. For $|\eta| > 1$, we assume the the azimuthal acceptance is 1.0, and the effective tracking efficiency is 1.0±0.1. Table 24 lists the η density

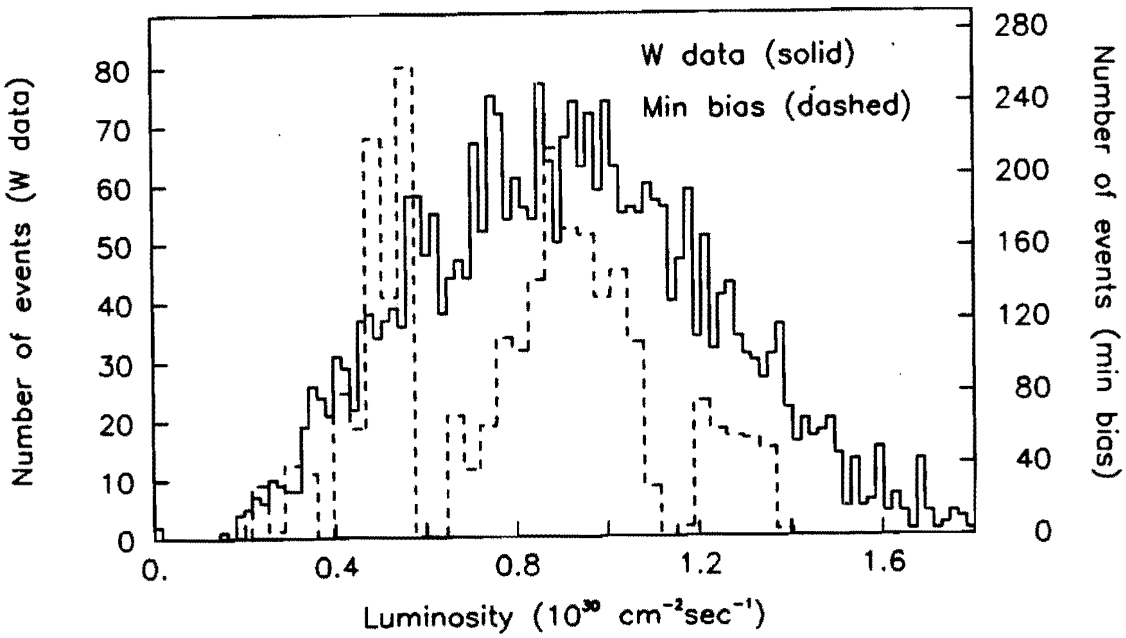

Figure 63. Distribution of luminosities for minimum bias and W events. The number of W events should be read from the left-hand scale, and minimum bias events from the right-hand scale.

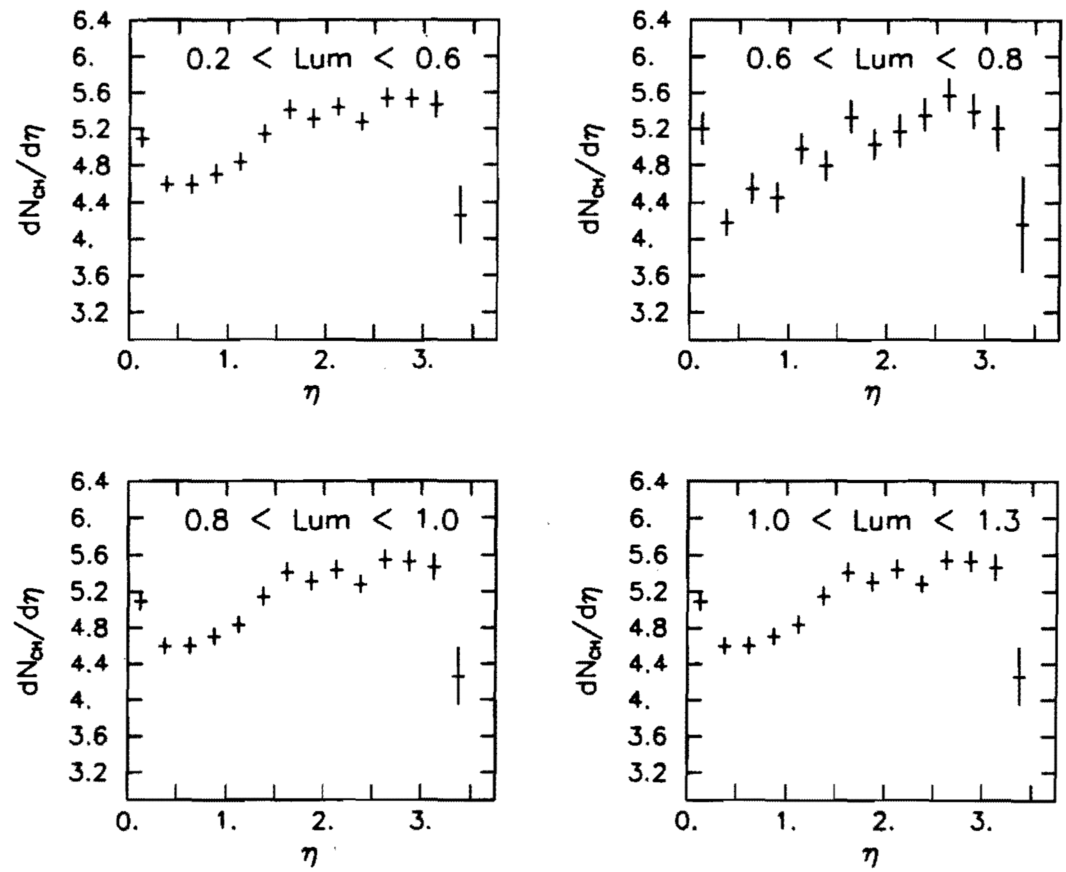

Figure 64. Instantaneous luminosity dependence of $dN_{ch}/d\eta$. The luminosity is quoted in units of $10^{30}\mathrm{cm}^{-2}\mathrm{sec}^{-1}$.

subtracted from $dN_{ch}/d\eta$ for W and Z events in order to account for the decay electrons. The mean values within $|\eta| < 1$, 2 and 3 are also listed. We subtract the same distribution from all p_t^W bins. Although we do not expect the distribution to be independent of p_t the correction, and therefore the error, is small. Figure 65 shows the uncorrected $dN_{ch}/d\eta$ distributions for minimum bias, W and Z events after subtraction of the decay electrons.

Table 24. η distribution of W and Z decay electrons.

η range		W events		Z events	
		N_{ele}	η density	N_{ele}	η density
−3.0	−2.5	0	—	8	0.114±0.011
−2.5	−2.0	0	—	9	0.119±0.012
−2.0	−1.5	0	—	18	0.24±0.02
−1.5	−1.0	21	0.028±0.003	8	0.106±0.011
−1.0	−0.5	349	0.41±0.02	58	0.69±0.04
−0.5	0.0	387	0.46±0.03	56	0.67±0.03
0.0	0.5	381	0.45±0.03	51	0.61±0.03
0.5	1.0	364	0.43±0.03	53	0.63±0.03
1.0	1.5	26	0.034±0.003	8	0.106±0.011
1.5	2.0	0	—	17	0.23±0.02
2.0	2.5	0	—	7	0.093±0.009
2.5	3.0	0	—	6	0.087±0.009
−1.0	1.0	1481	0.43±0.02	218	0.638±0.019
−2.0	2.0	1528	0.226±0.012	269	0.404±0.010
−3.0	3.0	1528	0.153±0.008	299	0.306±0.007

N_{ele} is the total number of decay electrons in the given η range.

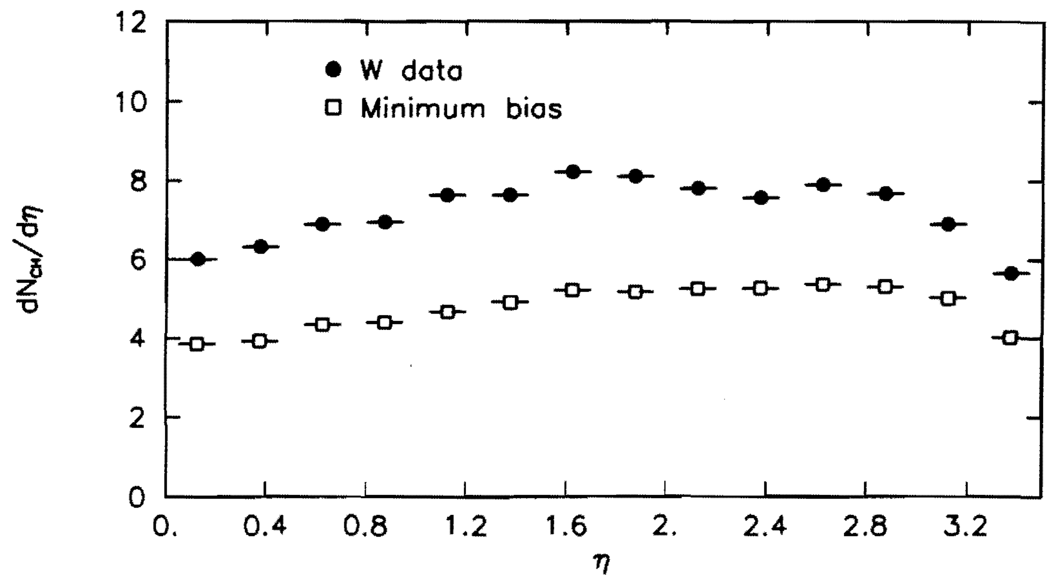

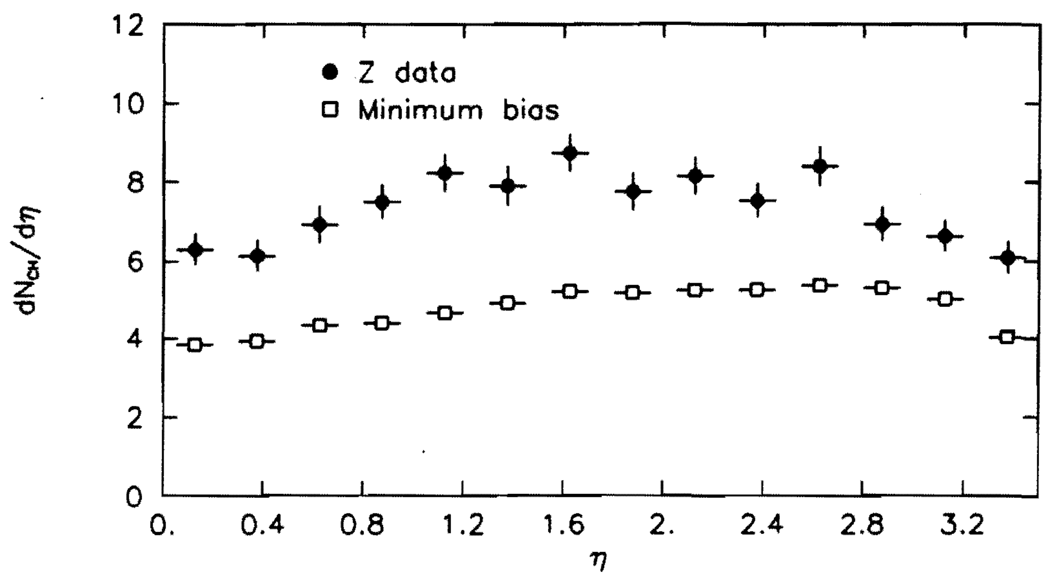

Figure 65. Uncorrected $dN_{ch}/d\eta$ distributions for minimum bias, W and Z data. The boson distributions are averaged over the boson p_t.

6.2.2 The W p_t distribution

We calculate the p_t of the W boson from the vector sum of the missing E_t (the E_t of the neutrino) and the p_t of the electron:

$$\begin{aligned} \vec{p}_t^{\,W} &= \vec{p}_t^{\,e} + \vec{p}_t^{\,\nu} \\ &= \vec{p}_t^{\,e} - (\vec{p}_t^{\,e} + \vec{p}_t^{\,\mathrm{under}}) \\ &= -\vec{p}_t^{\,\mathrm{under}}, \end{aligned} \tag{6.2}$$

where $\vec{p}_t^{\,W}$, $\vec{p}_t^{\,e}$ and $\vec{p}_t^{\,\nu}$ are the transverse momenta of the W, the electron and neutrino, respectively, and $\vec{p}_t^{\,\mathrm{under}}$ is the net transverse momentum of the underlying event. We obtain the value of $\vec{p}_t^{\,e}$ from the CEM calorimeter and include tower-by-tower corrections for non-linearities and calorimeter response. The value of $(\vec{p}_t^{\,e} + \vec{p}_t^{\,\mathrm{under}})$ is calculated by summing over individual calorimeter towers. No corrections are applied to obtain $\vec{p}_t^{\,\mathrm{under}}$. Figure 66 shows the observed p_t^W distribution for W events passing the $dN_{ch}/d\eta$ vertex cut.

6.2.3 The Z p_t distribution

Unlike the case of the W, the transverse momentum of the Z may be calculated directly from the vector sum of the energies of the decay electrons. Since energy corrections for high-E_t electrons are well understood, the value of the p_t^Z is measured more precisely than that of p_t^W. Figure 67 shows the p_t^Z spectrum for Z events that pass the $dN_{ch}/d\eta$ vertex cut.

6.2.4 The η distribution vs. p_t

Figure 65 shows the observed $dN_{ch}/d\eta$ distribution for minimum bias, W and Z events (averaged over p_t), corrected only for η acceptance. The $dN_{ch}/d\eta$ distribution as a function of the boson p_t is shown in figures 68 and 69. The value of $dN_{ch}/d\eta$ in the central region increases significantly with increasing boson p_t.

We will measure the ratio R as a function of the boson p_t, averaging the η distributions over the intervals $|\eta| < 1.0$, 2.0 and 3.0 before taking the ratio. Since there are very few events in the highest p_t bins, however, we cannot use the sample variance of the multiplicity distributions to estimate the statistical uncertainty in R within these bins. We therefore estimate the standard deviation in the high-p_t multiplicity distributions by extrapolating the width of the observed multiplicity distributions from the low-p_t bins into the two highest p_t bins (fig. 70). Figure 71 shows plots of $dN_{ch}/d\eta$ averaged within three η intervals, with statistical uncertainties.

6.3 Results of underlying event analysis

The values of $R^W(\eta)$ and $R^Z(\eta)$ (using $\Delta\eta = 0.25$) are shown in figures 72–74 both as a function of the boson p_t, and averaged over all p_t. Taking the average value of $dN_{ch}/d\eta$ within a large interval in η, then calculating the ratio yields the result shown in figure 75, plotted as a function of the boson p_t for three different η ranges. Tables 25 and 26 list the results. (The values of $dN_{ch}/d\eta$ from which the ratios are calculated are tabulated in Appendix J.) The rise in R with the boson p_t flattens as the η interval widens, which reflects the tendency for the recoil jet to lie in the central region. We estimate the systematic uncertainty using a number of systematic checks discussed in the next section.

6.4 Systematic uncertainties

To determine the systematic uncertainty, we will examine the degree to which systematic errors cancel in the ratios R^W and R^Z.

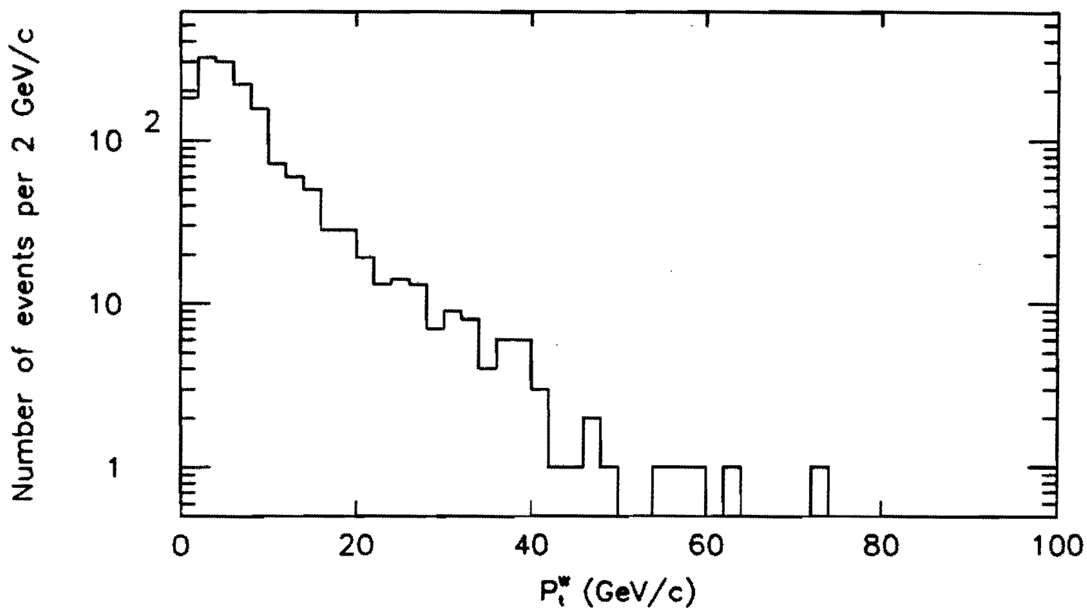

Figure 66. Distribution of W p_t (uncorrected).

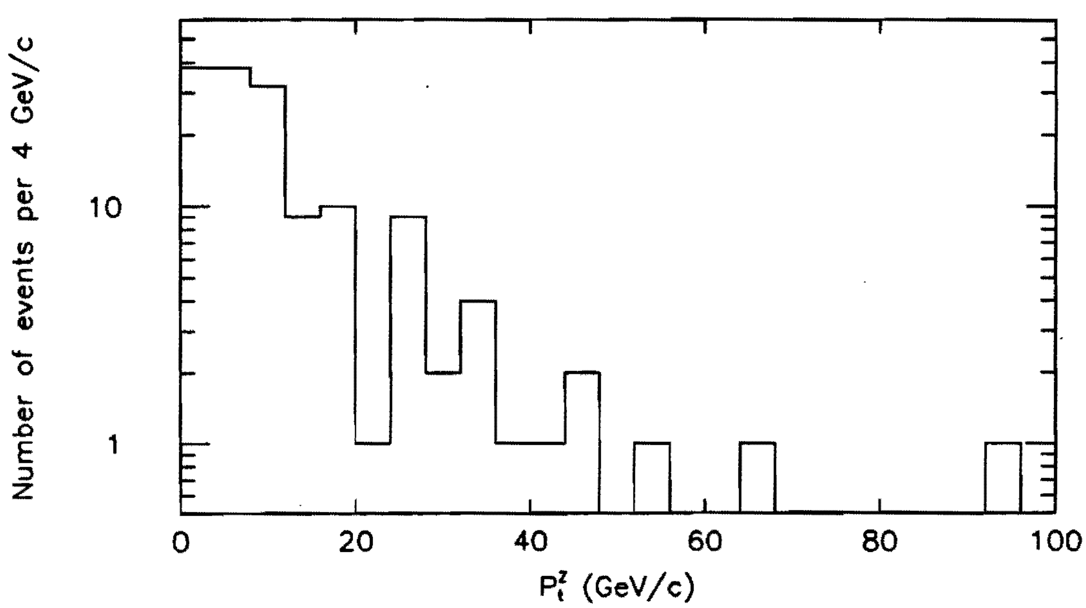

Figure 67. Distribution of Z p_t (uncorrected).

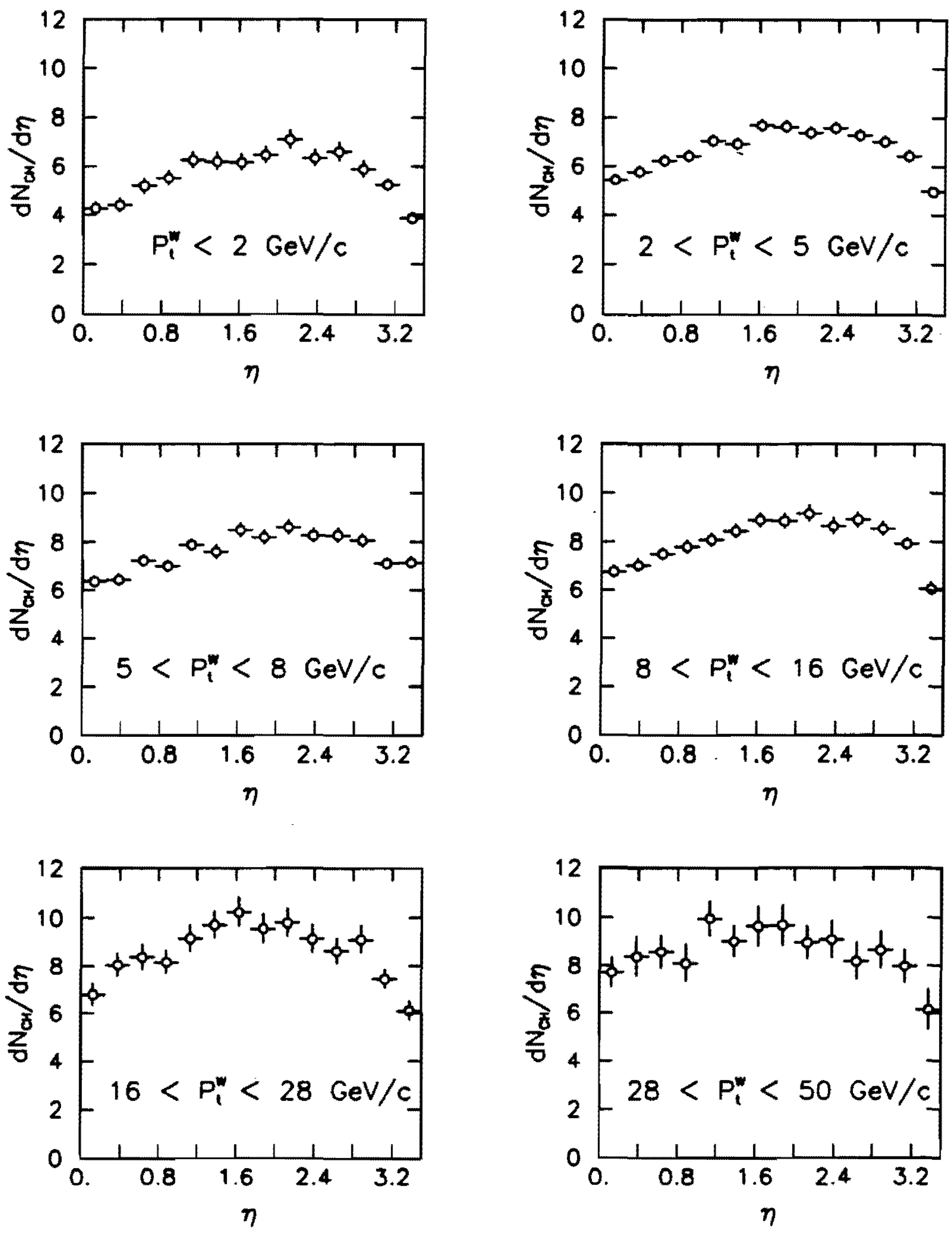

Figure 68. Uncorrected $dN_{ch}/d\eta$ distributions in p_t bins for W events.

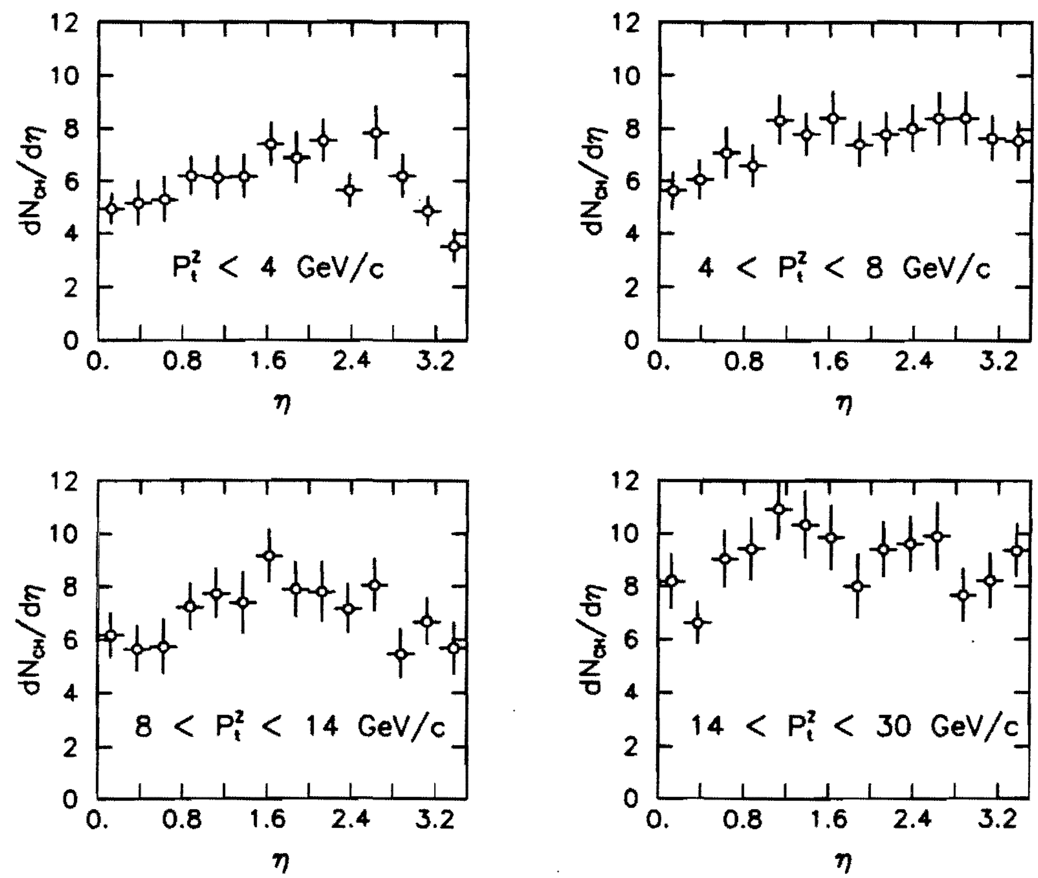

Figure 69. Uncorrected $dN_{ch}/d\eta$ distributions in p_t bins for Z events.

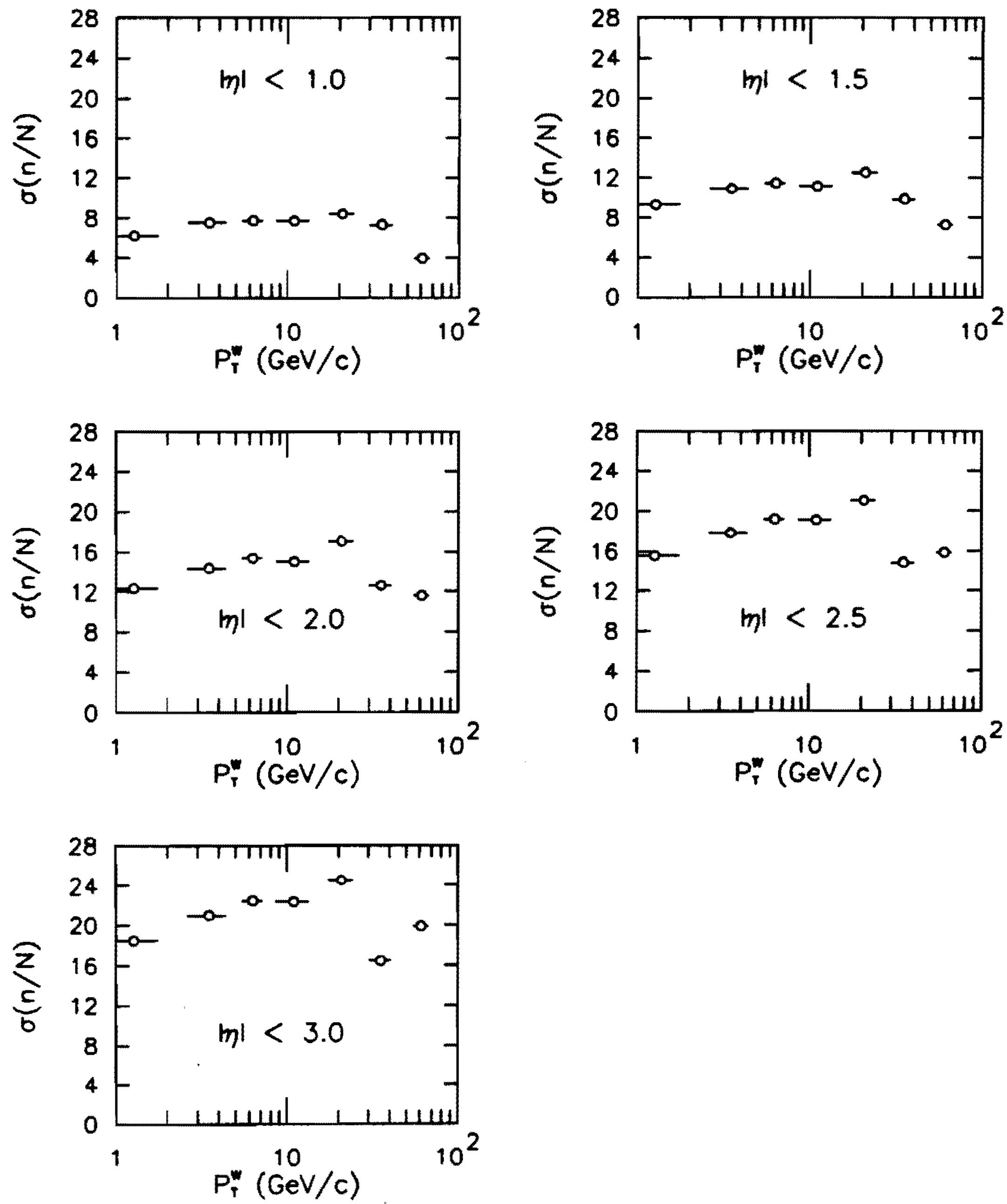

Figure 70. Standard deviation of the multiplicity distribution within η intervals. The standard deviation is calculated within bins in the W p_t. The values in the highest p_t bins are systematically low because the number of events in these bins is insufficient to estimate accurately the width of the multiplicity distribution.

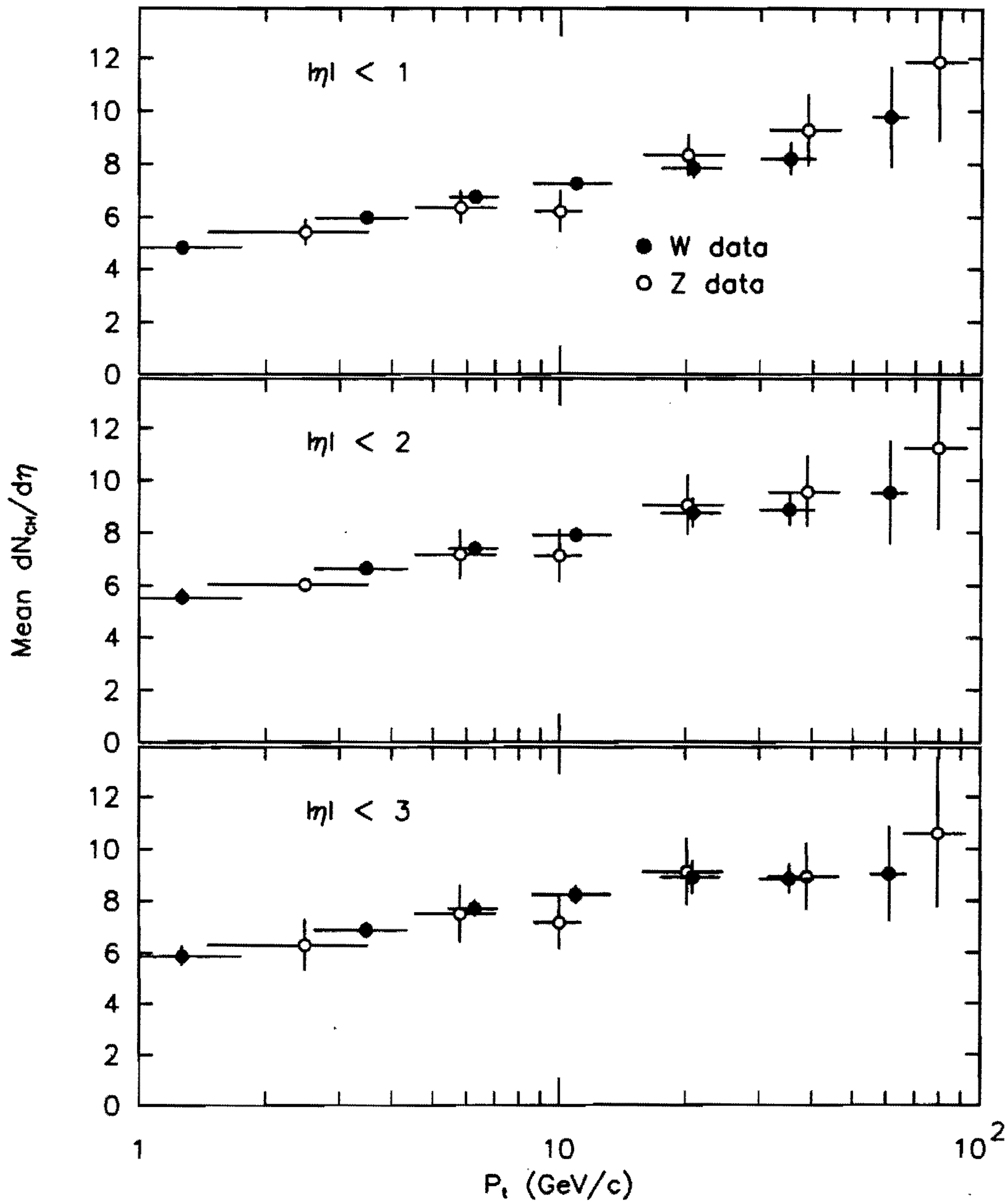

Figure 71. Average $dN_{ch}/d\eta$ versus p_t for W and Z . The η distribution is averaged within the indicated η intervals. The uncertainties are purely statistical.

Table 25. R^W vs. p_t^W final result including the estimated statistical and systematic uncertainties, respectively.

N_{ev}	p_t bin	$\langle p_t \rangle$	σ_{p_t}	R^W for $dN_{ch}/d\eta$ averaged over: $\|\eta\| < 1$	$\|\eta\| < 2$	$\|\eta\| < 3$
181	0–2	1.3	0.5	1.17±0.06±0.12	1.21±0.07±0.12	1.22±0.08±0.12
461	2–5	3.5	0.9	1.44±0.05±0.18	1.45±0.05±0.17	1.43±0.06±0.16
378	5–8	6.3	0.8	1.63±0.05±0.23	1.62±0.06±0.20	1.60±0.07±0.19
338	8–16	11.0	2.3	1.76±0.06±0.29	1.73±0.07±0.25	1.71±0.07±0.23
115	16–28	20.9	3.4	1.90±0.10±0.34	1.92±0.12±0.30	1.85±0.14±0.28
48	28–50	35.4	5.2	1.98±0.15±0.39	1.94±0.14±0.35	1.84±0.12±0.32
5	50–100.	61.	6.	2.36±0.46±0.42	2.09±0.43±0.41	1.88±0.38±0.44

Values of p_t are given in GeV/c. The W p_t is uncorrected.

Table 26. R^Z vs. p_t^Z final result including the estimated statistical and systematic uncertainties, respectively.

				R^Z for $dN_{ch}/d\eta$ averaged over:		
N_{ev}	p_t bin	$\langle p_t \rangle$	σ_{p_t}	$\lvert\eta\rvert < 1$	$\lvert\eta\rvert < 2$	$\lvert\eta\rvert < 3$
38	0–4	2.5	1.0	1.31±0.12±0.11	1.32±0.18±0.11	1.31±0.21±0.11
38	4–8	5.8	1.3	1.54±0.16±0.14	1.57±0.20±0.14	1.56±0.23±0.14
35	8–14	10.0	1.3	1.50±0.20±0.17	1.56±0.22±0.17	1.49±0.21±0.17
27	14–30	20.	4.	2.02±0.19±0.20	1.98±0.25±0.20	1.89±0.27±0.20
10	30–60	39.	7.	2.24±0.33±0.22	2.09±0.30±0.22	1.86±0.27±0.22
2	60–100	79.	13.	2.87±0.73±0.22	2.46±0.68±0.22	2.21±0.60±0.22

Values of p_t are given in GeV/c. The Z p_t is measured directly.

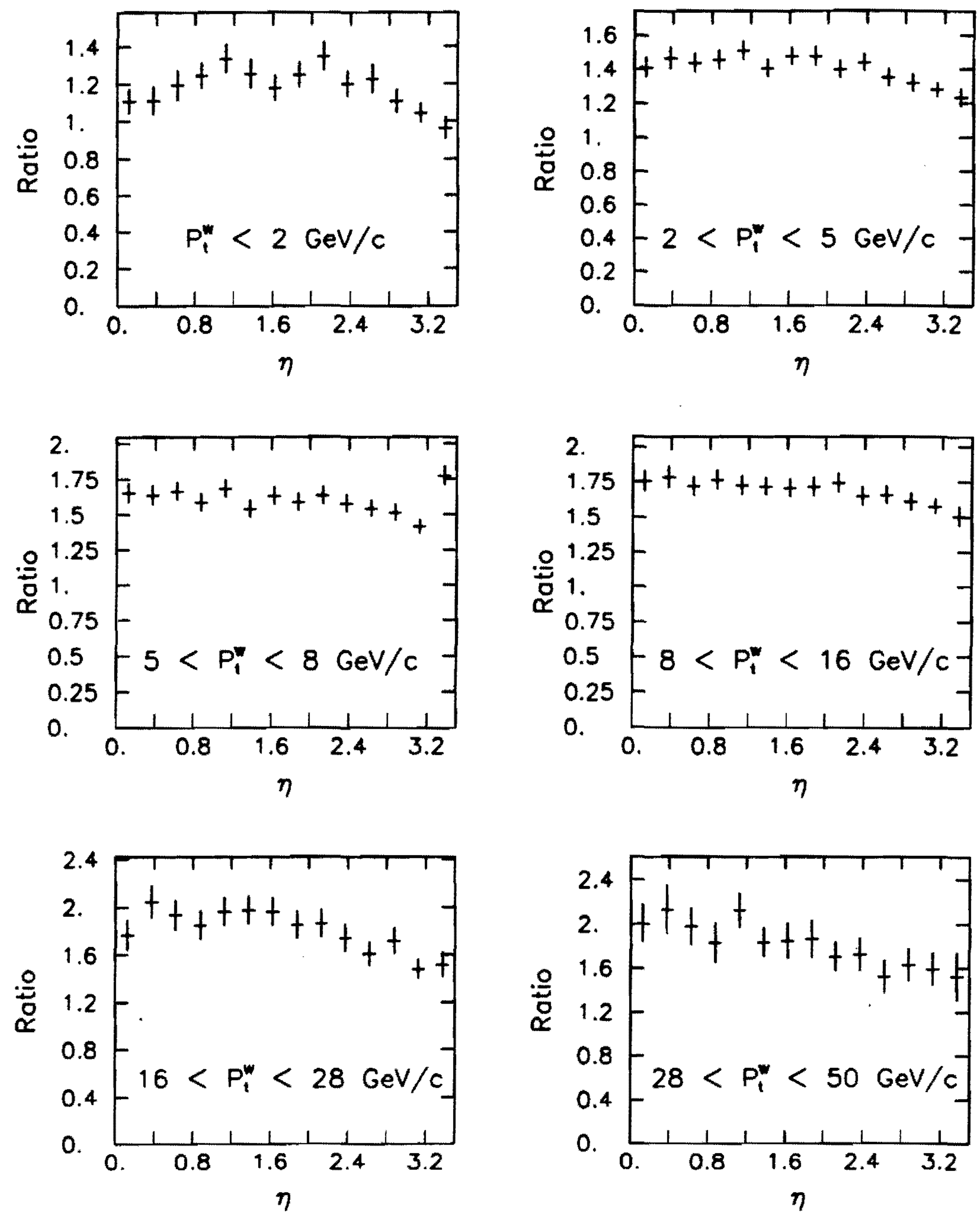

Figure 72. Final result for R^W vs. η within intervals in (uncorrected) p_t^{W}.

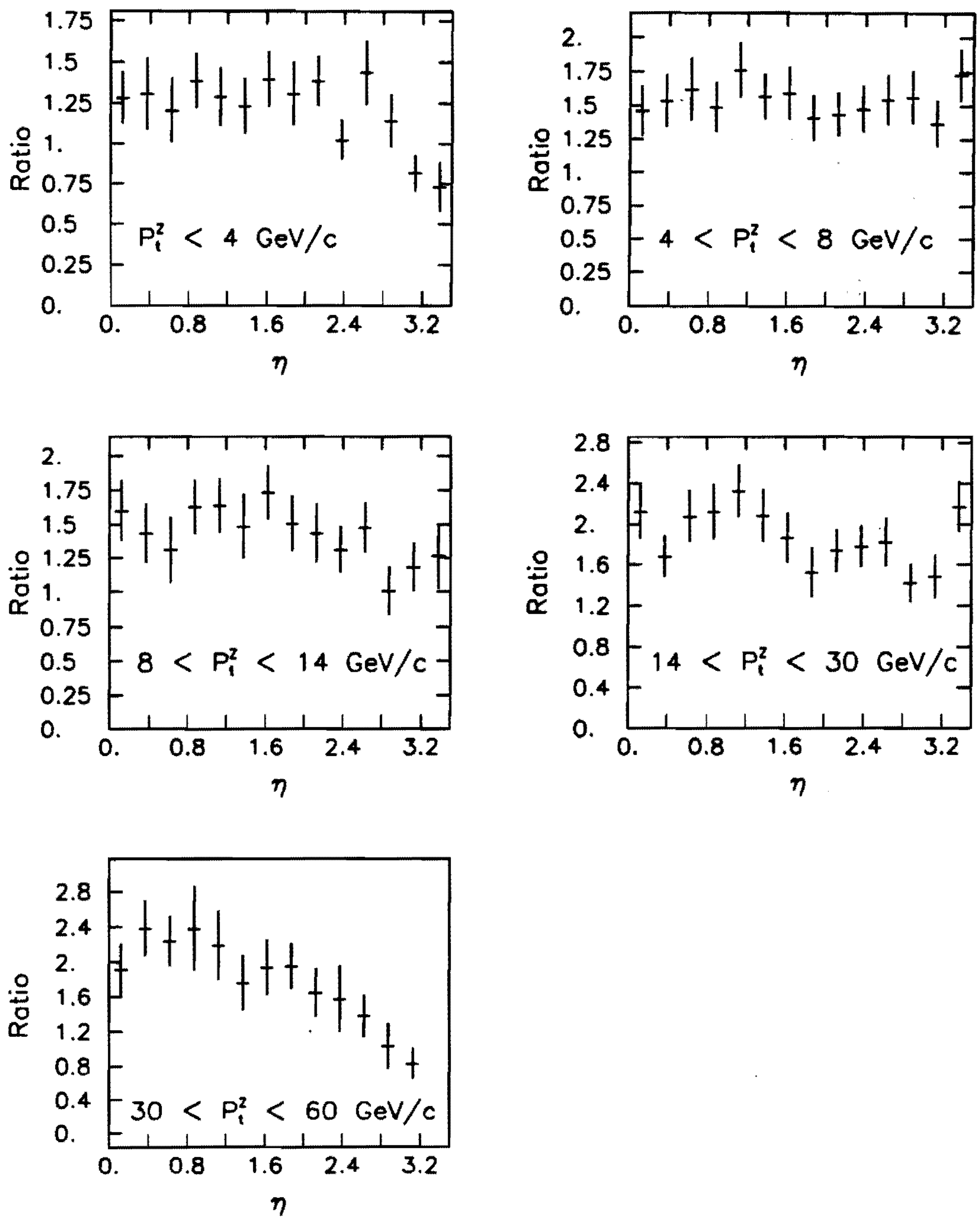

Figure 73. Final result for R^Z vs. η within intervals in p_t^Z.

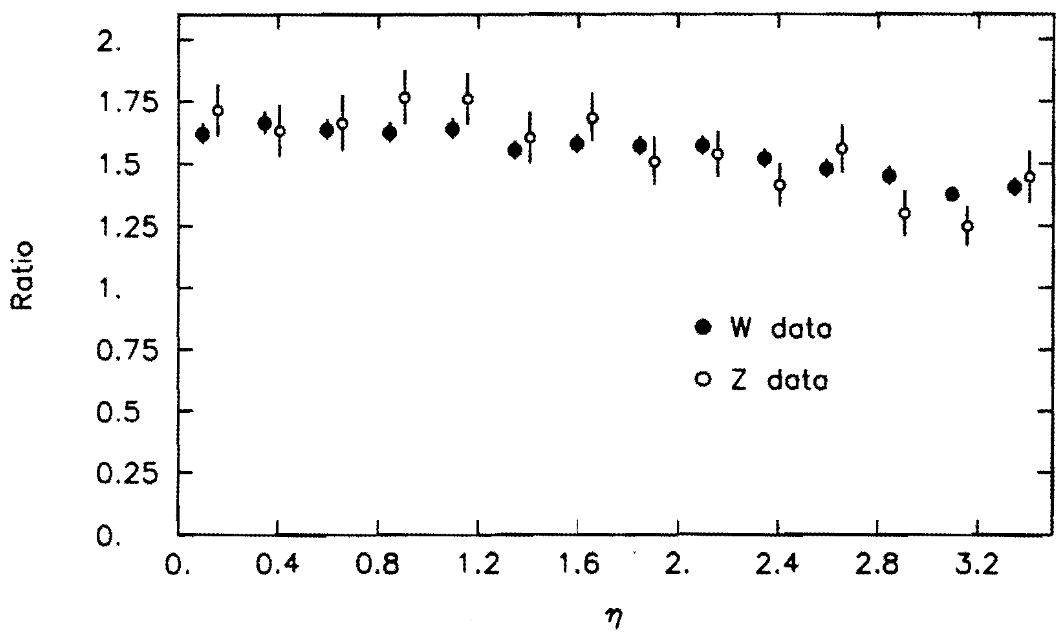

Figure 74. Final result for R^W and R^Z vs. η averaged over the boson p_t.

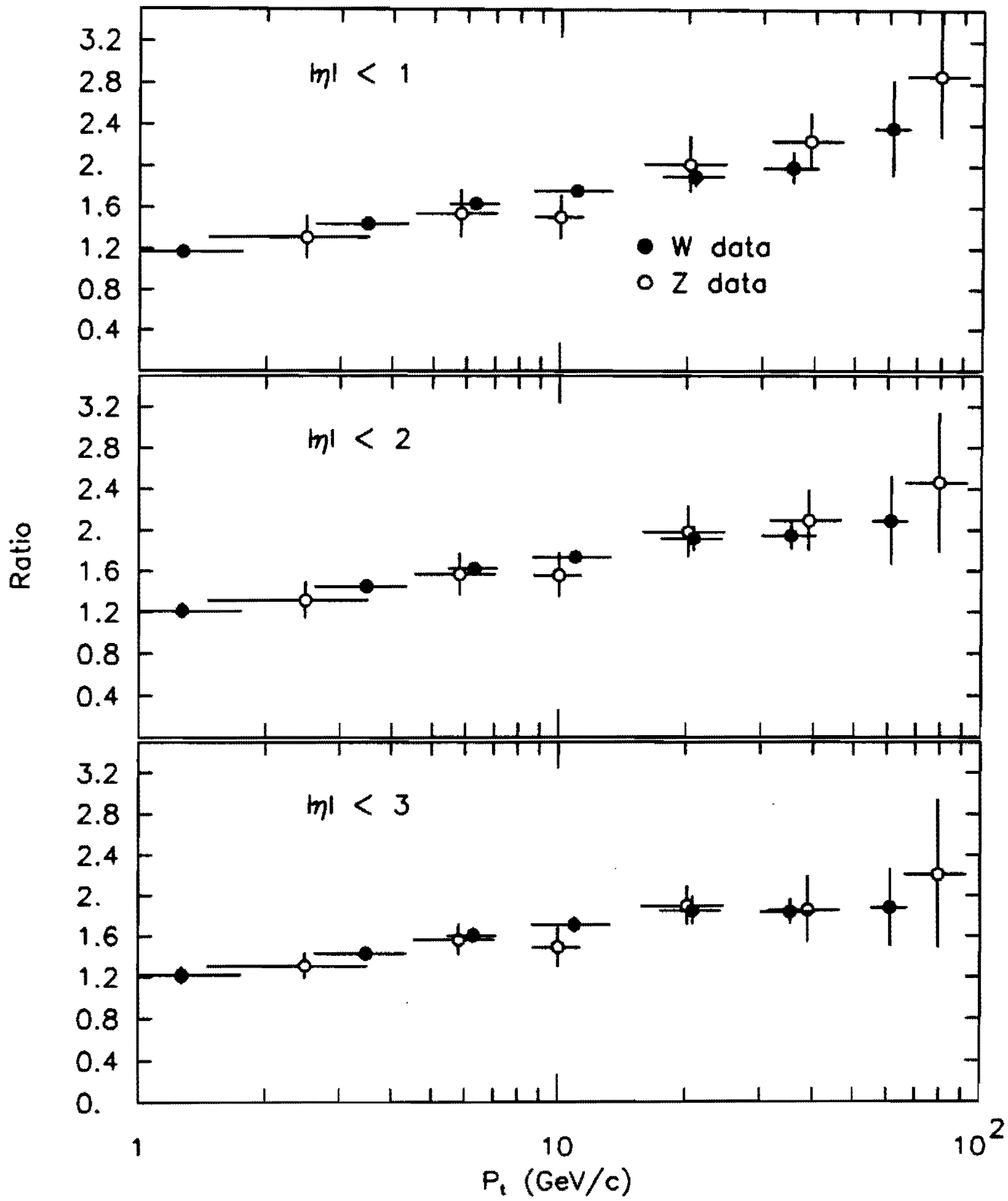

Figure 75. Final result for R^W and R^Z vs. the boson p_t. The values of $dN_{ch}/d\eta$ are averaged within the indicated η intervals before taking the ratio. The W p_t is uncorrected. The indicated uncertainties are statistical.

6.4.1 Cancellation of tracking efficiency correction

In certain regions of η, the tracking efficiency exhibits a strong dependence upon the vertex position. If we study R within such an η region as a function of the vertex position, then we can set an upper bound on the degree to which efficiency corrections fail to cancel.

To perform this test, we divide the data sets into two sections: events with vertices within 6 cm of the center of a VTPC module, and those with vertices within 6–12 cm from the center of the nearest module. The η distributions plotted in fig. 76 show that the efficiency is indeed significantly different for the two vertex regions. The ratios in fig. 77, however, do not depend significantly on the vertex region. The values of the R versus p_t and the vertex position are tabulated in tables 27 and 28.

6.4.2 Cancellation of charged particle background

The fraction of tracks contributed by background that pass track selection depends mainly on the value of the impact parameter cut used in the track selection, provided this value is sufficiently large. By choosing an impact parameter cut well out along the tail of the impact parameter distribution, we may assume that most of the change in $dN_{ch}/d\eta$ induced by a change in the impact parameter cut results from the differing amounts of background admitted by the track selection.

By studying the sensitivity of R as a function of the impact parameter, we can set an upper bound on the residual effect of background on our result. The plots in fig. 78 show that R^W is not sensitive to the choice of impact parameter cut.

Tables 29 and 29 list the values of R^W and R^Z as a function of p_t, the η interval and the impact parameter cut.

6.4.3 The effect of energy scale and smearing in p_t^{W}

Energy measurements of low energy hadrons are subject to significant non-linearities in the calorimeter response. Since the contribution of the underlying event to the measured value of p_t^{W} consists primarily of low energy particles, those most affected by large calorimeter non-linearities, we should expect significant scale errors in the W p_t distribution. Furthermore, the energy measurement fluctuations of the underlying event introduce an additional source of measurement errors. Naively, we might expect that the ratio measurement is relatively insensitive to p_t measurement errors, since R depends only logarithmically on p_t (see fig. 75). Here, we will test this intuitive conclusion by reproducing the W p_t measurement in the Z system, where we assume the directly measured p_t of the Z is better known than the indirectly measured p_t of the W.

The Z system provides an excellent cross check of the W p_t measurement, although the statistical power of the check is limited. The $\vec{p}_t$ of the Z should be exactly balanced by the $\vec{p}_t$ of the underlying event. Therefore, if we plot the difference in the *magnitude* of $\vec{p}_t^{\mathrm{Z}}$ calculated directly from the electron E_t and the value deduced from the $\vec{p}_t$ of the underlying event, then we obtain a measure of the precision of the underlying event p_t measurement. Since $R^W(p_t^{\mathrm{W}})$ is equal to $R^Z(p_t^{\mathrm{Z}})$ for all p_t, we can assume that the difference distribution applies to the W system as well.

Calculating p_t^{Z} from the underlying event follows the prescription described in eq. 6.2. Figure 79 shows the effect of the modified calculation on the p_t^{Z} distribution.

If we then recalculate R^Z versus p_t^Z using the value of p_t^Z calculated indirectly from the underlying event, we find that the additional smearing does not significantly alter the result (fig. 80). The values of the ratio R^Z versus p_t^Z from the underlying event are listed in table 31.

6.4.4 Estimating the systematic uncertainty

We estimate the systematic uncertainties by looking at the changes in R^W and R^Z as a function of the various parameters discussed in the preceding sections, and listed in tables 27–31. The systematic uncertainty in R^W from smearing of the W p_t distribution is assumed to be equal to the change in R^Z which results from calculating the Z p_t indirectly (table 31). Summing the individual contributions to the systematic uncertainty in quadrature yields the final systematic uncertainties quoted in tables 25 and 26. (See Appendix J for tables with individual contributions to the systematic uncertainty.)

6.5 Discussion

6.5.1 Comparison with previous data

We have measured the ratio of $dN_{ch}/d\eta$ in W and Z events to that in minimum bias events (R^W and R^Z, respectively) at $\sqrt{s}$ = 1800 GeV as a function of the boson p_t and the η interval (figs. 75 and tables 25 and 26). Averaging $dN_{ch}/d\eta$ within $|\eta| < 2$, for example, we find for a boson p_t near zero that the ratio $R^W(p_t = 0) = 1.21 \pm 0.07(\text{stat}) \pm 0.12(\text{sys})$, and $R^Z(p_t = 0) = 1.32 \pm 0.18(\text{stat}) \pm 0.11(\text{sys})$. If we average over all boson p_t and within $|\eta| < 2$, we find $R^W = 1.61 \pm 0.04(\text{stat})$.

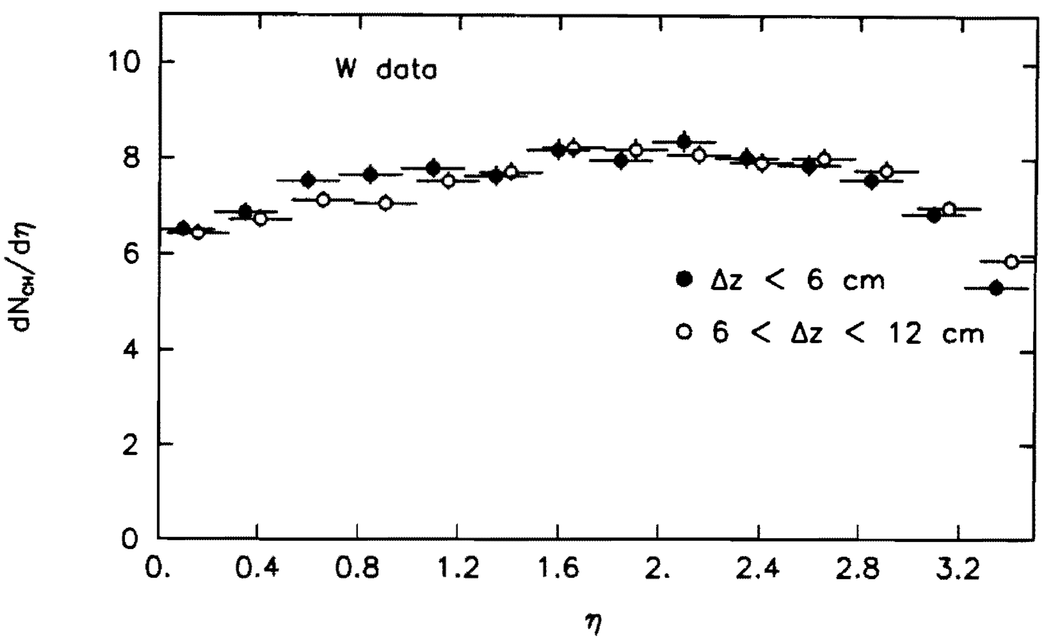

Figure 76. Dependence of $dN_{ch}/d\eta$ for W events on the vertex position. The distributions are averaged over the W p_t; the ranges in Δz, the distance from the event vertex to the center of the nearest VTPC module, are in centimeters. (The decay electrons have not been subtracted.)

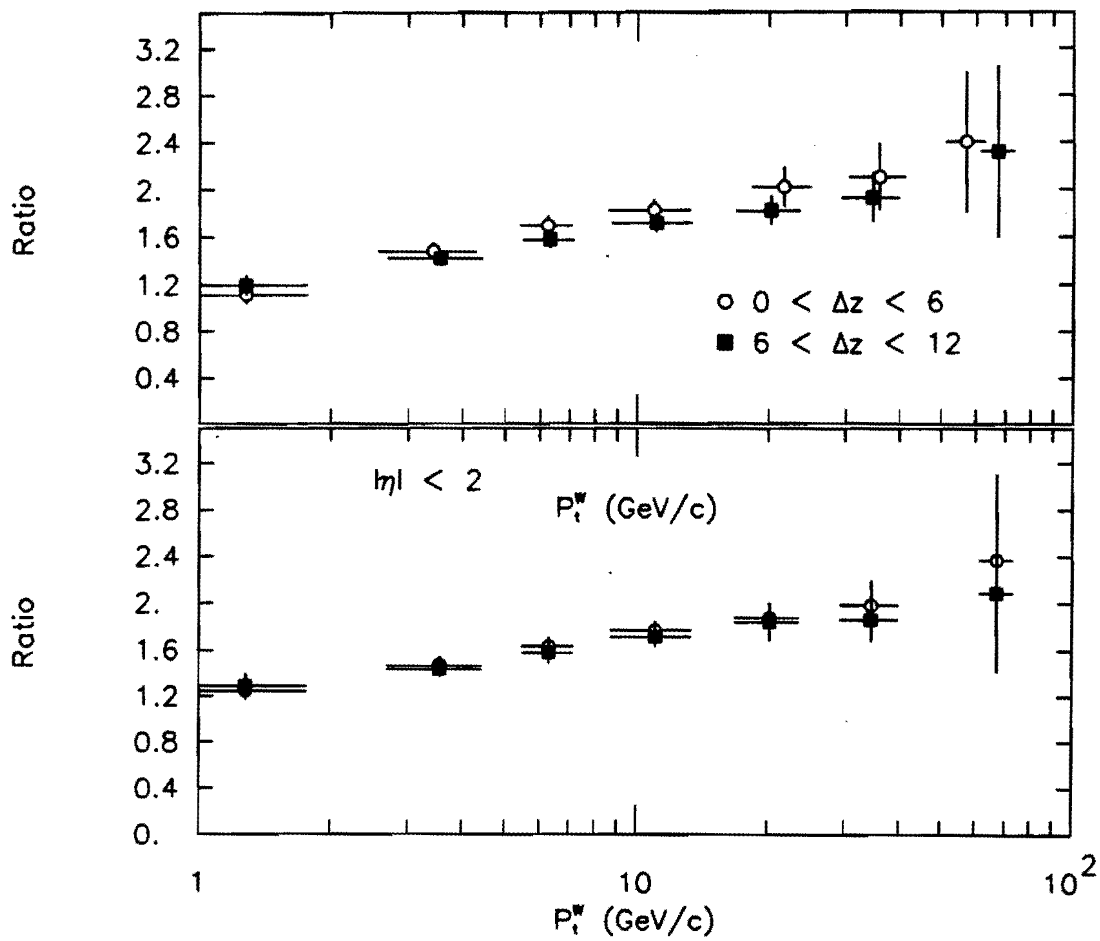

Figure 77. R^W vs. W p_t as a function of vertex position. The values of Δz are in centimeters.

Table 27. R^W vs. p_t^W as a function of the distance from the event vertex to the center of the nearest VTPC module (Δz).

	All	Δz (cm)	
p_t bin	data	0–6	6–12
R^W for $dN_{ch}/d\eta$ averaged over $\lvert\eta\rvert < 1$:			
0.0–2.0	1.17±0.06	1.11±0.08	1.19±0.08
2.0–5.0	1.44±0.05	1.48±0.07	1.42±0.07
5.0–8.0	1.63±0.05	1.69±0.08	1.57±0.08
8.0–16.0	1.76±0.06	1.82±0.09	1.71±0.08
16.0–28.0	1.90±0.10	2.02±0.17	1.82±0.13
28.0–50.0	1.98±0.15	2.10±0.28	1.93±0.21
50.0–100.0	2.36±0.46	2.40±0.60	2.31±0.73
R^W for $dN_{ch}/d\eta$ averaged over $\lvert\eta\rvert < 2$:			
0.0–2.0	1.21±0.07	1.11±0.10	1.29±0.10
2.0–5.0	1.45±0.05	1.46±0.08	1.44±0.08
5.0–8.0	1.62±0.06	1.66±0.09	1.58±0.09
8.0–16.0	1.73±0.07	1.78±0.10	1.71±0.09
16.0–28.0	1.92±0.12	2.03±0.20	1.84±0.16
28.0–50.0	1.94±0.14	2.10±0.29	1.86±0.19
50.0–100.0	2.09±0.43	2.09±0.55	2.09±0.68
R^W for $dN_{ch}/d\eta$ averaged over $\lvert\eta\rvert < 3$:			
0.0–2.0	1.22±0.08	1.09±0.12	1.31±0.12
2.0–5.0	1.43±0.06	1.42±0.09	1.42±0.08
5.0–8.0	1.60±0.07	1.63±0.10	1.57±0.10
8.0–16.0	1.71±0.07	1.76±0.11	1.68±0.10
16.0–28.0	1.85±0.14	2.00±0.24	1.74±0.17
28.0–50.0	1.84±0.12	1.98±0.25	1.76±0.18
50.0–100.0	1.88±0.38	1.95±0.49	1.77±0.60

The column heading "all data" refers to the range 0–12 cm in Δz. Uncertainties are purely statistical.

Table 28. R^Z vs. p_t^Z as a function of the distance from the event vertex to the center of the nearest VTPC module (Δz).

	All	Δz (cm)	
p_t bin	data	0–6	6–12
R^Z for $dN_{ch}/d\eta$ averaged over $\lvert\eta\rvert < 1$:			
0.0–4.0	1.31±0.12	1.13±0.16	1.48±0.19
4.0–8.0	1.54±0.16	1.79±0.27	1.33±0.17
8.0–14.0	1.50±0.20	1.34±0.26	1.62±0.28
14.0–30.0	2.02±0.19	2.05±0.26	1.98±0.27
30.0–60.0	2.24±0.33	2.01±0.39	2.79±0.60
R^Z for $dN_{ch}/d\eta$ averaged over $\lvert\eta\rvert < 2$:			
0.0–4.0	1.32±0.18	1.13±0.22	1.51±0.27
4.0–8.0	1.57±0.20	1.74±0.35	1.43±0.23
8.0–14.0	1.56±0.22	1.51±0.73	1.60±0.63
14.0–30.0	1.98±0.25	1.80±0.39	2.12±0.32
30.0–60.0	2.09±0.30	1.90±0.35	2.54±0.54
R^Z for $dN_{ch}/d\eta$ averaged over $\lvert\eta\rvert < 3$:			
0.0–4.0	1.31±0.21	1.12±0.24	1.50±0.32
4.0–8.0	1.56±0.23	1.72±0.42	1.43±0.25
8.0–14.0	1.49±0.21	1.35±0.26	1.59±0.24
14.0–30.0	1.89±0.27	1.74±0.46	2.01±0.31
30.0–60.0	1.86±0.27	1.72±0.32	2.17±0.49

The column heading "all data" refers to the range 0–12 cm in Δz. Uncertainties are purely statistical.

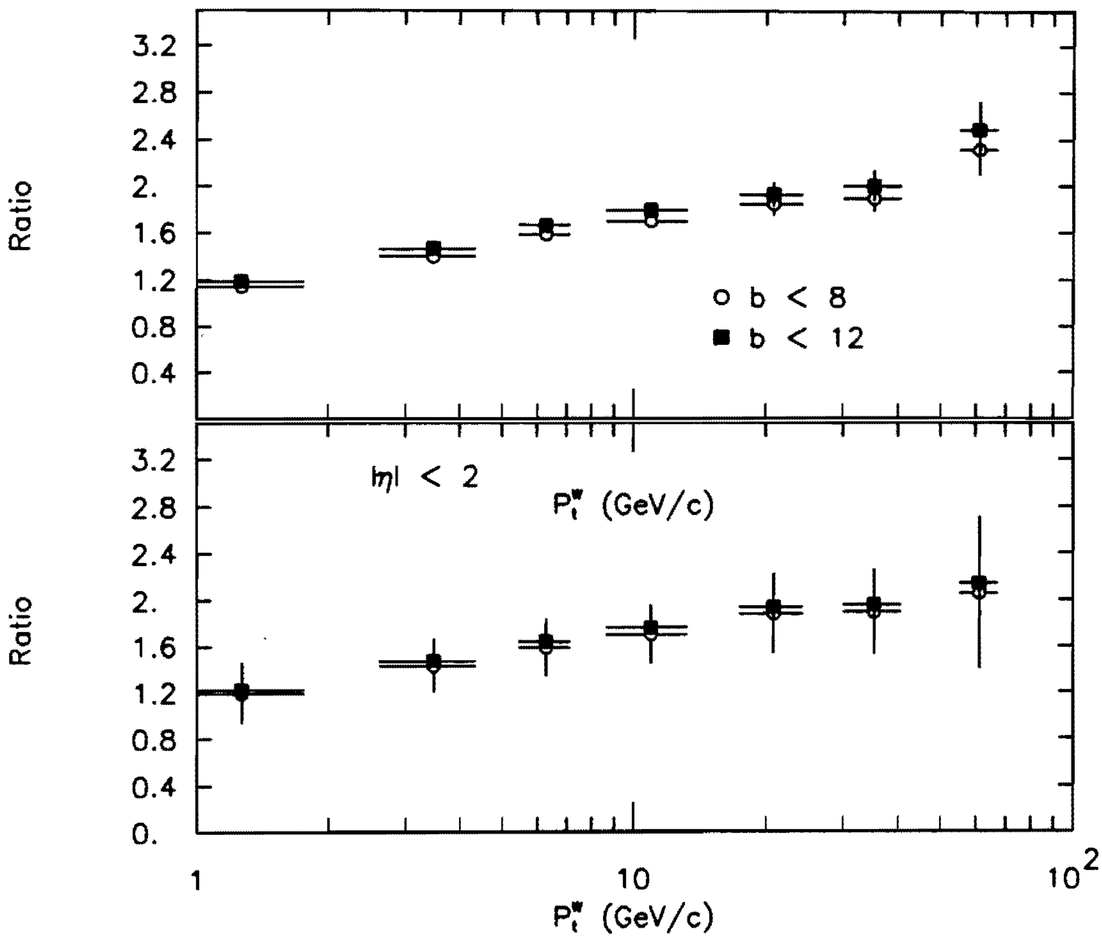

Figure 78. R^W vs. p_t as a function of impact parameter (b).

Table 29. R^W vs. p_t as a function of the maximum allowed track impact parameter (b_{max}).

p_t bin	$b_{max} = 8.0$	$b_{max} = 10^*$	$b_{max} = 12$
R^W for $dN_{ch}/d\eta$ averaged over $\lvert\eta\rvert < 1$:			
0.0–2.0	1.14±0.06	1.17±0.06	1.19±0.06
2.0–5.0	1.40±0.05	1.44±0.05	1.46±0.05
5.0–8.0	1.58±0.05	1.63±0.05	1.66±0.05
8.0–16.0	1.70±0.06	1.76±0.06	1.79±0.06
16.0–28.0	1.84±0.10	1.90±0.10	1.93±0.10
28.0–50.0	1.89±0.15	1.98±0.15	2.00±0.15
50.0–100.0	2.31±0.46	2.36±0.46	2.48±0.46
R^W for $dN_{ch}/d\eta$ averaged over $\lvert\eta\rvert < 2$:			
0.0–2.0	1.19±0.07	1.21±0.07	1.22±0.07
2.0–5.0	1.42±0.05	1.45±0.05	1.47±0.05
5.0–8.0	1.59±0.06	1.62±0.06	1.64±0.06
8.0–16.0	1.70±0.06	1.73±0.07	1.76±0.07
16.0–28.0	1.88±0.12	1.92±0.12	1.94±0.13
28.0–50.0	1.89±0.13	1.94±0.14	1.95±0.13
50.0–100.0	2.05±0.43	2.09±0.43	2.14±0.43
R^W for $dN_{ch}/d\eta$ averaged over $\lvert\eta\rvert < 3$:			
0.0–2.0	1.20±0.08	1.22±0.08	1.23±0.08
2.0–5.0	1.40±0.06	1.43±0.06	1.44±0.06
5.0–8.0	1.57±0.07	1.60±0.07	1.62±0.07
8.0–16.0	1.68±0.07	1.71±0.07	1.74±0.08
16.0–28.0	1.81±0.14	1.85±0.14	1.87±0.14
28.0–50.0	1.79±0.12	1.84±0.12	1.85±0.12
50.0–100.0	1.85±0.38	1.88±0.38	1.92±0.38

*nominal.

Table 30. R^Z vs. p_t as a function of the maximum allowed track impact parameter (b_{max}).

p_t bin	$b_{max} = 8.0$	$b_{max} = 10^*$	$b_{max} = 12$
R^Z for $dN_{ch}/d\eta$ averaged over $\|\eta\| < 1$:			
0.0–4.0	1.28±0.12	1.31±0.12	1.34±0.13
4.0–8.0	1.47±0.15	1.54±0.16	1.56±0.16
8.0–14.0	1.45±0.19	1.50±0.20	1.52±0.20
14.0–30.0	1.94±0.19	2.02±0.19	2.04±0.20
30.0–60.0	2.18±0.33	2.24±0.33	2.34±0.33
60.0–100.0	2.87±0.73	2.87±0.73	2.87±0.73
R^Z for $dN_{ch}/d\eta$ averaged over $\|\eta\| < 2$:			
0.0–4.0	1.29±0.18	1.32±0.18	1.34±0.19
4.0–8.0	1.53±0.20	1.57±0.20	1.59±0.21
8.0–14.0	1.53±0.46	1.56±0.22	1.57±0.46
14.0–30.0	1.93±0.24	1.98±0.25	2.00±0.25
30.0–60.0	2.05±0.30	2.09±0.30	2.14±0.30
60.0–100.0	2.43±0.68	2.46±0.68	2.46±0.68
R^Z for $dN_{ch}/d\eta$ averaged over $\|\eta\| < 3$:			
0.0–4.0	1.28±0.20	1.31±0.21	1.33±0.21
4.0–8.0	1.52±0.23	1.56±0.23	1.57±0.23
8.0–14.0	1.46±0.21	1.49±0.21	1.50±0.21
14.0–30.0	1.85±0.26	1.89±0.27	1.91±0.27
30.0–60.0	1.82±0.27	1.86±0.27	1.90±0.27
60.0–100.0	2.15±0.60	2.21±0.60	2.21±0.60

*nominal.

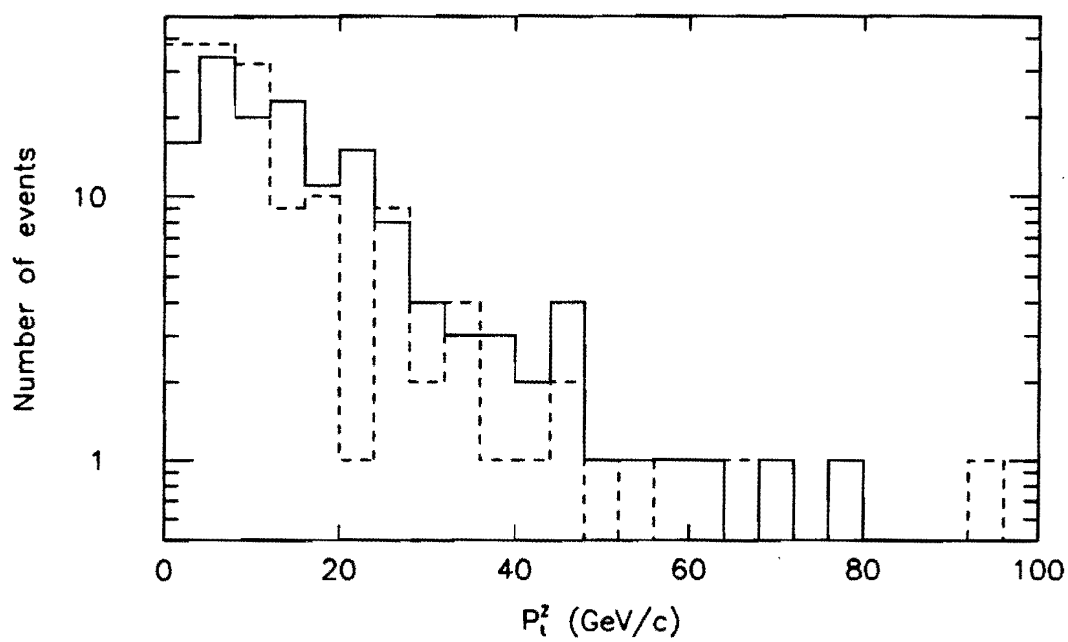

Figure 79. Distribution of p_t^Z calculated from underlying event. The dashed curve is the p_t^Z distribution measured using the electron energies directly.

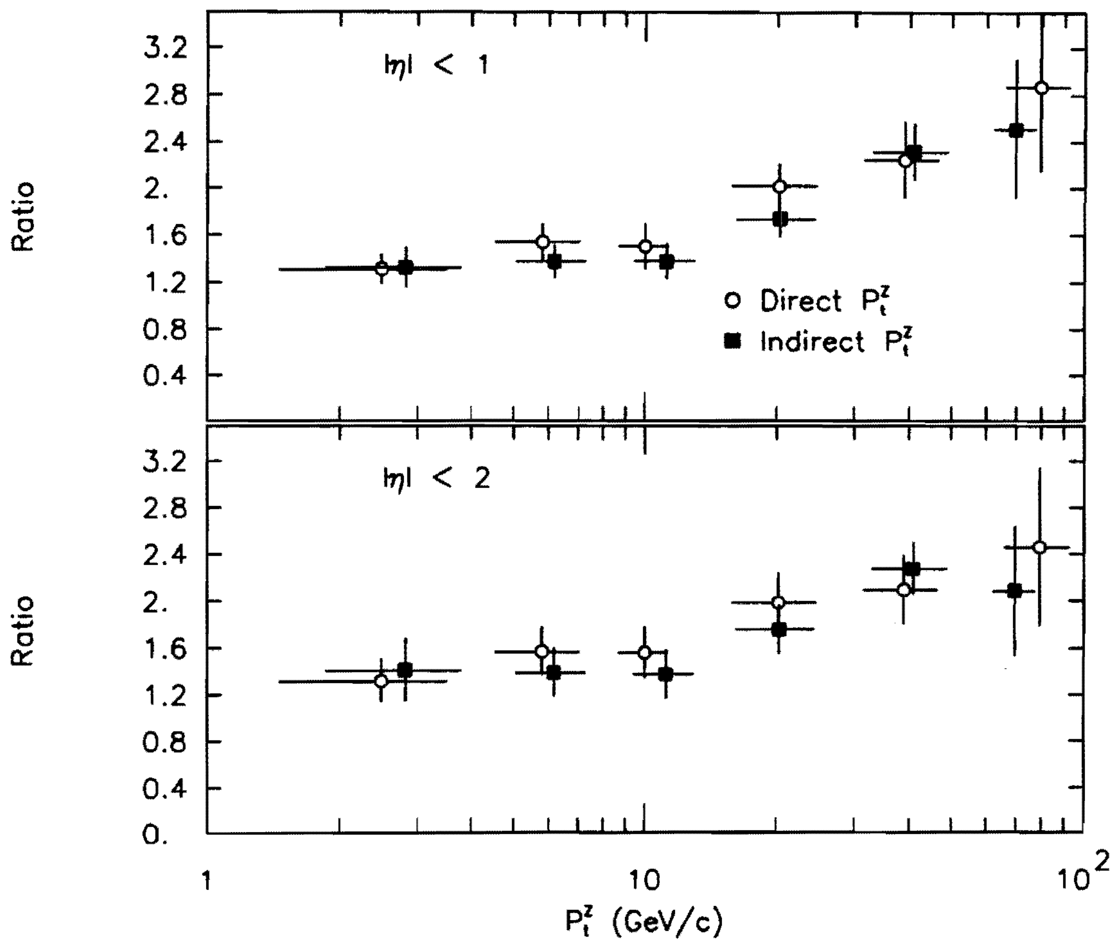

Figure 80. R^Z vs. p_t^Z using alternative p_t^Z calculations.

Table 31. The effect of an indirect p_t^Z measurement on R^Z vs. p_t^Z.

p_t bin	direct	indirect
R^Z for $dN_{ch}/d\eta$ averaged over $\lvert\eta\rvert < 1$:		
0.0–4.0	1.31±0.12	1.32±0.17
0.4–8.0	1.54±0.16	1.37±0.14
8.0–14.0	1.50±0.20	1.37±0.15
14.0–30.0	2.02±0.19	1.74±0.16
30.0–60.0	2.24±0.33	2.31±0.25
60.0–100.0	2.87±0.73	2.51±0.60
R^Z for $dN_{ch}/d\eta$ averaged over $\lvert\eta\rvert < 2$:		
0.0–4.0	1.32±0.18	1.41±0.27
4.0–8.0	1.57±0.20	1.39±0.21
8.0–14.0	1.56±0.22	1.38±0.21
14.0–30.0	1.98±0.25	1.75±0.21
30.0–60.0	2.09±0.30	2.27±0.22
60.0–100.0	2.46±0.68	2.08±0.55
R^Z for $dN_{ch}/d\eta$ averaged over $\lvert\eta\rvert < 3$:		
0.0–4.0	1.31±0.21	1.35±0.29
4.0–8.0	1.56±0.23	1.43±0.26
8.0–14.0	1.49±0.21	1.33±0.22
14.0–30.0	1.89±0.27	1.69±0.24
30.0–60.0	1.86±0.27	2.11±0.27
60.0–100.0	2.21±0.60	1.70±0.49

The uncertainties are statistical.

The UA1 and UA2 collaborations have previously measured properties of the underlying event associated with W and Z production and other hard scattering processes at the CERN $\bar{p}p$ collider. The CERN experiments, however, use not only the charged particle multiplicity to characterize the properties of the underlying event, as we have done, but also the mean transverse energy (excluding the decay electrons) and the mean transverse momentum of charged particles.

Using a sample of 37 $W^{\pm} \rightarrow e^{\pm}\nu$ candidates produced in $\sqrt{s}$ = 546 GeV $\bar{p}p$ collisions and characterized by p_t^e > 25 GeV/c and no jets with E_t > 3 GeV, the UA2 collaboration measures the average charged particle multiplicity ($\langle n_{ch} \rangle$) within $|\eta| < 2$ in W, Z and minimum bias events [6]. They report the values $\langle n_{ch} \rangle = 16.4 \pm 0.8$ in W and Z events, and $\langle n_{ch} \rangle = 14.7 \pm 0.2$ in minimum bias events. The electron is not counted in the multiplicity. The UA2 sample should consist primarily of W bosons produced with $p_t \approx 0$, and is therefore a low energy equivalent to our sample at $p_t^W = 0$. Taking the ratio of the UA2 values yields the result $R_{UA2}^W = 1.12 \pm 0.06$ at $p_t = 0$, which should be compared with the CDF values of $R^W = 1.21 \pm 0.14$, and $R^Z = 1.32 \pm 0.21$ at $p_t = 0$ quoted in the preceding paragraph. (The statistical and systematic uncertainties have been added in quadrature.) The CDF value lies less than one standard deviation above the UA2 result.

Comparing the average transverse energies in the two types of events, the UA2 experiment similarly found only a small difference between events with a W or Z at rest in the transverse plane and minimum bias events: $\langle E_t \rangle = 9.0 \pm 1.1$ GeV in W and Z events (excluding the electrons), and $\langle E_t \rangle = 8.8 \pm 0.2$ GeV in minimum bias events. Including jet events in the sample resulted in significant increases in all values for the boson events: $\langle n_{ch} \rangle = 19.3 \pm 1.9$ (corresponding to $R_{UA2}^W = 1.31 \pm 0.08$)

and $\langle E_t \rangle = 14.1 \pm 1.7$ GeV (yielding the ratio 1.60±.20 with the $\langle E_t \rangle$ in minimum bias events). These values suggest that the particles in the underlying event are not only more numerous, but also more energetic than those in a typical minimum bias event.

The UA2 ratios should be compared with the CDF p_t averaged ratio $R^W = 1.61 \pm 0.04$(stat) within $|\eta| < 2$. The CDF result suggests a still larger multiplicity in the average underlying event with increasing $\sqrt{s}$ energy. This could simply reflect the increased jet activity associated with the harder boson p_t spectrum at CDF energies.

The UA2 authors also investigate the underlying event associated with low-mass electron pair production. Since the leading order diagrams associated with production of intermediate vector bosons are topologically identical to those of Drell-Yan lepton pair production [82], the underlying event in the two types of events should be similarly related. For electron pairs within the mass region 11 GeV $< m_{e^+e^-} <$ 22 GeV, UA5 reports the values $\langle n_{ch} \rangle = 22.3 \pm 1.6$ and $\langle E_t \rangle = 14.8 \pm 1.6$ GeV for the mean charged particle multiplicity and mean transverse energy in the underlying event within $|\eta| < 2$. Since the data sample contains almost 50% background, primarily from heavy flavor production, the result is not easily interpreted, and probably should be ignored.

The UA1 collaboration reports the results of similar measurements using a sample of 240 $W^\pm \rightarrow e^\pm \nu$ candidates produced at $\sqrt{s}$ of 630 GeV, and a reference sample of 147,000 minimum bias events [5]. The UA1 W selection demands p_t^e and $\not{E}_t$ greater than 15 GeV. The measurements are confined to the region within $|\eta| < 2.5$. For

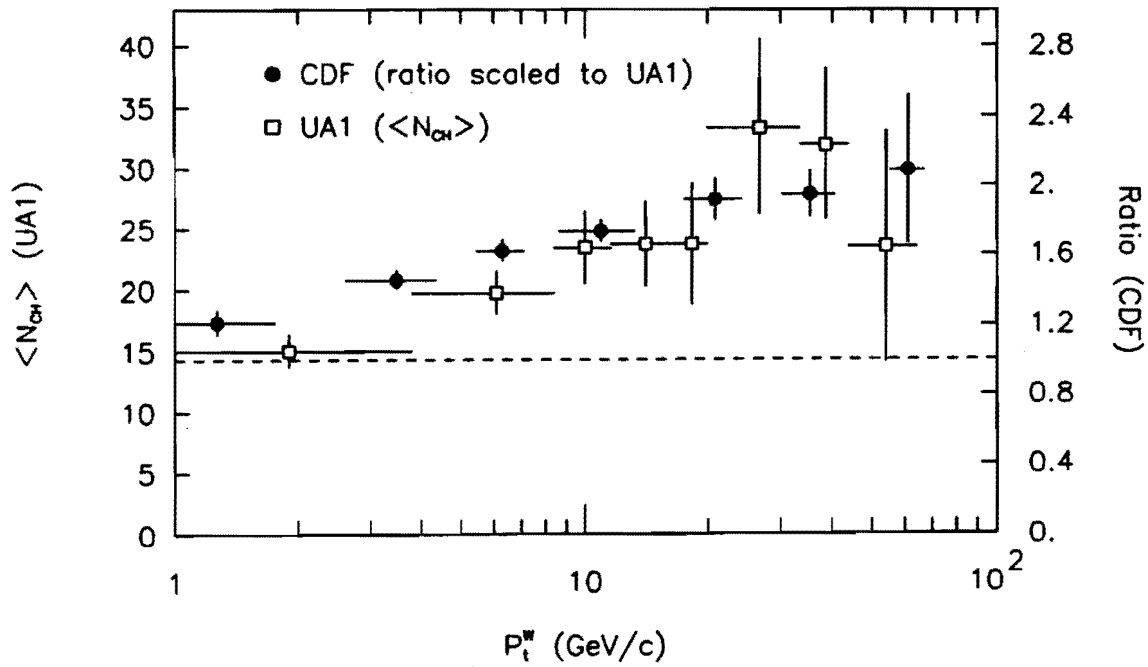

Figure 81. Charged particle multiplicity vs. p_t^W from UA1. The UA1 multiplicity (left-hand scale) is measured over the range $|\eta| < 2.5$. The CDF results (right-hand scale) for R^W within $|\eta| < 2$, scaled to the UA1 minimum bias multiplicity, are plotted also. The UA1 results are taken from [5]. The values of the W p_t for the CDF results are uncorrected.

the mean charged particle multiplicity in W events (averaged over the W p_t), UA1 reports the values $\langle n_{ch}^{\mathrm{W}} \rangle = 20.4 \pm 0.8 \pm 1.2$, compared to $\langle n_{ch}^{\mathrm{MB}} \rangle = 14.3 \pm 0.1 \pm 0.9$ in minimum bias events (where the uncertainties are statistical and systematic, respectively). These values correspond to the ratio 1.43±0.13, compared with the CDF value $R^W = 1.60 \pm 0.05$ within $|\eta| < 2.5$. Again, the multiplicity of the underlying event for all W events is observed to increase with increasing $\sqrt{s}$.

The mean multiplicity measured by UA1 within $|\eta| < 2.5$ as a function of the W p_t is plotted in fig. 81 superimposed upon the R^W values measured by CDF within $|\eta| < 2$. The CDF data points have been scaled to the UA1 minimum bias multiplicity. At low values of the W p_t the CDF results at $\sqrt{s} = 1800$ GeV lie above those of UA1 obtained at lower energy. In the lowest p_t bin, the UA1 multiplicities correspond to $R^W(p_t = 0) = 1.05 \pm 0.12$, to be compared with the CDF value $R^W = 1.21 \pm 0.14$ within $|\eta| < 2$.

UA1 also measures the mean transverse energy of particles in the underlying event, but in a somewhat different manner than does UA2: UA1 includes in the scalar sum only the energy of charged particles as measured in their tracking detectors. UA1 measures the mean transverse energy in W events, but includes only charged particles in the scalar sum. They report that $\langle \mathrm{E}_t \rangle = 13.9 \pm 0.6 \pm 0.8$ in W events, and $\langle \mathrm{E}_t \rangle = 7.68 \pm 0.04 \pm 0.46$ in minimum bias events. The result for W events is averaged over all boson p_t.

Compared to the previous data, we observe a slight increase in the multiplicity of the underlying event (for bosons nearly at rest in the transverse plane) relative to minimum bias events as the $\sqrt{s}$ energy increases, although the increase is not very significant. More significant is the increase in the multiplicity of the underlying event for inclusive bosons, perhaps indicative of the increased jet activity at the higher CM energy. So far in the analysis, we have not analyzed the possibility that changes in the detection efficiency with boson p_t have a significant effect on the average ratio.

6.5.2 Comparison with theoretical models

Recall that the Dual Parton model predicts that $R^W(p_t = 0) \equiv 1.5$, consistent with the UA1 p_t averaged result.[1] Both the UA1 and UA2 results at $\sqrt{s} = 546$ GeV differ significantly from the DPM prediction. The DPM authors subsequently argue that since W production at $\sqrt{s} = 546$ GeV is dominated by valence-valence annihilation processes (about 58–63% [59]), the DPM prediction for sea-sea production (see fig. 8) must be modified downward, although no specific prediction is provided [58].

At Tevatron energies, the previous objection is overcome: about 80% of the W production cross section arises from sea-sea and valence-sea contributions [59], both of which have DPM diagrams that each yield the prediction of $R = 1.5$ for a W p_t near zero. The DPM prediction should be insensitive to the remaining 20% from valence-valence production at the level of about 10% [84]. The CDF result does not support the DPM prediction. At $p_t = 0$, we find $R^W = 1.22 \pm 0.14$ within $|\eta| < 3$, a full two standard deviations below the DPM prediction. Although not a strong rejection, our result clearly favors a smaller enhancement in charged particle production for bosons produced at rest in the transverse plane. The slight rise in R^W observed between CDF and the CERN energies, although qualitatively consistent with the DPM intuition, is not sufficient to maintain quantitative consistency with DPM.

We should note that the DPM prediction applies to the multiplicity measured within the full phase space, whereas all of the experimental results apply to restricted pseudo-rapidity intervals. The effect of restricting the measurement to the central region, as we have done, is to increase the observed ratio, perhaps as much as 10–15% within $|\eta| < 3$ [84]. If the net effect of 20% valence-valence W production and the restricted rapidity interval results in an increase in the DPM prediction, then our rejection of the model becomes stronger.

[1] A preliminary result from CDF using 23 $W^{\pm} \to e^{\pm}\nu$ events from the 1987 run is also consistent with the value $R^W = 1.5$ [83]. The previous CDF work led directly into this analysis.

The second prediction, offered by Callen and Frankel [61], fares no better in the form first suggested. Using various functional forms for the spatial distributions, the authors obtain predictions for R ranging from 1.58 to 1.71, slightly above the DPM predictions. Since the model contains no provision for recoil jets, the authors suggest measuring the ratio at 90°to the boson p_t vector. We take this to be equivalent to measuring the value of R at $p_t = 0$. Again, the data does not support the simple impact parameter model of Callen and Frankel.

One possible explanation of the failure of this model is that the spatial distribution functions are too simple. For instance, Sjöstrand and van Zijl [60] found that their minimum bias model could not accommodate existing data using the simple spatial distributions proposed by Callen and Frankel, and used multicomponent distributions instead. Perhaps such a device could resurrect the simple impact parameter description proposed by Callen and Frankel.

Taking a more critical view, the model of Callen and Frankel is simply a generalized form of that proposed by Sjöstrand and van Zijl, a generalization obtained at the expense of a physically motivated framework. For this reason, we prefer to look at the R prediction of Sjöstrand and van Zijl. We should note that these authors have already reported that their model describes the underlying event in hard QCD scattering events in reasonable agreement with the data [60]. We regret that at the time of this writing, the author is unaware of any such published prediction.

Chapter 7

Conclusions

The angular distribution of secondaries produced in soft hadron-hadron interactions provides a probe into the mechanism of multiparticle production in such collisions. Measurements of the angular distribution have thus acquired an important role in testing our knowledge of this fundamental and striking characteristic of hadron physics. That multiparticle production processes are not well understood on a theoretical basis gives additional significance to measurements of this type.

There exist several models, however, which provide useful frameworks within which to interpret many features of multiparticle production. Within the context of the Dual Parton Model [55], for instance, particle production follows from fragmentation of "chains" connecting colored constituents of colliding hadrons. At high energies, the increasing contributions from the parton sea of the incident hadrons to the production of chains leads to a $\ln(s)$ dependence in the magnitude of $dN_{ch}/d\eta$ at $\eta = 0$ [55]. In Statistical Hydrodynamical Models [48,49,51], the details of the underlying interaction dynamics can be neglected by assuming a partial thermodynamic equilibrium is established in some fraction of the interacting matter. Under this assumption and further assuming that relativistic hydrodynamics governs the time evolution of the hadronic matter, the initial conditions specify entirely the multiparticle production properties. Using very general assumptions for the initial state, the SHM predicts that the mean multiplicity should increase as $s^{0.25}$, suggesting an energy dependence of $dN_{ch}/d\eta$ at $\eta = 0$ which is faster than any power of $\ln s$.

In this thesis, we present measurements of the pseudo-rapidity density of charged particles produced in $\bar{p}p$ collisions at $\sqrt{s}$ energies of 630 and 1800 GeV. The higher energy opens a new energy domain at a factor of two above the highest energy previously recorded. We measure the value of $dN_{ch}/d\eta$ at $\eta = 0$ to be 3.18±0.06±0.10 at 630 GeV, and 3.95±0.03±0.13 at 1800 GeV, where the first uncertainty denotes the statistical, and the second the systematic uncertainties. Upon comparison to similar results obtained at lower energies (fig. 82), we find that the central density increases faster than $\ln s$. Although this trend is evident in the UA5 data, the earlier results are also consistent with a linear dependence on $\ln s$ [7].

The DPM predicts a linear dependence in $dN_{ch}/d\eta$ at $\eta = 0$ up to $\sqrt{s}$ of 20 TeV (fig. 59). Our result appears inconsistent with this prediction.

The SHM predicts a power-law dependence in the multiplicity with an exponent of 0.25, and therefore a power-law in the central η density. The faster than $\ln(s)$ dependence of the central density is in qualitative agreement with the SHM. A power law-fit to our data and that of UA5 yields an exponent of 0.103±0.008.

Over the range $|\eta| < 3.5$, we find that the η distribution rises by about 20–25% as η increases[1] (fig. 83). The shape of the distribution for 1800 and 630 GeV data is approximately the same over this region. The CDF result lies somewhat above the UA5 result for $|\eta| > 1.5$, although the difference is less than 2 times the systematic uncertainty in the CDF values. Unfortunately, the geometry of the detector limits the CDF measurement to the central region. Thus, we are unable to test if fragmentation region scaling, observed to hold to the 10–20% level up to 900 GeV [7] continues to hold up to 1800 GeV.

By taking the ratio of the $\frac{dN_{ch}}{d\eta}$ distribution at two different energies, we take

[1]The values of $dN_{ch}/d\eta$ vs. η are compiled in table 18.

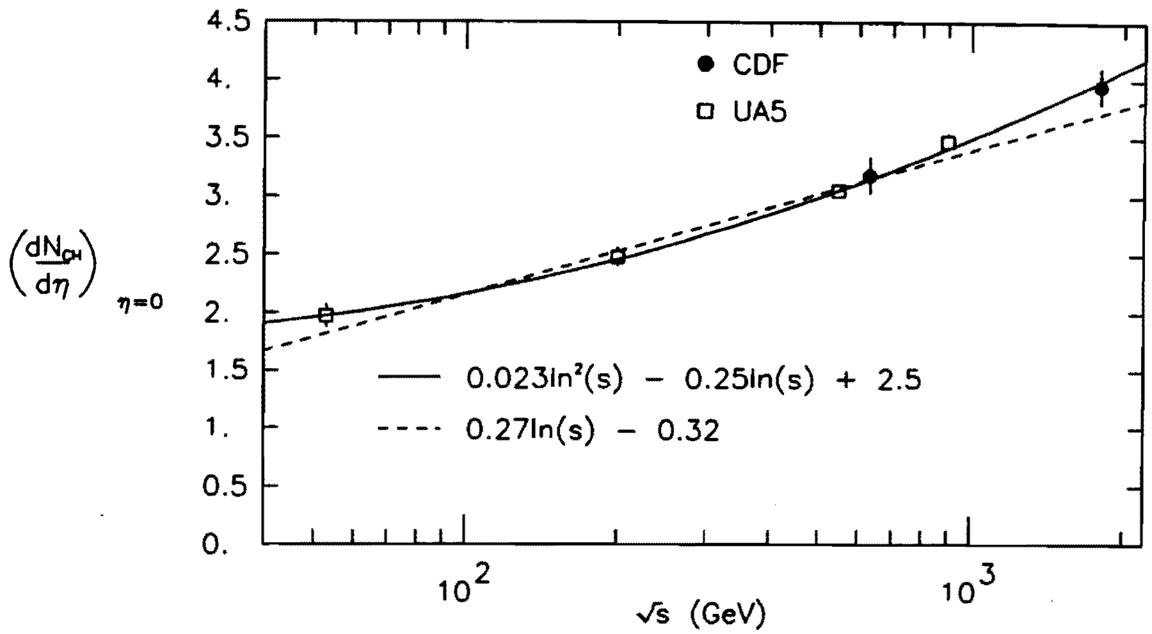

Figure 82. Energy dependence of $dN_{ch}/d\eta$ at $\eta = 0$. The UA5 results are taken from refs. [7].

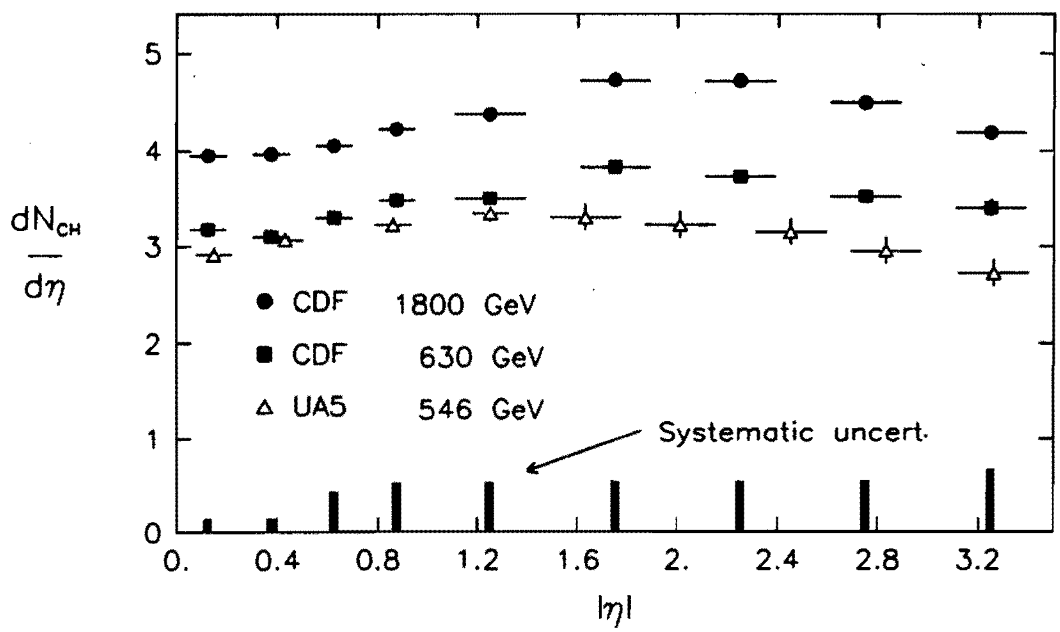

Figure 83. $dN_{ch}/d\eta$ distribution within $|\eta| < 3.5$. The UA5 data are from ref. [7].

advantage of the fact that some systematic errors in the $\frac{dN_{ch}}{d\eta}$ measurement are proportional to the multiplicity. These errors cancel almost completely in the ratio. The ratio[2] as a function of η (fig. 84) is consistent with being flat in the region $|\eta| < 3$, with an average value of $1.26\pm0.01\pm0.04$ within $|\eta| < 3$. The first uncertainty is statistical, while the second is systematic.

We further exploit the cancellation of systematic errors in the ratio of $dN_{ch}/d\eta$ in different data sets by studying the ratio of $dN_{ch}/d\eta$ in events in which we observe $W^{\pm} \rightarrow e^{\pm}\nu$ or $Z^0 \rightarrow e^+e^-$ decays, and that in minimum bias events. Since the final state leptons from the boson decays do not interact strongly, the ratio near a boson p_t of zero effectively isolates the contributions to particle production by the spectator system relative to other hard QCD sources (such as hard gluon radiation or quark-gluon Compton scattering). By comparing particle production in the spectator

[2]The values of the ratio are compiled in table 19.

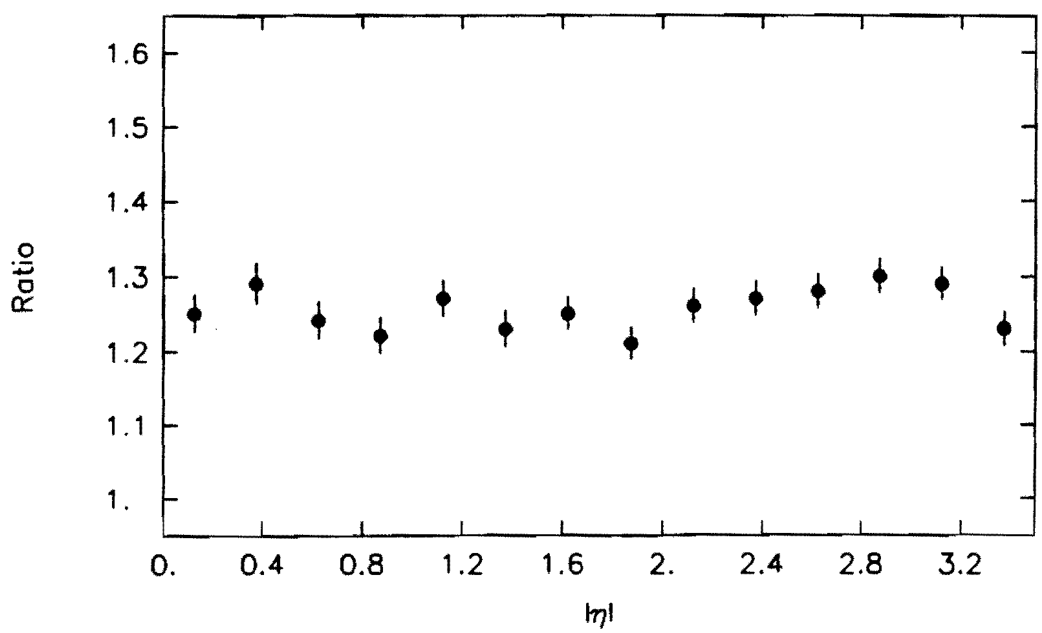

Figure 84. Ratio of $dN_{ch}/d\eta$ at 1800 GeV to that at 630 GeV.

system to that in minimum bias events, we may shed light on the multiparticle production mechanism in both.

In fig. 85, we show the ratio R^W and R^Z as a function of the boson p_t and the pseudo-rapidity interval[3], where R^W and R^Z are the ratio of $dN_{ch}/d\eta$ in W and Z events to that in minimum bias events. We find that the ratio R^W near p_t of zero is 1.22±0.08(stat)±0.12(sys), while R^Z is 1.31±0.21(stat)±0.11(sys), demonstrating a slight enhancement in the multiplicity within the central region for $W^\pm \rightarrow e^\pm \nu$ and $Z^0 \rightarrow e^+e^-$ events relative to minimum bias events. Neither the DPM [58] nor the impact parameter model of Callen and Frankel [61] correctly accounts for the observed enhancement at p_t of zero, although the latter leaves considerable room for modification (say along the lines of Sjöstand and van Zijl [60]). The CDF result is also somewhat higher than a comparable measurement by UA1 [5], which finds the ratio of multiplicities within $|\eta| < 2.5$ to be 1.05±0.12 near p_t^W of zero. Both experiments observe that the ratio increases as the p_t of the W increases, which has a simple qualitative explaination. The leading-order W production diagram produces W bosons at rest in the transverse plane, except for a small component of primordial p_t carried by the quarks. Boson production in the next-to-leading-order diagram is accompanied by a hard recoil gluon or quark producing a jet opposite the boson p_t.

[3]The values of R^W and R^Z are listed in tables 25 and 26.

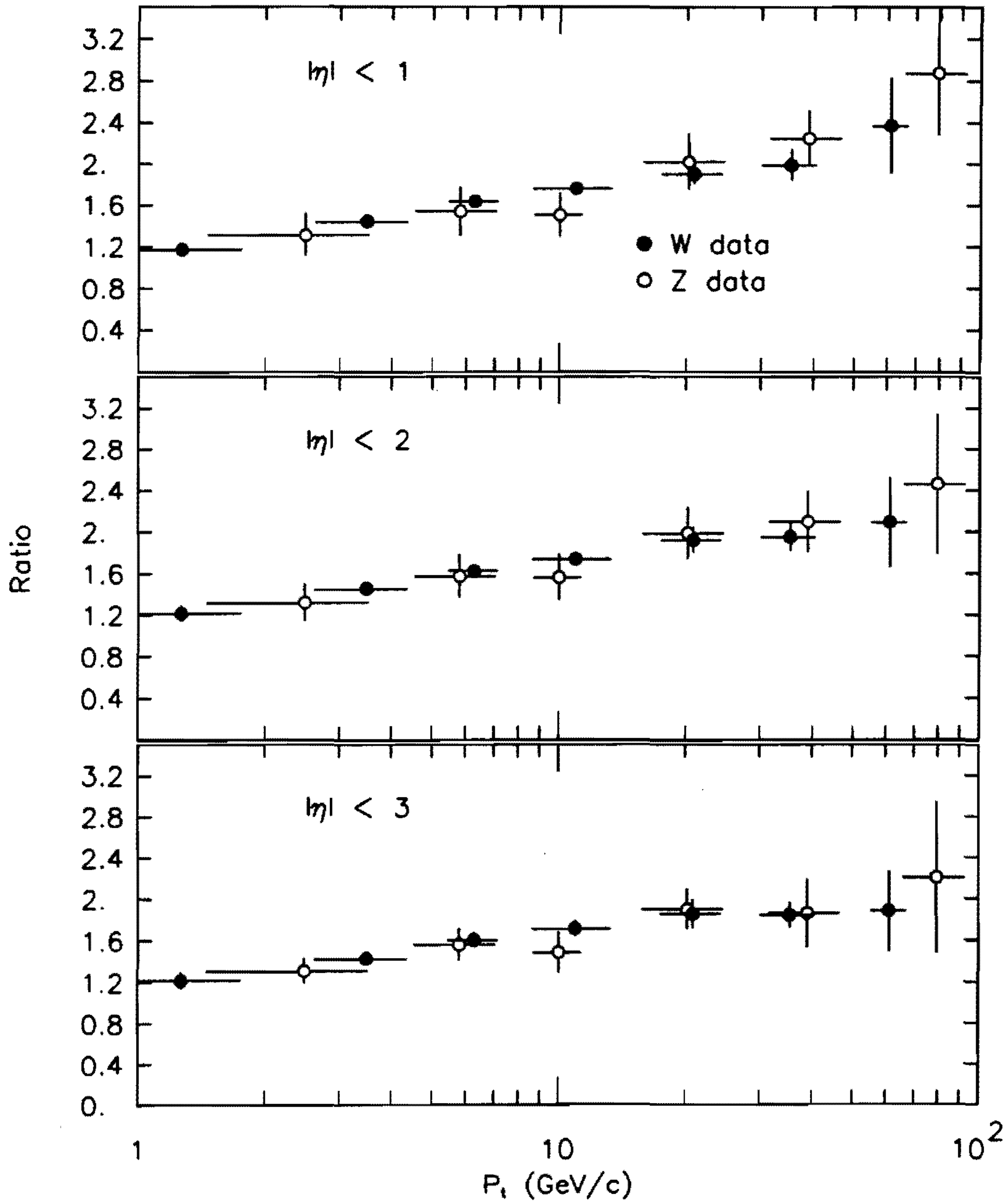

Figure 85. R^W and R^Z vs. the boson p_t. The values of $dN_{ch}/d\eta$ are averaged within the indicated η intervals before taking the ratio. The indicated uncertainties are statistical.

Appendix A

The 1987 CDF Collaboration

F. Abe,[16] D. Amidei,[3] G. Apollinari,[11] G. Ascoli,[7] M. Atac,[4] P. Auchincloss,[14] A. R. Baden,[6] A. Barbaro-Galtieri,[9] V. E. Barnes,[12] F. Bedeschi,[11] S. Belforte,[11] G. Bellettini,[11] J. Bellinger,[17] J. Bensinger,[2] A. Beretvas,[14] P. Berge,[4] S. Bertolucci,[5] S. Bhadra,[7] M. Binkley,[4] R. Blair,[1] C. Blocker,[2] J. Bofill,[4] A. W. Booth,[4] G. Brandenburg,[6] D. Brown,[6] A. Byon,[12] K. L. Byrum,[17] M. Campbell,[3] R. Carey,[6] W. Carithers,[9] D. Carlsmith,[17] J. T. Carroll,[4] R. Cashmore,[4] F. Cervelli,[11] K. Chadwick,[4,12] T. Chapin,[13] G. Chiarelli,[11] W. Chinowsky,[9] S. Cihangir,[15] D. Cline,[17] D. Connor,[10] M. Contreras,[2] J. Cooper,[4] M. Cordelli,[5] M. Curatolo,[5] C. Day,[4] R. DelFabbro,[11] M. Dell'Orso,[11] L. DeMortier,[2] T. Devlin,[14] D. DiBitonto,[15] R. Diebold,[1] F. Dittus,[4] A. DiVirgilio,[11] J. E. Elias,[4] R. Ely,[9] S. Errede,[7] B. Esposito,[5] A. Feldman,[6] B. Flaugher,[14] E. Focardi,[11] G. W. Foster,[4] M. Franklin,[6,7] J. Freeman,[4] H. Frisch,[3] Y. Fukui,[8] A. F. Garfinkel,[12] P. Giannetti,[11] N. Giokaris,[13] P. Giromini,[5] L. Gladney,[10] M. Gold,[9] K. Goulianos,[13] C. Grosso-Pilcher,[3] C. Haber,[9] S. R. Hahn,[10] R. Handler,[17] R. M. Harris,[9] J. Hauser,[3] T. Hessing,[15] R. Hollebeek,[10] L. Holloway,[7] P. Hu,[14] B. Hubbard,[9] P. Hurst,[7] J. Huth,[4] H. Jensen,[4] R. P. Johnson,[4] U. Joshi,[14] R. W. Kadel,[4] T. Kamon,[15] S. Kanda,[16] D. A. Kardelis,[7] I. Karliner,[7] E. Kearns,[6] R. Kephart,[4] P. Kesten,[2] H. Keutelian,[7] S. Kim,[16] L. Kirsch,[2] K. Kondo,[16] U. Kruse,[7] S. E. Kuhlmann,[12] A. T. Laasanen,[12] W. Li,[1] T. Liss,[3] N. Lockyer,[10] F. Marchetto,[15] R. Markeloff,[17] L. A. Markosky,[17] P. McIntyre,[15] A. Menzione,[11] T. Meyer,[15] S. Mikamo,[8] M. Miller,[10] T. Mimashi,[16] S. Miscetti,[5] M. Mishina,[8] S. Miyashita,[16] N. Mondal,[17] S. Mori,[16] Y. Morita,[16] A. Mukherjee,[4] C. Newman-Holmes,[4] L. Nodulman,[1] R. Paoletti,[11] A. Para,[4] J. Patrick,[4] T. J. Phillips,[6] H. Piekarz,[2] R. Plunkett,[13] L. Pondrom,[17] J. Proudfoot,[1] G. Punzi,[11] D. Quarrie,[4] K. Ragan,[10] G. Redlinger,[3] J. Rhoades,[17] F. Rimondi,[4] L. Ristori,[11] T. Rohaly,[10] A. Roodman,[3] A. Sansoni,[5] R. Sard,[7] V. Scarpine,[7] P. Schlabach,[7] E. E. Schmidt,[4] P. Schoessow,[1] M. H. Schub,[12] R. Schwitters,[6] A. Scribano,[11] S. Segler,[4] M. Sekiguchi,[16] P. Sestini,[11] M. Shapiro,[6] M. Sheaff,[17] M. Shibata,[16] M. Shochet,[3] J. Siegrist,[9] P. Sinervo,[10] J. Skarha,[17] D. A. Smith,[7] F. D. Snider,[3] R. St. Denis,[6] A. Stefanini,[11] Y. Takaiwa,[16] K. Takikawa,[16] S. Tarem,[3] D. Theriot,[4] A. Tollestrup,[4] G. Tonelli,[11] Y. Tsay,[3] F. Ukegawa,[16] D. Underwood,[1] R. Vidal,[4] R. G. Wagner,[1] R. L. Wagner,[4] J. Walsh,[10] T. Watts,[14] R. Webb,[15] T. Westhusing,[7] S. White,[13] A. Wicklund,[1] H. H. Williams[10] T. Yamanouchi,[4] A.Yamashita,[16] K. Yasuoka,[16] G. P. Yeh,[4] J. Yoh,[4] and F. Zetti,[11]

[1]*Argonne National Laboratory, Argonne, Illinois 60439*
[2]*Brandeis University, Waltham, Massachusetts 02254*
[3]*University of Chicago, Chicago, Illinois 60637*
[4]*Fermi National Accelerator Laboratory, Batavia, Illinois 60510*
[5]*Laboratori Nazionali di Frascati, Istituto Nazionale di Fisica Nucleare, Frascati, Italy*
[6]*Harvard University, Cambridge, Massachusetts 02138*
[7]*University of Illinois, Urbana, Illinois 61801*
[8]*National Laboratory for High Energy Physics (KEK), Tsukuba-gun, Ibaraki-ken 305, Japan*
[9]*Lawrence Berkeley Laboratory, Berkeley, California 94720*
[10]*University of Pennsylvania, Philadelphia, Pennsylvania 19104*
[11]*Istituto Nazionale di Fisica Nucleare, University and Scuola Normale Superiore of Pisa, Pisa, Italy*
[12]*Purdue University, West Lafayette, Indiana 47907*
[13]*Rockefeller University, New York, New York 10021*
[14]*Rutgers University, Piscataway, New Jersey 08854*
[15]*Texas A&M University, College Station, Texas 77843*
[16]*University of Tsukuba, Ibaraki 305, Japan*
[17]*University of Wisconsin, Madison, Wisconsin 53706*

Appendix B

Coordinate Systems

The coordinate conventions used throughout this document conform to the scheme adopted by CDF for descriptions of the detector and event structures.

B.1 Cartesian coordinates

When specifying a point in Cartesian coordinates with respect to the entire CDF detector, we use the following conventions:

- The origin is at B0, the nominal interaction point located at the exact center of the detector
- The z-axis lies parallel to the beam axis with protons travelling toward positive z.
- The y-axis lies parallel to the vertical and increases in the upward direction.
- The x-axis, chosen such that a right-handed coordinate system results, lies in the horizontal plane and increases in the direction away from the center of the accelerator ring.

To put this in more geographical terms (all directions are based on "site" north):

- Since protons enter the detector from the west travelling east (and, obviously, anti-protons from the east travelling west), the z-axis increases to the east.
- The x-axis increases to the north.
- The y-axis still points up.

B.2 Polar coordinates

When specifying a point in polar coordinates:

- The origin is at B0.
- The polar angle θ is measured from the positive z-axis toward the negative z-axis, and is specified within the range 0–π. For descriptions of physical

processes, it is often more convenient to specify the polar angle in terms of pseudo-rapidity ($\eta = -\ln\tan(\theta/2)$). In this form, negative η points in the negative z direction, while positive η points in the positive z direction.

- Azimuth, ϕ, is measured from the positive x-axis toward the positive y-axis, and is specified within the range 0–2π.

Appendix C

Track Trajectories, Projections, and Fits

Charged particles moving within a uniform magnetic field travel in helical trajectories. Represented in Cartesian coordinates, a track originating from a vertex located at z_0 on the z-axis follows the curve described by:

$$\begin{aligned} x &= \rho\left[\sin\left(\frac{t}{\rho\cot\theta} \pm \phi_0\right) \mp \sin\phi_0\right] \\ y &= \rho\left[-\cos\left(\frac{t}{\rho\cot\theta} \pm \phi_0\right) \pm \cos\phi_0\right] \\ z &= \begin{cases} z_0 \text{ for } \cot\theta = 0 \\ z_0 + t \text{ otherwise} \end{cases} \end{aligned} \tag{C.1}$$

where ρ = the radius of curvature, $\phi_0 = \phi$ of the tangent to the track at the vertex, θ = the polar angle of the track trajectory at the vertex, t = a parameterization variable, and the upper sign is applied to the curvature of positively charged particles.

Using only wire data, a VTPC octant measures the projection of this trajectory onto the plane passing through the center of the octant, perpendicular to the wires. If we define a local y-axis along the intersection of the mid-plane and the wire plane, this projection is described by:

$$y_{loc} = \rho\{\sin[\alpha(z - z_0) \pm (\phi_0 - \phi)] - \sin[\pm(\phi_0 - \phi_{mp})]\}, \tag{C.2}$$

where $\phi_{mp} = \phi$ of the mid-plane, and $\alpha = 1/(\rho\cot\theta)$. Inverting this equation to obtain an expression for z, we get:

$$z = z_0 + \rho\cot\theta\{\sin^{-1}[\frac{y_{loc}}{\rho} + \sin(\phi_0 - \phi)] - (\phi_0 - \phi)\}. \tag{C.3}$$

For $\rho \gg y$, we get an approximately linear trajectory:

$$z \approx z_0 + \frac{y_{loc}\cot\theta}{\cos(\phi_0 - \phi_{mp})}. \tag{C.4}$$

But if $\rho \sim y$, then significant deviations from linearity occur.

Since the VTPC measures neither the curvature nor the exact azimuthal position, we fit tracks such that hits closest to the beam axis, those least susceptible to deviations from linearity, are weighted more heavily than the hits farther away. We determine the amount to "de-weight" the outer hits by averaging the deviation from linearity, assuming a track with the average p_t, over relevant values of ϕ_0:

$$\langle \Delta z_d(y_{loc}) \rangle = \left(\frac{4}{\pi}\right) \rho \cot\theta \int_{-\frac{\pi}{8}}^{\frac{\pi}{8}} d\phi \left\{ \sin^{-1}\left[\frac{y}{\rho} + \sin\phi\right] - y \right\}. \tag{C.5}$$

The mean deviation at a given wire is obtained by evaluating the integral for a value of y_{loc} corresponding to the wire position. We arrive at the weight for a hit by first subtracting from the mean deviation at the wire position the deviation for the inner-most wire, $\langle \Delta z_d(y_0) \rangle$:

$$\Delta z = \langle \Delta z_d(y_{loc}) \rangle - \langle \Delta z_d(y_0) \rangle.$$

The hit is then given the statistical weight, w, defined by:

$$w = \frac{1}{(\Delta z)^2 + \sigma_z^2}, \tag{C.6}$$

where $\sigma_z =$ the expected z resolution of the hit.

Appendix D

Rules for Interactive Reconstruction

Below are the scanning rules used throughout the visual scan. Along with the listed rules, the scanners are instructed to resolve geometical ambiguities in such a manner as to minimize the number of tracks consistent with all the data under consideration. The reconstruction program similarly attempts to minimize the number of tracks in its solution of ambiguities. The comments within brackets have been added for clarity.

D.1 Scanning rules

A. What to do:

1) Any track which is reconstructed properly should be left alone.

2) Any track which is reconstructed properly except for the number of hits found or the specific hits chosen (see 11 below) should be modified to completion.

3) Pairs of 2D tracks which are unambiguously merged into 3D tracks should be merged.

4) 3D tracks which result from incorrectly matched 2D segments should be split.

5) Tracks which are unambiguously spurious (i.e., reconstructed through noise or some set of unrelated secondaries) should be deleted. Any track found by the automatic reconstruction which belongs to a spiral (see 8) or other track which does not originate in the beam pipe should be considered spurious and deleted.

6) Tracks originating in the beam pipe in the region of the vertex (see next section) which are not found by the automatic reconstruction should be created.

B. To which tracks:

7) Consider only tracks which originate in the beam pipe. Any evidence to the contrary is sufficient cause to ignore the track OR DELETE IT IF IT WAS FOUND BY THE AUTOMATIC RECONSTRUCTION. [*Emphasis in original.*]

8) Any track which completes one full turn of its spiral within the radius of the VTPC should be ignored. Pieces of such tracks which are found by the automatic reconstruction should be deleted.

9) Ignore tracks which exit the ends of the VTPC before crossing wire 6. For tracks which exit below wire 6:

   a) do not create it if not found by the automatic reconstruction.

   b) do not modify it if improperly reconstructed by the automatic reconstruction.

10) Nothing with fewer than four hits is a track.

11) Modify tracks according to the following rules:

    a) for tracks with greater than about 10 hits, modify only if 2 or more hits have been improperly chosen or missed.

    b) for tracks with fewer that about 10 hits, modify if any hit is improperly chosen or missed.

    c) any hit which could be reasonably chosen for two or more distinct tracks should be deleted from both (or considered as improperly chosen for the purposes of (a) and (b) above).

12) Apply the above criteria to any track which intersects the beam axis within one full module (or two half-modules) [*about 36 cm*] of the primary vertex. All other tracks may be ignored (neither created nor modified).

C. To which events:

13) Consider only events with a primary vertex position within ± 50 cm of B_0 [*the nominal interaction point*]. This event selection will be performed

automatically on the input file. Thus, the event numbers of a given file may not be sequential (but the B/F= feature [*refers to a command used to start the display program at a particular event*] will still work as before).

[*Note: This vertex cut was changed during the middle of middle of the scan to* $\pm$ *75 cm.*]

14) If the primary vertex of any event is chosen improperly, make a note on the log sheet and go to the next event.

Appendix E

Check of Systematic Uncertainty in C_{eff}

The reconstruction program allows apparent over-efficiencies in regions where tracks cross more than one module. Segments of a single track which appear in different VTPC modules are sometimes reconstructed as two distinct tracks. Within the region $0.75 < |\eta| < 1.25$, we find that the fraction of all tracks which belong to this class of module-crossing tracks is a strong function of the event vertex position. Studying the efficiency corrected $dN_{ch}/d\eta$ distribution as a function of Δz (the distance from the event vertex to the middle of the nearest VTPC module) within this η range provides a means to estimate the systematic uncertainty in the efficiency measurement for module-crossing tracks.

For convenience, we use the following notation: $\rho(\eta) = (dN_{ch}/d\eta)_\eta$, the track density at a given η; $\sigma_{\mathbf{stat}}$ = the statistical error in ρ; $\sigma_{\mathbf{eff(stat)}}$ = the systematic error in ρ due to the statistical error in the efficiency; and $\sigma_{\mathbf{eff(sys)}}$ = the systematic error in ρ due to the systematic error in the efficiency measurement (which we want to estimate). Next, we note that within $0.75 < |\eta| < 1.25$, events for which 8 cm $< \Delta z <$ 12 cm have a relatively low fraction of module crossing tracks compared to those for which $\Delta z < 4$ cm. It is therefore reasonable to assume that within this $|\eta|$ range, $\rho(\eta)$ for the former Δz range is unbiased, whereas $\rho'(\eta)$ for the latter Δz range is subject to the systematic error in question (where the primed quantity is introduced only to distiguish $\rho(\eta)$ measured in different Δz ranges). The differences $(\rho(\eta_1) - \rho'(\eta_1))$, and $(\rho(\eta_2) - \rho'(\eta_2))$, where η_1 and η_2 denote the two η bins within $0.75 < |\eta| < 1.25$, indepedently sample this systematic error. Taking these as a two point estimate of the total variance, $\sigma^2_{\mathrm{tot}} = (\sigma_{\mathbf{stat}} + \sigma_{\mathbf{eff(stat)}} + \sigma_{\mathbf{eff(sys)}})^2$, we find that $\sigma_{\mathbf{eff(sys)}}/\rho(\eta) \approx 0.067$. This method thus arrives at an estimated systematic uncertainty that is somewhat smaller than that calculated in Section 3.2.3. We choose to use the more conservative estimate for the final result.

Appendix F

Run Statistics and Information

Table 32. Run statistics for minimum bias runs used in $dN_{ch}/d\eta$ measurements.

Run	$\sqrt{s}$ (GeV)	t_{live} (sec)	Bnch	N_{trig}	Rejected events N_{CTC}	$N_{MR/CR}$	N_{bg}	N_{bb}	N_{all}
6384	1800	18.20	ABC	2079	27	4	479	1569	1003
6385	1800	19.32	ABC	2061	27	8	483	1543	924
6985	1800	10.71	B	1787	36	13	46	1692	991
6986	1800	13.89	B	1729	5	0	48	1676	987
7242	1800	18.38	B	6767	36	1	240	6490	4035
7292	1800	1.96	ABC	1791	5	0	73	1713	1033
7444	1800	10.07	ABC	6647	37	1	347	6262	4005
7484	1800	6.66	ABC	3271	21	0	275	2975	1833
7536	630	371.58	BC	8108	20	1	3351	4736	2837
7559	1800	?	B	5168	32	1	269	4866	2926
7560	1800	?	B	5577	29	0	316	5232	3233

The column under t_{live} indicates the detector live time for the run; "bnch", the filled $\bar{p}p$ bunches (denoted "A"–"C") in the machine (only events from filled bunches contribute to the final distributions); N_{trig}, the total number of detector triggers recorded for the filled bunches; N_{CTC}, the number of events rejected on the basis of noise in the CTC; $N_{MR/CR}$, the number of events with out-of-time hits in the calorimetry, indicating possible background from the main ring accelerator or cosmic rays; N_{bg}, the number of events classified as beam-gas; N_{bb}, the number of events classified as beam-beam; and N_{all}, the number of events passing all cuts and used to obtain the $dN_{ch}/d\eta$ distribution. The question marks indicate that no statistics were available for those runs.

Table 33. Event classification summary by run and bunch.

Run	$\sqrt{s}$ (GeV)	Bnch	N_p ($\times 10^9$)	$N_{\bar{p}}$ ($\times 10^9$)	N_{trig}	N_{bg}	N_{bb}
6384	1800	A	30.31	0.38	654	154	502
		B	26.34	0.55	875	165	716
		C	26.55	0.31	550	160	393
6385	1800	A	29.52	0.37	667	163	505
		B	25.90	0.51	892	171	722
		C	26.11	0.27	502	149	353
6985	1800	A	35.34	0.00	37	37	0
		B	39.51	6.16	1787	46	1751
		C	42.41	0.00	35	31	4
6986	1800	A	35.07	0.00	55	52	3
		B	39.38	5.35	1729	48	1700
		C	41.94	0.00	50	49	1
7242	1800	A	30.09	0.00	51	51	0
		B	43.92	3.59	6767	240	6573
		C	28.94	0.00	58	58	0
7292	1800	A	40.07	3.64	678	19	664
		B	35.43	2.02	333	26	311
		C	40.57	4.05	780	28	759
7444	1800	A	24.94	1.83	1741	96	1658
		B	31.16	2.36	2911	153	2777
		C	25.91	1.96	1995	98	1904
7484	1800	A	37.28	2.43	1133	95	1046
		B	41.62	2.15	1097	95	1009
		C	33.22	2.44	1041	85	963
7536	630	A	36.69	0.00	1279	1274	5
		B	44.46	1.89	4316	1781	2560
		C	39.68	1.46	3792	1570	2245
7559	1800	A	45.98	0.00	129	127	2
		B	44.78	2.18	5168	269	4925
		C	0.00	0.00	0	0	0
7560	1800	A	46.13	0.00	129	128	1
		B	46.04	1.93	5577	316	5305
		C	0.00	0.00	0	0	0

The column under N_p lists the number of protons in the bunch; $N_{\bar{p}}$, the number of anti-protons; N_{trig}, the total number of detector triggers recorded for the bunch; N_{bg}, the number of events classified as beam-gas; and N_{bb}, the number of events classified as beam-beam.

Appendix G

Effect of Smearing on a Sample Distribution

Suppose that we have some distribution of η measurements described by $\rho(\eta)$. Now assume that measurement errors in η are described by the probability density $f(\eta,\eta')$, where η = the true η, and η' = the measured value. The observed distribution of tracks, $\rho'(\eta')$, will be given by:

$$\rho'(\eta') = \int_{-\infty}^{\infty} d\eta\, \rho(\eta) f(\eta,\eta').$$

The average track density within some interval in η', $(\eta'_{max} - \eta'_{min}) = \Delta\eta'$, is:

$$\langle\rho'\rangle = \frac{1}{\Delta\eta'}\int_{\eta'_{min}}^{\eta'_{max}} d\eta' \int_{-\infty}^{\infty} d\eta\, \rho(\eta) f(\eta,\eta'). \tag{G.1}$$

Now consider a special case applicable to the VTPC. Assume that the η measurement errors are normally distributed, with mean η and standard deviation σ. For simplicity, assume σ to be independent of η over the interval defined by $\eta_1 = \eta'_{min} - 3\sigma$, and $\eta_2 = \eta'_{max} + 3\sigma$.

Consider now a simple choice for $\rho(\eta)$, such as the quadratic $\rho(\eta) = (a + b\eta + c\eta^2)$. Substituting these choices into equation G.1, we obtain:

$$\begin{aligned}
\langle\rho'\rangle &= \frac{1}{\Delta\eta'}\int_{\eta'_{min}}^{\eta'_{max}} d\eta' \int_{-\infty}^{\infty} d\eta\,(a + b\eta + c\eta^2)\frac{1}{\sigma\sqrt{2\pi}}e^{-\frac{1}{2}\left(\frac{\eta-\eta'}{\sigma}\right)^2} && \text{(G.2)}\\
&= \frac{1}{\Delta\eta'}\int_{\eta'_{min}}^{\eta'_{max}} d\eta' \left\{(a + b\eta' + c\eta'^2) + c\int_{-\infty}^{\infty} d\eta \frac{\eta^2}{\sigma\sqrt{2\pi}}e^{-\frac{1}{2}\left(\frac{\eta}{\sigma}\right)^2}\right\} && \text{(G.3)}\\
&= \langle\rho\rangle + c\sigma^2. && \text{(G.4)}
\end{aligned}$$

Thus, only the quadratic term (and in general, all higher order terms) introduces a bias in the measured average density, $\langle\rho'\rangle$.

Note that since the observed $dN_{ch}/d\eta$ distribution is nearly flat over the entire η range measured with the VTPC, we can conclude that measurement errors in η (for $\sigma \approx 0.1$) should have no effect on the measured $dN_{ch}/d\eta$ distribution.

Appendix H

Background Subtractions

H.1 Calculation of background distributions

Consider a process by which a particular particle species produced directly in $\bar{p}p$ collisions gives rise to charged secondaries. Depending upon the momentum of the secondaries, the portion of the chamber in which they are produced, and the direction they are travelling, there is some probability that one or more of them will produce a track that is found by the reconstruction, passes the track selection, and contributes to $\rho_{obs}(\eta)$ the observed distribution of charged particles. For any given process, we can easily estimate the average η distribution of secondaries which contribute to ρ_{obs}, provided that we understand the physics of the process by which secondaries are produced, and know the transverse momentum and η distributions of the primary particle species. In the following exercise, we will start from a complicated and cumbersome, but more-or-less complete specification of the problem, and derive a form sufficiently tractable to be used for an analysis.

The calculation proceeds in four steps. First, determine how secondaries produced at a particular point in the chamber by a promary with some momentum are distributed in η. Second, weight this distribution by the probability that the secondary track passes track selection (assuming 100% tracking efficiency inside some fiducial volume, and 0% outside). Third, integrate over the incident momentum of the primary. Finally, to obtain the background into a given η, we need only sum the previous distribution over all points in the chamber at which interactions or decays can occur, weighting each point by the probability that secondary production occurs multiplied by the frequency at which the point is traversed by primaries. For the discussion which follows, define $\rho_i(\alpha, z)$ as the density of particle species 'i' in the set of variables α, and the event vertex position, z. We will use the convention (unless otherwise noted) that primed variables refer to quantities relating to primary products of $\bar{p}p$ collision, using unprimed variables for secondaries.

Consider a process by which a neutral particle species 'i' gives rise to charged secondaries. Assume that 'i' is produced with joint (η', p_t') distribution $\rho_i(\eta', p_t')$.

Let $\Gamma(\mathbf{p}', z_v)$ represent the contour of the trajectory of a particular primary of type 'i' with momentum $\mathbf{p}'$, originating from the z vertex position z_v. Next, define $P(\mathbf{p}', \mathbf{r}(\Gamma), z_v)$ as the probability per unit length that a primary with momentum $\mathbf{p}'$, and which originates from z_v, generates charged secondaries at the point $\mathbf{r}$ along the trajectory $\Gamma(\mathbf{p}', z_v)$. These two functions allow us to calculate the probability that a given primary particle produces secondaries.

We calculate the distribution of secondaries which contribute to background by convolving the distribution of secondaries produced at a given point with the probability that a secondary is reconstructed and passes track selection. Therefore, first define $\rho_s^i(\eta, p_t; \eta', p_t', \mathbf{r}(\Gamma), z_v)$ as the distribution of secondaries with transverse momentum p_t produced into η (as would be reconstructed in the chamber), generated by primaries from z_v into η' with p_t'. The distribution is defined for each point $\mathbf{r}$ along the primary's trajectory Γ. Next define $P_s(\eta, p_t, \mathbf{r}(\Gamma))$ as the probability that a secondary produced with p_t into η at the point $\mathbf{r}$ in the chamber is reconstructed and subsequently passes the track selection. Integrating these distributions over the trajectory of a given primary, then averaging over all primaries by integrating over $\rho_i(\eta', p_t')$, yields an expression for $\rho_B^i(\eta, z_v)$, the background distribution of secondaries:

$$\rho_B^i(\eta, z_v) = \iiint dp_t\, dp_t'\, d\eta'\, \rho_i(\eta', p_t') \\ \times \int_{\Gamma(\mathbf{p}', z_v)} dl\, P(\mathbf{p}', \mathbf{r}(\Gamma), z_v) \rho_s^i(\eta, p_t; \eta', p_t', \mathbf{r}(\Gamma), z_v) P_s(\eta, p_t, \mathbf{r}(\Gamma)), \quad \text{(H.1)}$$

where dl denotes the element of path length along the particle trajectory Γ. Integrals over azimuth are implicit. Fortunately, this expression (and the task of estimating the functions in the integrand) can be simplified by assuming that the primary η and p_t distibutions are independent[1], and that the probability function P reduces

[1] They are not quite independent, but since the change in the p_t spectrum is relatively small over a broad range of η, this fact is irrelevant. Also, the distributions we seek tend not to be very sensitive to the p_t spectrum.

to the product of a piece which depends only upon the value of η', and one which contains all the position and momentum dependence:

$$P(\mathbf{p}', \mathbf{r}(\Gamma), z_v) = P(\eta', z_v) f(\eta', p_t', \mathbf{r}(\Gamma), z_v), \tag{H.2}$$

subject to the constraint:

$$\int_{\Gamma(\mathbf{p}', z_v)} dp_t' \, dl \, f(\eta', p_t', \mathbf{r}(\Gamma), z_v) = 1.$$

In this form, $P(\eta', z_v)$ denotes the average probability that secondary production occurs for a primary at a given value of η', while $f(\eta', p_t', \mathbf{r}(\Gamma), z_v)$ describes how secondary production is distributed about the chamber geometry and depends upon p_t' of the primary. Substituting equation H.2 into equation H.1 and integrating over p_t and p_t' yields:

$$\begin{aligned} \rho_B^i(\eta, z_v) &= \iiint dp_t \, dp_t' \, d\eta' \, \rho_i(\eta', p_t') P(\eta', z_v) \\ &\times \int_{\Gamma(\mathbf{p}', z_v)} dl \, f(\eta', \mathbf{p}', \mathbf{r}(\Gamma), z_v) \rho_s^i(\eta, p_t; \eta', p_t', \mathbf{r}(\Gamma), z_v) P_s(\eta, p_t, \mathbf{r}(\Gamma)) \\ &= \int d\eta' \, \rho_i(\eta') P(\eta', z_v) \rho_s^i(\eta; \eta', z_v), \end{aligned} \tag{H.3}$$

where $\rho_s^i(\eta; \eta', z_v)$ is defined by the equation

$$\begin{aligned} &\rho_s^i(\eta; \eta', z_v) = \\ &\iint dp_t \, dp_t' \int_{\Gamma(\mathbf{p}', z_v)} dl \, f(\eta', \mathbf{p}', \mathbf{r}(\Gamma), z_v) \rho_s^i(\eta, p_t; \eta', p_t', \mathbf{r}(\Gamma), z_v) P_s(\eta, p_t, \mathbf{r}(\Gamma)) \end{aligned} \tag{H.4}$$

Defined in this manner, ρ_s^i is the distribution of secondaries that pass the track selection, weighted over the p_t' of primaries into η' and the relative frequency of occurrence at the appropriate locations in the detector.

If $\mathcal{A}(\eta, z_v)$ denotes the chamber η acceptance, then the average η distribution for secondaries that pass the track selection, and therefore contribute to background, is:

$$\rho_B^i(\eta) = \int dz \, P_v(z) \mathcal{A}(\eta, z) \rho_B^i(\eta, z), \tag{H.5}$$

where P_v = the vertex distribution in the event sample. In order to subtract the background, we must obtain estimates for the distributions ρ_s^i, ρ_i, and P and evaluate the integral in equation H.3.

H.2 Examples

H.2.1 Photon conversions

Since the large majority of inclusive photons in $\bar{p}p$ collisions are produced by electromagnetic decays of neutral primaries, it is reasonable to consider photons themselves as primaries. The probability that a photon conversion occurs depends upon the photon conversion cross section and the distribution of material along the photon trajectory. In particular, for the momenta of photons under consideration, $P(\eta', z_v)$ is related to the average number of radiation lengths traversed by a photon at a given η', while $f(\eta', p_t', \mathbf{r}, z_v)$ describes the relative distribution of material along a given trajectory. Assuming that for all relevant energies

$$\rho_s^\gamma(\eta; \eta', z_v) = N_e(\eta, z_v)\delta(\eta - \eta'),$$

where N_e = the effective number of electrons per conversion which contribute to background (ie., pass track selection), then equation H.3 becomes

$$\begin{aligned} \rho_B^\gamma(\eta, z_v) &= \int d\eta' \, \rho_\gamma(\eta') P(\eta', z_v) N_e(\eta, z_v) \delta(\eta - \eta') \\ &= \rho_\gamma P(\eta, z_v) N_e(\eta, z_v). \end{aligned} \tag{H.6}$$

Calculations for N_e and P are described in section 4.5.2.2.

H.2.2 Charged primary particles

If the primary particles under consideration are charged, then an additional term must be added to equation H.3 in order to compensate for the loss of primary particles to secondary interactions or decays, as the case may be. Since the form of this problem is basically the same as that of calculating background distributions, we can immediately write down the additional term as:

$$\begin{aligned}\rho^i_{\mathrm{loss}} &= \int d\eta' \, \rho_i(\eta') P(\eta', z_v)(1 - P^i_{\mathrm{loss}}(\eta'))\delta(\eta - \eta') \\ &= \rho_i(\eta) P(\eta, z_v)(1 - P^i_{\mathrm{loss}}(\eta)).\end{aligned} \tag{H.7}$$

We have introduced $P^i_{\mathrm{loss}}(\eta)$ as the average probability that a primary into η that produces secondaries is not reconstructed or otherwise fails to pass track selection, and therefore does not contribute to $\rho_{\mathrm{obs}}(\eta)$, the observed η distribution of charged particles. The distribution ρ_{loss} must contribute to the correction of ρ_{obs} with the opposite sign of ρ^i_B.

For secondary hadronic interactions, we may assume $P^{\mathrm{had}}_{\mathrm{loss}}(\eta) \approx 1$, since most interactions occur at the inner radius of the chamber, before the primaries are detected.

Appendix I

Description of W and Z Selection Cuts

The selection of W and Z events from a sample of central electron trigger events consists of two steps. The first defines and identifies a low background sample of high-E_t electrons, while the second selects on properties characteristic of W or Z decays. The tables below list the cuts used to define the W and Z data samples. (These tables are copies of tables 22 and 23.) Brief descriptions of each cut, listed according to function, follow in the next sections. More complete descriptions can be found in refs. [81,77,78,79]. Figures 86 and 87 show distributions of the electron identification parameters for a typical set of electron candidates, and global event measures for the W sample. The electron candidates are chosen as the leading electromagnetic cluster in events selected requiring only that $\not{E}_t > 20$ GeV.

I.1 Electron identification

I.1.1 Cluster fiducial cuts

The W and Z analysis requires at least one "well-identified" electron in the central EM calorimeter for two reasons: the CEM calorimeter is well understood, and the VTPC and CTC provide the greatest redundancy to electron identification in the central region. Background from conversion electrons is eliminated using VTPC and CTC data. Although the CEM covers the range $|\eta| < 1.1$, the end towers are not full-sized, and electron tracks do not traverse all layers in the CTC. Therefore, only candidates in the region $|\eta| < 1.0$ are considered. To further ensure full response in the calorimeter, electron candidates must enter the calorimeter at least 2.1 cm away from the ϕ boundaries in the active elements of the wedges, and at least 9 cm from the plane at $\eta = 0$ between arches. A "well identified" electron candidate must have a minimum E_t of 20 GeV either before or after energy corrections.

The fiducial requirements for the second electron in $Z^0 \to e^+e^-$ decays are less stringent in order to improve the overall acceptance: all candidates within $|\eta| <$ 3.1 are considered. A second electron in the CEM calorimeter must satsify the

Table 34. W selection cuts (copy of table 22.)

Electron identification			
EM cluster position:	$\|\eta\|$	$<$	1.0
	$\phi > 2.1$ cm from edge of ϕ segments		
	$z > 9$ cm from crack at 90°		
Cluster E_t:	E_t	$>$	20 GeV
Leakage into hadronic compartment:	HAD/EM	$<$	0.05
Cluster E_t/track $p_t(E/p)$:	$0.5 < E/p < 2.0$		
CTC track/strip chamber match:	$\Delta\phi$	$<$	2.5 cm
	Δz	$<$	3.0 cm
Strip chamber shower profile:	χ^2_{strip}	$<$	15
Energy sharing between lateral towers:	L_{share}	$<$	0.2
Global event measures			
Electron isolation (within $r = 0.4$):	$I(r = 0.4)$	$<$	0.1
Missing transverse energy:	$\not{E}_t$	$>$	20 GeV
Vertex position:	$\|z_v\|$	$<$	60 cm
Excluded EM pair mass:	$50 < m_{ee} < 150$ GeV		

Table 35. Z selection cuts (copy of table 23).

First electron identification			
EM cluster position:	$\lvert\eta\rvert$	>	1.0
	$\phi > 2.1$ cm from edge of ϕ segments		
	$z > 9$ cm from crack at 90°		
Cluster E_t:	E_t	>	20 GeV
Leakage into hadronic compartment:	HAD/EM	<	0.05
Cluster E_t/track p_t (E/p):	$0.5 < E/p < 2.0$		
CTC track/strip chamber match:	$\Delta\phi$	<	2.5 cm
	Δz	<	3.0 cm
Strip chamber shower profile:	χ^2_{strip}	<	15
Energy sharing between lateral towers:	L_{share}	<	0.2
Second electron identification			
EM cluster position:	$\lvert\eta\rvert$	<	3.1
	CEM: same cuts as for first electron		
	FEM and PEM: $\phi > 5°$from quadrant edge		
Cluster E_t:	E_t	>	10 GeV
Leakage into hadronic compartment:	HAD/EM	<	0.10
Cluster E_t/track p_t (E/p) (CEM only):	$0.5 < E/p < 2.0$		
PEM shower profile (3 × 3 pads):	$\chi^2_{3\times3}$	<	20
Global event measures			
Electron isolation (first):	$I(r = 0.4)$	<	0.1
Electron isolation (second):	$I(r = 0.4)$	<	0.2
e^+e^- invariant mass ($M_{e^+e^-}$):	65 GeV $< M_{e^+e^-} <$ 115 GeV		
Vertex position:	$\lvert z_v\rvert$	<	60 cm

same requirements as the first electron. The two large-$|\eta|$ annuli in the PEM are not included in the detector trigger because of high background rates, and second electron candidates in these regions are therefore excluded. Electrons in the Plug EM or Forward EM calorimeters must be greater than 5° in ϕ from quadrant boundaries. A second electron for a Z candidate must have at least 10 GeV in E_t.

I.1.2 Leakage into hadronic compartment

A central electron typically deposits between 95–100% of its energy in the EM compartment of the central calorimeter. Charged pions which shower in the EM calorimeter, on the other hand, generally leave a larger fraction in the hadronic compartment owing to the longer longitudinal profile of hadronic cascades. Analysis of test beam data reveals that the ratio of energy in the hadronic compartment to that in the EM compartment (HAD/EM ratio) efficiently discriminates electrons from early showering pions. Constraining the HAD/EM ratio by the formula

$$\frac{\mathrm{HAD}}{\mathrm{EM}} < 0.055 + 0.45\mathrm{E}_t/100GeV$$

produces an electron sample virtually free of background from early showering pions, and gives greater than 98% efficiency at all E_t. We require

$$\frac{\mathrm{HAD}}{\mathrm{EM}} < 0.05$$

for all electron candidates, which is still fully efficient for the p_t ranges in question. Figure 86(a) shows the HAD/EM distribution for a typical set of electron candidates (see above).

I.1.3 Cluster E_t/track p_t comparison

The CTC provides an independent measurement of the momentum of charged particles. Demanding consistency between the CTC momentum and calorimetry energy measurements improves the quality of the electron identification and removes possible background from superposition of photon and electron showers. The consistency test requires that the ratio of E_t from the calorimetry to the p_t from tracking (E/p) fall in the range $0.5 < E/p < 2.0$. Figure 86(b) shows the E/p distribution for the set of electron candidates.

I.1.4 CTC track/strip chamber match

Since high-p_t electrons are detected with high efficiency in the CTC, electron candidates should have a stiff track in the CTC pointing at the position of the shower within the calorimeter. In order to qualify as an electron candidate, the position of the shower as determined from the strip chambers must agree with the extrapolation of the nearest high p_t track in the CTC to within $\Delta\phi = 2.5$ cm, and $\Delta z = 3$ cm in the plane of the strip chambers. Figures 86(c)–(d) show the track/strip match distributions for a set of electron candidates.

I.1.5 Strip chamber shower profile

The distribution of the spatial response of the strip chambers to a single isolated electron has been measured in a test beam. Comparing the shape of the strip chamber response for a given electromagnetic shower to this distribution of responses, one can calculate the probability that a single electron produced the observed signal. We quantify this test in terms of a χ^2 value, and demand that $\chi^2 < 15.0$ for an electron candidate. Figure 86(e) shows the strip χ^2 distribution for a typical set of electron candidates.

I.1.6 PEM shower profile

A typical electron shower in the PEM calorimeter will deposit energy over serveral towers. As in the case of the central strip chambers, the distribution of pad responses to single, isolated electrons has been measured in a test beam. Comparing the observed response over a 3×3 pad region centered on the cluster to the measured distribution of responses allows calculation of a χ^2 value characterizing the probability that the shower resulted from an isolated electron. The second electron candidate in Z events must have $\chi^2_{3\times3} < 20$. Figure 86(f) shows the pad $\chi^2_{3\times3}$ distribution for a typical set of electron candidates.

I.1.7 Lateral energy sharing

The projective geometry of calorimetry towers serves to reduce the fraction of energy observed in adjacent towers deposited by a single particle from the nominal interaction point. Nevertheless, incident electrons may leave some energy in adjacent towers in η, either because the shower has a non-zero lateral size, or the electron does not originate from the exact center of the detector (the nominal interaction point). The cracks in the ϕ boundaries of wedges are too large to permit sharing across ϕ.

Studies conducted in an electron test beam have measured and parameterized the degree to which high energy electrons, incident at a given angle and location within a tower, will share energy among adjacent towers. The figure of merit for this sharing is termed L_{share}, and is required to be less than 0.2 for all electron candidates. The L_{share} distribution for a typical set of electron candidates is shown in fig. 87(a).

I.2 Global event cuts

I.2.1 Isolation

In the lowest order hadronic production diagram, the W or Z boson is the only final state particle resulting from $q\bar{q}$ annihilation. Except for the boson decay products, the remaining particles in the event result from the underlying event. Since the underlying event particles generally have very low momentum compared to the boson mass, they deposit little energy in the calorimetry. In the next to leading order diagram, the bosons are produced opposite a gluon radiated by an initial state parton. The resulting event contains a jet opposite the boson transverse momentum. Since the boson masses are large compared with the typical transverse momentum of the radiated gluon, the electron momenta are largely uncorrelated with that of the gluon. We can therefore expect that electrons from W and Z decays are "isolated" in the sense that the energy found in the region immediately surrounding the electron should be small compared to the energy of the electron.

We quantify this idea by defining isolation as the ratio

$$I = \frac{\mathrm{E}_t{}^{cone} - \mathrm{E}_t{}^{clus}}{\mathrm{E}_t{}^{clus}},$$

where $\mathrm{E}_t{}^{clus}$ is the transverse energy of the electron candidate, and $\mathrm{E}_t{}^{cone}$ is the transverse energy in a cone of size $r = 0.4$ ($r = \sqrt{(\Delta\phi)^2 + (\Delta\eta)^2}$) around the cluster centroid. A well identified isolated electron must have $I < 0.1$, while the second electron from a Z decay must have $I < 0.2$. Figure 87(b) shows the I distribution for a typical set of electron candidates in events with large $\not{E}_t$ ($\not{E}_t > 20$ GeV).

I.2.2 Missing E_t

Since the neutrino in W decays is undetected, W events generally have a significant quantity of missing energy ($\not{E}_t$). The $\not{E}_t$ is defined as the vector sum of E_t in the calorimetry (corrected for the position of the event vertex). Calculation of the $\not{E}_t$ vector includes corrections for abnormal calorimetry channels and noise. Minimum bias data recorded concurrently with high E_t triggers provide checks for these corrections. To ensure a significant measurement of $\not{E}_t$, we require the corrected $\not{E}_t$ to be greater than 20 GeV. To eliminate loss of energy between the plug and forward calorimetry, we require the event vertex (z_v) to lie within 60 cm of the center of the detector. The $\not{E}_t$ distribution for the W sample is shown in fig. 87(c).

I.2.3 Excluded EM mass region

For W candidate events, we calculate the invariant mass of all electromagnetic energy cluster pairs in the event. We exclude any event which contains an electromagnetic pair invariant mass near the Z mass region. Figure 87(d) shows the distribution of electromagnetic pair masses in all W events that contain more than one electron candidate. A total of 37 events lie within the excluded region.

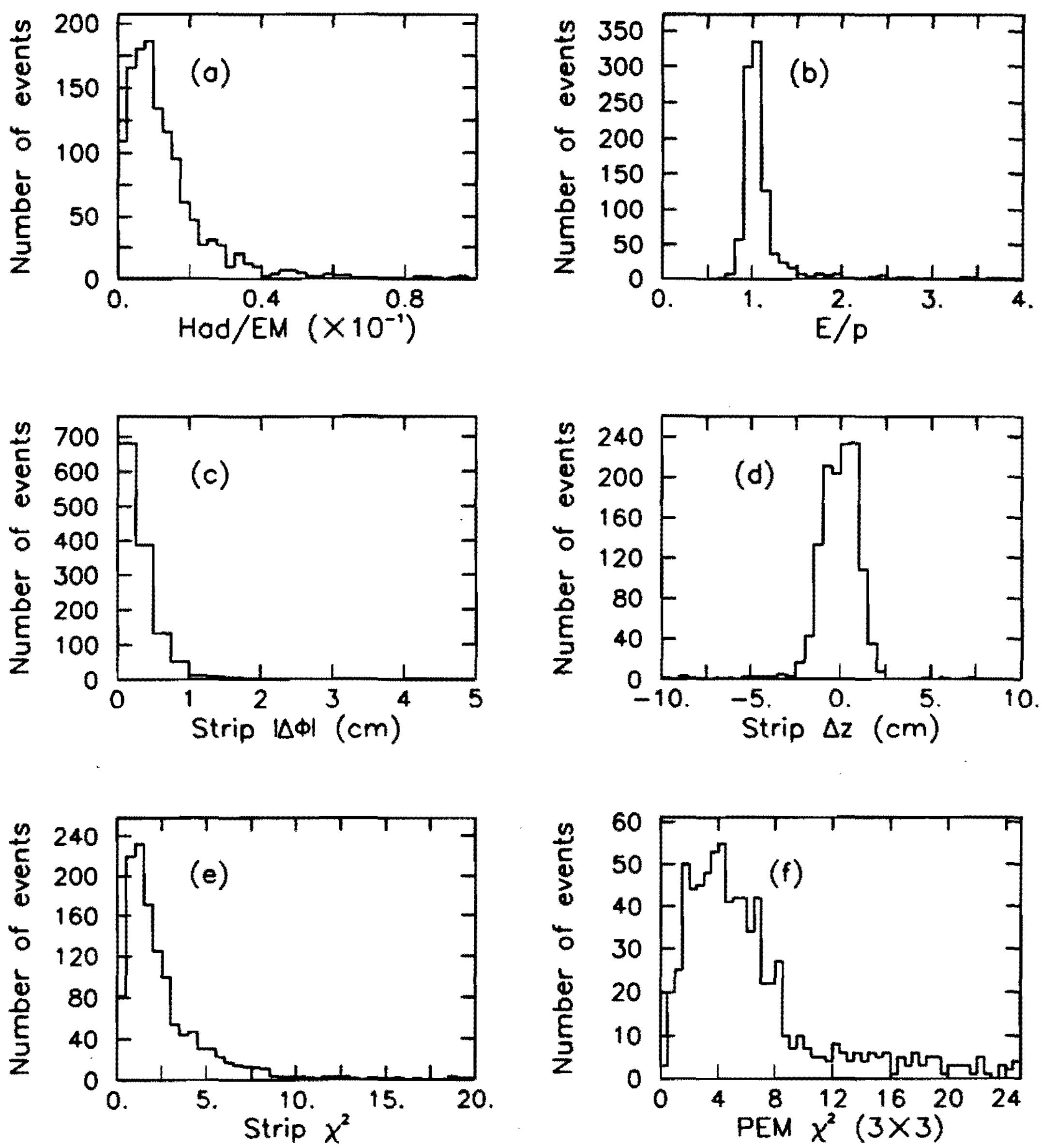

Figure 86. Distributions of parameters used in electron identification for a typical set of electron candidates. (a) The HAD/EM ratio. (b) The E/p ratio. (c) CTC track/strip chamber match in ϕ. (d) CTC track/strip chamber match in z. (e) Strip chamber χ^2 for lateral shower profile. (f) PEM $\chi^2_{3\times3}$ for lateral shower profile.

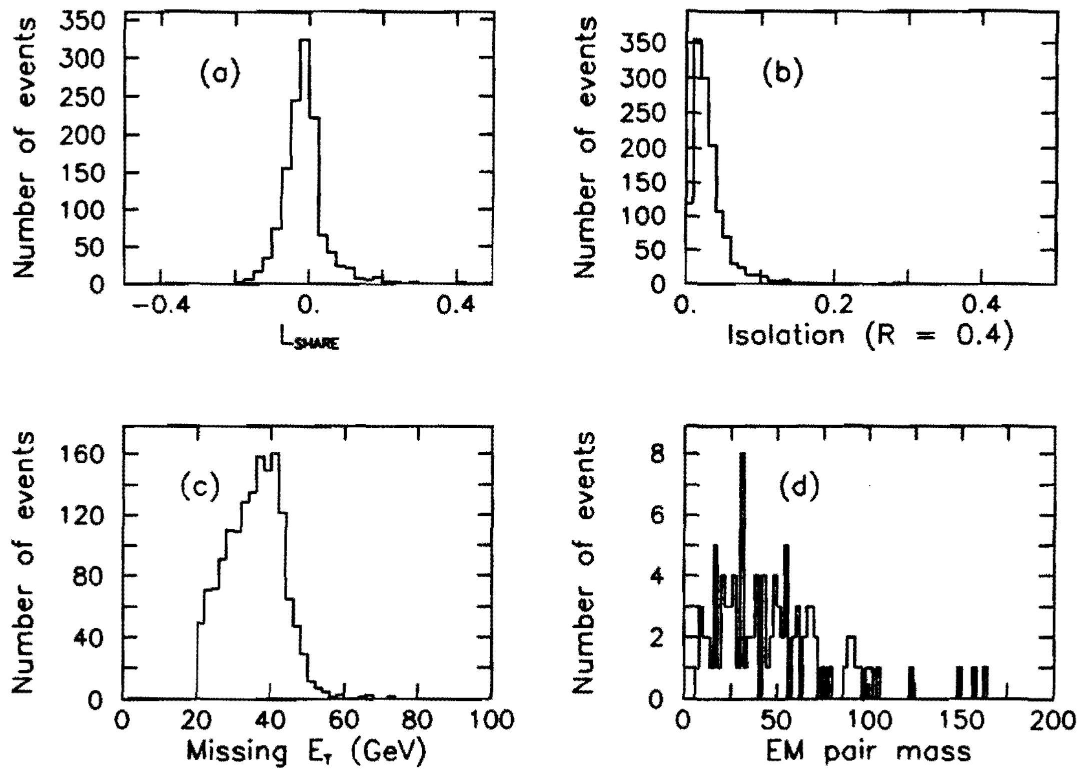

Figure 87. Distribution of parameters used in electron identification and W event selection. (a) The L_{share} distribution (for lateral energy sharing between towers). (b) The distribution of isolation (I for $R = 0.4$). (c) The missing E_t distribution for W events. (d) The invariant mass distribution for electromagnetic cluster pairs in W events with more than a single electron candidate.

Appendix J

Tables Used in R^W and R^Z Analysis

This appendix contains tables with the values of $\langle \rho \rangle$ for minimum bias, $W^{\pm}$ and Z^0 events used to determine R^W and R^Z, and the estimated systematic uncertainties in R^W and R^Z. The systematic uncertainties are estimated from the changes in the value of R induced by changes in the tracking parameters and p_t^W calculations. We extract the actual contributions from each effect using plots of the change in R versus the boson p_t, smoothing by hand and interpolating where appropriate. We assume that the systematic uncertainties arising from tracking efficiency and charged particle background cancellation are the same for W and Z data, and use the W sample (with significantly better statistics than the Z sample) to determine the values. We also neglect the effects of p_t smearing in the Z system, since it should be a much less significant effect than in the W system, and the uncertainties in the Z system are dominated by statistics. The total systematic uncertainty is obtained by summing in quadrature over contributions.

Table 36. Mean $\rho^{\mathrm{W}}(\eta)$ vs. p_t^{W} and mean $\rho^{MB}(\eta)$ as a function of the η interval.

	$\langle\rho^{\mathrm{W}}(\eta)\rangle$ within:		
p_t bin	$\lvert\eta\rvert < 1$	$\lvert\eta\rvert < 2$	$\lvert\eta\rvert < 3$
0.0–2.0	4.82±0.23	5.53±0.32	5.84±0.40
2.0–5.0	5.95±0.17	6.63±0.24	6.85±0.28
5.0–8.0	6.75±0.20	7.39±0.28	7.69±0.34
8.0–16.0	7.25±0.21	7.91±0.29	8.20±0.35
16.0–28.0	7.83±0.39	8.74±0.56	8.88±0.66
28.0–50.0	8.19±0.61	8.87±0.61	8.82±0.59
50.0–100.0	9.76±1.90	9.52±1.96	9.02±1.83
Min. bias:	4.13±0.06	4.46±0.04	4.80±0.04

The uncertainties are purely statistical.

Table 37. Mean $\rho^Z(\eta)$ vs. p_t^Z and mean $\rho^{MB}(\eta)$ as a function of the η interval.

	$\langle\rho^Z(\eta)\rangle$ within:		
p_t bin	$\lvert\eta\rvert < 1$	$\lvert\eta\rvert < 2$	$\lvert\eta\rvert < 3$
0.0–4.0	5.40±0.51	6.02±0.83	6.27±0.99
4.0–8.0	6.35±0.63	7.16±0.93	7.48±1.12
8.0–14.0	6.20±0.80	7.12±1.00	7.13±1.02
14.0–30.0	8.32±0.79	9.05±1.14	9.09±1.30
30.0–60.0	9.26±1.34	9.55±1.34	8.91±1.29
60.0–100.0	11.86±3.01	11.22±3.09	10.59±2.89
Min. bias:	4.13±0.06	4.46±0.04	4.80±0.04

The uncertainties are purely statistical.

Table 38. Contributions to the systematic uncertainty in R^W.

Systematic uncertainties in R^W ($\|\eta\| < 1$):					
p_t bin	Sub.	Eff.	BG	p_t	Sys.
0.0–2.0	0.006	0.08	0.08	0.05	0.12
2.0–5.0	0.006	0.10	0.08	0.13	0.18
5.0–8.0	0.006	0.12	0.08	0.18	0.23
8.0–16.0	0.006	0.15	0.08	0.23	0.29
16.0–28.0	0.006	0.18	0.08	0.28	0.34
28.0–50.0	0.006	0.21	0.08	0.32	0.39
50.0–100.0	0.006	0.21	0.08	0.36	0.42
Systematic uncertainties in R^W ($\|\eta\| < 2$):					
0.0–2.0	0.003	0.08	0.08	0.05	0.12
2.0–5.0	0.003	0.10	0.08	0.11	0.17
5.0–8.0	0.003	0.12	0.08	0.15	0.20
8.0–16.0	0.003	0.15	0.08	0.19	0.25
16.0–28.0	0.003	0.18	0.08	0.23	0.30
28.0–50.0	0.003	0.21	0.08	0.27	0.35
50.0–100.0	0.003	0.21	0.08	0.35	0.41
Systematic uncertainties in R^W ($\|\eta\| < 3$):					
0.0–2.0	0.002	0.08	0.08	0.04	0.12
2.0–5.0	0.002	0.10	0.08	0.10	0.16
5.0–8.0	0.002	0.12	0.08	0.13	0.19
8.0–16.0	0.002	0.15	0.08	0.16	0.23
16.0–28.0	0.002	0.18	0.08	0.20	0.28
28.0–50.0	0.002	0.21	0.08	0.23	0.32
50.0–100.0	0.002	0.21	0.08	0.38	0.44

The column labelled "Sub." refers to the subtraction of decay electron tracks; "Eff." to the cancellation of efficiency corrections; "BG" to the cancellation of charged particle background; and "p_t" to the uncertainty introduced through smearing of the p_t^W distribution; "Sys." to the total estimated systematic uncertainty.

Table 39. Contributions to systematic uncertainty in R^Z.

Systematic uncertainties in R^Z:				
p_t bin	Sub.	Eff.	BG	Sys.
0.0–4.0	0.005	0.08	0.08	0.11
4.0–8.0	0.005	0.12	0.08	0.14
8.0–14.0	0.005	0.15	0.08	0.17
14.0–30.0	0.005	0.18	0.08	0.20
30.0–60.0	0.005	0.21	0.08	0.22
60.0–100.0	0.005	0.21	0.08	0.22

Column headings are the same as in the previous table. These values are valid for all $|\eta|$ intervals.

References

[1] The theory of Quantum Chromodynamics grew from the work of many people. Below is a short list some (but by no means all) of the definitive results leading to the current form of the theory. For the proposal of an SU(3) symmetry to extend isospin symmetry to include strange particles:
M. Gell-Mann, CTSL-20 (1961);
M. Gell-Mann, Phys. Rev. **125**, 1067 (1962);
Y. Ne'eman, Nucl. Phys. **26**, 214 (1964).
For the interpretation of the symmetry in terms of fractionally charged particles (quarks):
M. Gell-Mann, Phys. Lett. **8**, 214 (1964);
G. Zweig, CERN report TH 401, 1964 (unpublished); CERN report 412, 1964 (unpublished).
For a review of theoretical and experimental evidence for fractional charges and three types of quarks (colors) for each flavor:
E. Reya, Phys. Rep. **69**, 195, section 1 and section 5 (1981).
For the realization that quarks, although tightly bound into hadrons (confinement), must behave essentially as free particles within the hadron (asymptotic freedom):
J.D. Bjorken, Phys. Rev. **179**, 1547 (1969);
J.D. Bjorken and E.A. Paschos, Phys. Rev. **185**, 1975 (1969);
J.D. Bjorken and E.A. Paschos, Phys. Rev. **D1**, 3151 (1970).
For the introduction of a gluon octet as the carriers of the strong force between quarks:
H. Fritzsch, M. Gell-Mann and H. Leutwyler, Phys. Lett. **47B**, 365 (1973).
For theorems proving that non-abelian gauge theories are asymptotically free:
H.D. Politzer, Phys. Rev. Lett. **30**, 1346 (1973);
D.J. Gross and F. Wilczek, Phys. Rev. Lett. **30**, 1343 (1973).

Finally, that only non-abelian gauge theories are asymptotically free:
S. Coleman and D.J. Gross, Phys. Rev. Lett. **31**, 851 (1973).

[2] F. Abe *et al.*, Phys. Rev. Lett. **62**, 613 (1989);
F. Abe *et al.*, Phys. Rev. Lett. **62**, 3020 (1989);
F. Abe *et al.*, Phys. Rev. Lett **64**, 157 (1990).

[3] G. Arnison *et al.*, Phys. Lett. **132B**, 214 (1983);
G. Arnison *et al.*, Phys. Lett. **158B**, 494 (1985);
G. Arnison *et al.*, Phys. Lett. **172B**, 461 (1986);
G. Arnison *et al.*, Phys. Lett. **177B**, 244 (1986);
C. Albajar *et al.*, Phys. Lett. **209B**, 127 (1988).

[4] P. Bagnaia *et al.*, Phys. Lett. **138B**, 430 (1984);
P. Bagnaia *et al.*, Phys. Lett. **144B**, 283 (1984);
J.A. Appel *et al.*, Phys. Lett. **160B**, 349 (1985);
J.A. Appel *et al.*, Phys. Lett. **165B**, 441 (1985);
J.A. Appel *et al.*, Z. Phys. **C30**, 341 (1986).

[5] C. Albajar *et al.*, Z. Phys. **C44**, 15 (1989).

[6] P. Bagnaia *et al.*, Z. Phys. **C24**, 1 (1984).

[7] G.J. Alner *et al.*, Z. Phys. **C33**, 1 (1986).

[8] See, for example:
U. Camerini *et al.*, Phil. Mag. **42**, 1241 (1951);
W.O. Lock and G. Yekutieli, Phil. Mag. **43**, 231 (1952).

[9] See, for example:
W. B. Fretter, Phys. Rev **76**, 511 (1949);
A. Lovati *et al.*, Phys. Rev. **77**, 284 (1950).

[10] W.B. Fowler *et al.*, Phys. Rev. **95**, 1026 (1954).

[11] R.E. Marshak, *Meson Physics*, 1st ed. (McGraw-Hill, New York, 1952).

[12] Particularly important was the work done using electron-sensitive emulsions. See, for example:
M.F. Kaplon, B. Peters and H.L. Bradt, Phys. Rev. **76**, 1735 (1949);
M.L. Vidale and M. Schein, Phys. Rev **84**, 593 (1951);
G.W. Rollosson, Phys. Rev. **87**, 71 (1952);
W. Bosley and H. Muirhead, Phil. Mag. **43**, 783 (1952).

[13] H.L. Anderson *et al.*, Phys. Rev. **91**, 155 (1953).

[14] A. Roberts and J. Tinlot, Phys. Rev. **90**, 951 (1953).

[15] L.M. Eisberg *et al.*, Phys. Rev. **97**, 797 (1955).

[16] W.F. Baker *et al.*, Phys. Rev. Lett **7**, 101 (1961).

[17] E. Pickup, D.K. Robinson, and O.E. Salant, Phys. Rev. **125**, 2091 (1962).

[18] E.L. Hart *et al.*, Phys. Rev. **126**, 747 (1962).

[19] L.G. Ratner *et al.*, Phys. Rev. Lett **18**, 1218 (1967).

[20] G. Cocconi, Nuovo Cim. **57A**, 837 (1968).

[21] See Frazer *et al.* in ref. [29].

[22] E.W. Anderson *et al.*, Phys. Rev. Lett **16**, 855 (1966).

[23] D. Dekkers *et al.*, Phys. Rev. **137**, B962 (1965).

[24] D.B. Smith, R.J. Sprafka, and J.A. Anderson, Phys. Rev. Lett **23**, 1064 (1970).

[25] E.W. Anderson *et al.*, Phys. Rev. Lett **19**, 198 (1967).

[26] R.P. Feynman, Phys. Rev. Lett. **23**, 1415 (1969).

[27] J. Benecke *et al.*, Phys. Rev **188**, 2159 (1969).

[28] Z. Koba, H.B. Nielsen, and P. Olesen, Nucl. Phys. **B40**, 317 (1972).

[29] For reviews of the theoretical situation, see:
W.R. Frazer *et al.*, Rev. Mod. Phys. **44**, 284 (1972);
D. Horn, Phys. Rep. **4C**, 1 (1972);
For reviews of the existing experimental data, see:
R.L. Lander, Proc. of APS Div. of Part. and Fields, Rochester (1971);
A. Krisch, *ibid.*.

[30] L.G. Ratner *et al.*, Phys. Rev. Lett **27**, 68 (1971).

[31] B. Alper *et al.*, Phys. Lett. **44B**, 521 (1973);
P. Capiluppi *et al.*, Nucl. Phys. **B70**, 1 (1974);
P. Capiluppi *et al.*, Nucl. Phys. **B79**, 189 (1974).

[32] F.W. Büsser *et al.*, Phys. Lett. **46B**, 471 (1973);
F.W. Büsser *et al.*, Nucl. Phys. **B106**, 1, (1976).

[33] J.W. Cronin *et al.*, Phys. Rev. D. **11**, 3105 (1975).

[34] See Aurenche and Bopp in reference [55].

[35] W. Thome *et al.*, Nucl. Phys. **B129**, 365 (1977).

[36] G.J. Alner *et al.*, Phys. Rep. **154**, 247 (1987).

[37] J. Whitmore *et al.*, Phys. Rep. **10C**, 273 (1974);
W.M. Morse *et al.*, Phys. Rev. **D15**, 66 (1977);
C.P. Ward *et al.*, Nucl. Phys. **B153**, 299 (1979).

[38] C.S. Lam, Phys. Lett. **B217**, 530 (1989).

[39] D. Amati, S. Fubini, and A. Stanghellini, Nuovo Cim. **26**, 896 (1962);
T.W. Kibble, Phys. Rev. **131**, 2282 (1963);
K.A. Ter-Martirosyan, Sov. Phys. JETP **17**, 233 (1963);
S. Fubini, in *Strong Interactions and High Energy Physics*, edited by K.G. Moorhouse (Oliver and Boyd, Edinburgh and London, 1964). For further references, see Frazer *et al.* and Horn in ref. [29].

[40] R. Lipes, G. Zweig, and W. Robertson, Phys. Rev. Lett **22**, 433 (1969).

[41] For example, see:
I. Sarcevic, Los Alamos Report No. LA-UR-86-2704, 1986;
W.R. Chen and R.C. Hwa, Phys. Rev. D. **36**, 760 (1987);
R.C. Hwa, in *Hadronic Multiparticle Production*, edited by P. Carruthers (World Scientific, Singapore, 1988), pp. 556–613.

[42] X. Artru, Phys. Rev. D. **29**, 840 (1984).

[43] R. Hwa, presented at the Third International "Blois" Conference on Elastic and Diffractive Scattering, Northwestern University, Evanston, Ill., 1989 (unpublished).

[44] G. Wataghin, Z. Phys. **88**, 92 (1934).

[45] W. Heisenberg, Z. Phys. **101**, 61 (1936).

[46] C.M.G. Lattes, Y. Fujimoto, and S. Hasegawa, Phys. Rep. **65**, 151 (1980).

[47] W. Heisenberg, Z. Phys. **113**, 61 (1939).

[48] E. Fermi, Prog. Theor. Phys. **5**, 570 (1950);
E. Fermi, Phys. Rev. **81**, 683 (1951).

[49] L.D. Landau., Izv. Akad. Nauk SSSR, Ser. fiz. **17**, 51 (1953);
L.D. Landau and S.Z. Belen'kii, Uspekhi Fiz. Nauk **56**, 308 (1955);
L.D. Landau and S.Z. Belen'kii, Nuovo Cim. Suppl. **3**, 15 (1956).
All the above articles are reprinted in English translation in *Collected Papers of L.D. Landau*, edited by D. Ter Haar (Gordon and Breach, New York, 1965).

[50] G. Cocconi, Phys. Rev. **111**, 1699 (1958).

[51] S. Pokorski and L. Van Hove, Acta Phys. Pol. **B5**, 229 (1974);
L. Van Hove and S. Pokorski, Nucl. Phys. **B86**, 243 (1975).

[52] K. Wehrberger and R.M. Weiner, Phys. Rev. D. **31**, 222 (1985).

[53] R.P. Feynman, *Photon-Hadron Interactions*, 1st ed. (Benjamin, New York, 1972).

[54] F.E. Close, Rep. Prog. Phys. **42**, 1285 (1979).

[55] A. Pagnamenta and U. Sukhatme, Z. Phys. **C14**, 79 (1982);
P. Aurenche and F.W. Bopp, Phys. Lett. **114B**, 363 (1982);
A. Capella and J. Tran Thanh Van, Phys. Lett. **114B**, 450 (1982).

[56] A. Capella *et al.*, Brown University Preprint No. BROWN/HET/616, 1988; published in *Hadronic Multiparticle Production*, edited by P. Carruthers (World Scientific, Singapore, 1988), pp. 428–480.

[57] A.B. Kaidalov, in *Proceedings of the XIXth International Symposium on Multiparticle Dynamics*, edited by D. Schiff and J. Tran Thanh Van (Arles, France, 1988), pp. 407–434.

[58] A. Capella *et al.*, Brown University Preprint No. BROWN/HET/674, 1988.

[59] E.L. Berger *et al.*, Phys. Rev. D. **40**, 83 (1989).

[60] T. Sjöstrand, FNAL Pub. 85/119-T (1985);
T. Sjöstrand and M. van Zijl, Phys. Lett. **B188**, 149 (1987);
T. Sjöstrand and M. van Zijl, Phys. Rev. D. **36**, 2019 (1987).

[61] B. Callen and S. Frankel, Phys. Rev. D. **39** 745 (1989).

[62] F. Abe *et al.*, Nucl. Inst. and Meth. **A271**, 387 (1988).

[63] D. Amidei *et al.*, Nucl. Inst. and Meth. **A269**, 51 (1988).

[64] F. Snider *et al.*, Nucl. Inst. and Meth. **A268**, 75 (1988).

[65] J. Huth, CDF Internal Note 382, 1987 (unpublished).

[66] F. Bedeschi *et al.*, Nucl. Inst. and Meth. **A268**, 50 (1988).

[67] M. Sekiguchi, Ph.D. thesis, University of Tsukuba, 1988.

[68] G. Arnison *et al.*, Phys. Lett. **118B**, 167 (1982).

[69] F. Abe *et al.*, Phys. Rev. Lett. **61**, 1819 (1988).

[70] K. Alpgard *et al.*, Phys. Lett. **115B**, 71 (1982).

[71] F. Abe *et al.*, Phys. Rev. D. **40**, 3791 (1989).

[72] G.J. Alner *et al.*, Nucl. Phys. **B258**, 505 (1988).

[73] D.E. Lyon, C. Risk, and D.M. Tow, Phys. Rev. D. **3**, 104 (1971).

[74] A.V. Tollestrup, CDF Internal Note 584, 1987 (unpublished).

[75] P. Carruthers and Minh Duong-Van, Phys. Lett. **41B**, 597 (1972).

[76] See, for instance, P. Carruthers and Minh Duong-Van, Phys. Rev. D. **28**, 130 (1983).

[77] F. Abe *et al.*, Phys. Rev. Lett **62**, 1005 (1989).

[78] F. Abe *et al.*, Phys. Rev. Lett **64**, 152 (1990);
C. Bowers *et al.*, CDF Internal Note 1026, 1989 (unpublished).

[79] F. Abe *et al.*, Phys. Rev. Lett **63**, 720 (1989).

[80] L. Balka *et al.*, Nucl. Inst. and Meth. **A267**, 92 (1988);
Y. Fukui *et al.*, Nucl. Inst. and Meth. **A267**, 280 (1988);
G. Brandenburg *et al.*, Nucl. Inst. and Meth. **A267**, 257 (1988).

[81] M. Miller, Ph.D. thesis, University of Pennsylvania, 1989.

[82] P. Bagnaia *et al.*, Phys. Lett. **154B**, 338 (1985).

[83] F.D. Snider, presented at the XXIVth Rencontres de Moriond: New Results in Hadronic Interactions, Les Arcs, Savoie, France, 1989 (unpublished).

[84] U. Sukhatme, private communication.